Seismic Modelling for the Sub-Basalt Imaging Problem Including an Analysis and Development of the Boundary Element Method

Andrew Dobson

Thesis submitted in fulfilment of
the requirements for the degree of
Doctor of Philosophy
to the
University of Edinburgh
September 2004

Declaration

I declare that this thesis has been composed solely by myself and that it has not been submitted, either in whole or in part, in any previous application for a degree. Except where otherwise acknowledged, the work presented is entirely my own.

Andrew Dobson
September, 2004

Abstract

The north-east Atlantic margin (NEAM) is important for hydrocarbon exploration because of the growing evidence of hydrocarbon reserves in the region. However, seismic exploration of the sub-surface is hampered by large deposits of flood basalts, which cover possible hydrocarbon-bearing reservoirs underneath. There are several hypotheses as to why imaging beneath basalt is a problem. These include: the high impedance contrast between the basalt and the layers above; the thin-layering of the basalt due to the many flows which make up a basalt succession; and the rough interfaces on the top-basalt interface caused by weathering and emplacement mechanisms.

I perform forward modelling to assess the relative importance of these factors for imaging of sub-basalt reflections. The boundary element method (BEM) is used for the rough-interface modelling. The method was selected because only the interfaces between layers need to be discretized, in contrast to grid methods such as finite difference for which the whole model needs to be discretized, and so should lead to fast generation of shot gathers for models which have only a few homogeneous layers.

I have had to develop criteria for accurate modelling with the boundary element method and have considered the following: source near an interface, two interfaces close together, removal of model edge effects and precise modelling of a transparent interface. I have improved efficiency of my code by: resampling the model so that fewer discretization elements are required at low frequencies, and suppressing wrap-around so that the time window length can be reduced. I introduce a new scheme which combines domain decomposition and a far-field approximation to improve the efficiency of the boundary element code further. I compare performance with a standard finite difference code. I show that the BEM is well suited to seismic modelling in an exploration environment when there are

only a few layers in the model and when a seismic profile containing many shot gathers for one model is required. For many other cases the finite difference code is still the best option.

The input models for the forward modelling are based on real seismic data which were acquired in the Faeroe-Shetland Channel in 2001. The modelling shows that roughness on the surface of the basalt has little effect on the imaging in this particular area of the NEAM. The thin layers in the basalt act as a low-pass filter to the seismic wave. For the real-data acquisition, even the top-basalt reflection is a low frequency event. This is most likely to be due to high attenuation in the layers above the basalt. I show that sea-surface multiple energy is considerable and that it could mask possible sub-basalt events on a seismic shot gather, but any shallow sub-basalt events should still be visible even with the presence of multiple energy. This leaves the possibility that there is only one major stratigraphic unit between the base of the basalt and the crystalline basement.

The implication of the forward modelling and real data analysis for acquisition is that the acquisition parameters must emphasize the low frequencies, since the high frequencies are attenuated before they even reach the top-basalt interface. The implication for processing is that multiple removal is of prime importance.

Acknowledgements

I wish to thank my supervisors Prof. Anton Ziolkowski and Dr. Xiang-Yang Li for all their help with the preparation of this thesis. Special thanks go to Dr. Enru Liu for all his help with the boundary element method. You warned me that BEM would take over my Ph.D. and you were right. Thanks to Derek Ritchie and David McInroy for the help they gave me on the geological side.

Bärbel Traub gets a special mention for putting up with me for the last 4 years. Maybe if you're very good I'll give you some chocolate. I also wish to thank Steve 'Shaggy' Davison, who provided me with bubbles to pop in the latter stages of my thesis and Sonja Maultzsch, who gave me hours (and hours) of her time to help me travel the long and winding road of Aki and Richards (but only up to Chapter 3). Thankyou also Li-Feng Wang and Jinghua Zhang.

I wish to thank my friends on the 'other side': Robin Lee, David Wright, Magnus Hagdorn and many others who have kept my mind off the Ph.D. beast. Many of the people who were here when I began my Ph.D. have now gone away. Some to Oman, some to Germany, some to Norway and some to Aberdeen (in fact, most to Aberdeen). Of these I thank in particular: Fahad Al Kindi (music maestro and comedy supremo), Fabio Mancini ('come on guys, where's the defence?') and Ira Ojala ('zum hei'). Also, Peter Hanssen has helped me greatly with matters of Unix, GMT and of course basalt.

I thank Ruth Addinall, Brian Bainbridge and Jane Robertson for computing support with a cheery face.

Very special thanks go to my parents who have helped me (over the telephone from Coventry) to keep going with this thing. It's been a difficult 4 years, but I got there.

Contents

List of Tables

List of Figures

Notations and Conventions

Tensors, vectors and the summation convention

Tensors such as the strain tensor are denoted as: e_{ij} where the indices (e.g. i, j) go from 1 to 3 unless otherwise stated.

The summation convention is used throughout this thesis:

$$a_i b_i = a_1 b_1 + a_2 b_2 + a_3 b_3.$$

Bold type denotes a vector or a matrix:

$$\mathbf{a} = (a_1, a_2, a_3)$$

Partial derivatives with respect to time are:

$$\dot{\mathbf{a}} = (\frac{\partial a_1}{\partial t}, \frac{\partial a_2}{\partial t}, \frac{\partial a_3}{\partial t})$$

The dot product of two vectors is:

$$\mathbf{a} \cdot \mathbf{b} = a_i b_i$$

The spatial partial derivative of a tensor is denoted as:

$$e_{ij,k} = \frac{\partial e_{ij}}{\partial x_k}.$$

Special Functions

δ_{ij} is the Kronecker Delta where:

$$\delta_{ij} = 1 \quad \text{for} \quad i = j \qquad \text{and} \qquad \delta_{ij} = 0. \quad \text{for} \quad i \neq j$$

ε_{ijk} is the alternating tensor where $\varepsilon_{ijk} = 0$ if any of i, j, k are equal, otherwise $\varepsilon_{123} = \varepsilon_{312} = \varepsilon_{213} = -\varepsilon_{213} = \varepsilon_{321} = \varepsilon_{132} = 1$.

∇ is the Del operator where:

$$\nabla = (\frac{\partial}{\partial x_1}, \frac{\partial}{\partial x_2}, \frac{\partial}{\partial x_3})$$

$\text{curl}\,\mathbf{a} = \nabla \times \mathbf{a}$

$\text{grad}\,\mathbf{a} = \nabla \mathbf{a}$

$\text{div}\,\mathbf{a} = \nabla \cdot \mathbf{a}$

The following identities are used in the text:

$(a_{ij} - a_{ji})b_j = \varepsilon_{ijk}\varepsilon_{jlm}a_{ml}b_k,$

$\varepsilon_{ijk}a_j b_k = (\mathbf{a} \times \mathbf{b})_i.$

Divergence Theorem

Gauss's divergence Theorem:

$$\iint_S (\mathbf{a} \cdot \mathbf{n})\, dS = \iiint_V (\nabla \cdot \mathbf{a})\, dV$$

where S is the surface surrounding volume V and $\mathbf{n}$ is the normal to S.

Symbols

Frequency domain quantities for displacements, tractions and Green's functions are denoted by $\hat{.}$.

$\mathbf{A}$	Displacement/traction matrix
$\mathbf{B}$	Displacement/traction matrix
$\mathbf{C}$	Matrix
c_{ijkl}	4th order tensor where $\tau_{ij}c_{ijkl} = e_{kl}$
$\mathbf{D}$	Propagator matrix
D	Depth
D	Number of sub-domains in domain decomposition
$\mathbf{E}$	Propagator matrix
e_{ij}	Strain tensor

$\mathbf{F}$	Force or incident field matrix
$\mathbf{f}$	Body force
f	Frequency
$\mathbf{G}$	Displacement Green's function (Time domain)
g	Gravitational acceleration
$\mathbf{H}$	Contribution of wavefield to update sub-domain
H_n	Hankel function of order n
h	Length
I	Number of iterations in domain decomposition
K_n	Number of elements making up interface n
L	Line (integral)
l	Length
$\mathbf{n}$	Normal to surface S
$\mathbf{P}$	Traction Green's function (Time domain)
$\mathbf{p}$	Traction vector
P	Pressure
$\mathbf{Q}$	Secondary source matrix
R_i	Residual for iteration i
r_{12}	Reflection coefficient
r	Length
$\mathbf{s}$	Source location
S	Surface (integral)
t	Time
$\mathbf{u}$	Displacement
$\mathbf{v}$	Receiver location
V	Volume (integral)
$\mathbf{x}$	Position vector
α	P-wave velocity
β	S-wave velocity
κ	Number of boundary elements per wavelength
Λ	Absorbing zone length
λ	Wavelength
μ	Lamé parameter
ν	Poisson's ratio
π	$= 3.141592654$
ϕ	Secondary source strength
ρ	Density
θ	Angle
τ_{ij}	Stress tensor
τ	Time delay
ξ	Position vector
ω	Angular frequency

Chapter 1

Introduction

1.1 Thesis objectives

Basalts cover large areas of the north-east Atlantic margin (NEAM). Beneath the basalts lie sedimentary basins which, up until now, have been poorly imaged due to the effect of basalts on propagation of seismic waves. Improved imaging of these basins would increase the chances of finding hydrocarbons, of which there is growing evidence.

The most important problems with sub-basalt imaging have been cited in the past as:

- High impedance contrast between the basalt and the rocks above (Kerrane et al., 2002).
- Thin layering within the basalt (Mack, 1997).
- Roughness on the surface of the basalt (Martini, 2001).
- Multiples (Longshaw et al., 1998).

The purpose of this thesis is to study the effects of basalt on the propagation of seismic waves by forward modelling, with a view to discovering the true reasons why it is so difficult to image beneath basalt. With this knowledge, acquisition parameters and processing sequences could be chosen to provide the best chances for sub-basalt imaging.

A secondary purpose of the thesis is to study the indirect boundary element for forward modelling and assess advantages and disadvantages over other modelling methods. The boundary element method has been selected for analysis because of the possibility of large speed increases for forward modelling compared with the standard grid methods of finite difference and finite element. In the boundary element method only the interfaces between homogeneous layers are discretised. Grid methods require the whole model space to be discretised by a grid and the solution must be found at every point. Therefore, models with a few homogeneous layers are defined efficiently using the boundary element method compared with grid methods and should provide fast computation of synthetic seismograms.

The development and testing of the boundary element code is a large part of this thesis. Because it is a method mainly used in the field of global seismology, which deals with rather different sources and models, I conduct a whole array of tests to determine the suitability of the method for an exploration survey set-up. Later in this thesis I introduce a technique to improve the efficiency of the code and then use the boundary element method for forward modelling.

One of the major causes of poor imaging beneath basalt is considered to be the rough interface at the top of the basalt succession (Martini and Bean, 2002; Lafond et al., 1999). In this thesis, I expand on the modelling previously carried out on rough-layered basalts by performing forward modelling using the boundary element method. The modelling involves roughness over many length scales, of several types and of different source frequencies. This is in contrast to previous studies which have tended to consider only one model computed over only one frequency range.

I cover also the effects of thin-layered basalts, mainly through the use of a reflectivity modelling package. Although work has previously been done in this area (Mack, 1997; Hanssen and Li, 2001), I take a more rigorous approach and attempt to link the seismic response to the thickness and velocity of the layers in a basalt succession.

Modelling in this thesis is very much based on real seismic data which were acquired in the Faeroe-Shetland Channel in 2001. I use an earth model derived from processed data as an input model for forward modelling. The modelling concentrates on sub-basalt imaging in a ‘real’ setting and leads to analysis of

the importance of rough interfaces, thin layers and sea-surface multiples when imaging beneath basalt.

1.2 Claim

In this thesis I look at the possible causes of poor imaging beneath basalt in the Faeroe-Shetland Channel. Through forward modelling I find that neither rough interfaces nor thin layers have a large effect on the sub-basalt image in this region. The most important causes are more likely to be the effect of sea-surface multiples which mask sub-basalt primary events and high attenuation in the layers above the basalt. There is also the possibility that there are no strong reflectors beneath the basalt in this region.

In my analysis of the boundary element method, I develop a method for reducing edge effects from model truncation to a point where they are negligible at low and high frequencies. I find rules of thumb for modelling with the boundary element method for particular model scenarios including: source near an interface, thin-layer modelling and transparent interfaces.

I then describe a new method for improving the efficiency of the boundary element method which combines domain decomposition with a far-field approximation. This method speeds up the computation time of synthetic seismograms considerably and provides the possibility of using larger models than the models which are permitted by the standard boundary element method because of memory restrictions.

Performance of the boundary element method is compared with that of the finite difference method and I conclude that, in some cases, the boundary element method is more efficient, but that in many cases the finite difference method is more suitable.

1.3 Thesis layout

This thesis starts (Chapter 2) with the background to the basalt problem and what has been tried so far to solve it. Chapters 3, 4, 5 and 6 describe the boundary element method used to perform forward modelling in this thesis. Chapters

7, 8, 9 and 10 contain modelling studies which partly use the boundary element method and partly use other forward modelling techniques. The final chapter is conclusions and recommendations for further work in the area.

In Chapter 2, I describe the problems with imaging beneath basalt which are known to date. I then summarise techniques which have been tried so far to image beneath basalt in the north-east Atlantic margin.

In Chapter 3, I give a history of the boundary element method for modelling seismic waves. This is followed by a detailed derivation of the equations necessary to perform forward modelling using the indirect boundary element method.

In Chapter 4, I briefly outline how the boundary element method can be implemented to generate synthetic seismograms.

In Chapter 5, I show the results of many tests which I have conducted on the boundary element method. I make comparisons between the boundary element, finite difference and reflectivity methods.

In Chapter 6, I introduce a technique for improving the efficiency of the boundary element method. The technique utilises domain decomposition and a far-field approximation to speed up computation time.

In Chapter 7, I perform forward modelling on basalt with rough interfaces using the boundary element method. I consider many length scales and types of heterogeneity. .

In Chapter 8, I use the reflectivity method and the Treitel and Robinson normal-incidence method to carry out forward modelling on a thin horizontally-layered basalt succession. I attempt to link the seismic response to the thickness and velocity of the layers in the basalt.

In Chapter 9, I return to the boundary element method to model basalt in a 'real' setting. The input model is derived from real data acquired in the Faeroe-shetland

channel. Effects of lateral heterogeneity are considered in this real setting.

In Chapter 10, an alternative 'real' model is built using traveltime inversion and a real data shot gather. Modelling is performed using reflectivity code. Thin layers and sea-surface multiples are modelled in this real setting.

In Chapter 11, I make conclusions about the suitability of the boundary element method for forward modelling in an exploration seismic environment. I also state what I think are the major problems with imaging beneath basalt in the Faeroe-Shetland Channel, and give recommendations for further work in this area.

Chapter 2

Background to sub-basalt imaging and modelling

2.1 Geological background

2.1.1 Basaltic rocks

Basalt is a fine-grained igneous rock, widespread throughout the surface of the Earth. A large percentage of basalts are found on the ocean floor. These are formed by partially melted mantle material, which rises to the surface at mid-ocean ridges, and solidifies.

Though hardly rivalling in scale the extent of mid-oceanic ridge basalt, flood basalts cover large areas of South America, Africa, Antarctica, India, Siberia, the north-west United States and also the north-east Atlantic Margin (NEAM). These basalts can accumulate very quickly with most of the Atlantic margin flood basalts being extruded within 2-3 million years (White, 1988).

2.1.2 Basalt in the north-east Atlantic margin

Igneous activity in the north-east Atlantic margin is thought to have started around 62 million years ago and continued for around 3 million years until the breakup and the opening of the North Atlantic Ocean (Ritchie et al., 1999). Figure 2.1 shows the extent of the flood basalts along with other Paleogene igneous rocks. The flood basalts were extruded on rifted margins as a result of passive upwelling

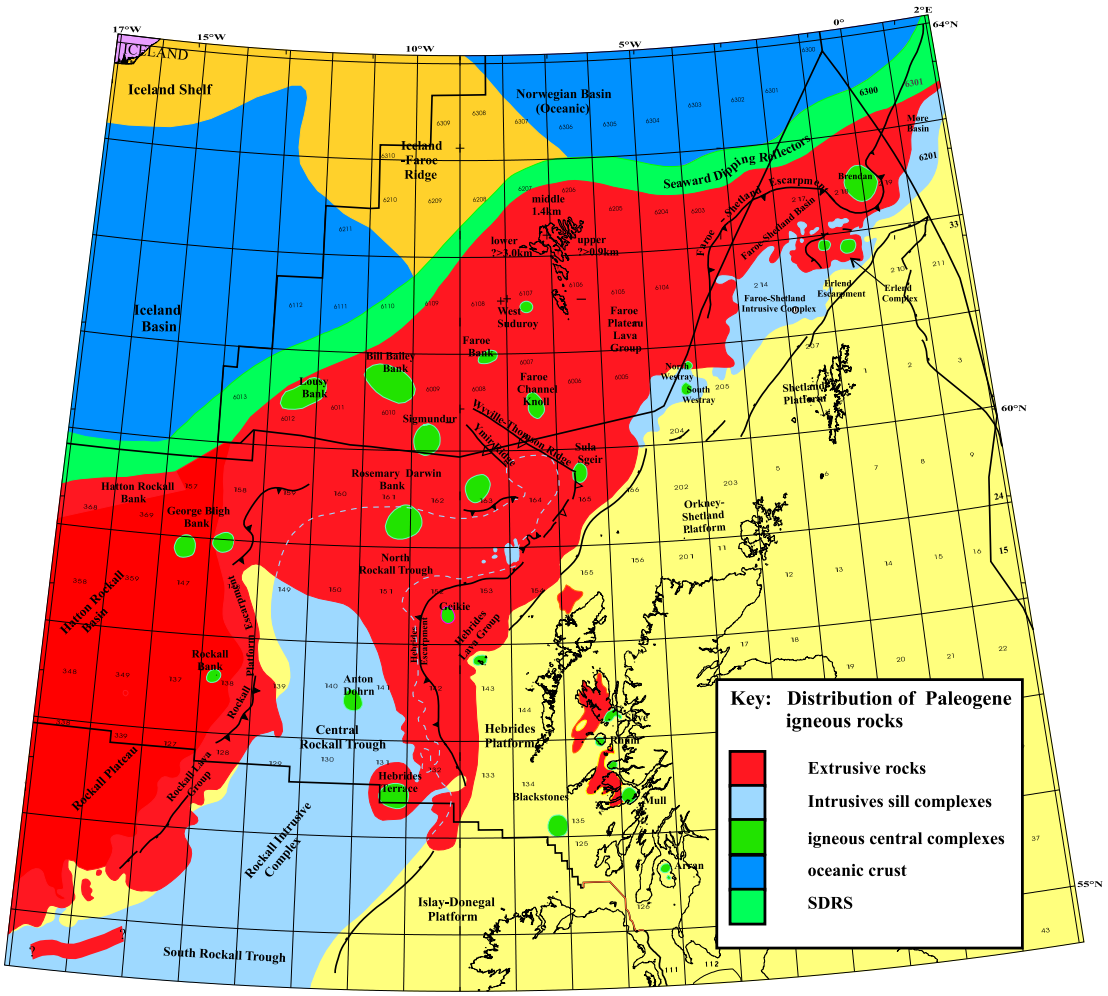

Figure 2.1: Basalt covered areas of the north-east Atlantic margin with igneous centres marked (from Ritchie et al., 1999).

and decompression melting of asthenospheric mantle which was $150-200^{o}$C hotter than normal. The elevated mantle temperature was associated with the initiation of the Iceland Plume which was also responsible for extrusives on Greenland (Ritchie et al., 1999).

The flood basalts initially filled in the local topography and were subsequently able to flow long distances away from the rift (Fliedner and White, 2003). East of the Faeroes flows extend 150km over the earliest Tertiary sediments.

Another main feature of the NEAM are the large areas of intrusives. These are basaltic sills and dykes which have been formed around the same time as the flood basalts.

2.1.3 Pre-Tertiary geology and the search for hydrocarbons

The Atlantic Margin has a history of extensional episodes starting from the late Carboniferous through to the early Paleocene. These have created a series of half-grabens, which were later filled with younger sediments (Fliedner and White, 2003). The deep basement across the entire region between the Shetland and the Faeroe Islands is probably Lewisian gneiss.

There is plentiful evidence of hydrocarbons in the area. Five basins have been explored on the inboard (landward) side of the margin since the 1970s: Halten terrace, the Northern North Sea, the Faeroe-Shetland Basin, the Slyne-Erris troughs and the Porcupine Basin (Spencer et al., 1999). These basins contain proven petroleum systems. The hydrocarbons in most of these basins are in Jurassic sandstone reservoirs within late Jurassic fault traps.

On the outboard (towards the north-west of the margin) side are four frontier areas in which exploration is just beginning: Vøring Basin, Møre Basin, Rockall Basin and the Faeroes Shelf. These have Cretaceous strata many kilometres thick. There are fault traps and compressional dome traps too, though the presence and maturity of source rocks is unknown (Spencer et al., 1999).

Further evidence of hydrocarbons has been found on the Faeroe Islands. Gases and traces of oil were observed in the outflowing water of the deep Lopra-1 well, drilled in 1981. There is a strong indication that the oil was derived from a mature source rock deposited in an anoxic environment. This suggests that the source rock must lie beneath the known basalts (Laier et al., 1997).

2.2 Problems with imaging beneath basalt

2.2.1 Characterisation of basalt in the north-east Atlantic margin

The basalts in the region can take on many forms. Many of the basalts are extruded subaerially. These basalts are characterised by expansive flows of a few metres, which have relatively planar surfaces. The tops and bases of these flows are generally vesicular due to degassing on cooling (Planke et al., 1999; Hald and

Waagstein, 1984) and chemically altered as a result of percolation of fluids through the rock after emplacement. The centres of the flows are for the most part massive with very little vesicularity (under 2%) and some fracturing (Planke et al., 1999). However, when basalt is extruded into water the resulting hyaloclastites (glassy basalt fragments which have been quickly cooled on contact with the water) are very inhomogeneous and can show considerable lateral heterogeneity (Planke and Flovenz, 1996).

2.2.2 High impedence contrast

Basalts of the type seen in the north Atlantic tend to have high velocity and density. The interior of a flow can have a velocity as high as $6.0km/s$ and a density of $2.8g/cm^3$ (Planke, 1994). The sedimentary rock above the basalt in this region has a much lower velocity and density; typically 2-3km/s and $2.0g/cm^3$. This high velocity and density contrast means a high impedence contrast for seismic waves passing through the top or base basalt interface. The higher the impedence contrast, the lower the transmission of energy through the basalt, and the more the reflected energy. This means that the chances of imaging structure beneath the basalt are greatly reduced.

2.2.3 Thin layering

Many studies in the past have treated the basalt as a flat homogeneous layer (e.g. Fliedner and White, 2001; Li and MacBeth, 1997; Kerrane et al., 2002). However, basalt sequences are made up of many flows of varying thickness. The margins of each flow tend to have much lower velocities than the core (Planke et al., 1999) due to chemical alteration and vesicles. Most of the north-east Atlantic margin is covered with basalt sequences which consist of alternating high and low velocity layers (Stoker et al., 1993). In addition, flows are often interbedded with volcaniclastic sediments of 0.5-2m which also act as low velocity layers (Hald and Waagstein, 1984).

It has been shown that a single thin layer can act as a low pass filter (e.g. Ziolkowski and Fokkema, 1986). Mack (1997) showed that the response of a sequence of thin basalt layers is also low pass; as did Hanssen and Li (2001). This suggests that acquisition systems which are tailored to the lower frequency ranges

may have more success in basalt covered areas. This has led to a low-frequency seismic survey being carried out in the Faeroe-Shetland Basin (see section 2.3.4).

2.2.4 Lateral heterogeneity

The tops and bases of basalt flows are typically planar, but possess variable rugosities and are locally irregular due to both eruptive and erosion processes (Bergman, 1997). This rugosity can have a large effect on the seismic wave given the high impedence contrasts present.

One of the earliest studies to consider scattering of seismic energy, due to interface rugosity on the order of a seismic wavelength, was carried out by Paul and Campillo (1988). They found that the scattering of energy which is converted on reflection (PS converted waves) is considerable. P-waves which are reflected at the rough interface are also affected, but to a lesser extent. Martini and Bean (2002) showed that the scattering from the surface of the basalt can be significant enough to mask any reflected energy from beneath the basalt. This led them to develop a wave-equation datuming technique to refocus the scattered energy in the processing.

Studies by Dobson et al. (2002) and Purnell et al. (1990) indicate that the transmitted waves are affected far less than the reflected waves. Thus, the main problem is with scattered energy from interfaces above the target sub-basalt interface.

2.2.5 Multiples

Multiple energy is a major problem for seismic surveying in the north-east Atlantic margin (Longshaw et al., 1998). The most significant multiple energy comes from sea-surface multiples. In many cases, this energy can easily mask sub-basalt reflections, which tend to be weaker.

Removal of this energy is carried out using such techniques as wave equation demultiple and radon demultiple, though such techniques are not always completely successful. Ziolkowski et al. (1999) presented a method to remove all multiple energy associated with the sea surface. However, this method requires perfect sampling in five dimensions (two dimensions for receivers for each shot, two dimensions for shots for each receiver, and time).

2.2.6 Attenuation

Several studies have been caried out to determine the seismic attenuation of basalt. Pujol and Smithson (1991) studied VSP data from Columbia Plateau basalts and found that the scattering effect of the basalt layering is substantially larger than the intrinsic attenuation of the basalt; this was found also to be the case for the Lopra-1 well on the Faeroes (Ker and Rodriguez, 2002), and for the basalts in the region of north Norway (Rutledge and Winkler, 1989). Kiørbie and Petersen (1995) found that the intrinsic attenuation of basalt is no greater than that of sedimentary rock.

2.2.7 Anisotropy

Weak azimuthal anisotropy in basalts has been observed by Kiørbie and Petersen (1995) and Christie et al. (2002) in the Lopra-1 well. The anisotropy was found to be consistent with mapped master joints at the surface. Li et al. (1997) suggest that two sources of anisotropy may be present in the basalt: transverse isotropy from sequences of lava flows, and azimuthal anisotropy from fractures, joints and vesicles. The total effect could be anything between 5 and 30% for both P- and S-waves.

2.3 Seismic exploration in the region

2.3.1 Early surveys

Exploration in the area started in the late 60s and early 70s and consisted mainly of refraction seismic. Pálmason (1965) conducted a refraction survey on the Faeroes to determine the velocity the basalt on the islands while Scrutton (1972) used refraction and gravity to study the structure of the Rockall Plateau.

The most extensive coverage of commercial data was shot by Western Geophysical between 1972 and 1985 with the bulk of coverage being on the Hebridean and West shetland shelves (Bulat, 1991). The quality of these data is good down to the top basalt but reveals little at deeper levels.

2.3.2 Converted-wave surveys

In a bid to improve the imaging of structure beneath the basalt, converted-wave acquisition and processing were attempted. The reasoning behind using converted waves lies in the strong conversion which is expected on transmission at the top and base of the basalt. The converted energy has been shown to be strongest when the S-wave velocity of the basalt is equal to the P-wave velocity of the surrounding sediment (Purnell, 1992). Velocity matching of the P- and S-modes also minimises the geometrical spreading loss suffered by the mode conversion. Processing using this converted wave mode can be carried out in the standard way because the ray-path is symmetric just as in the pure P-wavemode.

Preliminary investigations using this technique were described by Li et al. (1997) while Kerrane et al. (2002) claim improved imaging using the converted waves. However, studies by Hanssen et al. (2003) have shown that converted-wave processing is unlikely to give any major improvements over standard P-wave processing.

2.3.3 Wide-angle surveys

Wide-angle data, which have been acquired throughout the last two decades, can be split into to main groups: converted-wave imaging (see above), and traveltime inversion of refracted waves and wide angle P-wave reflections. Joppen and White (1990) describe a two-boat acquisition system deployed around the Rockall trough. Because the streamer lengths in the early days were generally only a few kilometers long, wide-angle data were recorded by shooting from one boat and receiving at another. Ray-tracing and reflectivity modelling were used to update subsurface models, and the results were analysed in conjunction with data from standard reflection surveys.

Refracted arrivals circumvent many of the problems normally encountered in sub-basalt imaging because the first arrivals outside the water cone have to be primary energy. Multiple energy is only present at near-offsets or further down the seismogram. The FLARE project (e.g. Fruehn et al., 2001) has made extensive use of refracted arrivals to build velocity models of sub-basalt layers in the Faeroe Shetland basin.

2.3.4 Low-frequency surveys

As a result of the thin-layered basalt modelling by Mack (1997), and previous knowledge about the low-pass nature of a thin layer (e.g. Ziolkowski and Fokkema, 1986), an acquisition system was designed which enhances the low-frequency ranges (Ziolkowski et al., 2003). This was achieved by adding two large 2000 cu. in. airguns to the standard array. In addition, the airgun array and the hydrophone streamer were towed at a greater depth of 15m, compared with 5m for a standard acquisition system. This has the effect of boosting the low-frequencies because of the interference between the direct wave and the source and receiver ghosts from the sea surface.

Improvements in reflections below the top basalt were observed in the data when compared with a previous standard-frequency survey along the same line.

A low-frequency survey of the Slyne Basin described by Dancer and Pillar (2002) also shows that low-frequency acquisition can greatly improve the image beneath the basalt.

Low-frequency, long-offset data were acquired in the summer of 2002 by the iSIMM project (White et al., 2002; Spitzer et al., 2004). Low-frequency energy was generated from a large, deep-towed source array tuned on the first bubble (Avedik et al., 1993; Lunnon et al., 2003). Both OBS and towed-streamer acquisitions were carried out.

2.4 Summary

Seismic exploration in the north-east Atlantic margin is of interest because of the evidence of hydrocarbons in the region. However, it has proved difficult to image beneath the basalts, which cover possible hydrocarbon-bearing basins. Imaging beneath basalt is a difficult problem because of one or a combination of the following reasons:

- The high velocity and density of the basalt.
- Thin layering within the basalt.
- Lateral heterogeneity on the surface of the basalt (rugosity).

- Sea-surface multiples
- Attenuation
- Anisotropy

Many techniques have been attempted in order to solve the sub-basalt imaging problem including:

- Converted-wave surveys.
- Wide-angle surveys.
- Low-frequency surveys.

These techniques have had limited success. In the following chapters I consider several of the problems listed above and perform forward modelling to enhance knowledge of what the important factors are, and why it is so difficult to image beneath basalt.

Chapter 3

Introduction to the boundary element method

3.1 Introduction

In Chapter 2, I present a summary of the problems encountered when trying to image beneath basalt. I also give examples of some of the modelling studies which have been undertaken to aid understanding of these problems. In this chapter, I describe how the indirect boundary method is used to generate synthetic seismograms for single and multi-layer models. In later chapters the boundary element method is implemented for generating seismograms (Chapter 4), tested (Chapter 5), made more efficient (Chapter 6) and finally used for modelling (Chapters 7 and 9).

3.2 Boundary methods for seismic modelling

Boundary methods have been used extensively for modelling earthquakes in heterogeneous media (e.g. Pedersen et al., 1996; Sánchez-Sesma and Campillo, 1991). However, very little research has been done on use of these methods for exploration geophysics. Boundary methods differ from numerical grid methods (such as finite difference and finite element methods) in that only the interfaces between homogeneous layers are discretized. Grid methods require the whole model space to be discretized by a grid and the solution must be found at every

point. The grid spacing must generally be much smaller than the shortest seismic wavelength, which means computation of seismograms can be time consuming. Advantages of boundary methods over grid methods include higher accuracy and reduced memory requirements to specify a given input model. Boundary methods are more suited to models which can be easily represented by a few interfaces and by large homogeneous regions.

The origins of boundary methods for modelling seismic waves can be traced back to pioneering work by Aki and Larner (1970). Their method begins by expressing the displacement as an integral over wavenumber. They set the boundary conditions of continuity of traction and displacement at a boundary between two elastic layers, and vanishing traction at the free surface. These boundary conditions result in two integral equations over wavenumber, which are solved by assuming a periodicity in the interface depth. The assumption of periodicity permits the integral equations to be approximated by finite sum equations which are solved via the use of the Fourier transform. The Aki and Larner method has found many applications in seismology. However, it is unstable for models containing steeply dipping interfaces and for high frequencies (Sánchez-Sesma et al., 1989).

Bouchon (1985) introduced a discrete wavenumber method (Bouchon and Aki, 1977) in which the scattered wavefield is represented by a distribution of forces along the diffracting interface . The approach consists of determining the surface forces which cancel the incident stress. The model is assumed to be periodic as in the Aki and Larner method so that the integral can be approximated by a finite summation. In contrast to the Aki and Larner method though, the model is also discretized. The solution was shown to be stable for high frequencies and steep dips. The effects of periodicity in the model are removed by making use of complex frequency (see Chapter 5).

Direct methods (e.g. Kawase, 2002) find the displacement and stress directly from a set of boundary equations. The method of Bouchon (1985) is known as an 'indirect' method because the solution to the set of boundary equations is the surface force, i.e., a quantity that does not directly describe the state of the medium (Bouchon et al., 1989; Campillo and Bouchon, 1985; Sánchez-Sesma and Campillo, 1991). To find the state of the medium at a particular location a second step must be carried out which involves equations relating the indirect

quantity to the state of the medium at that location. In the method described by Bouchon (1985), the displacement in the medium can only be found after the secondary sources on the surface have been computed. The idea of surface forces can be regarded as a numerical realisation of Huygens' principle (Sánchez-Sesma and Luzón, 1995). The direct and indirect methods have been shown to be mathematically equivalent (Banerjee and Butterfield, 1981).

Although the discrete wavenumber method used by Bouchon and others is accurate for many types of heterogeneity, it is computationally intensive. In 1991, Sanchez-Sesma and Campillo presented a boundary element method which was based on the Somigliana representation theorem. In their formulation, full-space Green's functions are used. This method was adapted for multi-layered media by Pedersen et al. (1996) using the propagator matrix formulation outlined by Bouchon et al. (1989).

In the next section, I describe the formulation used to compute synthetic seismograms using the indirect boundary element method (IBEM).

3.3 Stress and strain in an elastic medium

This derivation of the stress and strain tensors follows that of Aki and Richards (1980).

3.3.1 The strain tensor

If a particle, initially at position $\mathbf{x}$, is moved to position $\mathbf{x} + \mathbf{u}$ then the displacement for that particle is described as $\mathbf{u}(\mathbf{x})$. The displacement for a particle initially at position $\mathbf{x} + \delta\mathbf{x}$ is $\mathbf{u}(\mathbf{x} + \delta\mathbf{x})$. The difference in displacement between points $\mathbf{x}$ and $\mathbf{x} + \delta\mathbf{x}$ is $\delta\mathbf{u} = \mathbf{u}(\mathbf{x} + \delta\mathbf{x}) - \mathbf{u}(\mathbf{x})$.

Since $|\delta\mathbf{x}|$ is arbitrarily small, $\mathbf{u}(\mathbf{x} + \delta\mathbf{x})$ can be expanded as $\mathbf{u} + (\delta\mathbf{x} \cdot \nabla)\mathbf{u}$ plus negligible terms of order $|\delta\mathbf{x}|^2$. Thus

$$\delta\mathbf{u} = (\delta\mathbf{x} \cdot \nabla)\mathbf{u}, \qquad or \qquad \delta u_i = \frac{\partial u_i}{\partial x_j}\delta x_j. \tag{3.1}$$

The partial derivative shown above can be written as a second order tensor

$$V_{ij} = \frac{\partial u_i}{\partial x_j}, \tag{3.2}$$

which, as with all second order tensors, can be split into a symmetric and an anti-symmetric part as follows:

$$V_{ij} = \frac{1}{2}(u_{i,j} + u_{j,i}) + \frac{1}{2}(u_{i,j} - u_{j,i}), \tag{3.3}$$

so the expression for the difference in displacement becomes

$$\delta u_i = \frac{1}{2}(u_{i,j} + u_{j,i})\delta x_j + \frac{1}{2}(u_{i,j} - u_{j,i})\delta x_j \tag{3.4}$$

By use of tensor identities (shown in the notation section at the start of this thesis) the second term can be rewritten to give

$$\delta u_i = \frac{1}{2}(u_{i,j} + u_{j,i})\delta x_j + \frac{1}{2}(\mathrm{curl}\mathbf{u} \times \delta\mathbf{x})_i. \tag{3.5}$$

Under the assumption that the partial derivatives $|u_{i,j}| \ll 1$, the second term can be interpreted as a rigid body rotation, i.e., it does not affect the length of the line $\delta\mathbf{x} + \delta\mathbf{u}$ and, therefore, the effect of true distortion on the line element δx_i is to change the relative position of the end points by $e_{ij}\delta x_j$ where

$$e_{ij} = \frac{1}{2}(u_{i,j} + u_{j,i}), \tag{3.6}$$

and is known as the strain tensor.

3.3.2 Traction and the stress tensor

Traction is defined by the equation

$$\mathbf{p}(\mathbf{n}) = \delta\mathbf{F}/\delta S \qquad as \qquad \delta S \to 0, \tag{3.7}$$

where $\delta\mathbf{F}$ is an infinitesimal force acting across an infinitesimal area δS and $\mathbf{n}$ is the normal to the area δS. Traction can be written in the form

$$\mathbf{p}(\mathbf{n}) = \mathbf{p}(\hat{\mathbf{x}}_j)n_j, \tag{3.8}$$

where $\hat{\mathbf{x}}_j$ is the unit vector in direction j (Aki and Richards, 1980). The stress tensor is defined as

$$\tau_{ij} = p_j(\hat{\mathbf{x}}_i), \tag{3.9}$$

so that τ_{ij} is the jth component of traction acting across the plane normal to the ith axis. The stress tensor is symmetric (Aki and Richards, 1980), therefore the traction can be written

$$p_i = \tau_{ij}n_j. \tag{3.10}$$

3.3.3 Equation of motion

There are two types of force to which a volume V can be subjected: surface forces and body forces. The sum of surface and body forces is, by Newton's second law, equal to the rate of change of momentum. Expressed another way:

$$\iiint_V \rho\frac{\partial^2\mathbf{u}}{\partial t^2}\,dV = \iiint_V \mathbf{f}\,dV + \iint_S \mathbf{p}(\mathbf{n})\,dS, \tag{3.11}$$

where the first term on the right is the contribution from body forces ($\mathbf{f}$ is force per unit volume) and the second term is the contribution from the surface forces. The surface integral can be written as a volume integral by applying Gauss's divergence theorem and Equation 3.10 to give

$$\iint_S p_i\,dS = \iint_S \tau_{ij}n_j\,dS = \iiint_V \tau_{ij,j}\,dV, \tag{3.12}$$

so for a volume V the following is valid:

$$\iiint_V (\rho\ddot{u}_i - f_i - \tau_{ij,j})\,dV = 0. \tag{3.13}$$

The integrand must be zero wherever it is continuous, otherwise a volume V

could be found that violates Equation 3.13, hence

$$\rho\ddot{u}_i = f_i + \tau_{ij,j}. \tag{3.14}$$

3.3.4 Hooke's law

The modern generalisation of Hooke's law states that each component of the stress tensor is a linear combination of all components of the strain tensor, i.e., there exists a constant tensor c_{ijkl} for which

$$\tau_{ij} = c_{ijkl}e_{kl}. \tag{3.15}$$

This fourth-order tensor has the following symmetries:

$$c_{jikl} = c_{ijkl} \qquad (\text{due to } \tau_{ji} = \tau_{ij}), \tag{3.16}$$

$$c_{ijlk} = c_{ijkl} \qquad (\text{due to } e_{lk} = e_{kl}), \tag{3.17}$$

and

$$c_{klij} = c_{ijkl}, \tag{3.18}$$

which can be proved from a thermodynamic argument (Aki and Richards, 1980).

3.3.5 Betti's reciprocal theorem

Consider a volume V with a surface S. The displacement field $\mathbf{u} = \mathbf{u}(\mathbf{x}, t_1)$ within volume V is due to body forces $\mathbf{f}$, boundary conditions on S and initial conditions at time $t_1 = 0$. A different displacement field $\mathbf{v} = \mathbf{v}(\mathbf{x}, t_2)$ within volume V is due to body forces $\mathbf{g}$, a different set of boundary conditions on S and initial conditions at time $t_2 = 0$. The two sets of forces and displacements are related by Betti's reciprocal theorem:

$$\begin{aligned}&\iiint_V (\mathbf{f} - \rho\ddot{\mathbf{u}}) \cdot \mathbf{v}\, dV + \iint_S \mathbf{p}(\mathbf{n}) \cdot \mathbf{v}\, dS \\ &= \iiint_V (\mathbf{g} - \rho\ddot{\mathbf{v}}) \cdot \mathbf{u}\, dV + \iint_S \mathbf{q}(\mathbf{n}) \cdot \mathbf{u}\, dS,\end{aligned} \tag{3.19}$$

where $\mathbf{p}$ is the traction relating to $\mathbf{u}$ and $\mathbf{q}$ is the traction relating to $\mathbf{v}$ This result can be proved by first substituting Equations 3.10 and 3.14 into Equation 3.19 to give

$$\begin{aligned}&\iiint_V -\tau^u_{ij,j} v_i\, dV + \iint_S (\tau^u_{ij} v_i) n_j\, dS \\ &= \iiint_V -\tau^v_{ij,j} u_i\, dV + \iint_S (\tau^v_{ij} u_i) n_j\, dS\end{aligned} \quad , \tag{3.20}$$

where the superscripts on the stress tensors denote which displacement field they refer to. Gauss's divergence theorem can be applied to the surface integral on the left-hand side to give

$$\iint_S (\tau^u_{ij} v_i) n_j\, dS = \iiint_V \frac{\partial(\tau^u_{ij} v_i)}{\partial x_j}\, dV. \tag{3.21}$$

I next evaluate the partial derivative:

$$\frac{\partial(\tau^u_{ij} v_i)}{\partial x_j} = \tau^u_{ij} v_{i,j} + v_i \tau^u_{ij,j}. \tag{3.22}$$

The surface integral on the right-hand side can be evaluated in a similar manner so Equation 3.20 now becomes

$$\begin{aligned}&\iiint_V -\tau^u_{ij,j} v_i\, dV + \iiint_V [\tau^u_{ij} v_{i,j} + v_i \tau^u_{ij,j}]\, dV \\ &= \iiint_V -\tau^v_{ij,j} u_i\, dV + \iiint_V [\tau^v_{ij} u_{i,j} + u_i \tau^v_{ij,j}]\, dV,\end{aligned} \tag{3.23}$$

Through cancellation of terms and application of Equations 3.6 and 3.15 the following equation is yielded:

$$\iiint_V c_{ijkl} u_{k,l} v_{i,j}\, dV = \iiint_V c_{ijkl} v_{k,l} u_{i,j}\, dV \tag{3.24}$$

The left-hand side and right-hand side are equal because of the symmetry in the c_{ijkl} tensor (Equation 3.18). This proves that Equation 3.19 is correct.

If t_1 and t_2 are chosen such that $t_1 = t$ and $t_2 = \tau - t$ and integration over all time is carried out, then Equation 3.19 becomes:

$$\begin{aligned}
&\int_{-\infty}^{\infty} dt \iiint_V \{\mathbf{u}(t) \cdot \mathbf{g}(\tau - t) - \mathbf{v}(\tau - t) \cdot \mathbf{f}(t)\} dV + \\
&\int_{-\infty}^{\infty} dt \iiint_V \rho\{\ddot{\mathbf{u}}(t) \cdot \mathbf{v}(\tau - t) - \ddot{\mathbf{v}}(\tau - t) \cdot \mathbf{u}(t)\} dV \\
&= \int_{-\infty}^{\infty} dt \iint_S \{\mathbf{v}(\tau - t) \cdot \mathbf{p}(t) - \mathbf{u}(t) \cdot \mathbf{q}(\tau - t)\} dS.
\end{aligned} \tag{3.25}$$

By changing the order of integration, the second integral can be written:

$$\begin{aligned}
&\iiint_V dV \int_{-\infty}^{\infty} \rho\{\ddot{\mathbf{u}}(t) \cdot \mathbf{v}(\tau - t) - \ddot{\mathbf{v}}(\tau - t) \cdot \mathbf{u}(t)\} dt \\
&= \iiint_V dV \int_{-\infty}^{\infty} \rho \frac{\partial}{\partial t} \{\dot{\mathbf{u}}(t) \cdot \mathbf{v}(\tau - t) + \dot{\mathbf{v}}(\tau - t) \cdot \mathbf{u}(t)\} dt \\
&= \iiint_V dV \rho \big[\dot{\mathbf{u}}(t) \cdot \mathbf{v}(\tau - t) + \dot{\mathbf{v}}(\tau - t) \cdot \mathbf{u}(t)\big]_{-\infty}^{\infty}
\end{aligned} \tag{3.26}$$

If there is some time before which $\mathbf{u}$ and $\mathbf{v}$ (and therefore $\dot{\mathbf{u}}$ and $\dot{\mathbf{v}}$) are zero

everywhere throughout V, the integral goes to zero and Equation 3.25 becomes,

$$\int_{-\infty}^{\infty} dt \iiint_V \{\mathbf{u}(t) \cdot \mathbf{g}(\tau - t) - \mathbf{v}(\tau - t) \cdot \mathbf{f}(t)\} dV$$
$$= \int_{-\infty}^{\infty} dt \iint_S \{\mathbf{v}(\tau - t) \cdot \mathbf{p}(t) - \mathbf{u}(t) \cdot \mathbf{q}(\tau - t)\} dS. \tag{3.27}$$

3.3.6 Green's functions

The displacement Green's function for an elastic medium $G_{in}(\mathbf{x}, t; \boldsymbol{\xi}, \tau)$ gives the displacement resulting in direction i at point $\mathbf{x}$ and time t from a unidirectional unit impulsive force applied in direction n at point $\boldsymbol{\xi}$ and time τ. From Equation 3.14, it satisfies the equation:

$$\rho \frac{\partial^2}{\partial t^2} G_{in} = A\delta_{in}\delta(\mathbf{x} - \boldsymbol{\xi})\delta(t - \tau) + \frac{\partial}{\partial x_j}\Big(c_{ijkl}\frac{\partial}{\partial x_l} G_{kn}\Big), \tag{3.28}$$

where A is a unit constant with units of impulse (force $\times$ time). If the boundary conditions for the Green's function are independent of time, then $\mathbf{G}$ depends on t and τ only via the combination $t - \tau$. Therefore the Green's function has the following property.

$$G_{ij}(\mathbf{x}, t; \boldsymbol{\xi}, \tau) = G_{ij}(\mathbf{x}, t - \tau; \boldsymbol{\xi}, 0) \tag{3.29}$$

Knopoff and Gangi (1959) showed that if $\mathbf{G}$ satisfies homogeneous boundary conditions on S, the following reciprocity relation results:

$$G_{ij}(\mathbf{x}, t; \boldsymbol{\xi}, \tau) = G_{ji}(\boldsymbol{\xi}, \tau; \mathbf{x}, t). \tag{3.30}$$

The Green's function for traction is found from the displacement Green's function via Hooke's law:

$$P_{in}(\mathbf{x}, t; \boldsymbol{\xi}, \tau) = c_{ijkl} n_j G_{kn,l}(\mathbf{x}, t; \boldsymbol{\xi}, \tau). \tag{3.31}$$

3.3.7 Representation theorems

The purpose of a representation theorem is to find an expression for the displacement $\mathbf{u}$ due to body forces $\mathbf{f}$ throughout V and to boundary conditions

on S. This can be achieved by substituting into Equation 3.27 the body force $g_i(\mathbf{x},t) = \delta_{in}\delta(\mathbf{x}-\boldsymbol{\xi})\delta(t)$, (where the constant A from Equation 3.28 is equal to 1 kg.m/s) for which the corresponding solution is $v_i(\mathbf{x},t) = G_{in}(\mathbf{x},t;\boldsymbol{\xi},0)$ to find

$$\begin{aligned} u_n(\boldsymbol{\xi},\tau) = &\int_{-\infty}^{\infty} dt \iiint_V f_i(\mathbf{x},t)G_{in}(\mathbf{x},\tau-t;\boldsymbol{\xi},0)\,dV_{\mathbf{x}} \\ &+ \int_{-\infty}^{\infty} dt \iint_S \{G_{in}(\mathbf{x},\tau-t;\boldsymbol{\xi},0)p_i(\mathbf{u}(\mathbf{x},t),\mathbf{n}) \\ &\qquad -u_i(\mathbf{x},t)P_{in}(\mathbf{x},\tau-t;\boldsymbol{\xi},0)\}\,dS_{\mathbf{x}}. \end{aligned} \tag{3.32}$$

In order to give more physical insight into this equation, the symbols $\mathbf{x}$ and $\boldsymbol{\xi}$ are interchanged along with t and τ to give

$$\begin{aligned} u_n(\mathbf{x},t) = &\int_{-\infty}^{\infty} d\tau \iiint_V f_i(\boldsymbol{\xi},\tau)G_{in}(\boldsymbol{\xi},t-\tau;\mathbf{x},0)\,dV_{\boldsymbol{\xi}} \\ &+ \int_{-\infty}^{\infty} d\tau \iint_S \{G_{in}(\boldsymbol{\xi},t-\tau;\mathbf{x},0)p_i(\mathbf{u}(\boldsymbol{\xi},\tau),\mathbf{n}) \\ &\qquad -u_i(\boldsymbol{\xi},\tau)P_{in}(\boldsymbol{\xi},t-\tau;\mathbf{x},0)\}\,dS_{\boldsymbol{\xi}}. \end{aligned} \tag{3.33}$$

The representation theorem now gives the displacement at a point $\mathbf{x}$ in terms of a sum of forces in V, and displacements and tractions on surface S.

The right-hand side of Equation 3.33 consists only of convolutions in the time domain, which are equivalent to multiplications in the frequency domain. Thus, taking the Fourier transform of both sides of Equation 3.33

$$\begin{aligned} \hat{u}_n(\mathbf{x},\omega) = &\iiint_V \hat{f}_i(\boldsymbol{\xi},\omega)\hat{G}_{in}(\boldsymbol{\xi},\mathbf{x},\omega)\,dV_{\boldsymbol{\xi}} \\ + &\iint_S \{\hat{G}_{in}(\boldsymbol{\xi},\mathbf{x},\omega)\hat{p}_i(\boldsymbol{\xi},\omega) - \hat{u}_i(\boldsymbol{\xi},\omega)\hat{P}_{in}(\boldsymbol{\xi},\mathbf{x},\omega)\}\,dS_{\boldsymbol{\xi}}, \end{aligned} \tag{3.34}$$

where $\hat{\cdot}$ denotes the Fourier transform of a function. This is a useful form for the representation theorem since it can be seen that the displacement at one particular frequency is independent of contributions from other frequencies.

3.3.8 2-D considerations

Equation 3.34 can be applied in two dimensions by defining the body force $\hat{\mathbf{f}}$ as a line force which is constant for changing x_2. Because $\hat{\mathbf{f}}$ is constant with changing x_2, it can be taken outside the integral over x_2 which is one of the integrals making up the volume integral in Equation 3.34. If V is a cylinder parallel to the x_2 axis, the integral of the 3-D Green's function with respect to x_2 results in the 2-D Green's function (given in Appendix A). The volume integral in Equation 3.34 can therefore be written in a 2-D format:

$$\iiint_V \hat{f}_i(\boldsymbol{\xi},\omega)\hat{G}_{in}(\boldsymbol{\xi},\mathbf{x},\omega)\,dV_{\boldsymbol{\xi}} = \iint_{S^2} \hat{f}_i(\boldsymbol{\xi},\omega)\hat{G}^2_{in}(\boldsymbol{\xi},\mathbf{x},\omega)\,dS^2_{\boldsymbol{\xi}}, \tag{3.35}$$

where $\mathbf{G}^2$ is the displacement Green's function in two dimensions and S^2 is a cross-section of V in the $x_1 - x_3$ plane. Let L be the intersection of V and S^2. If $\hat{\mathbf{u}}$ and $\hat{\mathbf{p}}$ in V are independent of x_2 then, in a similar manner to the force in the volume integral, $\hat{\mathbf{u}}$ and $\hat{\mathbf{p}}$ can be taken outside the integral over x_2. As before, the integrals of the 3-D Green's functions (traction and displacement) with respect to x_2 become 2-D Green's functions:

$$\begin{aligned}\hat{u}_n(\mathbf{x},\omega) = &\iint_{S^2} \hat{f}_i(\boldsymbol{\xi},\omega)\hat{G}^2_{in}(\boldsymbol{\xi},\mathbf{x},\omega)\,dS^2_{\boldsymbol{\xi}} \\ &+ \int_L \{\hat{G}^2_{in}(\boldsymbol{\xi},\mathbf{x},\omega)\hat{p}_i(\boldsymbol{\xi},\omega) - \hat{u}_i(\boldsymbol{\xi},\omega)\hat{P}^2_{in}(\boldsymbol{\xi},\mathbf{x},\omega)\}\,dL_{\boldsymbol{\xi}},\end{aligned} \tag{3.36}$$

where $\hat{P}^2_{in}$ is given in Appendix A. In two-dimensions, the in-plane (P-SV) and anti-plane (SH) displacements are decoupled. For the rest of this chapter, I consider only in-plane waves. Therefore, the above equation is utilised with the indices i and n taking the values 1 and 3 only and henceforth the cross-section S^2 will be referred to as the region S.

3.4 The indirect boundary element method

3.4.1 The representation theorem for indirect quantities

The indirect boundary element method described by Sánchez-Sesma and Campillo (1991) uses, as a starting point, the representation theorem derived above. Before the representation theorem can be used to find a displacement field due to body forces $\hat{\mathbf{f}}$, some consideration must be given to where the relations apply. It is clear that they describe the displacement at any point within region S. However, the 2-D displacement and traction Green's functions contain singularities when the source and receiver points are coincident (Appendix A), resulting in integration over singularities when $\mathbf{x}$ is on the boundary L.

Consider what happens to the Green's functions as $\mathbf{x}$ approaches $\boldsymbol{\xi}$. They are a function of $\omega r/\alpha$ and $\omega r/\beta$ where α and β are the P and S-wave velocities of the medium and $r = |\mathbf{x}-\boldsymbol{\xi}|$. Therefore, the limit as $r \to 0$ is the same as the limit as $\omega \to 0$ which is given by the static Green's functions. The 2-D displacement Green's function in the static limit is (Banerjee and Butterfield, 1981)

$$\hat{G}^s_{ij} = \frac{-1}{8\pi\mu(1-\nu)}\{(3-4\nu)\delta_{ij}\log|r| - \hat{r}_i\hat{r}_j\} + A_{ij}, \qquad i,j = 1,3, \tag{3.37}$$

where ν is Poisson's ratio, $\hat{r}_i = (x_i - \xi_i)/r$, A_{ij} is a constant tensor and the superscript s denotes the function in the static limit. The singularity occurring when $\mathbf{x} = \boldsymbol{\xi}$ is logarithmic and therefore integrable. The accuracy of numerical integration over this function is discussed in Chapter 5.

The 2-D traction Green's function in the static limit is (Banerjee and Butterfield, 1981)

$$\begin{aligned}\hat{P}^s_{ij}(\mathbf{x},\boldsymbol{\xi}) = \frac{-1}{4\pi r(1-\nu)}\{&(1-2\nu)(n_j\hat{r}_i - n_i\hat{r}_j) \\ &+[(1-2\nu)\delta_{ij} + 2\hat{r}_i\hat{r}_j]\hat{r}_k n_k\}, \qquad i,j = 1,3,\end{aligned} \tag{3.38}$$

which has a $1/r$ singularity and so is not integrable when $\mathbf{x}$ is on the boundary L. The integral over the traction Green's function must be considered in the limit as point $\mathbf{x}$ approaches a point on the boundary $\mathbf{x}^L$ (Figure 3.1).

The following derivation takes exactly the same form as that of Pointer et al.

(1998). The aim is to evaluate the integral

$$\lim_{\mathbf{x}\to\mathbf{x}^L} \int_L \hat{P}_{ij}(\boldsymbol{\xi},\mathbf{x})\hat{u}_i(\boldsymbol{\xi})dL_{\boldsymbol{\xi}} \tag{3.39}$$

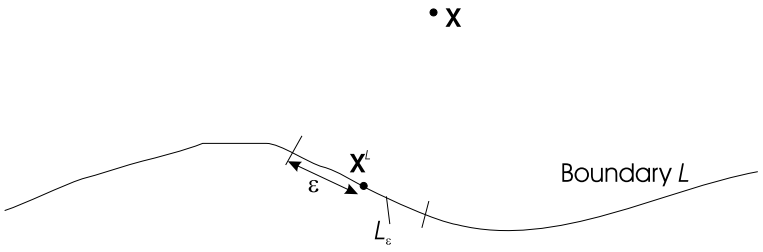

Figure 3.1: The boundary L is divided into two parts by taking out a section L_ϵ of length 2 ϵ, with the boundary point $\mathbf{x}^L$ in the middle. After Pointer et al. (1998).

The first step is to split the integral into two parts, an integral over the line element L_ϵ and an integral over the rest of the line. The integral over L_ϵ is split into two further parts:

$$\begin{aligned}\int_{L_\epsilon} \hat{P}_{ij}(\boldsymbol{\xi},\mathbf{x})\hat{u}_i(\boldsymbol{\xi})dL_{\boldsymbol{\xi}} &= \hat{u}_i(\mathbf{x}^L)\int_{L_\epsilon} \hat{P}_{ij}(\boldsymbol{\xi},\mathbf{x})dL_{\boldsymbol{\xi}} \\ &+ \int_{L_\epsilon} \hat{P}_{ij}(\boldsymbol{\xi},\mathbf{x})[\hat{u}_i(\boldsymbol{\xi}) - \hat{u}_i(\mathbf{x}^L)]dL_{\boldsymbol{\xi}}.\end{aligned} \tag{3.40}$$

If $\mathbf{u}$ is Hölder continuous on L then the second integral is integrable and bounded when $\mathbf{x} = \mathbf{x}^L$, therefore I concentrate now on evaluating the integral

$$\int_{L_\epsilon} \hat{P}_{ij}(\boldsymbol{\xi},\mathbf{x})dL_{\boldsymbol{\xi}} \tag{3.41}$$

This problem is easier to solve if the axes are orientated such that $\mathbf{x}^L$ lies at the origin, the x_1-axis is the tangent to L_ϵ (so that $\boldsymbol{\xi} = (x_1, 0), -\epsilon \le x_1 \le \epsilon$) and the x_3-axis points into the region S (so that $\mathbf{x} = (0, \eta)$ and $\mathbf{n}(\boldsymbol{\xi}) = (0, -1)$ as shown in Figure 3.2). An integration along the axis x_1 between $-\epsilon$ and ϵ is equal

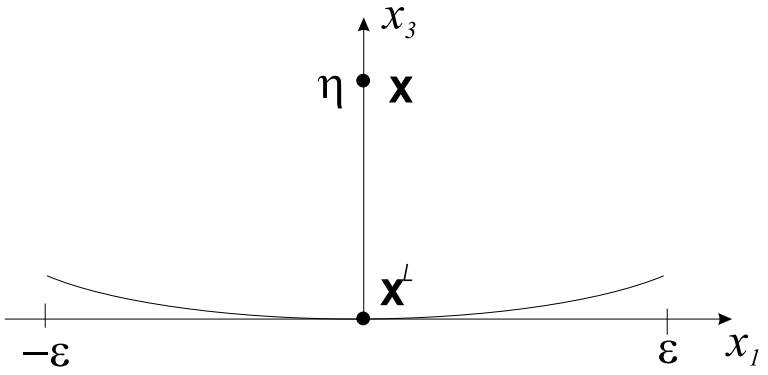

Figure 3.2: The section of boundary L_ϵ is replaced by an interval $[-\epsilon, \epsilon\,]$ on the tangent at point $\mathbf{x}^L$. After Pointer et al. (1998).

to the integral along line element L_ϵ with an error of the order ϵ so that

$$\int_{L_\epsilon} \hat{P}_{ij}(\boldsymbol{\xi}, \mathbf{x}) dL_{\boldsymbol{\xi}} = \int_{-\epsilon}^{\epsilon} \hat{P}_{ij}(\boldsymbol{\xi}, \mathbf{x}) dx_1 + O(\epsilon) \tag{3.42}$$

Since $|\mathbf{x} - \boldsymbol{\xi}|$ is arbitrarily small, the static form for $\hat{P}_{ij}$ may be used. Substituting for $\mathbf{x}$, $\boldsymbol{\xi}$ and $\mathbf{n}$ into Equation 3.38, the following results are obtained:

$$\begin{aligned}
\hat{P}_{11}(\boldsymbol{\xi}, \mathbf{x}) &= \frac{-1}{4\pi r(1-\nu)} \frac{\eta}{r} \Big\{ 1 - 2\nu + 2\frac{x_1^2}{r^2} \Big\}, \\
\hat{P}_{13}(\boldsymbol{\xi}, \mathbf{x}) &= \frac{-1}{4\pi r(1-\nu)} \Big\{ -(1-2\nu)\frac{x_1}{r} - \frac{2\eta^2 x_1}{r^3} \Big\}, \\
\hat{P}_{31}(\boldsymbol{\xi}, \mathbf{x}) &= \frac{-1}{4\pi r(1-\nu)} \Big\{ (1-2\nu)\frac{x_1}{r} - \frac{2\eta^2 x_1}{r^3} \Big\}, \\
\hat{P}_{11}(\boldsymbol{\xi}, \mathbf{x}) &= \frac{-1}{4\pi r(1-\nu)} \frac{\eta}{r} \Big\{ 1 - 2\nu + 2\frac{\eta^2}{r^2} \Big\},
\end{aligned} \tag{3.43}$$

where $r = (x_1^2 + \eta^2)^{1/2}$. The integrals of $\hat{P}_{13}$ and $\hat{P}_{31}$ go to zero because they are

odd functions of x_1. The remaining integrals are

$$\int_{-\epsilon}^{\epsilon} \hat{P}_{11}(\boldsymbol{\xi},\mathbf{x})dx_1 = \frac{-\eta}{4\pi(1-\nu)} \int_{-\epsilon}^{\epsilon} \Big\{ \frac{1-2\nu}{x_1^2+\eta^2} + \frac{2x_1^2}{(x_1^2+\eta^2)^2} \Big\} dx_1$$
$$= \frac{-1}{4\pi(1-\nu)} \Big\{ 4(1-\nu)\tan^{-1}(\epsilon/\eta) - \frac{2\epsilon\eta}{(\epsilon^2+\eta^2)} \Big\},$$
$$\int_{-\epsilon}^{\epsilon} \hat{P}_{33}(\boldsymbol{\xi},\mathbf{x})dx_1 = \frac{-\eta}{4\pi(1-\nu)} \int_{-\epsilon}^{\epsilon} \Big\{ \frac{1-2\nu}{x_1^2+\eta^2} + \frac{2\eta^2}{(x_1^2+\eta^2)^2} \Big\} dx_1$$
$$= \frac{-1}{4\pi(1-\nu)} \Big\{ 4(1-\nu)\tan^{-1}(\epsilon/\eta) + \frac{2\epsilon\eta}{(\epsilon^2+\eta^2)} \Big\}. \tag{3.44}$$

As $\mathbf{x} \to \mathbf{x}^L$ then $\eta \to 0$ giving

$$\int_{L_\epsilon} \hat{P}_{ij}(\boldsymbol{\xi},\mathbf{x})dL_{\boldsymbol{\xi}} = -\frac{1}{2}\delta_{ij} + O(\epsilon). \tag{3.45}$$

Finally ϵ is allowed to tend to zero. The second integral in Equation 3.40 goes to zero yielding

$$\lim_{\mathbf{x}\to\mathbf{x}^L} \int_L \hat{P}_{ij}(\boldsymbol{\xi},\mathbf{x})\hat{u}_i(\boldsymbol{\xi})dL_{\boldsymbol{\xi}} = \mathscr{PV} \int_L \hat{P}_{ij}(\boldsymbol{\xi},\mathbf{x}^L)\hat{u}_i(\boldsymbol{\xi})dL_{\boldsymbol{\xi}} - \frac{1}{2}\hat{u}_j(\mathbf{x}^L), \tag{3.46}$$

where $\mathscr{PV}$ means that the integral over L is a Cauchy Principal Value. Combining the result 3.46 with Equation 3.36 yields

$$c\hat{u}_n(\mathbf{x}) = \iint_S \hat{f}_i(\boldsymbol{\xi})\hat{G}_{in}(\boldsymbol{\xi},\mathbf{x})\, dS_{\boldsymbol{\xi}}$$
$$+ \int_L \hat{G}_{in}(\boldsymbol{\xi},\mathbf{x})\hat{p}_i(\boldsymbol{\xi})dL_{\boldsymbol{\xi}} - \mathscr{PV} \int_L \hat{u}_i(\boldsymbol{\xi})\hat{P}_{in}(\boldsymbol{\xi},\mathbf{x})\, dL_{\boldsymbol{\xi}}, \tag{3.47}$$

where the constant c takes the value 1 when $\mathbf{x}$ is inside S and is equal to 0.5 when $\mathbf{x}$ is on the boundary L.

Now consider the region outside S. Assume that this region is made up of the

same material as S. In the absence of body forces, the displacement is given by

$$c'\hat{u}'_n(\mathbf{x}) = -\int_L \hat{G}_{in}(\boldsymbol{\xi},\mathbf{x})\hat{p}'_i(\boldsymbol{\xi})dL_{\boldsymbol{\xi}} + \mathscr{P}\mathscr{V}\int_L \hat{u}'_i(\boldsymbol{\xi},\omega)\hat{P}_{in}(\boldsymbol{\xi},\mathbf{x})\,dL_{\boldsymbol{\xi}}, \tag{3.48}$$

where c' is 1 if the point $\mathbf{x}$ is outside S and 0.5 when $\mathbf{x}$ is located on the boundary L.

Summing Equations 3.47 and 3.48 at the boundary L gives

$$\frac{1}{2}[\hat{u}_n(\mathbf{x}) + \hat{u}'_n(\mathbf{x})] = \iint_S \hat{f}_i(\boldsymbol{\xi})\hat{G}_{in}(\boldsymbol{\xi},\mathbf{x})\,dS_{\boldsymbol{\xi}} + \int_L \{\hat{G}_{in}(\boldsymbol{\xi},\mathbf{x})[\hat{p}_i(\boldsymbol{\xi}) - \hat{p}'_i(\boldsymbol{\xi})]dL_{\boldsymbol{\xi}} - \mathscr{P}\mathscr{V}\int_L [\hat{u}_i(\boldsymbol{\xi}) - \hat{u}'_i(\boldsymbol{\xi})]\hat{P}_{in}(\boldsymbol{\xi},\mathbf{x})\}\,dL_{\boldsymbol{\xi}}. \tag{3.49}$$

If displacement and traction are chosen such that $\hat{u}_i(\boldsymbol{\xi}) = \hat{u}'_i(\boldsymbol{\xi})$ and $\hat{p}_i(\boldsymbol{\xi}) - \hat{p}'_i(\boldsymbol{\xi}) = \phi_i(\boldsymbol{\xi})$ the the above expression becomes

$$\hat{u}_n(\mathbf{x}) = \iint_S \hat{f}_i(\boldsymbol{\xi})\hat{G}_{in}(\boldsymbol{\xi},\mathbf{x})\,dS_{\boldsymbol{\xi}} + \int_L \hat{G}_{in}(\boldsymbol{\xi},\mathbf{x})\phi_i(\boldsymbol{\xi})dL_{\boldsymbol{\xi}}. \tag{3.50}$$

Invoking reciprocity in the displacement Green's function and interchanging the indices i and n gives

$$\hat{u}_i(\mathbf{x}) = \iint_S \hat{f}_n(\boldsymbol{\xi})\hat{G}_{in}(\mathbf{x},\boldsymbol{\xi})\,dS_{\boldsymbol{\xi}} + \int_L \hat{G}_{in}(\mathbf{x},\boldsymbol{\xi})\phi_n(\boldsymbol{\xi})dL_{\boldsymbol{\xi}}, \tag{3.51}$$

which, at last, is a representation theorem dependent on the indirect quantities $\boldsymbol{\phi}$ (Figure 3.3).

The equivalent expression for traction is yielded by applying Hooke's law. However, as before, care must be taken when $\mathbf{x} = \boldsymbol{\xi}$ on the boundary. From a similar argument to the one shown above, the integral over the traction Green's function produces an additional term equal to half the the source strength at

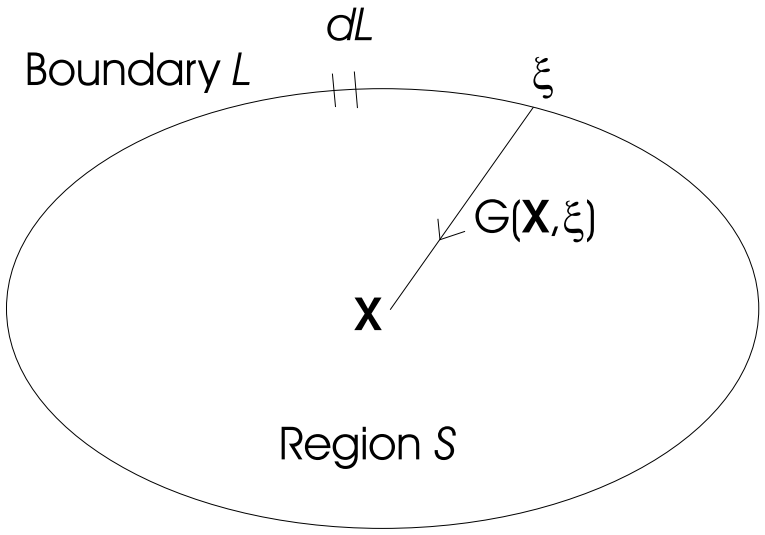

Figure 3.3: Displacement inside a region S

point $\mathbf{x}$, and the integral becomes a Cauchy Principal Value. Hence,

$$\hat{p}_i(\mathbf{x}) = \frac{1}{2}\phi_i(\mathbf{x}) + \mathscr{PV}\iint_S \hat{f}_n(\boldsymbol{\xi})\hat{P}_{in}(\mathbf{x},\boldsymbol{\xi})\,dS_{\boldsymbol{\xi}} + \mathscr{PV}\int_L \hat{P}_{in}(\mathbf{x},\boldsymbol{\xi})\phi_n(\boldsymbol{\xi})dL_{\boldsymbol{\xi}}, \quad (3.52)$$

where the first term is included only where $\mathbf{x}$ is located on the boundary L. Equations 3.51 and 3.52 are the basis of the indirect boundary element method. If the region outside S is now replaced with a material which is different from the material inside S, the displacement outside S can be written as

$$\hat{u}_i^E(\mathbf{x}) = \iint_S \hat{f}_n^E(\boldsymbol{\xi})\hat{G}_{in}^E(\mathbf{x},\boldsymbol{\xi})\,dS_{\boldsymbol{\xi}} + \int_L \hat{G}_{in}^E(\mathbf{x},\boldsymbol{\xi})\phi_n^E(\boldsymbol{\xi})dL_{\boldsymbol{\xi}}, \quad (3.53)$$

and the traction as

$$\hat{p}_i^E(\mathbf{x}) = -\frac{1}{2}\phi_i^E(\mathbf{x}) + \mathscr{PV}\iint_S \hat{f}_n^E(\boldsymbol{\xi})\hat{P}_{in}^E(\mathbf{x},\boldsymbol{\xi})\,dS_{\boldsymbol{\xi}} + \mathscr{PV}\int_L \hat{P}_{in}^E(\mathbf{x},\boldsymbol{\xi})\phi_n^E(\boldsymbol{\xi})dL_{\boldsymbol{\xi}}, \quad (3.54)$$

where the quantities $\hat{G}_{in}^E$ and $\hat{P}_{in}^E$ are the displacement and traction Green's functions for the material exterior to S, and ϕ_n^E represents the secondary source

distribution on the outside of boundary L. The term of a half is now negative because the the limit is found for $\mathbf{x}$ approaching the boundary L from outside S.

3.4.2 Single-layer formulation

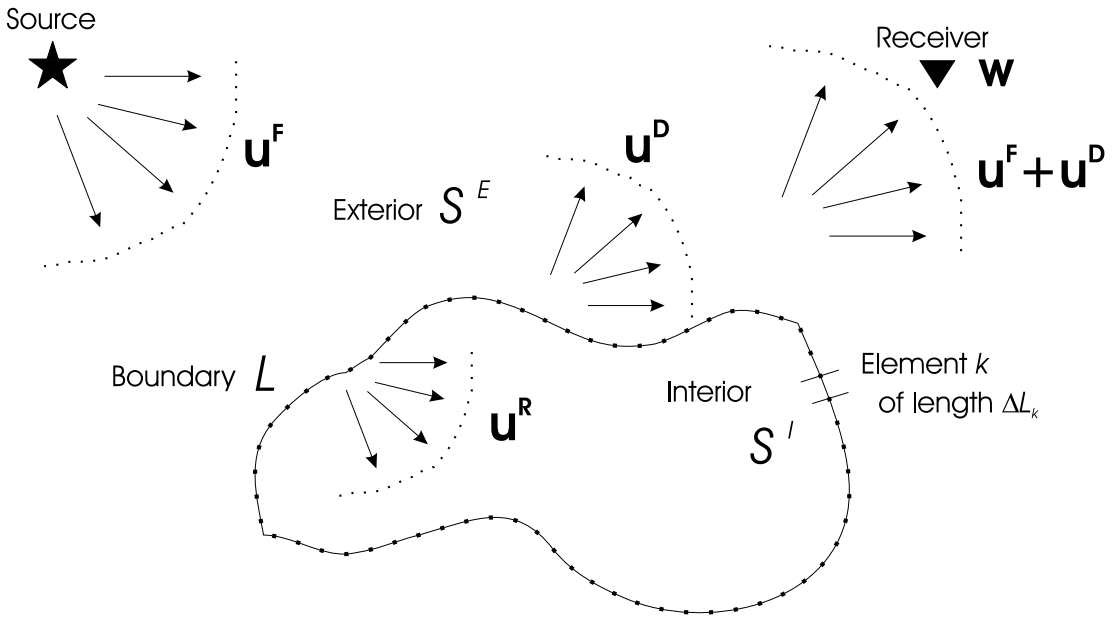

Figure 3.4: Problem configuration for the indirect BEM for one layer (after Pointer et al., 1998). The total wavefield in the exterior region S^E is the sum of the incident wavefield $\mathbf{u}^F$ and the scattered wavefield $\mathbf{u}^D$.

Consider the configuration shown in Figure 3.4. The displacement at point $\mathbf{x}$ is the superposition of the direct wave from the source (incident field) and the scattered waves:

$$\hat{u}_i^T(\mathbf{x}) = \hat{u}_i^F(\mathbf{x}) + \hat{u}_i^D(\mathbf{x}), \tag{3.55}$$

where $\hat{u}_i^T(\mathbf{x})$ is the total displacement, $\hat{u}_i^F(\mathbf{x})$ is the displacement from the incident field and $\hat{u}_i^D(\mathbf{x})$ is the displacement from the scattered waves.

If the boundary L is discretized into K elements then Equations 3.53 and 3.54 can be rewritten as summations and the following expressions are obtained for displacement and traction:

$$\hat{u}_i^T(\mathbf{x}) = \hat{u}_i^F(\mathbf{x}) + \sum_{k=1}^{K} \phi_j(\boldsymbol{\xi}_k) g_{ij}(\mathbf{x}, \boldsymbol{\xi}_k), \tag{3.56}$$

where

$$g_{ij}(\mathbf{x}, \boldsymbol{\xi}_k) = \int_{\boldsymbol{\xi}_k - \Delta L_k/2}^{\boldsymbol{\xi}_k + \Delta L_k/2} \hat{G}_{ij}(\mathbf{x}, \boldsymbol{\xi}_k) dL_{\boldsymbol{\xi}}, \tag{3.57}$$

and

$$\hat{p}_i^T(\mathbf{x}) = \hat{p}_i^F(\mathbf{x}) + \sum_{k=1}^{K} \phi_j(\boldsymbol{\xi}_k) p_{ij}(\mathbf{x}, \boldsymbol{\xi}_k), \tag{3.58}$$

where

$$p_{ij}(\mathbf{x}, \boldsymbol{\xi}_k) = \int_{\boldsymbol{\xi}_k - \Delta L_k/2}^{\boldsymbol{\xi}_k + \Delta L_k/2} \hat{P}_{ij}(\mathbf{x}, \boldsymbol{\xi}_k) dL_{\boldsymbol{\xi}}, \tag{3.59}$$

where ΔL_k is the length of the kth surface element. For the case where $\mathbf{x} = \boldsymbol{\xi}_k$, $p_{ij} = -0.5$ for $i = j$ and 0 for $i \neq j$. The equivalent equations for the region inside S^I are the same except the incident field term is dropped and the -0.5 becomes 0.5 in the traction function. These discrete sums are good approximations if the elements are small compared with the wavelength, and sufficiently small to represent the geometry of S well. Studies to determine the accuracy of this approximation are presented in Chapter 5.

The region S^I is made up of a different material from that in S^E. Applying continuity of displacement and traction at the boundary L, the following expressions are yielded:

$$\hat{u}_i^F(\mathbf{x}) = \hat{u}_i^R(\mathbf{x}) - \hat{u}_i^D(\mathbf{x}), \tag{3.60}$$

and

$$\hat{p}_i^F(\mathbf{x}) = \hat{p}_i^R(\mathbf{x}) - \hat{p}_i^D(\mathbf{x}), \tag{3.61}$$

where $\mathbf{x}$ lies on L and $\hat{u}_i^R(\mathbf{x})$ and $\hat{p}_i^R(\mathbf{x})$ are the displacement and traction inside region S^I respectively. Equations 3.60 and 3.61 are applicable at any point along the boundary L. Applying these equations at the centre of each element generates a system of simultaneous equations:

$$\sum_{k=1}^{K} \phi_j^E(\boldsymbol{\xi}_k) g_{ij}^I(\mathbf{x}_l, \boldsymbol{\xi}_k) - \sum_{k=1}^{K} \phi_j^E(\boldsymbol{\xi}_k) g_{ij}^E(\mathbf{x}_l, \boldsymbol{\xi}_k) = \hat{u}_i^F(\mathbf{x}_l), \qquad l = 1, K, \tag{3.62}$$

$$\sum_{k=1}^{K} \phi_j^E(\boldsymbol{\xi}_k) p_{ij}^I(\mathbf{x}_l, \boldsymbol{\xi}_k) - \sum_{k=1}^{K} \phi_j^E(\boldsymbol{\xi}_k) p_{ij}^E(\mathbf{x}_l, \boldsymbol{\xi}_k) = \hat{p}_i^F(\mathbf{x}_l), \qquad l = 1, K, \tag{3.63}$$

These equations can be simplified by use of matrix notation. I follow the same notation described by Pedersen et al. (1996), though I simplify it by considering only P-SV wave propagation. First, I define the vector $\mathbf{Q}^E$ to be

$$\mathbf{Q}^E = [\phi_1^E(\boldsymbol{\xi}_1), ..., \phi_1^E(\boldsymbol{\xi}_K); \phi_3^E(\boldsymbol{\xi}_1), ..., \phi_3^E(\boldsymbol{\xi}_K)]. \tag{3.64}$$

This is a vector of length $2K$; the equivalent vector for the sources in the region V^I is $\mathbf{Q}^I$. Next, I define two matrices $\mathbf{A}$ and $\mathbf{B}$ which are of the form

$$\mathbf{A} = \begin{bmatrix} \mathscr{G}_{11} & \mathscr{G}_{13} \\ \mathscr{G}_{31} & \mathscr{G}_{33} \\ \mathscr{P}_{11} & \mathscr{P}_{13} \\ \mathscr{P}_{31} & \mathscr{P}_{33} \end{bmatrix}, \tag{3.65}$$

where $\mathscr{G}_{ij}$ and $\mathscr{P}_{ij}$ are K x K matrices. Each element of these matrices is defined as

$$(\mathscr{G}_{ij})_{kl} = g_{ij}(\mathbf{x}_l, \boldsymbol{\xi}_k), \tag{3.66}$$

$$(\mathscr{P}_{ij})_{kl} = p_{ij}(\mathbf{x}_l, \boldsymbol{\xi}_k). \tag{3.67}$$

Matrix $\mathbf{A}$ applies to the region S^E and matrix $\mathbf{B}$ to the region S^I. The incident field in region S^E is defined by the matrix $\mathbf{F}$ where

$$\mathbf{F} = [\hat{u}_1^F(\mathbf{x}_1), ..., \hat{u}_1^F(\mathbf{x}_K); \hat{u}_3^F(\mathbf{x}_1), ..., \hat{u}_3^F(\mathbf{x}_K); \hat{p}_1^F(\mathbf{x}_1), ..., \hat{p}_1^F(\mathbf{x}_K); \hat{p}_3^F(\mathbf{x}_1), ..., \hat{p}_3^F(\mathbf{x}_K)]. \tag{3.68}$$

$\mathbf{F}$ is a matrix of length $4K$ containing displacements and tractions due to the incident field. Using this notation, Equations 3.62 and 3.63 can be written in one matrix equation:

$$\mathbf{B}(\mathbf{Q}^I)^T - \mathbf{A}(\mathbf{Q}^E)^T = \mathbf{F}, \tag{3.69}$$

Where T now denotes the transpose of the vector. The next step is to solve this equation for $\mathbf{Q}^I$ and $\mathbf{Q}^E$. A simple rearrangement gives

$$[\mathbf{B}; -\mathbf{A}][\mathbf{Q}^I; \mathbf{Q}^E]^T = \mathbf{F} \tag{3.70}$$

A suitable routine can be used to solve this system of simultaneous equations. Alternatively, the square matrix containing **A** and **B** can be inverted. The final step is to find the displacement at some receiver point **w** (Figure 3.4). For a receiver point in the region V^E, the summation is given as

$$\hat{u}_i(\mathbf{w}) = \sum_{k=1}^{K} g_{ij}^E(\mathbf{w}, \boldsymbol{\xi}_k)\phi_j^E(\boldsymbol{\xi}_k) \tag{3.71}$$

3.4.3 Multi-layer formulation

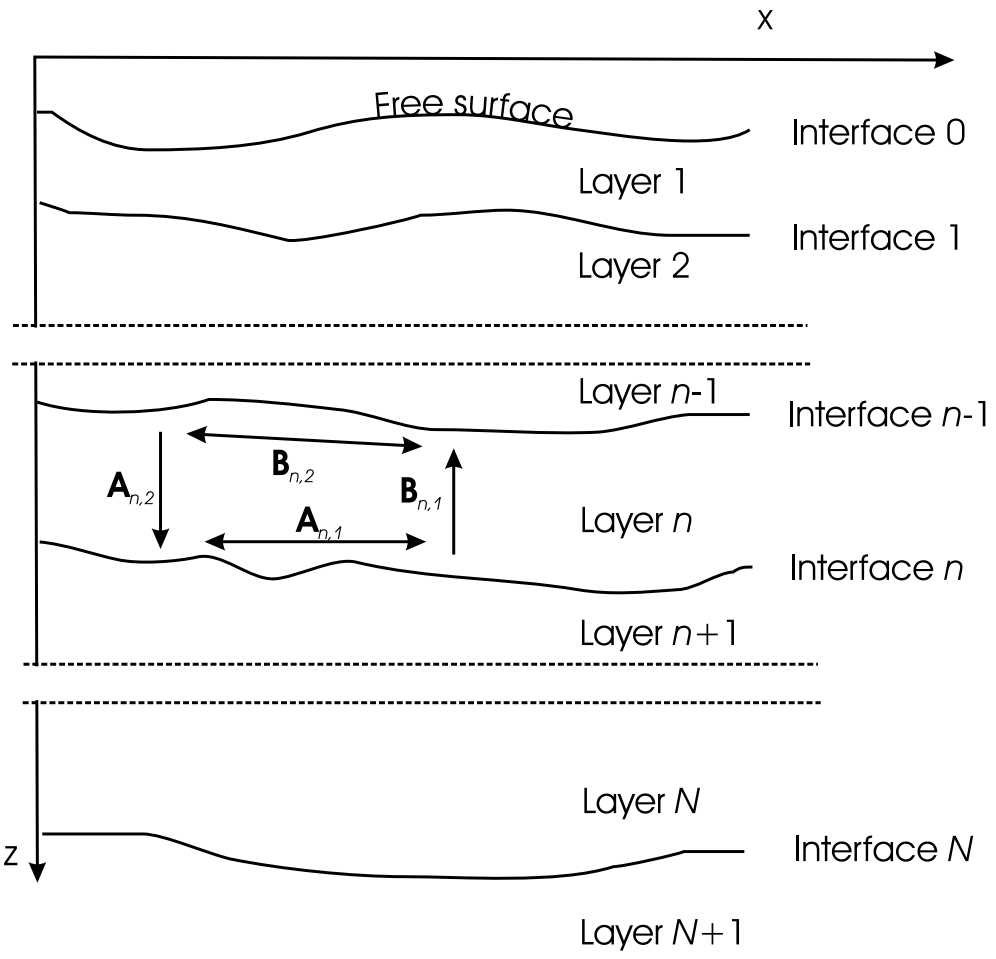

Figure 3.5: Multi-layer model configuration (after Pedersen et al. 1996)

This multi-layer formulation follows that of Pedersen et al. (1996) and Bouchon et al. (1989). Figure 3.5 shows the model configuration. $N + 1$ layers (including the half-space) are separated by N irregular interfaces. The upper layer

is delimited by the free surface. The layers are numbered from 1 (uppermost layer) to $N+1$ (half-space) and the interfaces are numbered from 0 (free surface) to N (deepest interface). K_n is the number of boundary elements making up interface n. There are now $\mathbf{A}$ and $\mathbf{B}$ matrices for each interface which are defined as follows:

$\mathbf{A}_{1,n}$ (of dimension $4K_n$ x $2K_n$) contains the displacements and tractions for receivers on interface n due to the sources on interface n.

$\mathbf{A}_{2,n}$ (of dimension $4K_n$ x $2K_{n-1}$) contains the displacements and tractions for receivers on interface n due to the sources on interface $n-1$.

$\mathbf{B}_{1,n}$ (of dimension $4K_{n-1}$ x $2K_n$) contains the displacements and tractions for receivers on interface $n-1$ due to the sources on interface n.

$\mathbf{B}_{2,n}$ (of dimension $4K_{n-1}$ x $2K_{n-1}$) contains the displacements and tractions for receivers on interface $n-1$ due to sources on interface $n-1$.

$\mathbf{Q}_{n,1}$ is a $2K$ vector containing the secondary sources on interface n which propagate energy upwards into layer n. $\mathbf{Q}_{n,2}$ is a $2K$ vector containing the secondary sources on interface n which propagate energy downwards into layer $n+1$. $\mathbf{Q}_n$ is a $4K$ matrix such that $\mathbf{Q}_n = [\mathbf{Q}_{n,1}; \mathbf{Q}_{n,2}]$.

$\mathbf{F}_{1,n}$ is the incident-field contribution at interface n from sources in the layer above. $\mathbf{F}_{2,n}$ is the incident-field contribution at interface n from sources in the layer below.

Continuity of displacement and traction on the nth interface gives the following expression:

$$\mathbf{A}_{n,2}\mathbf{Q}^T_{n-1,2} + \mathbf{A}_{n,1}\mathbf{Q}^T_{n,1} + \mathbf{F}^T_{n,1} = \mathbf{B}_{n+1,2}\mathbf{Q}^T_{n,2} + \mathbf{B}_{n+1,1}\mathbf{Q}^T_{n+1,1} + \mathbf{F}^T_{n,2}. \tag{3.72}$$

At the deepest interface (N), these conditions become

$$\mathbf{A}_{N,2}\mathbf{Q}^T_{N-1,2} + \mathbf{A}_{N,1}\mathbf{Q}^T_{N,1} + \mathbf{F}^T_{N,1} = \mathbf{B}_{N+1,2}\mathbf{Q}^T_{N,2} + \mathbf{F}^T_{N,2}, \tag{3.73}$$

and at the free surface tractions are zero,

$$\mathbf{B}^{inf}_{N,2}\mathbf{Q}^T_{0,2} + \mathbf{B}^{inf}_{1,1}\mathbf{Q}^T_{1,1} + (\mathbf{F}^{inf}_{0,2})^T = 0. \tag{3.74}$$

The superscript inf indicates that only the lower half of the matrix is used, i.e., the traction part of the $\mathbf{B}$ matrix. Rearrangement of Equation 3.72 yields

$$\mathbf{A}_{n,2}\mathbf{Q}^T_{n-1,2} = [-\mathbf{A}_{n,1}; \mathbf{B}_{n+1,2}]\mathbf{Q}^T_n + \mathbf{B}_{n+1,1}\mathbf{Q}^T_{n+1,1} + \mathbf{\Delta F}^T_n, \tag{3.75}$$

where

$$\mathbf{\Delta F}_n = \mathbf{F}_{n,2} - \mathbf{F}_{n,1} \tag{3.76}$$

Equation 3.28 gives the force on the lower side of interface $n-1$ as a function of the forces on interfaces n and $n+1$. Suppose that Equation 3.75 can be written in the form

$$\mathbf{A}_{n,2}\mathbf{Q}^T_{n-1,2} = \mathbf{D}_n\mathbf{Q}^T_n + \mathbf{E}^T_n, \tag{3.77}$$

where $\mathbf{D}_n$ is a matrix and $\mathbf{E}_n$ is a vector. Rearrangement of Equation 3.77 gives

$$\mathbf{Q}^T_{n+1} = \mathbf{D}^{-1}_{n+1}(\mathbf{A}_{n+1,2}\mathbf{Q}^T_{n,2} - \mathbf{E}^T_{n+1}), \tag{3.78}$$

which leads to

$$\mathbf{Q}^T_{n+1,1} = (\mathbf{D}^{-1}_{n+1})^{sup}(\mathbf{A}_{n+1,2}\mathbf{Q}^T_{n,2} - \mathbf{E}^T_{n+1}), \tag{3.79}$$

where the superscript sup indicates that only the upper half of the matrix is used. Insertion of Equation 3.79 into 3.75 yields

$$\begin{aligned}\mathbf{A}_{n,2}\mathbf{Q}^T_{n-1,2} = [-\mathbf{A}_{n,1}; \mathbf{B}_{n+1,2}]\mathbf{Q}^T_n + \mathbf{B}_{n+1,1}(\mathbf{D}^{-1}_{n+1})^{sup}\mathbf{A}_{n+1,2}\mathbf{Q}^T_{n,2} \\ -\mathbf{B}_{n+1,1}(\mathbf{D}^{-1}_{n+1})^{sup}\mathbf{E}^T_{n+1} + \mathbf{\Delta F}^T_n,\end{aligned} \tag{3.80}$$

which leads to

$$\begin{aligned}\mathbf{A}_{n,2}\mathbf{Q}^T_{n-1,2} = [-\mathbf{A}_{n,1}; \mathbf{B}_{n+1,2} + \mathbf{B}_{n+1,1}(\mathbf{D}^{-1}_{n+1})^{sup}\mathbf{A}_{n+1,2}]\mathbf{Q}^T_n \\ -\mathbf{B}_{n+1,1}(\mathbf{D}^{-1}_{n+1})^{sup}\mathbf{E}^T_{n+1} + \mathbf{\Delta F}^T_n.\end{aligned} \tag{3.81}$$

By identification of terms between Equations 3.81 and 3.77, it can be seen that Equation 3.77 is equivalent to Equation 3.75 when

$$\mathbf{D}_n = [-\mathbf{A}_{n,1}; \mathbf{B}_{n+1,2} + \mathbf{B}_{n+1,1}(\mathbf{D}^{-1}_{n+1})^{sup}\mathbf{A}_{n+1,2}], \tag{3.82}$$

$$\mathbf{E}^T_n = -\mathbf{B}_{n+1,1}(\mathbf{D}^{-1}_{n+1})^{sup}\mathbf{E}^T_{n+1} + \Delta\mathbf{F}^T_n. \tag{3.83}$$

At the deepest interface equation 3.75 can be written as

$$\mathbf{A}_{N,2}\mathbf{Q}^T_{N-1,2} = [-\mathbf{A}_{N,1}; \mathbf{B}_{N+1,2}]\mathbf{Q}^T_N + \mathbf{\Delta F}^T_N, \tag{3.84}$$

which provides the initial conditions

$$\mathbf{D}_N = [-\mathbf{A}_{N,1}; \mathbf{B}_{N+1,2}], \tag{3.85}$$

$$\mathbf{E}^T_N = \Delta\mathbf{F}^T_N, \tag{3.86}$$

for the recursive Equations 3.82 and 3.83. Recursive relations have now been found for $\mathbf{D}_n$ and $\mathbf{E}_n$ which do not involve the unknown forces on the interfaces. Thus, it is possible to calculate the $\mathbf{D}$ and $\mathbf{E}$ matrices up to $n = 1$. Combining Equations 3.74 and 3.77 permits the construction of a system of linear equations

$$\mathbf{C}\mathbf{x}^T = \mathbf{y}^T, \tag{3.87}$$

with

$$\mathbf{C} = \begin{bmatrix} -\mathbf{D}^{left}_1 & -\mathbf{D}^{right}_1 & \mathbf{A}_{1,2} \\ \mathbf{B}^{inf}_{1,1} & 0 & \mathbf{B}^{inf}_{1,2} \end{bmatrix}, \tag{3.88}$$

$$\mathbf{x} = [\mathbf{Q}_{1,1}; \mathbf{Q}_{1,2}; \mathbf{Q}_{0,2}], \tag{3.89}$$

$$\mathbf{y} = [\mathbf{E}_1; -\mathbf{F}^{inf}_{0,2}]. \tag{3.90}$$

Solving Equation 3.87 yields the force distributions $\mathbf{Q}_{0,2}$, $\mathbf{Q}_{1,1}$ and $\mathbf{Q}_{1,2}$. The force distributions for any layer can then be found by Equation 3.78. The final step, as with the single layer formulation is to sum the contributions from all the elements making up the interfaces directly above and below the receiver. The incident field should also be added to the solution if the receiver is in the same layer as the source.

The remaining operation is to multiply each frequency by some wavelet (e.g. Ricker) and transform back into the time domain.

3.5 Summary

A technique has been presented for computing synthetic seismograms using the boundary element method. This method is derived from Betti's reciprocal relation. The method presented here was constrained to a two dimensional case for P-SV waves only, though it could easily be adapted to full three-dimensional wave propagation. The method operates in the frequency domain where the situation is simplified because the response of one frequency has been shown to be independent of all the others. The method accounts for all multiples and can be implemented for a single- or multi-layer model.

Chapter 4

Implementation of the boundary element method

4.1 Introduction

In Chapter 3 I present the formulation for modelling with the indirect boundary element method in the frequency domain. In this short chapter I outline how the formulation is implemented in practice.

4.2 Program flow

The program flow for the boundary element code is shown in Figure 4.1. The input file consists of: the velocity (P and S) and density information for each layer in the model; coordinates for all the discretization points making up each of interfaces in the model; source coordinates; receiver coordinates; and information on the length of the time window and the sample rate.

The interfaces in the model are redefined in terms of boundary elements, whose length is determined by the distance between two adjacent discretization points and whose coordinates are defined as the mid-point between two adjacent discretization points. The normals for each of the boundary elements in the model are computed.

The maximum frequency to be computed and the frequency step Δf are calculated from the length of the time window and the time step. A frequency

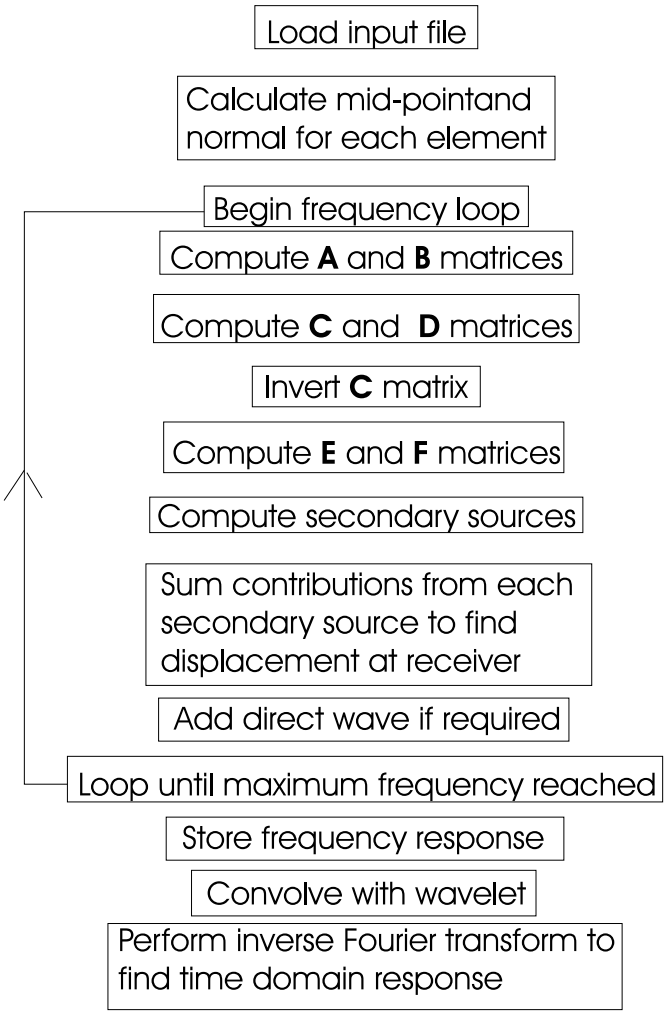

Figure 4.1: Flow diagram for the basic boundary element code.

loop is then initiated which starts with the lowest frequency and increases in steps of Δf until the maximum frequency is reached.

4.3 Computations within the frequency loop

The **A** and **B** matrices are computed for all interfaces in the model. Each of the elements in these matrices involves an integration over the length of the element. The integration is performed by ten-point Gaussian quadrature (Press et al., 1992). For each integration point, the displacement and traction Green's functions are evaluated (Appendix A).

The **D** matrix for the lowest interface in the model is formed from the **A** and **B**

matrices (see Chapter 3, Equation 3.85). The **D** matrix can then be found for all interfaces in the model using Equation 3.82. This step involves matrix inversion which in this code is carried out using Gaussian elimination (SLATEC routines are used for this). The **C** matrix is formed from the **A**, **B** and **D** matrices, and then inverted.

Note that most of the computational cost in generating synthetic seismograms using the boundary element method is due to the steps described above. These steps can be carried out without prior knowledge of the location of the seismic source. This is a useful feature of this formulation which allows many shot gathers to be generated for little more computation than for one shot gather.

At this point, the **F** matrix (which is dependent on the source location) and the **E** matrix (which is dependent on the **F** matrix) are computed, and the **y** matrix is formed. Secondary sources for the top layer in the model are found by multiplying the **y** matrix by the inverse of the **C** matrix.

The displacement in the frequency domain for a particular receiver is computed by summing up contributions from all boundary elements in the interfaces above and below the receiver (see Equation 3.71). The contribution from the direct wave can be included here, if required, simply by adding the displacement Green's function between the source and the receiver.

The frequency domain response is stored at this point.

4.4 Computations after the frequency loop

A wavelet is chosen in the time domain which can be any function of time as long as there are no frequencies in the wavelet which are higher than the maximum frequency computed in the previous section. The wavelet is transformed into the frequency domain using a fast Fourier transform (Press et al., 1992), and multiplied by the displacement response frequency by frequency. The response in the time domain is yielded by performing an inverse Fourier transform.

The type and frequency of the wavelet can be changed at will with little extra computational cost because the frequency domain response from an impulse has been stored earlier.

4.5 Summary

This chapter describes the steps involved in implementing the boundary element method for computation of synthetic seismograms. In the next chapter, the BEM is tested and compared with other modelling methods.

Chapter 5

Aspects of modelling with the boundary element method

In Chapter 3, I present an introduction to the boundary element method (BEM) for seismic modelling and in Chapter 4 I outline the implementation of the method. This chapter deals with various different aspects of the BEM and demonstrates the validity of the method in different situations. The first section details various studies which were carried out in order to determine the input parameters required for accurate modelling. The second section shows several examples of seismograms generated using the BEM and compares them with results from the finite difference method. The third section discusses ways of improving the efficiency of the boundary element method whilst keeping the results accurate. The fourth section gives a brief description of how the code was altered to allow a water layer to be added to the models.

5.1 Accuracy studies

Though used extensively for modelling of earthquakes (e.g. Pedersen et al., 1996; Sanchez-Sesma and Campillo, 1991), little work has been done using the BEM method for modelling in an exploration geophysics environment. Because of the paucity of literature on this subject, it was necessary to carry out a number of studies to determine how accurate the BEM is in various circumstances. Tests are carried out by comparing seismograms generated using the BEM and seismograms

from equivalent stratified earth models generated using the reflectivity method (Appendix B). Various tests have already been carried out to test the number of elements required for numerical stability of the BEM. Bouchon et al. (1989) found that a discretization rate of 2-3 points per minimum wavelength is sufficient to keep numerical noise negligible, as long as the interface topography is sufficiently sampled.

5.1.1 Model truncation effects

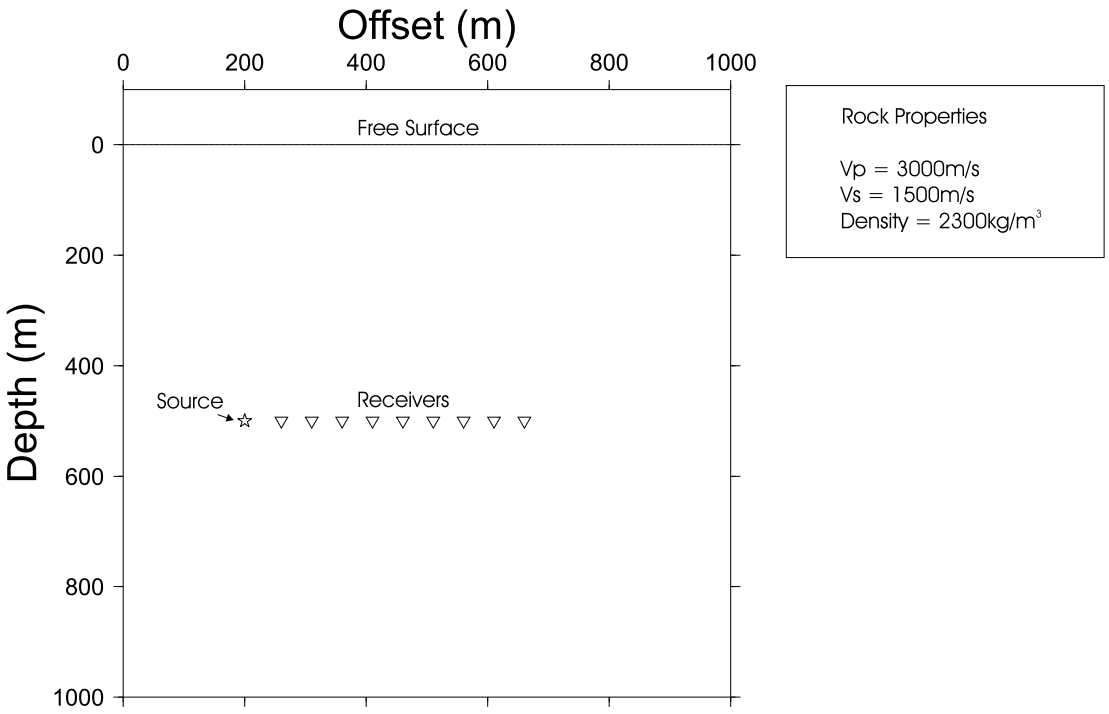

Figure 5.1: Test model 1. Preliminary model used to test accuracy of BEM code against reflectivity method code.

As with many modelling methods, the size and complexity of the model plays an important role in the computation time required to generate a seismogram. Therefore it is profitable to make the model area as small as possible. Unfortunately this means there are inaccuracies in the results due to model truncation.

To illustrate this problem I run the simple model shown in Figure 5.1. The model consists of a 2D-explosive source placed 500m away from a free surface and a line of receivers at the same depth with a maximum source-receiver offset of 700m.

The wavelet used is a Ricker wavelet of 15Hz central frequency and a 0.1s delay. For this model and all subsequent models in this chapter, the direct wave is not included in the seismograms. For computation with the BEM, the model has been truncated so that the free surface is defined only between 0 and 1000m.

The element length is determined by the minimum wavelength in the model at a particular frequency. From the studies by Bouchon et al. (1989), the element length should be no longer than

$$l_{max} = \frac{V_{min}}{\kappa f}, \tag{5.1}$$

where V_{min} is the minimum velocity in the model (P-wave or S-wave), f is the frequency; the constant κ is the number of elements required per wavelength, which can be as low as 2 for models with flat interfaces. In general, a higher value for κ gives more accurate results. For simplicity, I make the element length the same for all frequencies. The highest frequency that needs to be computed for a Ricker wavelet with a peak frequency 15Hz is 45Hz. Using Equation 5.1 with $V_{min} = 1500$m/s, f=45Hz and κ =3 gives $l_{max} \approx 11.2$m. I use an element length of 10m so that the free surface can be split into 100 elements of equal length.

The same model is input into the reflectivity modelling package Aniseis (Taylor, 1994) with the obvious difference that the reflectivity method treats the free surface as if it is infinite in length; this is treated as the ideal result. Figure 5.2 shows a comparison of the seismograms generated using the two methods. There is an excellent agreement down to a time of about 0.5 seconds. At later times spurious low-amplitude events appear on the traces. These events are due to diffractions from the edges of the interface (Pedersen et al., 1996). The zero-phase Ricker wavelet in both seismograms is not symmetric due to the near-field terms in the source signature.

Various methods of varying complexity have been attempted to counteract the effects of model truncation. The approach of Pedersen et al. (1996) is to apply an exponential taper to the strengths of the secondary sources near the extremities of the model. This serves to reduce the amplitude of the diffractions coming from the edges of the model as long as the size of the absorbing zones is at least the

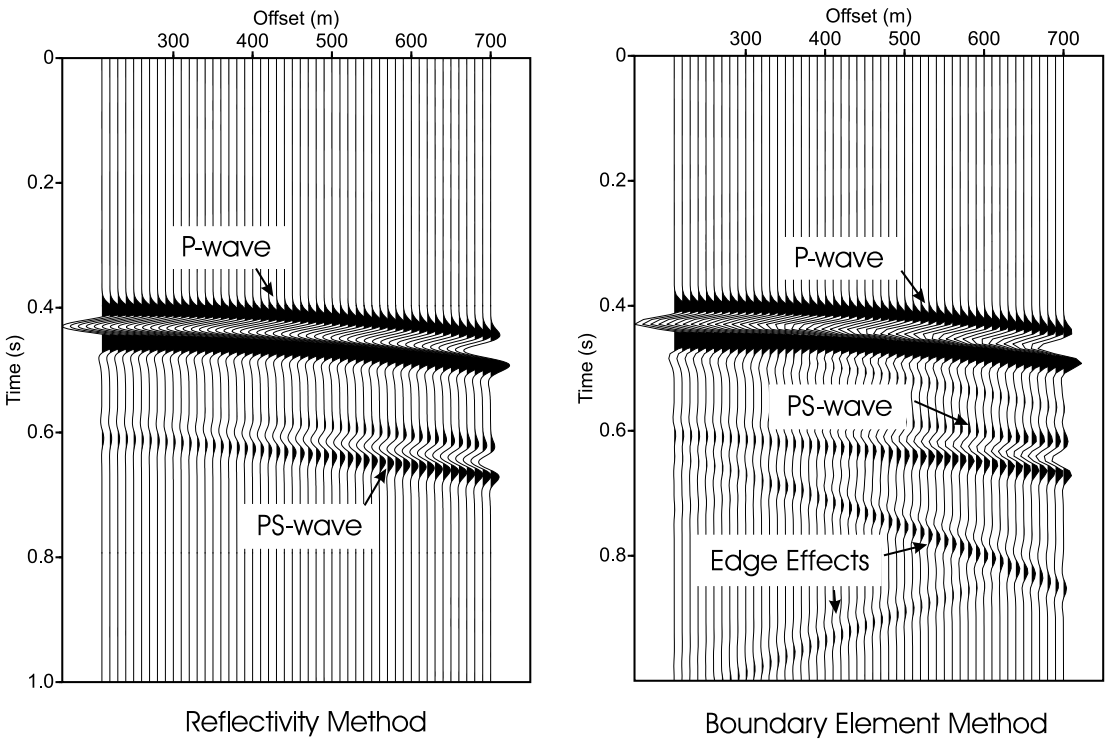

Figure 5.2: Comparison of seismograms generated from Model 1 using (left) the Reflectivity Method and (right) the Boundary Element Method. Seismograms display the vertical component of displacement. This and all other sections are displayed in SEG normal polarity, such that an upward movement of the earth is displayed as a white trough.

length of the maximum wavelength (i.e. the maximum P-wave velocity divided by the frequency being computed).

A more complicated approach by Yokoi and Takenaka (1995) is to compute the secondary sources of a reference model which is the same as the original model except that the heterogeneous part of the model is made flat. This reference model can be computed using the reflectivity method. The heterogeneous part of the model is then computed using the boundary element method. To find the final response, the secondary sources computed using the reflectivity method are used for the extremities of the model while the secondary sources computed using the boundary element method are used for the heterogeneous central part of the model. This method works well when the secondary sources of the edge zones of the model are not affected considerably by the heterogeneous central part.

I adopt an approach similar to that of Pedersen et al. (1996). I use an expo-

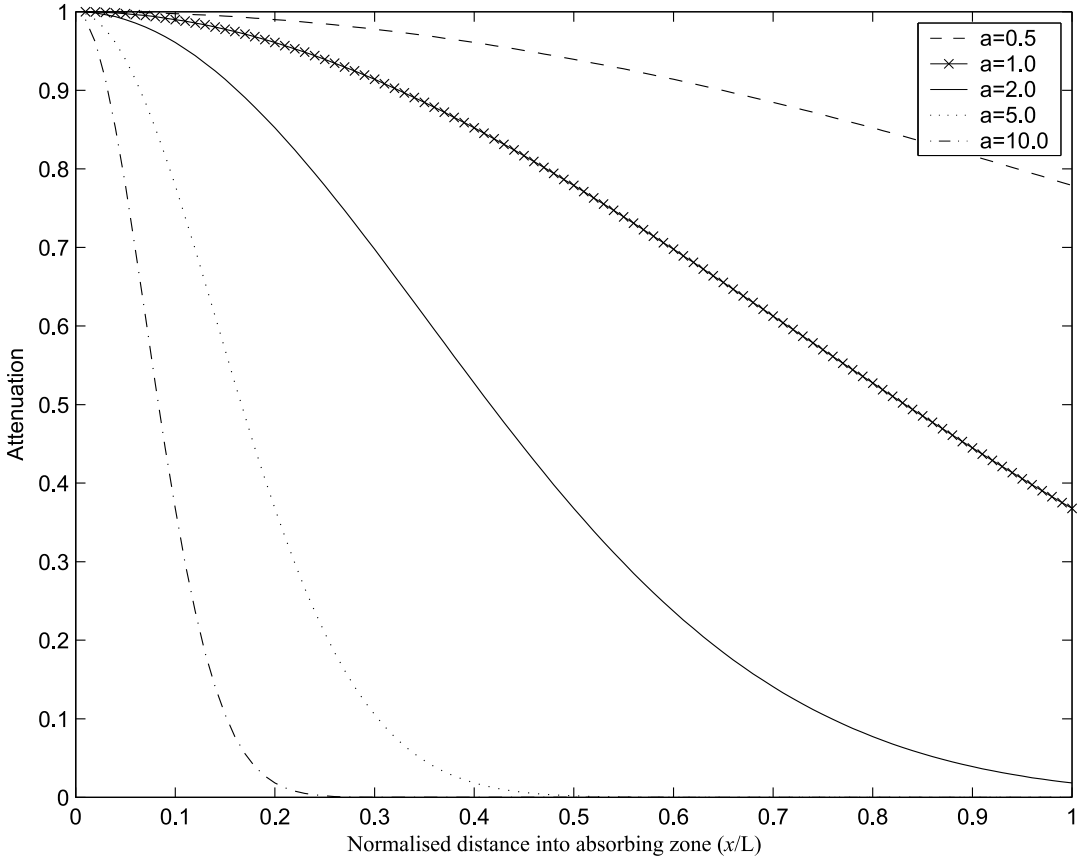

Figure 5.3: Graph to show absorption curves for different absorption factors (a) against offset which has been normalised to the length of the absorbing zone.

nential taper given by the following equation:

$$\gamma(x) = e^{-[a(L-x)]^2}, \qquad x < L \tag{5.2}$$

$$\gamma(x) = e^{-[a(x_{max}-L+x)]^2}, \qquad x > x_{max} - L, \tag{5.3}$$

where $\gamma(x)$ is the attenuation applied to the secondary sources. The variables a and L are the attenuation factor and the absorption zone width respectively (Cerjan et al., 1985). Figure 5.3 shows the shape of this exponential taper for varying values of a. The best taper should be the one which displays a decay which is not too sudden at any point within the absorbing zone. From the figure, $a = 2$ should produce the best results. This is the value taken for the absorbing zone.

The longest wavelength in the model at frequency f is given by the equation

$$\lambda_{max} = \frac{V_{max}}{f}, \tag{5.4}$$

where V_{max} is the highest velocity in the model. Pedersen et al. (1996) recommend that the absorbing zone be at least λ_{max} though, in general, the longer the absorbing zone is, the more efficient the absorption becomes. The required size of the absorbing zone changes with the frequency. Lower frequencies require longer absorbing zones than higher frequencies.

From Equation 5.1 it is clear that elements can be longer for low frequencies. Combining Equations 5.1 and 5.2, and defining absorbing zone length Λ gives

$$\frac{\Lambda}{\lambda_{max}} = \frac{n\kappa V_{min}}{V_{max}}, \tag{5.5}$$

where n is the number of elements in the absorbing zone. As an initial test, I choose an absorbing zone which consists of 20 elements. The length of the elements in the absorbing zone is calculated using κ=2.5. From Equation 5.5, the absorbing zone will be 4 times the maximum wavelength in the model at all frequencies.

Figure 5.4 shows a synthetic shot gather generated using the BEM with absorbing zones added. The situation is much improved. The diffracted events have been almost completely removed though they can still be seen with a 5 times magnification (Figure 5.6, left). This is probably due to the slightly less accurate computation using the wider elements in the absorbing zones.

Therefore, I refine the set-up of the absorbing zone slightly (Figure 5.5). I set the length of the closest absorbing-zone element to be the same as that of the elements within the central part of the model. The length of the absorbing-zone element furthest from the centre of the model is set using $\kappa = 2.5$. The length of the elements in between these two elements varies linearly from one end to the other.

With this set-up, the elements close to the model ensure good accuracy, whereas the elements far from the model allow the absorbing zones to be wide. These elements do not need to be so small because accuracy is less important far away from the model.

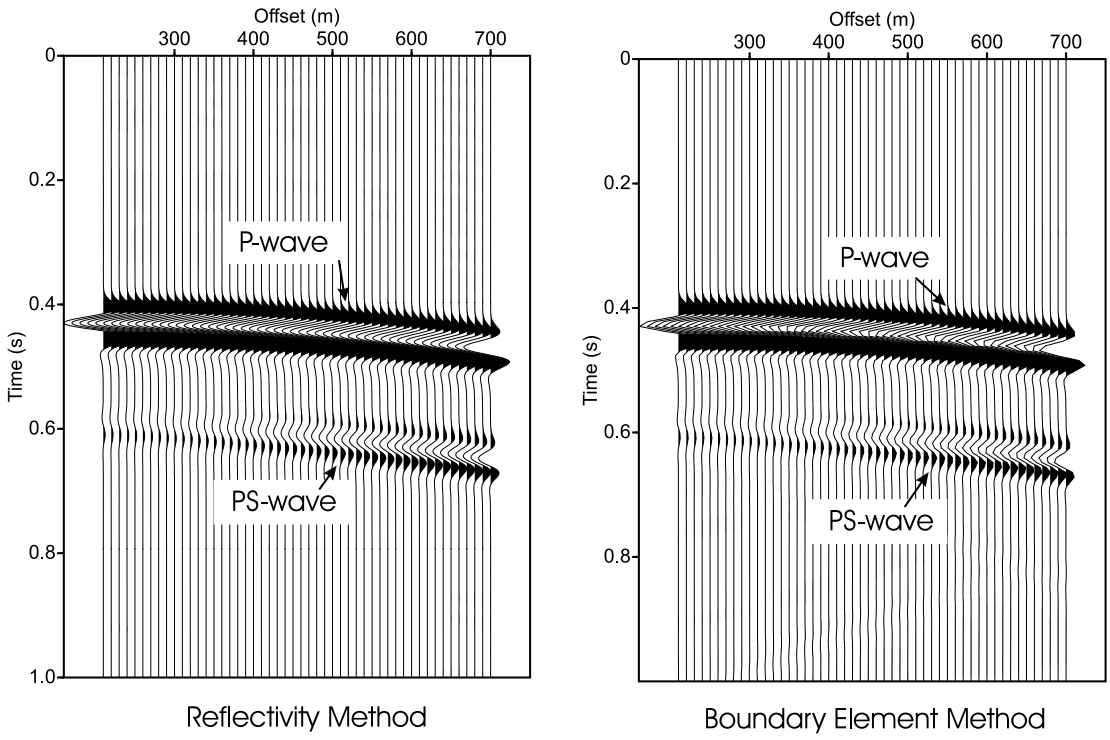

Figure 5.4: Comparison of Reflectivity Method and BEM with absorbing zones of 20 elements added.

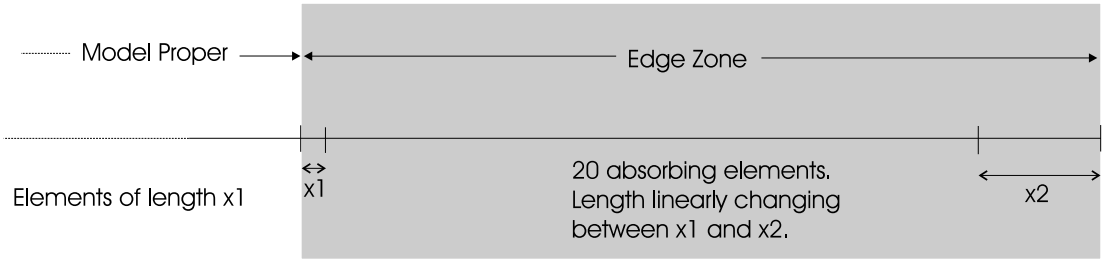

Figure 5.5: Diagram showing arrangement of elements used in model edge-zones.

The results after using the new absorbing-zone element lengths can be seen in Figure 5.6. The spurious events have now been completely removed and the results look almost identical to those from the reflectivity method.

The radius of the first Fresnel zone, that is, the area of the interface from which most of the energy arrives at a zero-offset receiver is given by (Yilmaz, 2001)

$$l \approx \sqrt{\frac{h\lambda}{2}}, \tag{5.6}$$

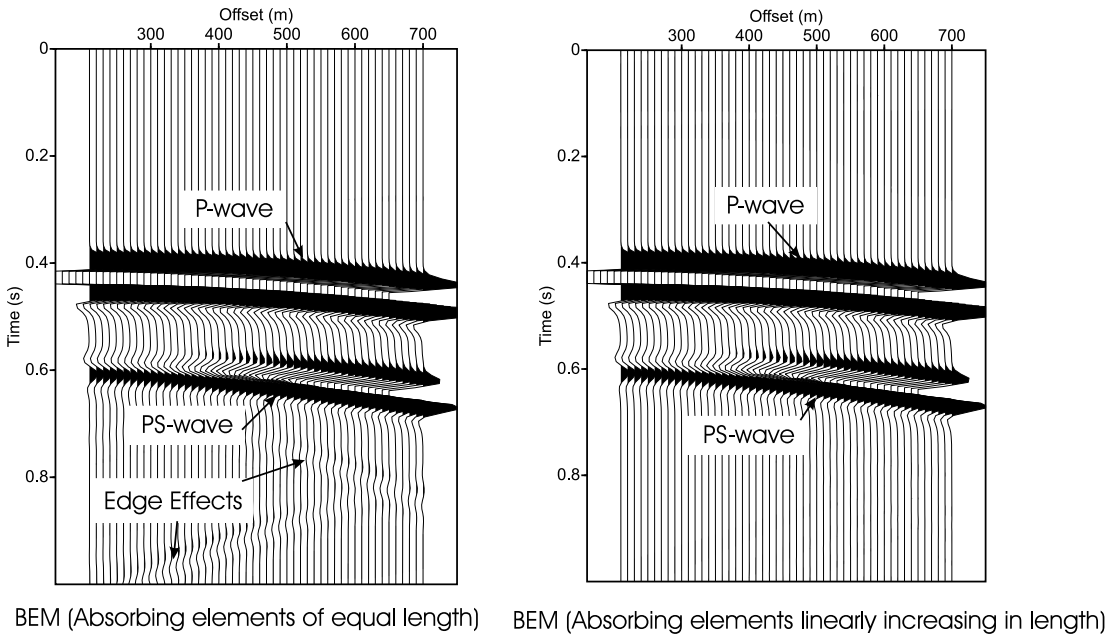

Figure 5.6: Seismograms generated using (left) absorbing zone with elements of equal length and (right) absorbing zone with elements of elements increasing linearly in length (seismograms magnified by 5 times).

where λ is the wavelength of the source and h is the distance of the source and receiver from a horizontal interface.

There is energy which should be reflected from the part of the interface in the absorbing zone, but is not because of the exponential taper applied to the secondary sources. Because of this, 20 additional elements are placed in the

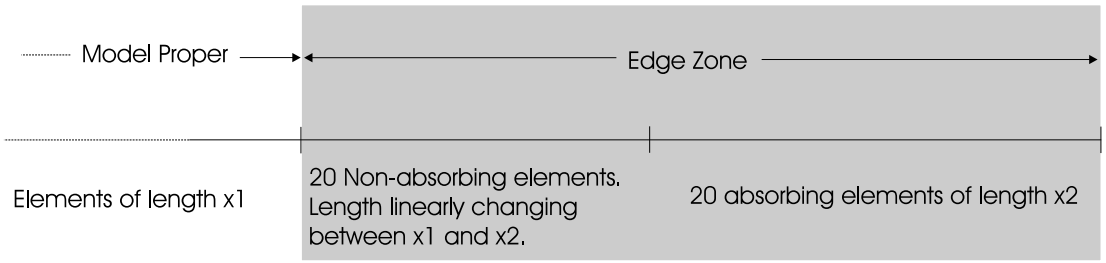

Figure 5.7: Diagram showing arrangement of elements used in model edge-zones. 20 additional non-absorbing elements have been added to each edge zone.

edge zone which are not absorbing, i.e. they act as normal elements. The final absorbing zone arrangement is shown in Figure 5.7. These additional elements make no difference for the model shown so far but are necessary for models where the source is near the edge of the model.

5.1.2 Source near interface

Because of the assumption that the secondary-source density is constant along the length of each interface element, there is likely to be some inaccuracy when the source is close to the free surface. The following section details tests which are designed to show the input parameters necessary for accurate boundary element modelling when the source approaches an interface.

The model is the same as for the previous section apart from the location of the source which is now at 5m depth. The receiver locations do not change. The comparison between the BEM and the reflectivity method is shown in Figure 5.8. There are clear differences, especially at near offsets for the P-wave and far offsets for the converted wave. When the source is moved 10m away from the free surface the agreement becomes very good (Figure 5.9). This indicates that there is indeed a limit to the permissible proximity of the source to an interface.

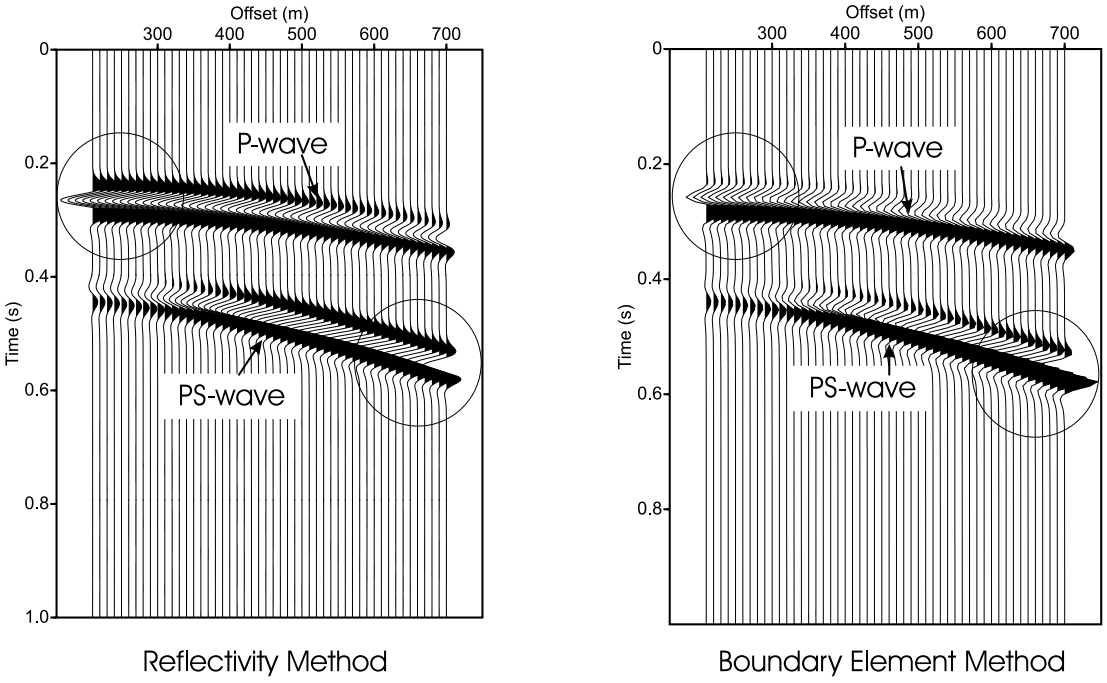

Figure 5.8: Seismograms to show comparison of reflectivity method and BEM when the source is 5m from the free surface. Element length is 10m. Differences between the two methods are shown by the circles.

For these models, the element length is 10m so two more points are added to the interface in the region of the source; one at 195m and one at 205m. The result of this modelling shows good agreement with the reflectivity method (Figure

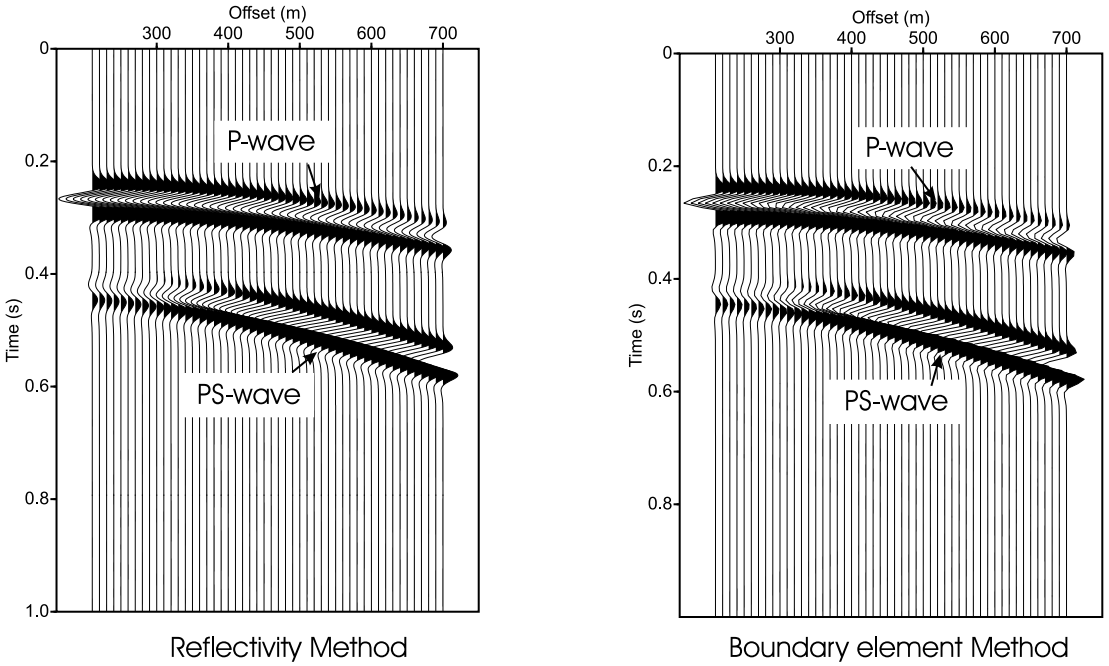

Figure 5.9: Seismograms to show comparison of reflectivity method and BEM when the source is 10m from the free surface. Element length is 10m.

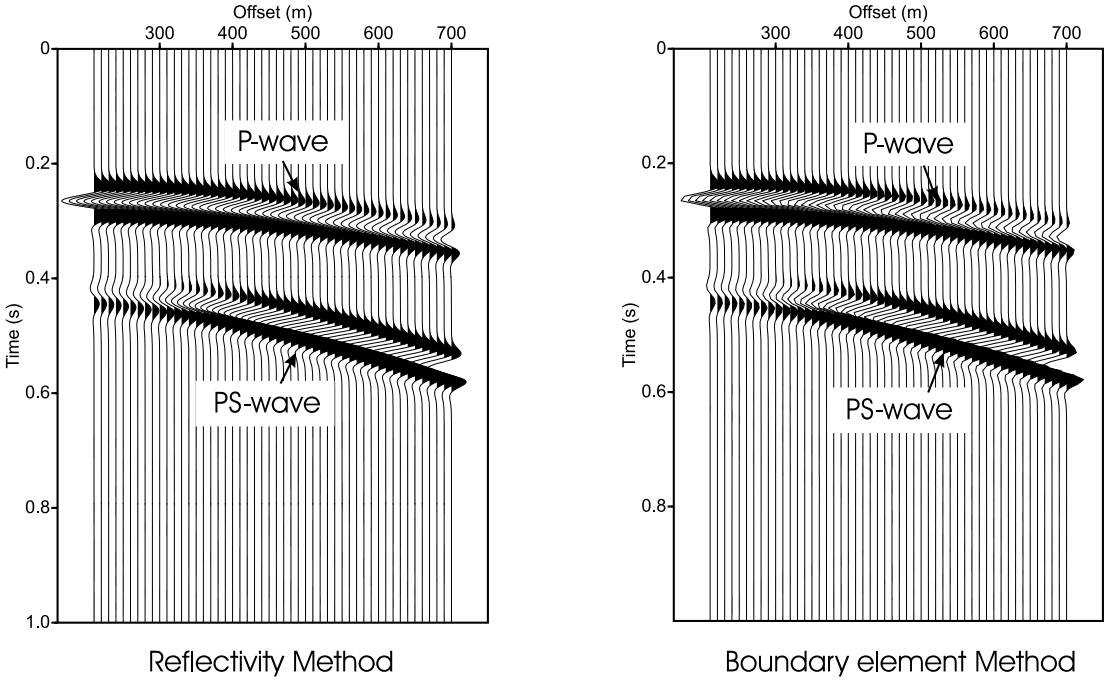

Figure 5.10: Seismograms to show comparison of reflectivity method and BEM when the source is 5m from the free surface. Element length is 5m in the region of the source.

5.10), suggesting a simple rule of thumb: the element should not be longer than the distance between it and the incident source. This rule was also tested for Ricker wavelets with a centre frequency of 10Hz and 20Hz and was found to hold also at these frequencies.

5.1.3 Reflections from a transparent boundary

A good test of whether a seismic modelling method is working well is to place a transparent interface in the model. This is an interface which has rock of the same velocity and density above and below it. I use Model 1 (Figure 5.1) again, but with an additional horizontal transparent interface at a depth of 800m. If the method is accurate the reflections from this boundary should be negligible.

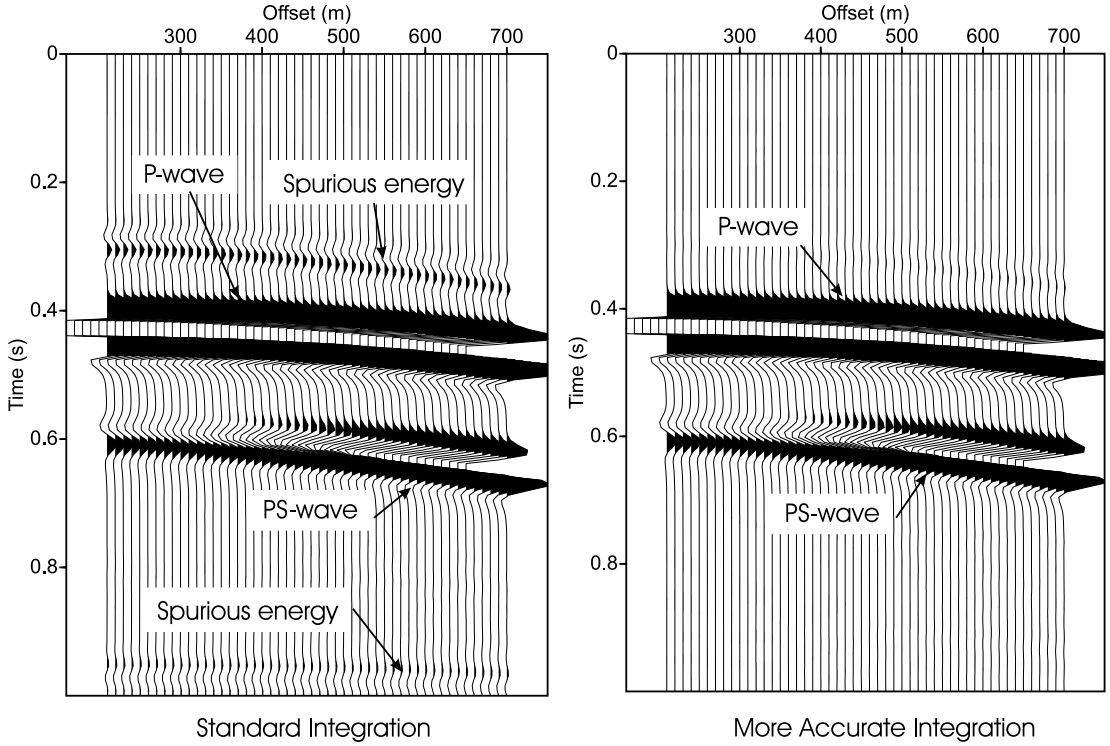

Figure 5.11: Seismograms generated from transparent interface model. Without (left) and with (right) more accurate integration of displacement Green's functions. Spurious reflections can be seen at around 0.3 and 1.0 seconds. These have been attenuated greatly by more accurate integration. Seismograms are shown with 5x gain applied.

Figure 5.11 shows a seismogram generated from the transparent interface model, with a 5 times gain applied. Spurious reflections can be seen at around 0.3 seconds. These are now much larger than any edge effects.

Because the amplitude of these events is much larger than I expected, every part of the modelling code was tested for accuracy. The only area where more accuracy could be achieved is in the integration of the Green's functions when the secondary-source element is coincident with the receiver element. As stated in Chapter 3, the singularity in the traction Green's function needs to be treated carefully and is exactly ± 0.5 or 0 depending on the components under consideration. However, no exact expression has been found for the displacement Green's functions. The error in a 10 point Gaussian integration scheme could be quite large because of the logarithmic singularity. Therefore, in the case where element source and receiver are coincident, more accurate integration was carried out (100 points used instead of 10). The result after more accurate integration can be seen in Figure 5.11. There is a clear improvement, with the reflections from the transparent interface attenuated greatly. I consider this result to be accurate enough for most situations.

5.1.4 Thin-layer modelling

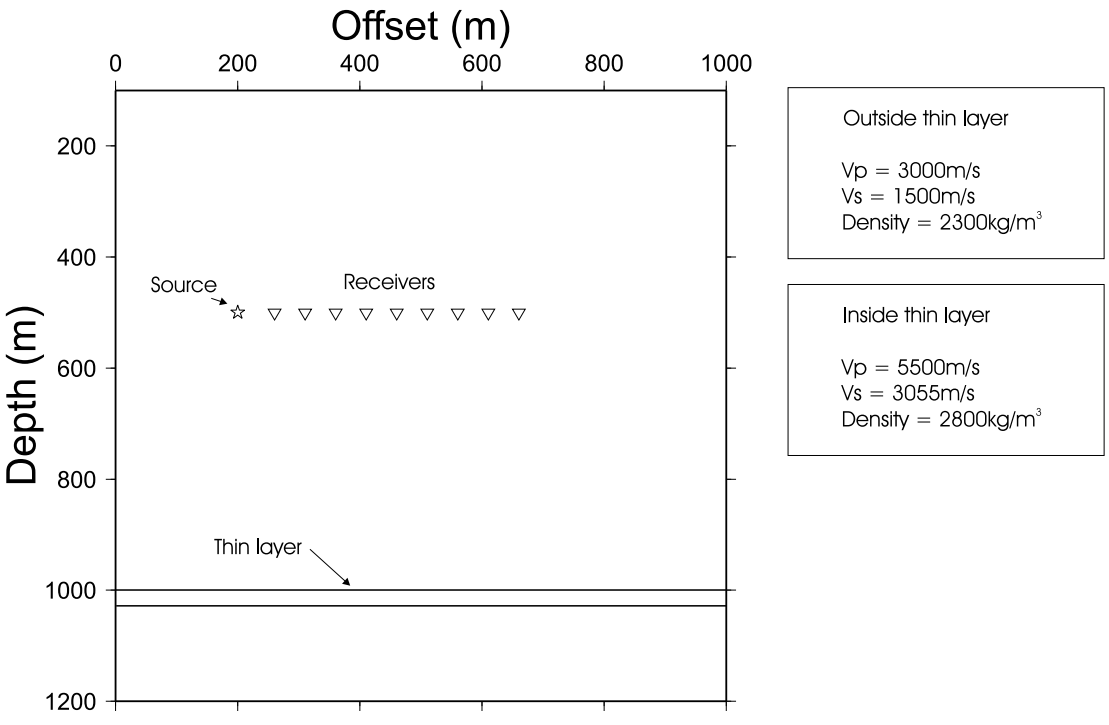

Figure 5.12: Model used for thin-layer testing

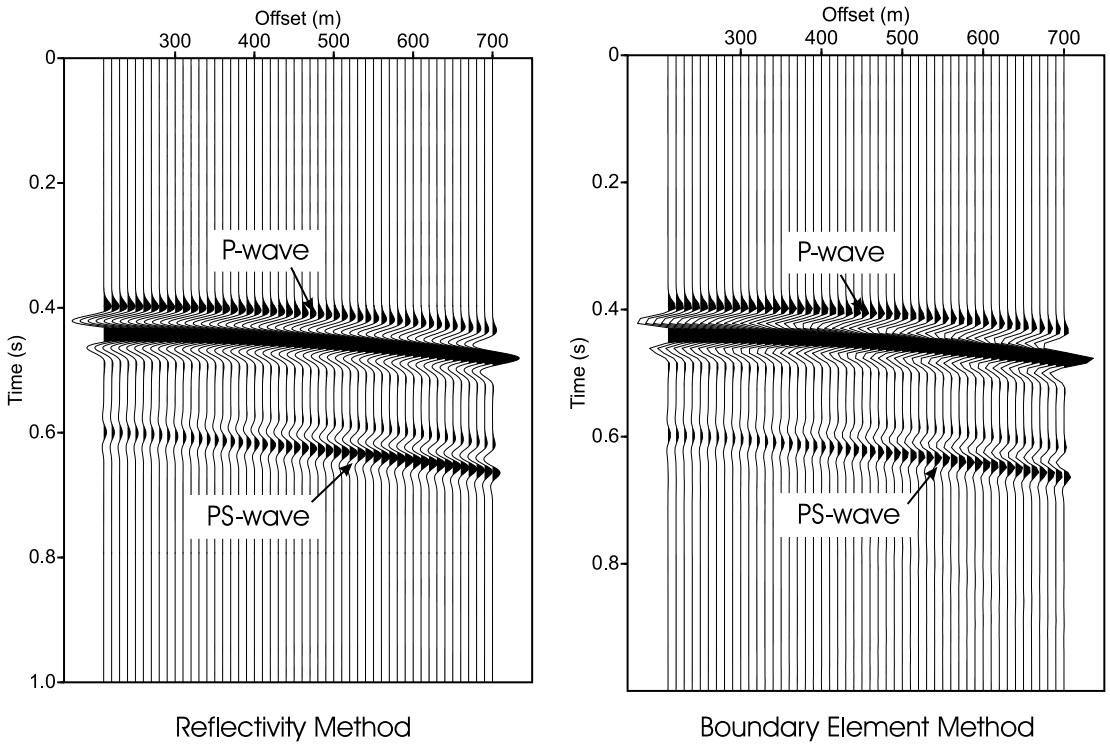

Figure 5.13: Comparison of seismograms generated using (left) reflectivity method and (right) BEM, for a thin layer of 5m.

The following tests are designed to find how close together two interfaces can be placed and still give accurate results. The input model for this test is given in Figure 5.12. For the first test, the thickness of the thin layer is set to 5m. Figure 5.13 shows the comparison between the BEM and the reflectivity method. There is fairly good agreement between the two so a model with a thin layer thickness of 1m is run. The results can be seen in Figure 5.14 There is a clear difference between the two methods, which is especially easy to see at far offsets. There is also evidence of diffractions coming from the edges of the absorbing zones.

In the previous section, more accurate integration was carried out for situations where source and receiver elements were coincident. However, the situation where one element is directly above the other and very close can also cause inaccuracies. This is of particular importance for traction Green's functions, which have a stronger singularity than the displacement Green's functions.

More accurate integration for those elements which are within one element length of each other was implemented in the code. As with the transparent interface situation, 100 integration points are used instead of 10. The results can

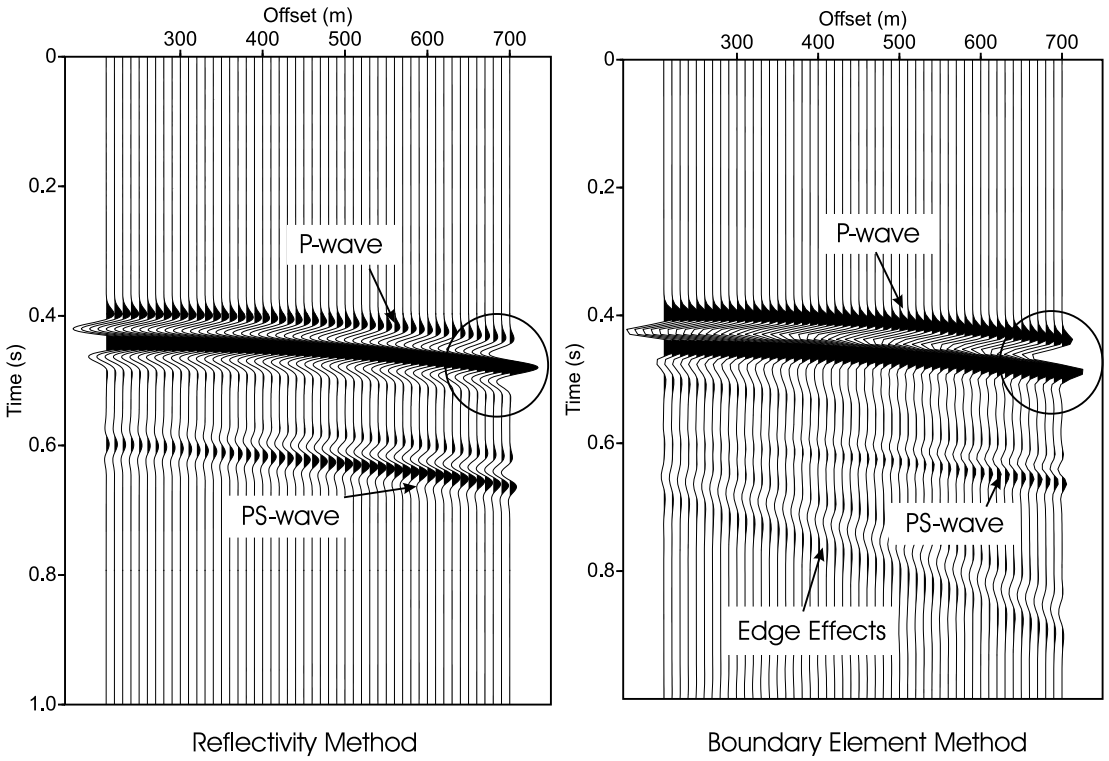

Figure 5.14: Comparison of seismograms generated using (left) reflectivity method and (right) BEM, for a thin layer of 1m. Differences are shown by the circles.

be seen in Figure 5.15. The agreement between the two methods is clearly better than before, although there are some small differences in amplitude, I consider these to be small enough to be unimportant.

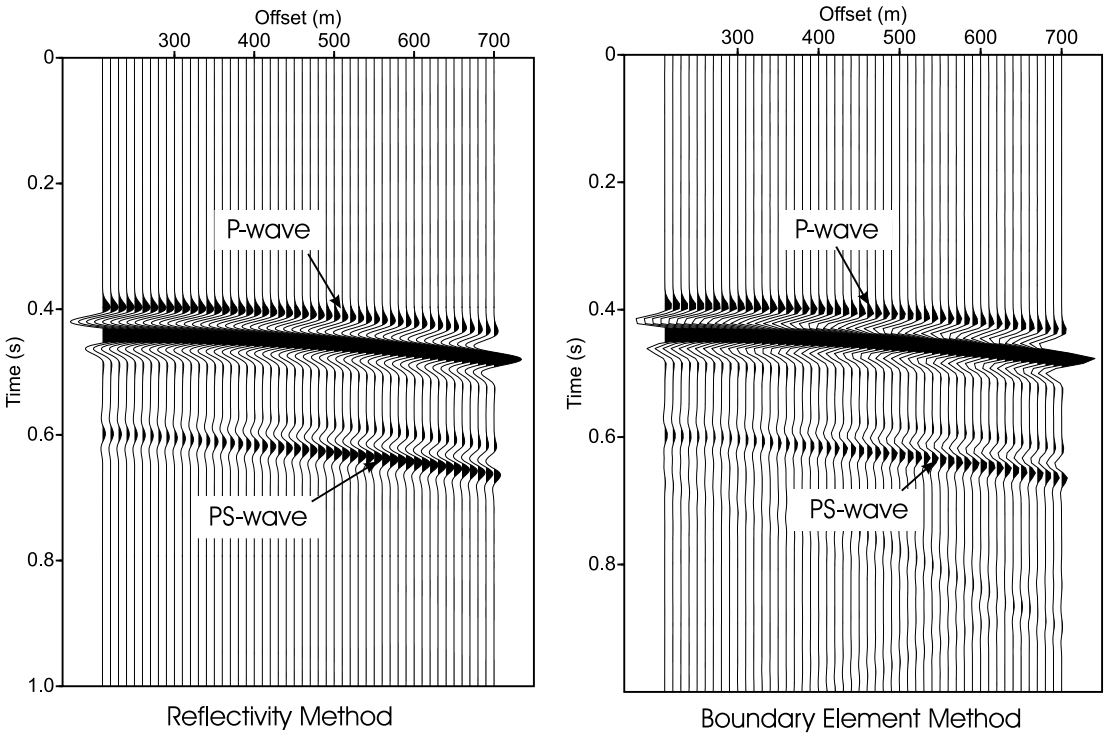

Figure 5.15: Comparison of seismograms generated using (left) reflectivity method and (right) BEM, for a thin layer of 1m. Integration over one element for the BEM is increased from 10 point to 100 point Gaussian quadrature.

5.2 Numerical testing of the BEM

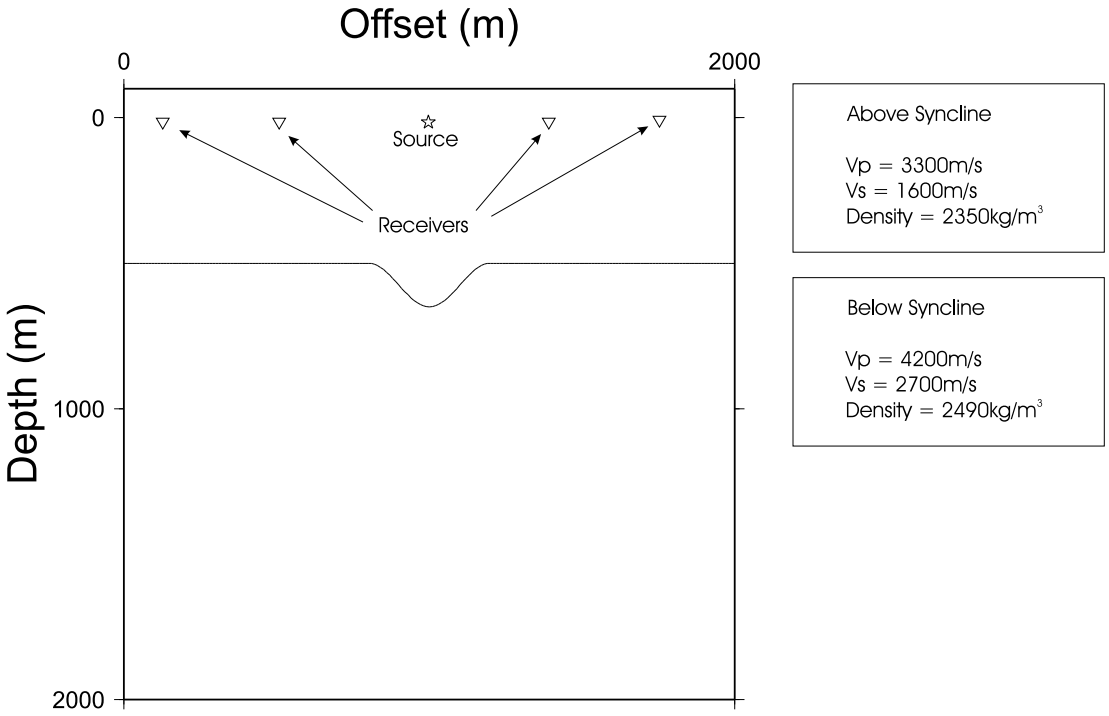

Figure 5.16: Syncline model used for input to FD and BEM codes

In this section two 2-D models are used to compare seismograms generated using the finite difference method and the BEM. The finite difference code used for these comparisons is ELA-2D from the University of Hamburg (Falk et al., 1994). Appendix C gives a brief description of how the finite difference method works.

The first model (Figure 5.16) tests the method on a simple syncline structure. Figure 5.17 shows a comparison of the finite difference and BEM results. There is an excellent agreement between the two. Even the smaller amplitude events are almost identical. The direct waves, which are automatically present in all FD seismograms, have been removed with a mute to enable a better comparison with the BEM seismogram.

The second model (Figure 5.18) consists of a rough-layered interface over a plane-layered interface. The rough interface is a varying sinewave with an average wavelength of 50m and an average amplitude of 7m. This model was selected because it was known beforehand that the rough interface would generate a lot

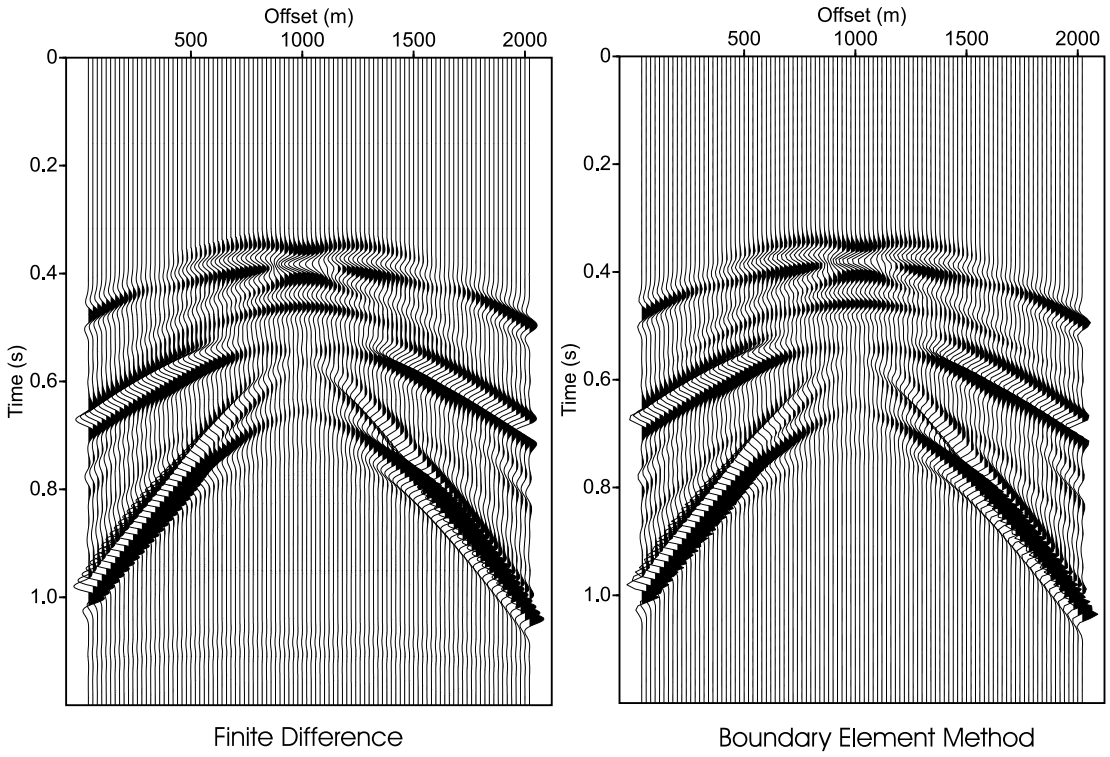

Figure 5.17: Comparison of seismograms generated using (left) Finite Difference and (right) Boundary Element Method for a syncline model.

of scattered energy, which should be a good test of the BEM code. Again, the results from the two methods agree very well (Figure 5.19).

5.2.1 Run-time considerations

It is of interest to compare the the speed of the BEM and FD codes. For the rough-interface model described above, the boundary element method requires 17 minutes on a 16-node 1Ghz cluster. The FD code is not easy to parallelise so is restricted to a single node. The time taken for the FD code is 60 minutes.

The boundary element code would take 272 minutes to run the mode on a single node, making the FD code 4.5 times faster. However, the BEM becomes more efficient when more shot gathers are required for the same model. The majority of the computation needs to be carried out only once. Thereafter, as many shot gathers as required can be generated for source and receiver locations anywhere in the model. This means a whole synthetic seismic profile can be generated with little more computational effort than that for a single shot gather.

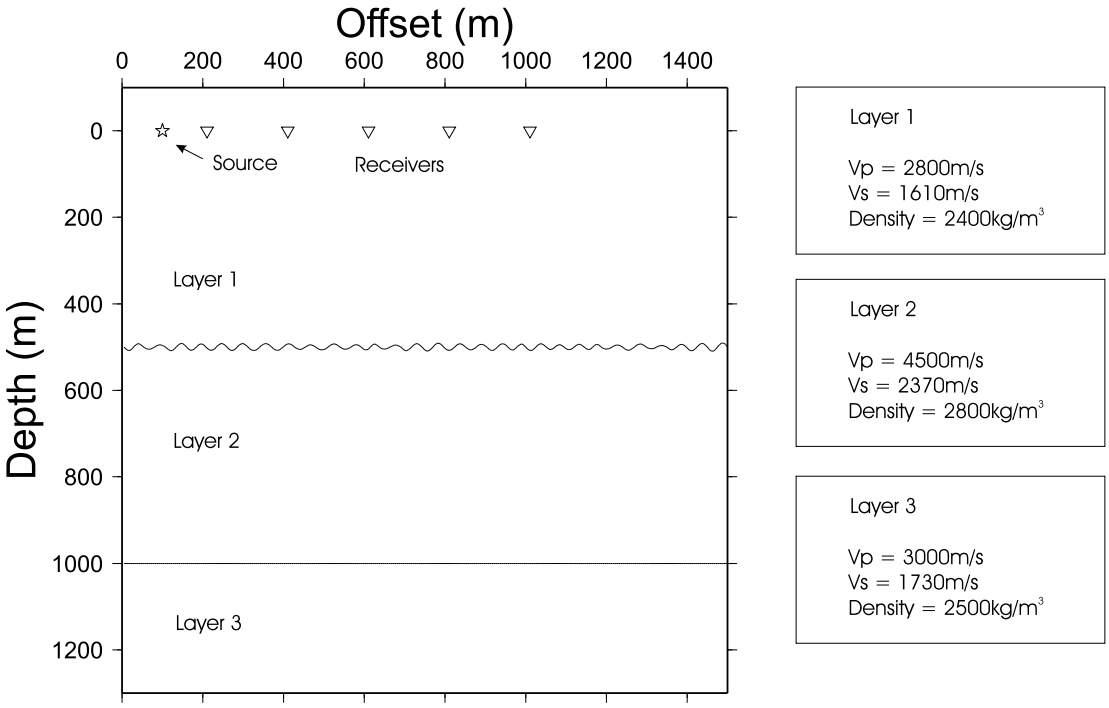

Figure 5.18: Rough interface model used for input to FD and BEM codes

The second advantage of the BEM over the FD is that the BEM code works in the frequency domain. Therefore, the wavelet can be defined after the model has run. As long as the wavelet does not have a maximum frequency greater than that computed by the code, the shape and frequency of the wavelet can be changed at will with very little extra computation.

The next part of this chapter focuses on ways in which the BEM can be made more efficient.

5.3 Improving the efficiency of the BEM

In the previous sections I presented the tests necessary to run an accurate model using the boundary element method, then showed that the method produces results that are consistent with the finite difference method. I now present two ways in which the BEM code can be made more efficient.

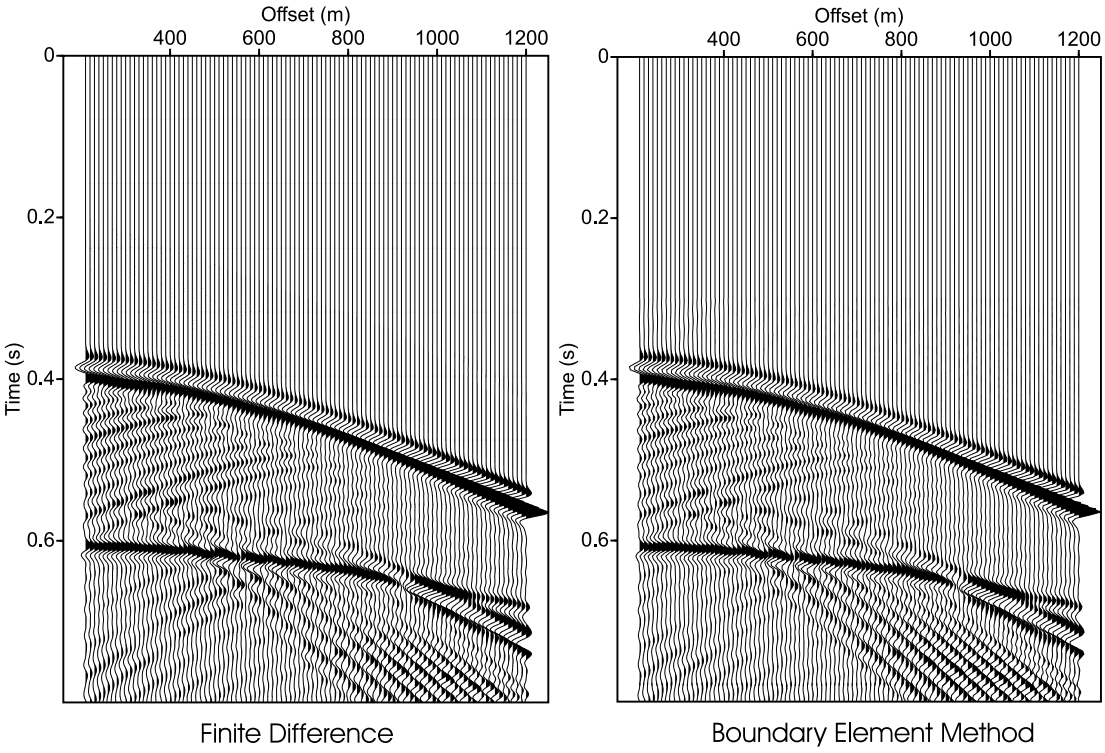

Figure 5.19: Comparison of seismograms generated using (left) finite difference and (right) boundary element method for a rough interface model. The events moving upwards at zero offset at 0.4s on the BEM gather are unremoved wrap-around.

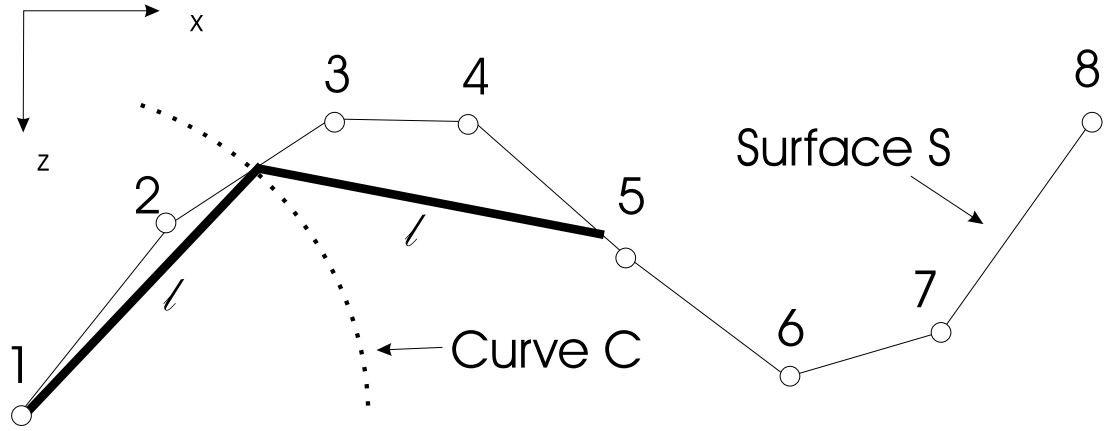

Figure 5.20: Diagram to show how the interfaces are resampled in the boundary element code.

5.3.1 Model resampling

In previous models, all interfaces were sampled with the same number of points for all frequencies. When computing the lower frequencies, it is not necessary to

use as many points as for the high frequencies since the length of one element need be only one third the length of the shortest wavelength for reasonably accurate modelling. For multilayer models it is also possible to use a different number of points for each interface in the model. The number of points used depends on the shortest wavelength travelling through the layers which are directly above and below the interface in question.

For plane-layered models, it is simple to perform resampling because the element length can be made just less than one third the minimum wavelength for each frequency. This gives considerable savings in computational time. Very long elements can be used for the low frequencies, generating small matrices which can be solved rapidly. However, the boundary element method is intended for modelling horizontally heterogeneous layers. Therefore, a slightly more sophisticated approach is necessary.

Consider the sinewave interface model depicted in Figure 5.18. For an interface which is similarly heterogeneous along its entire length, the most efficient way to distribute the elements is to ensure that they all have a similar length. Because the interface is not flat, detail will be lost if the sampling rate is set to be too small. On the other hand, it is clear that very long wavelengths will not see the fine detail in the interface so it is possible to use fewer points to define the interface in this case. The purpose of the studies in this section is to find a general rule for determining the optimum element length in the presence of lateral heterogeneity.

I start by describing a scheme for splitting each interface into a number of elements of length l, the optimum element length. The code starts from the left-hand side of the model and fixes the left of the element at the x and z coordinates of the first point in the model. To find the x and z coordinates of the right of the element, it is necessary to find the point P where the curve C crosses the surface of the interface S. This is achieved by solving the following equation:

$$mx + c = \sqrt{l^2 - x^2}, \tag{5.7}$$

where m and c are the gradient and intercept values of an element on surface S between two of the initial model points (see Figure 5.20). It is not known beforehand whether point P falls between initial model points 1 and 2, or 2 and 3 etc. so all pairs must be tried until the correct model point pair is found. The

coordinates of the start of the next element are made to be the same as the end of the previous one. The process of finding where the end of the element falls is repeated. This continues until the far end of the model is reached. To ensure that there is not an anomalously small element at the far end of the model, the difference is taken between the last element and the edge of the model. If this is more than 0.1m then the above process is repeated with a slightly refined element length. The process is iterative and is repeated until there is less than 0.1m error. Even for the higher frequencies the elements are generally no shorter than 5m. Therefore, to have an element only 0.1m longer than the rest makes no difference to the computation.

5.3.2 Element length determination

As stated above, it is possible to resample the model for a particular frequency as long as the rules from the previous sections are not contravened. To test how long the elements can be made without affecting the accuracy of the modelling, I run the sinewave model shown in Figure 5.18. The result when no resampling is performed, i.e. when all frequencies are computed with the maximum number of points per interface, is shown in Figure 5.21. The P-wave and C-wave reflections can be seen, as well as the large converted wave train caused by the sinewave interface. Because of the complexity of this resulting seismogram it can be assumed that any rule derived from this model can be applied to other situations. Figure 5.21 shows the result after resampling using 3 elements per wavelength.

It can be seen that the agreement is fairly good, although there are some differences in the wave-train further down the seismogram. Clearly, this would be good enough for some modelling applications, though it is interesting to find a point where almost no differences can be seen between the resampled and original results. Figure 5.22 shows the shot gather generated when the sinewave interface is resampled using 5 points per shortest wavelength.

There is clearly very little difference between this seismogram and the original. Therefore, the general rule for resampling is taken to be that the element length should not exceed a fifth of the shortest wavelength.

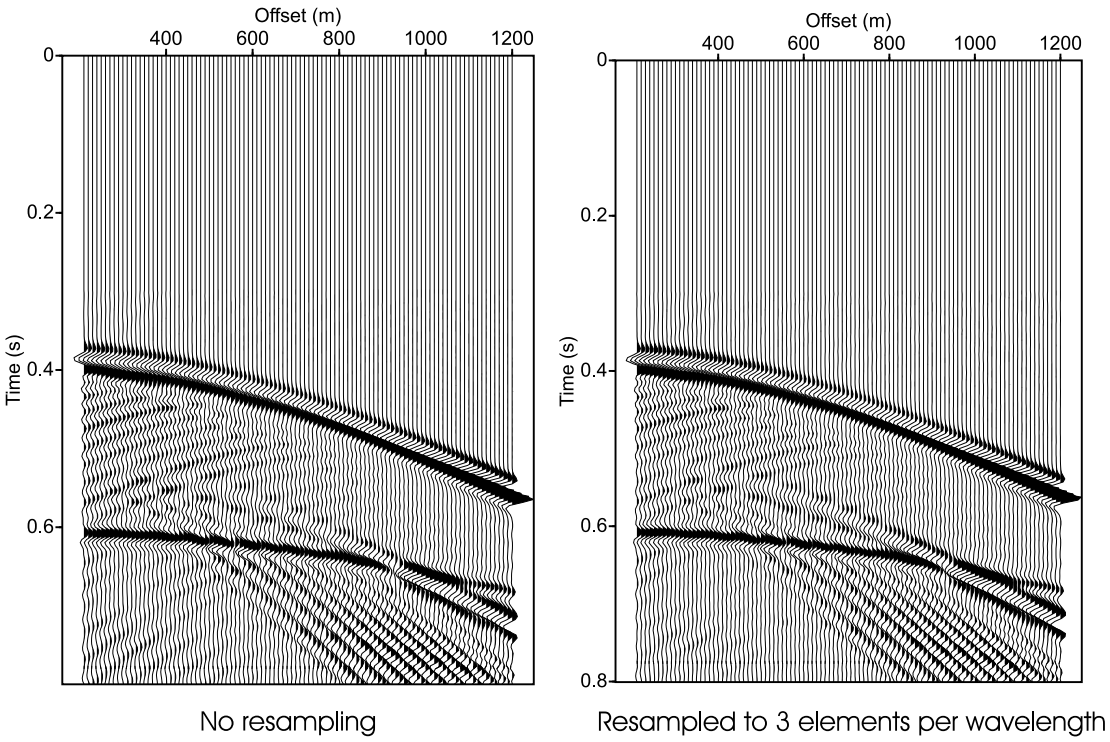

Figure 5.21: Comparison of seismograms for rough model with (left) no resampling and (right) resampling of 3 elements per wavelength.

5.3.3 Wrap-around suppression

Because the BEM is being used to generate seismograms in the frequency domain, there may be a problem with wrap-around when the signal is transformed back into the time domain. Wrap-around occurs when there is energy in the seismogram at times later than the window length. If the syncline model shown in Figure 5.16 is run with a time window of only 0.8 seconds, some of the energy appears at the top of the trace (Figure 5.23, left). This is the wrap-around. The standard way to avoid this effect is to make sure the time window is sufficiently long for no significant energy to be wrapped-around. In some cases, where there are many multiple events, the window has to be very long to avoid wrap-around. The longer the time window is, the longer the seismogram takes to compute. Therefore, it is sometimes beneficial to find another way of attenuating the energy which has been wrapped-around whilst leaving the earlier events unaffected. This can be done by adding a small imaginary part to the frequency before computation of the Green's functions. The technique is explained below.

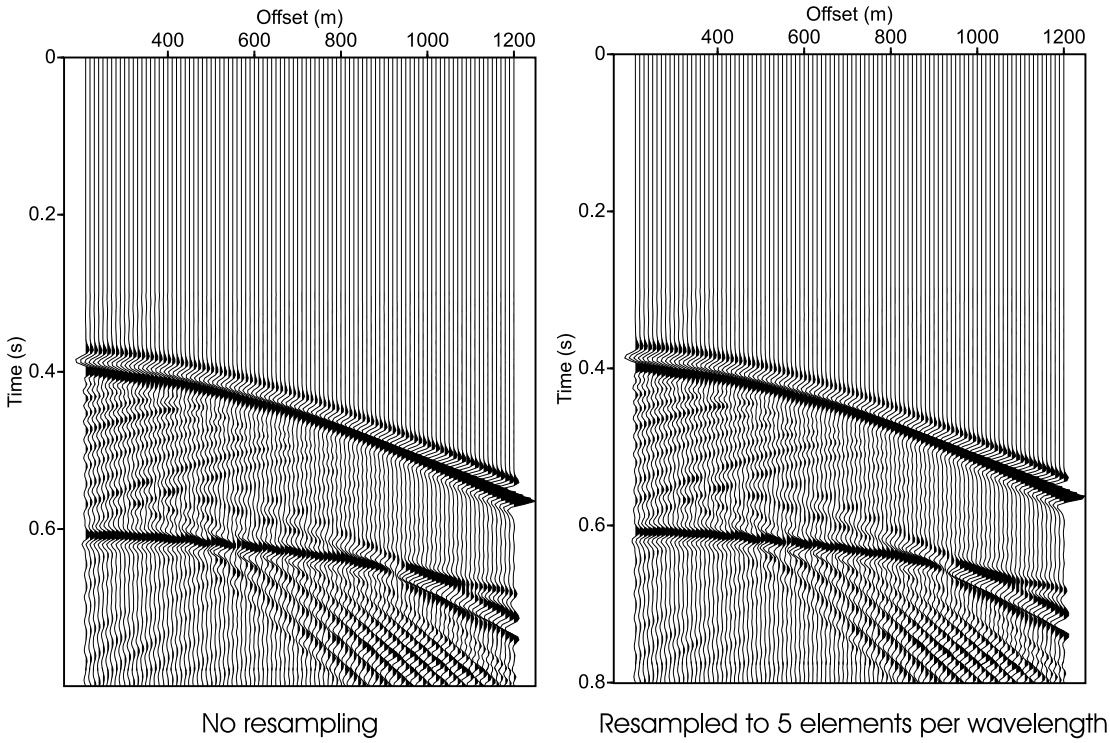

Figure 5.22: Comparison of seismograms for rough model with (left) no resampling and (right) resampling of 5 elements per wavelength.

The time domain response is given by the inverse Fourier transform:

$$f(t) = \frac{1}{2\pi} \int_{-\infty}^{\infty} e^{-i\omega t} F(\omega) d\omega, \tag{5.8}$$

where $f(t)$ is the function in the time domain, $F(\omega)$ is the function in the frequency domain and ω is angular frequency. Consider now the same inverse Fourier transform performed on function $F(\omega + ib)$ where ib is an imaginary number:

$$f_b(t) = \frac{1}{2\pi} \int_{-\infty}^{\infty} e^{-i\omega t} F(\omega + ib) d\omega. \tag{5.9}$$

Equation 5.9 can be written as

$$f_b(t) = \frac{1}{2\pi} \int_{-\infty}^{\infty} e^{-i(\omega+ib)t} e^{-bt} F(\omega + ib) d\omega, \tag{5.10}$$

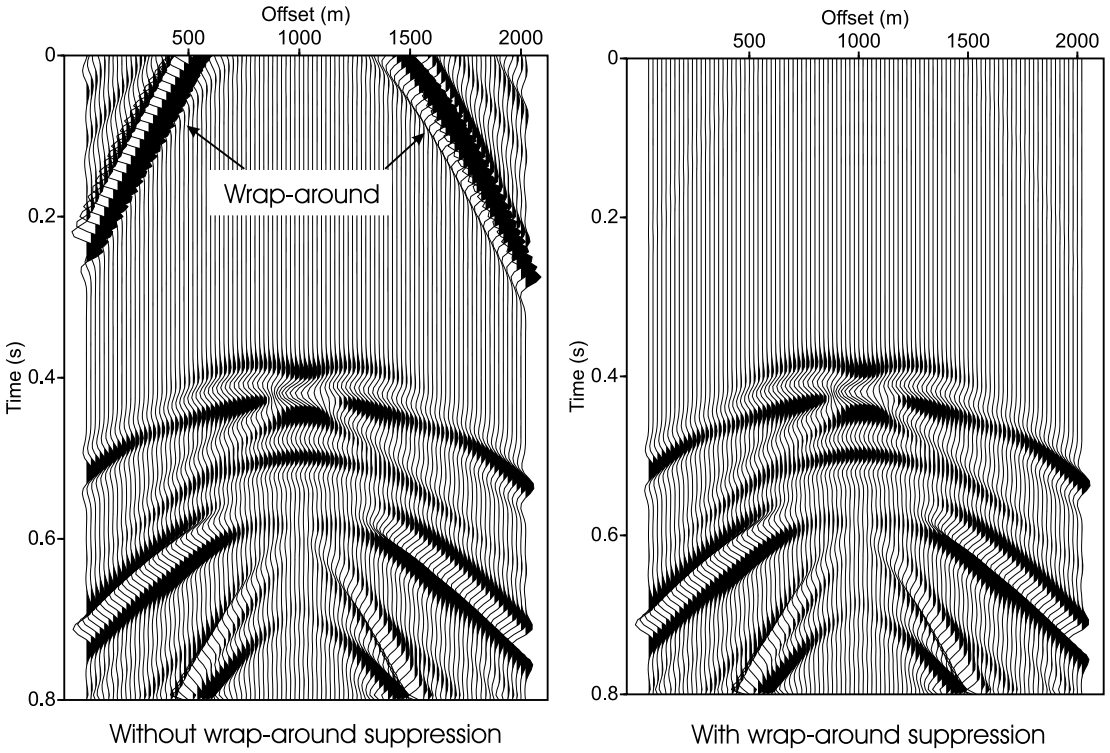

Figure 5.23: Seismograms generated from syncline model with time window reduced to 0.8 seconds (left) without and (right) with wrap-around suppression.

and the second exponential can be taken outside the integral

$$f_b(t) = \frac{1}{2\pi} e^{-bt} \int_{-\infty}^{\infty} e^{-i(\omega+ib)t} F(\omega + ib) d\omega. \tag{5.11}$$

Since the integral goes between plus and minus infinity, $f_b(t)$ becomes

$$f_b(t) = \frac{1}{2\pi} e^{-bt} \int_{-\infty}^{\infty} e^{-i(\omega)t} F(\omega) d\omega, \tag{5.12}$$

or

$$f_b(t) = e^{-bt} f(t). \tag{5.13}$$

The proof above shows that, by adding a complex part to the frequency, an exponential taper is applied in the time domain. An exponential gain equal to e^{bt} must then be applied to the time signal up to time T, the length of the time

window, to retrieve the correct amplitudes. Any energy outside the time window is left attenuated by at least a factor of e^{bt}.

The important factor in this procedure is the selection of b. Too small a value will not attenuate the wrap-around sufficiently, whilst too large a value could distort the events on the seismogram. If the events arriving at the bottom of the time window are to be attenuated by a factor c then,

$$c = \frac{f(T)}{f_b(T)} = e^{bT}. \tag{5.14}$$

Rearranging to give b yields

$$b = \frac{ln|c|}{T}. \tag{5.15}$$

In this case, b has been chosen to attenuate the amplitudes at the bottom of the 0.8s window to one hundredth of their original value, which gives b=5.756. The results can be seen in Figure 5.23. The wrapped-around events have been almost completely removed. The rest of the seismogram remains unaltered, which is the desired result.

5.4 Addition of a water layer

For models which contain a water layer, it is not possible to use exactly the same BEM formulation as for solid layer models. For the water later, acoustic Green's functions replace elastic Green's functions. These Green's functions include no shear stresses (Appendix A).

Also, the boundary conditions change. They now become the continuity of normal stresses and normal displacements, and the annulment of shear stresses within the fluid. Therefore, for the interface between a solid and fluid layer, the Green's functions must be rotated into the coordinates of the local element. This is performed through the use of a standard rotation matrix.

In a fluid, it is the singularity of the displacement Green's function which needs to be evaluated carefully. Using a similar argument to that for the evaluation of the traction Green's function in a solid (see Chapter 3), it has been found (Pointer et al., 1996) that the displacement Green's function integrated over one element is given by,

$$g_{ij}(\mathbf{x}_n, \zeta_k) = \frac{1}{2}\delta_{ij}\delta_{nk} + \int_{\zeta_k - \delta s_k/2}^{\zeta_k + \delta s_k/2} G_{ij}(\mathbf{x}_n, \zeta_k) dS_\zeta, \tag{5.16}$$

In this thesis I include a water layer only as the top layer of a model. Therefore, the special boundary conditions mentioned above only apply to the interface $n = 1$. This has the effect of reducing the size of the $\mathbf{C}$ matrix from a $6N$x$6N$ matrix to a $4N$x$4N$ matrix. The matrix, when left in the same form as for a solid-solid interface, was found to be unstable for some models and so was changed into the form

$$\mathbf{C} = \begin{bmatrix} \mathbf{B}_{12}(p_{33}) & \mathbf{B}_{11}(p_{33}) & 0 & 0 \\ \mathbf{A}_{12}(g_{33}) & \mathbf{A}_{11}(g_{33}) & \mathbf{B}_{22}(g_{31}) & \mathbf{B}_{22}(g_{33}) \\ \mathbf{A}_{12}(p_{13}) & \mathbf{A}_{11}(p_{13}) & \mathbf{B}_{22}(p_{11}) & \mathbf{B}_{22}(p_{13}) \\ \mathbf{A}_{12}(p_{33}) & \mathbf{B}_{11}(p_{33}) & \mathbf{B}_{22}(p_{31}) & \mathbf{B}_{22}(p_{33}) \end{bmatrix}, \tag{5.17}$$

Inversion of this matrix yields the secondary sources for the top two interfaces in the usual way (see Chapter 3). The final summation over all elements making up the top two interfaces is carried out using the Green's functions for stress in a fluid. The output is pressure, as would be measured by a standard hydrophone. Examples of models including water layers can be found in Chapter 8.

5.5 Conclusions

Basic tests have been carried out to determine the requirements for modelling using the boundary element method for seismic waves. The findings are as follows:

- The distance between the source and an element making up an interface must not be shorter than the length of the element.
- More accurate integration is required for secondary source and receiver elements which are coincident (for transparent boundaries).
- More accurate integration is required for secondary source and receiver elements which are closer than one element length (for thin layers).
- For heterogeneous interfaces, a sample rate of 5 elements per minimum wavelength is required for accurate results

Tests were conducted to find the size and type of absorbing zones required to suppress diffracted energy from the edges of the model. Results found that absorbing zones of 20 elements on both sides of the model is sufficient. The length of the edge elements varies linearly with distance from the model proper. The edge element closest to the model is equal in length to the element next to it in the model proper. The element furthest away has a length equal to 0.4 times the minimum wavelength in the model for a particular frequency. In this way the absorbing zones are shorter for higher frequencies and longer for low frequencies. This means the absorbing zone always has a length at least several times the maximum wavelength in the model. An exponential absorption factor of 2 is applied to the elements in the absorbing zone to suppress diffracted energy from this zone. Twenty non-absorbing elements were added to both sides of the model to take into account all energy within the Fresnel zone, which may be attenuated by the absorbing zones.

Tests were carried out to find the performance of the BEM when the source was located close to a boundary. It was found that accurate results were generated provided that each element in the model was no longer than the distance between it and the incident source. It is possible to improve the accuracy by adding several small elements to the model in the region of the source.

Transparent boundary tests revealed some inaccuracies in the boundary element code. Fairly high amplitude reflections from the transparent boundary were observed. These were attenuated greatly when more accurate integration of displacement Green's functions over the source element was carried out.

Similar inaccuracies were found to be significant when modelling thin layers. With more accurate integration of displacement and traction Green's functions, accuracy of modelling improved greatly. The effect was found to be much stronger for the traction Green's function as it has a stronger singularity in the case where secondary source and receiver are coincident.

2-D numerical testing of the BEM found the method to be stable and accurate. Comparison with the finite difference (FD) method showed an excellent agreement even when a rough interface is present in the model. In general the FD method is faster than the BEM, though advantages of the BEM over FD include:

- Ease of parallelisation.
- Ability to compute many shot gathers in one run
- Ability to change wavelet type and frequency after the model has run.

The efficiency of the BEM code can be improved in two ways. First, the model interfaces may be resampled for low frequencies where fine detail is not important. It was found that a sampling rate of 5 elements per wavelength was sufficient to generate accurate results. Second, wrap-around can be suppressed by adding a small imaginary part to the frequency before computation of the Green's functions. A test was conducted in which wrapped-around energy was attenuated by 100 times. This suppressed the wrap-around enough to make it negligible whilst leaving the energy which was within the time window unaltered.

The boundary element method can be adapted for models containing a water layer. In this case Green's functions for an acoustic medium are used. The boundary conditions change to the continuity of normal stresses and normal displacements, and the annulment of shear stresses at the interface between the solid and the fluid. This leads to a reduction in the size of the matrix to be inverted from $6K$x$6K$ to $4K$x$4K$.

Chapter 6

Domain decomposition and the far-field approximation

In the last chapter, important results are given which are necessary for accurate modelling using the boundary element method. In the later sections, I also describe two methods for speeding up the computation. This is an important aspect which must be considered when modelling with the boundary element method. The computationally most expensive part of the code is the inversion of the **D** and **C** matrices (see Chapter 3), which requires an amount of time proportional to N^3, where N is the number of elements required to make up a particular interface. This means it is sometimes not possible to compute seismograms for large models because of the computational power required to carry out such a task.

The task of speeding up the computation has been tackled in several different ways in recent years. Bouchon et al. (1995), Ortiz-Alemán et al. (1998) and Yokoi (2003) all take advantage of the rapid $1/r$ drop-off in amplitude of the Green's functions in 3D. They simplify the matrix by retaining only those elements which have an amplitude greater than a particular threshold. The matrix then becomes sparse and can then be efficiently solved using the conjugate-gradient method. This method has been shown to improve performance greatly, though more work needs to be done to develop reliable threshold criteria for element elimination Yokoi (2003).

Fujiwara (1998) uses the fast multipole method (FMM). This is a more

sophisticated approach which separates the source part and the receiver part of the Green's functions using a technique called multipole expansion. The Green's function for the SH case can be evaluated using the following expression:

$$G^{SH}(\mathbf{s},\mathbf{v}) \approx -\frac{i}{4\mu}\sum_{n=-p}^{p} O_n(k_\beta,\mathbf{s})I_n(k_\beta,\mathbf{v}), \tag{6.1}$$

for a source located at $\mathbf{s}$ and a receiver located at $\mathbf{v}$. I and O are the coefficients of the expansion which are dependent only on the source and the receiver location respectively (for one particular frequency and one medium). The accuracy of the method depends on the order p of the multipole expansion.

The method works by separating source elements into groups. A source reference point is chosen which is roughly in the centre of a group of sources. Source elements which are far away from this reference point require a higher order of multipole expansion than those which are close to the reference point.

Because it is possible to separate the Green's functions into source and receiver contributions, source coefficients can be computed once and used later for a number of receiver points. This eventually reduces the number of operations required to multiply two $N \times N$ matrices together from N^2 to $p^2 N log N$.

After some initial testing, I decided that the effort required to implement the FMM would not be worth the small gains in efficiency. Because of the wish to retain high accuracy in the computation of the synthetic seismograms high orders of multipole expansion would have been necessary.

In this chapter I propose the use of domain decomposition combined with a far-field approximation (FFA) to improve performance. First, I consider how the model size affects the computational requirements. The next section describes the principles behind domain decomposition and outlines how it has been incorporated into the boundary element code, including tests of accuracy. This is followed by a description of the far-field approximation and its application to the boundary element method. Criteria are developed for using the FFA so that it can be implemented in such a way that reasonable accuracy is retained.

Parameter	Computational cost
Number of interfaces	Linear
Number of frequencies	Linear (before resampling)
Number of elements per interface	N^3

Table 6.1: Model Parameters directly affecting model run-time

Parameter	Parameter affected
Lowest S-wave velocity in model	Number of elements per interface
Length of model	Number of elements per interface
Maximum frequency	No. of frequencies/no. of elements per interface
Seismogram window length	Number of frequencies

Table 6.2: Model Parameters indirectly affecting model run-time and how they relate to the parameters directly affecting run-time.

6.1 Model size considerations

Tables 6.1 and 6.2 summarise the most important direct and indirect parameters which control computational cost. The most important factor when considering computational speed in the BEM is the number of elements required to make up a particular interface. As was found in the last chapter, this is dependent on the minimum wavelength in the media situated on both sides of the interface. Therefore, high frequencies and low-velocity media require more elements. This has an N^3 dependence as stated above and is the most important consideration in model building.

Also of importance are the length of the time window and the number of layers in the model. The computation time has a linear dependence on these factors, i.e., if either the number of layers or the length of the time window is doubled then the computation time doubles.

The syncline model considered in Chapter 4 was 2km long and consisted of 1 interface made up of 200 elements. The maximum frequency computed was 45Hz and the time window was 2 seconds long. This model took 17 minutes to run on a 16 node linux cluster.

For a 12km-model containing 8 layers and with an 8-second time window computed over the same frequency range, the time required would be at least 20 days and the memory required to store the **D** matrix would be more than

a gigabyte, much larger than the capacity of the nodes. Therefore, domain decomposition is required, first, to speed up computation and, second, to split the model into pieces for which the memory requirements do not exceed the memory capacity of the nodes.

6.2 Domain decomposition

The domain decomposition method used to improve the speed of the BEM follows the ideas of the alternating Schwarz method (Smith et al., 1996). For simplicity, I describe the approach considering only two sub-domains.

Consider the syncline model shown in Figure 6.1. It is assumed to be too large to compute directly so is split into two sub-domains, A and B.

Step 1. Computation begins in sub-domain A as if sub-domain B did not exist. The **D** and **C** matrices are constructed using only the elements in sub-domain A. As with the standard BEM method, the **E** matrix is computed from the **F** matrix which contains only the body force due to the initial explosive source. The secondary sources for sub-domain A are then found in the usual manner (see Chapter 3).

Step 2. The **D** and **C** matrices are constructed using only the elements in sub-domain B. This time, to compute the **E** matrix, contributions from the explosive source and from all the secondary sources along the interface in sub-domain A are included. The equation for computing the **E** matrix now becomes:

$$ {}^{\mathbf{B}}\mathbf{E}_n^T = -{}^{\mathbf{BB}}\mathbf{B}_{n+1,1}({}^{\mathbf{B}}\mathbf{D}_{n+1}^{-1})^{sup}{}^{\mathbf{B}}\mathbf{E}_{n+1}^T + \Delta{}^{\mathbf{B}}\mathbf{F}_n^T. + {}^{\mathbf{A}}\mathbf{H}_n^T, \tag{6.2} $$

where ${}^{\mathbf{A}}\mathbf{H}_n^T$ is the contribution to the wavefield from sub-domain A,

$$ \begin{aligned} {}^{\mathbf{A}}\mathbf{H}_n^T = {}&{}^{\mathbf{AB}}\mathbf{A}_{n,2}{}^{\mathbf{A}}\mathbf{Q}_{n-1,2}^T + {}^{\mathbf{AB}}\mathbf{A}_{n,1}{}^{\mathbf{A}}\mathbf{Q}_{n,1}^T - \\ &{}^{\mathbf{AB}}\mathbf{B}_{n+1,2}{}^{\mathbf{A}}\mathbf{Q}_{n,2}^T - {}^{\mathbf{AB}}\mathbf{B}_{n+1,1}{}^{\mathbf{A}}\mathbf{Q}_{n+1,1}^T. \end{aligned} \tag{6.3} $$

The superscripts on the left of the matrices denote the sub-domain being referred to. ${}^{\mathbf{AB}}\mathbf{A}$ is a matrix containing every combination of source elements in sub-domain A and receiver elements in sub-domain B. The format is the same

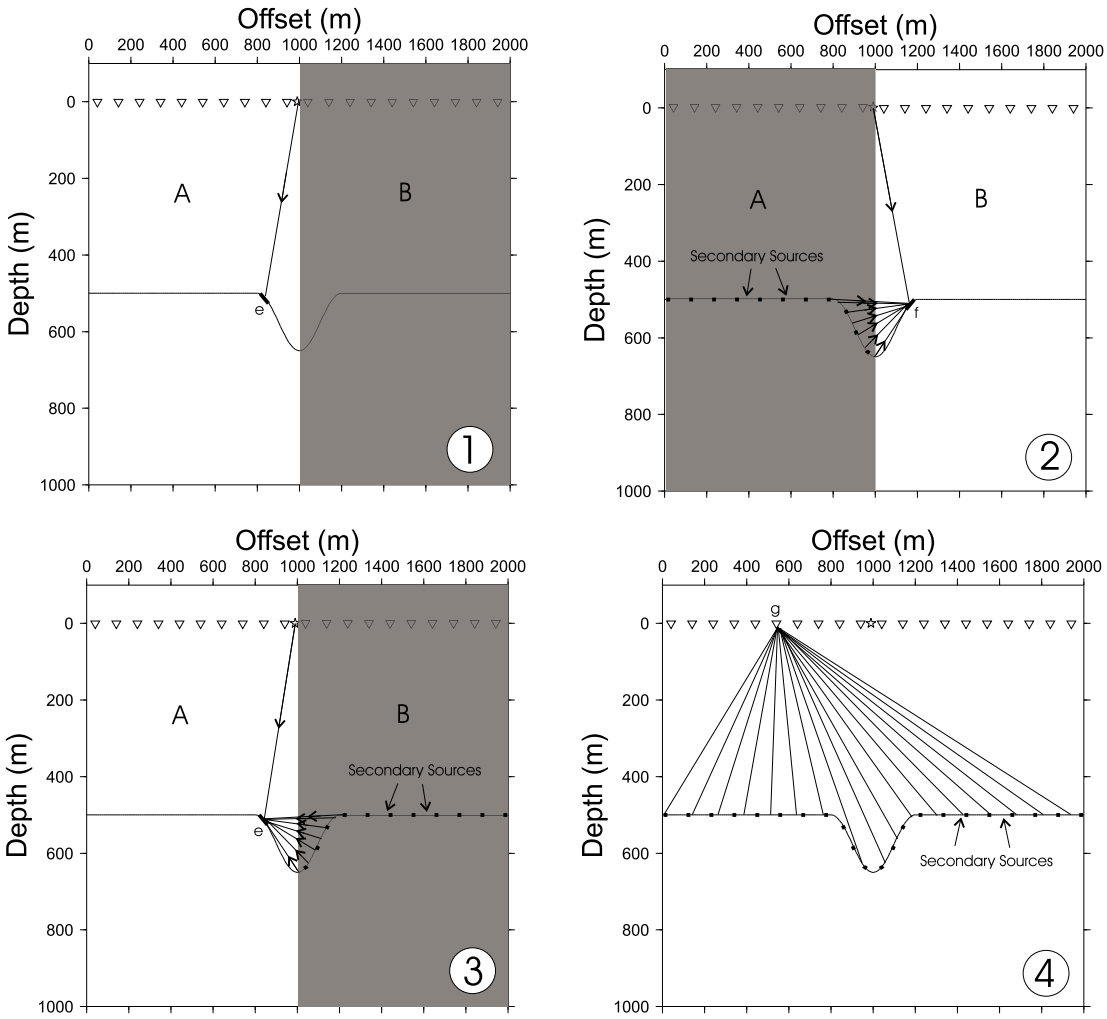

Figure 6.1: Steps involved in the domain decomposition scheme using the example of a syncline model. 1) Equations are solved for sub-domain A assuming that sub-domain B does not exist. Element e only considers the contribution from the initial explosive source. 2) The secondary sources computed for sub-domain A are propagated into sub-domain B and equations are solved for sub-domain B (the propagation from sub-domain A to element f in sub-domain B is shown). 3) The wavefield is propagated from sub-domain B back into sub-domain A and computation of secondary sources is again carried out. Steps 2 and 3 are repeated until sufficient accuracy is reached in the computation of the secondary sources. 4) After sufficient accuracy has been achieved, the final summation is carried out from all elements in the model.

as the standard $\mathbf{A}$ and $\mathbf{B}$ matrices described in Chapter 3. These matrices, in combination with the secondary source terms, describe the propagation of the wavefield from sub-domain A to sub-domain B.

Equation 6.3 includes all the interface elements which contribute to the response at interface n, although only the second and third terms are required for

the simple syncline model shown. A clearer representation of these terms can be seen in Figure 6.2. After computation of the **E** matrix, the secondary sources for sub-domain B are found in the usual manner.

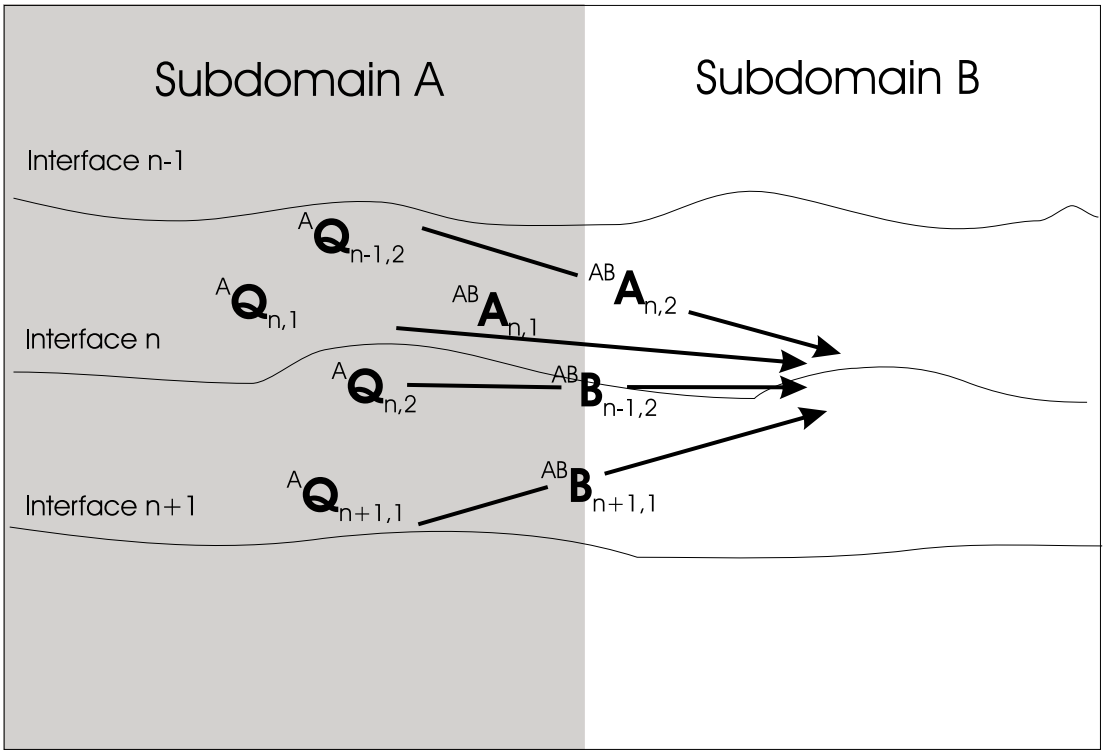

Figure 6.2: Diagram to show contributions to the wavefield propagation for interface n. Propagation direction in this case is from sub-domain A to sub-domain B.

Step 3. The **E** matrix is again computed for sub-domain A, after taking into consideration the contributions from sub-domain B. The new expression is:

$$^{\mathbf{A}}\mathbf{E}_n^T = -^{\mathbf{AA}}\mathbf{B}_{n+1,1}(^{\mathbf{A}}\mathbf{D}_{n+1}^{-1})^{sup\,\mathbf{A}}\mathbf{E}_{n+1}^T + \Delta^{\mathbf{A}}\mathbf{F}_n^T. + ^{\mathbf{B}}\mathbf{H}_n^T, \tag{6.4}$$

where $^{\mathbf{B}}\mathbf{H}_n^T.$ is the contribution to the wavefield from sub-domain B. The secondary sources can now be found directly after this step, since the **C** and **D** matrices and their inverses have already been computed in Step 1.

Steps 2 and 3 make up an iterative process which continues until the secondary sources in both sub-domains have been computed to a sufficient accuracy. When sufficient accuracy is reached, the secondary sources are summed as in the standard method. In this way, the displacement at each of the receivers is computed (Step 4, Figure 6.1).

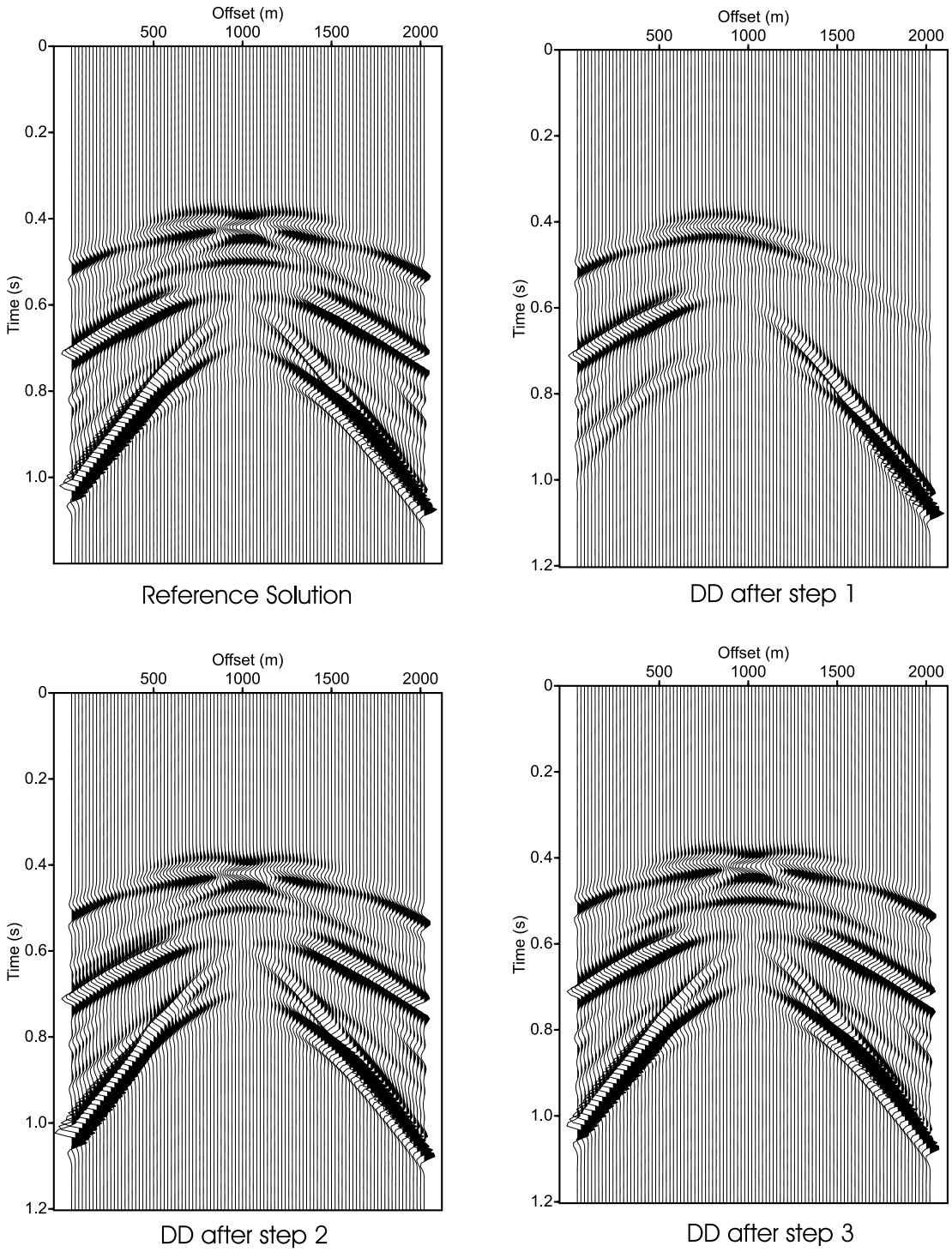

Figure 6.3: Seismograms generated using the domain decomposition routine after steps 1, 2 and 3. The reference solution, generated without using domain decomposition, is shown for comparison.

Figure 6.3 shows the response that would be seen at the receivers if the final summation were performed after Step 1. Only half of the secondary sources have been computed and the source strengths which have been computed do not take into account contributions from sub-domain B. After step 2, contributions from sub-domains A and B have been computed. The results are very similar to the reference solution. This shows that the method converges very quickly. After step 3 the seismogram generated can barely be distinguished from the reference solution.

The time taken by the domain decomposition can be split into two parts. The part involving matrix inversion requires an amount of time proportional to $2(N/2)^3 = N^3/4$. The part which propagates the wavefield from one sub-domain to the other requires a time proportional to $N^2/4$ each time a propagation has been performed. After step 3, two such propagations have been performed meaning a total computational cost proportional to $N^3/4 + N^2/2$. The second (propagation) term becomes negligible at high frequencies where the model is defined by 200 elements (i.e. N=200). Therefore, the new technique is 4 times faster than the standard method for the high frequencies in this model.

To give a better idea of the speed of convergence, residuals were computed for several frequencies over a number of iterations. The residual can be described as the difference in the solution between one iteration and the previous one. When the residual drops below a certain value the iteration is halted and the final summation can be carried out. The formula used to calculate the residual is as follows:

$$R_i = \frac{\sum |\phi_i - \phi_{i-1}|}{\sum |\phi_i|}, \tag{6.5}$$

where R_i is the residual for iteration i. The summation is over all elements in the model; ϕ_i is the source strength of one element after i iterations. The residual is given as a fraction of the secondary source strength. Equation 6.5 defines a rate of convergence. It was found through comparision of the multi-domain solution with the single-domain solution that the domain decomposition approach does converge to the single-domain result. This was also tested for many different models.

Figure 6.4 displays the residuals graph for the syncline model split into

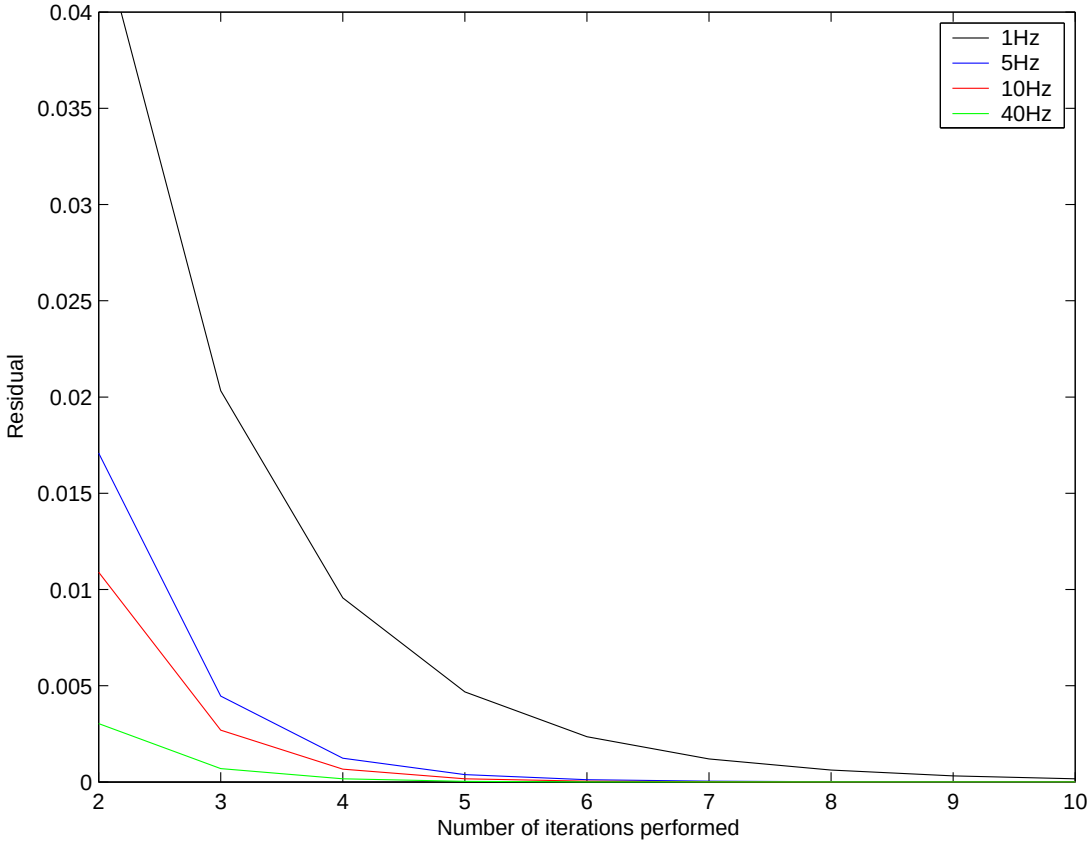

Figure 6.4: Residuals graph for syncline model with 2 sub-domains. High frequencies converge faster than low frequencies.

two sub-domains. Curves are shown for frequencies of 1Hz, 5Hz, 10Hz and 40Hz. There is a more rapid convergence for the higher frequencies. The lower frequencies are quick to compute anyway if the model is resampled (see chapter 4), it is the high frequencies which benefit the most from the domain decomposition. It can be seen from the graph that if a solution accuracy within 1% is required, it is necessary to perform 2 iterations at 40Hz and 4 at 1Hz.

The next step is to consider how domain decomposition would work with more sub-domains. Instead of alternating between two sub-domains it is now necessary to start with the first sub-domain and work along the line to the last sub-domain. When the last sub-domain is reached, computation again continues backwards along the line to the start again (Figure 6.5). Once the start of the model is reached, one iteration has been performed. The second iteration then starts by updating the B sub-domain and continues as for the first iteration. From many

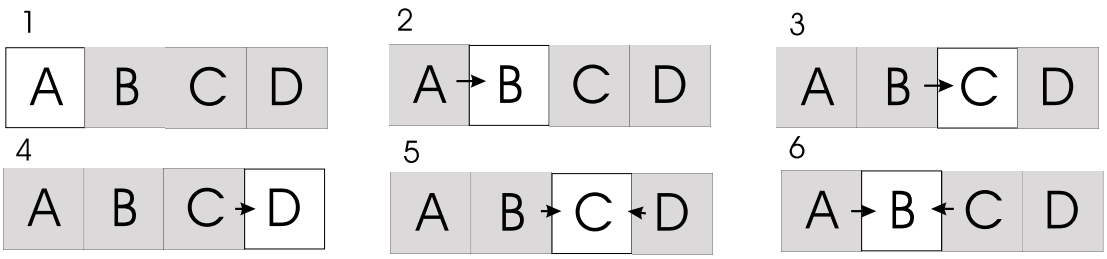

Figure 6.5: Diagram to show scheme for computing seismograms when more than 2 sub-domains are used. Secondary sources are first computed for sub-domain A, then computation progresses to the right. Once computation for sub-domain D has been completed propagation then continues back towards the start.

tests of the method, this was found to be the most efficient and stable order in which to carry out the computation.

Figure 6.6 shows the speed of convergence at 10Hz for 2, 6 and 10 sub-domains. It is clear from this plot that convergence slows for a model defined with more sub-domains. Though a larger number of sub-domains means more iterations, it does not necessarily mean more computational cost. As stated before, there are now two parts of the computation which contribute considerably to the total computational cost. The time taken for the inversion of the matrices is proportional to $D(N/D)^3 = N^3/D^2$, where N is the number of elements per layer and D is the number of sub-domains. This part of the implementation will always become very efficient with increasing number of sub-domains. The time taken for the iteration loop is $2DI(N^2/D) = 2IN^2$ where I is the number of iterations required to achieve the required accuracy.

The previous figures have shown that the number of iterations required is dependent on frequency and number of sub-domains. A further dependence on the model can be observed if a much larger scale model is considered. Figure 6.7 shows a long-offset (12km) rough interface model which could not be computed using the standard BEM because of the size of the matrices involved. Figure 6.8 shows the graph of convergence for this model at 10Hz and 40Hz for 10 and 20 sub-domains. Again, a greater number of sub-domains and a decrease in frequency means an increase in the number of iterations required. However, the convergence is much faster for this model than the shorter syncline model shown in Figure 6.1. This is because sub-domains far from each other have little effect on each other so the convergence becomes fast. Therefore, longer models converge more quickly.

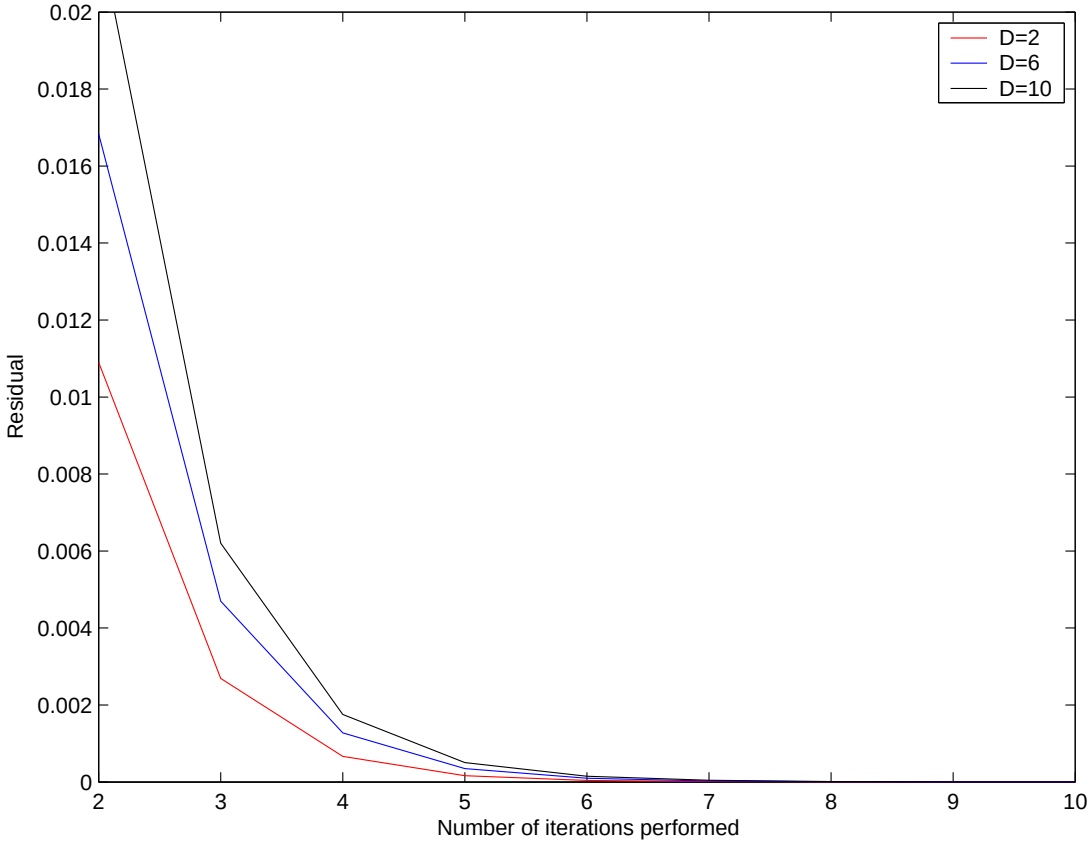

Figure 6.6: Residuals graph for syncline model with 2,6 and 10 sub-domains at 10Hz. Residuals show the difference between secondary sources after i and i-1 iterations.

So far, I have shown that the number of required iterations increases as frequency and model length decrease. More iterations are required for a larger number of sub-domains. Theoretically, an ideal number of sub-domains could be found for which the computational cost is minimised. However, the number of iterations is not only dependent on the model length but also the type of model. Therefore, the number of sub-domains used is not computed by the code itself but is a variable which can be decided on by the user on a trial and error basis.

A flow diagram for the implementation of domain decomposition is shown in Figure 6.9. First, all the **D** and **C** matrices necessary for each of the sub-domains are computed. The iteration loop then begins with the first sub-domain and continues moving back and forth across the model until the residual falls below a threshold value which is set depending on the accuracy required. I find a threshold of 1% to be adequate for the models I consider.

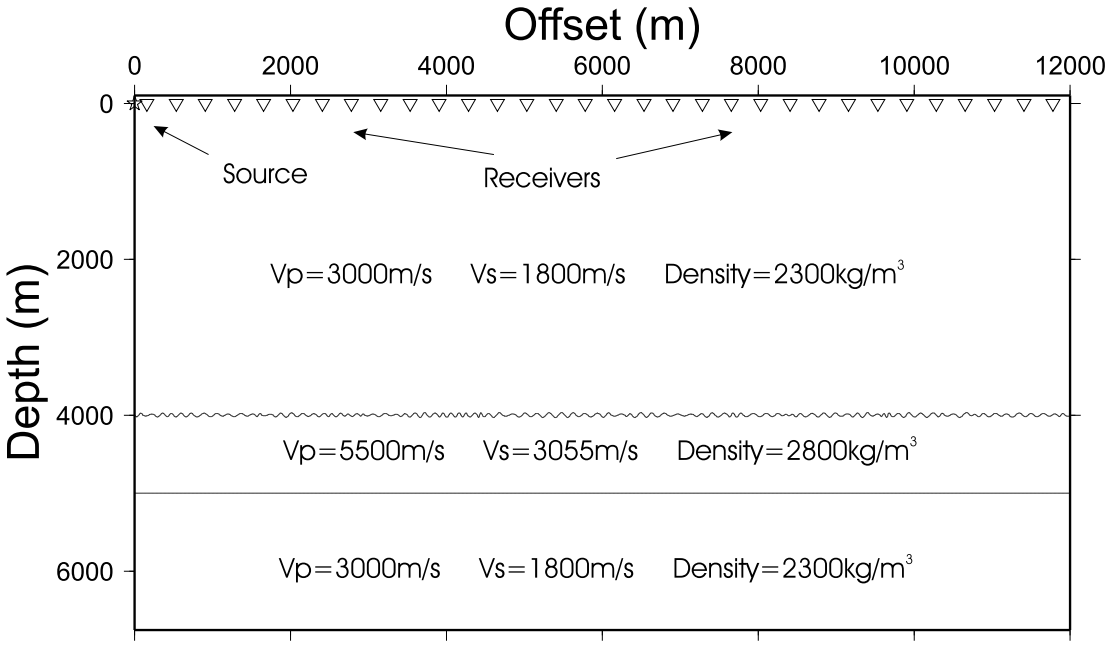

Figure 6.7: Rough-interface model used to test domain decomposition convergence for a long-offset model.

The section of the implementation which performs the wavefield propagation is shown in Figure 6.10. Each time a new sub-domain is updated, contributions from every other sub-domain must be included in the computation. The only sub-domains which are not included are those for which the secondary sources have not yet been computed.

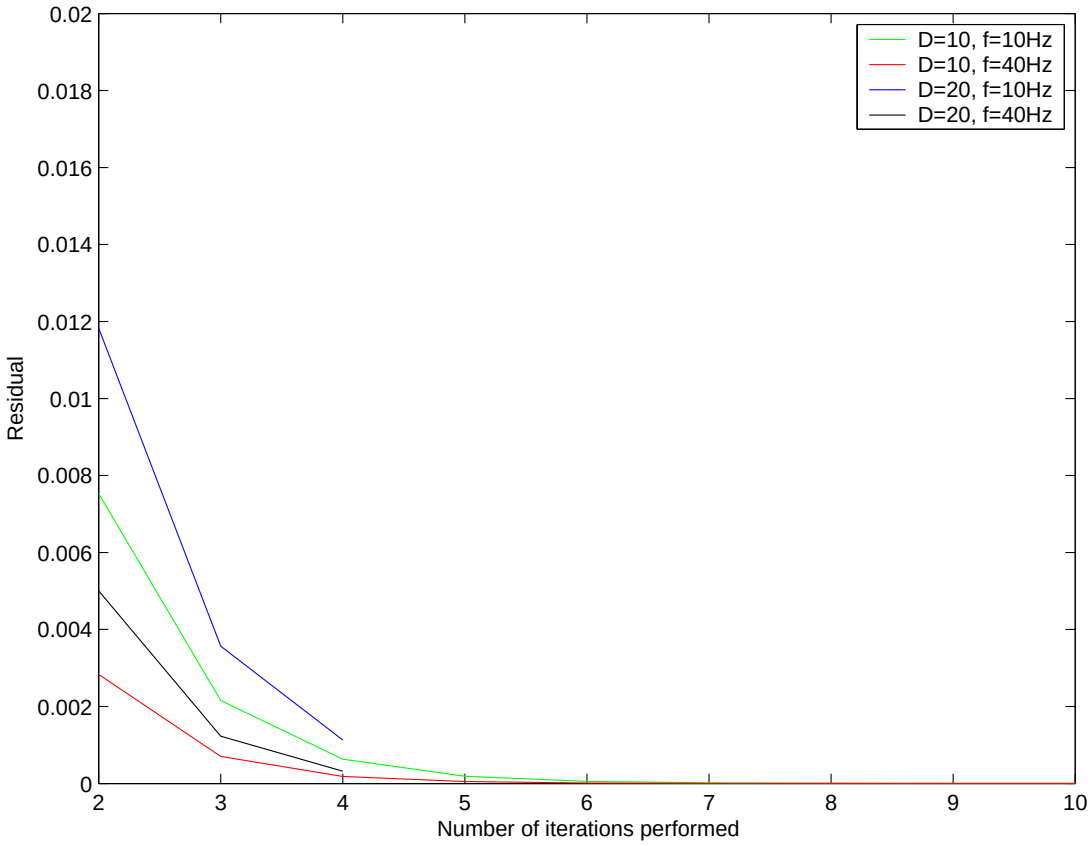

Figure 6.8: Residuals graph for rough-interface model at frequencies of 10 and 40Hz. Results displayed for 10 and 20 sub-domains.

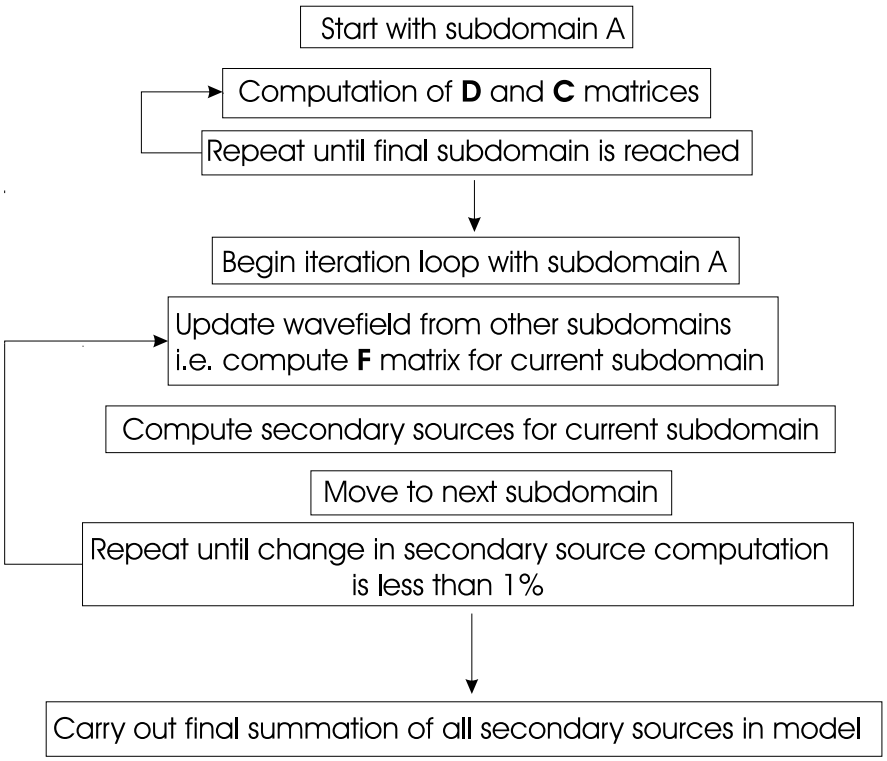

Figure 6.9: Flow diagram for the domain decomposition version of the BEM code. Flow is shown for computation of one frequency.

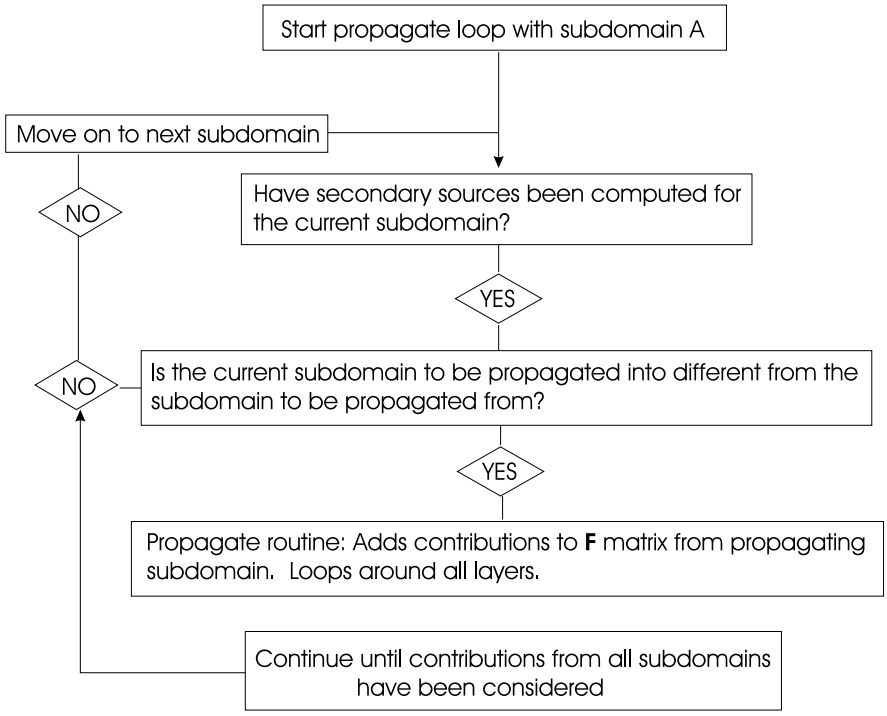

Figure 6.10: Flow diagram for wavefield propagation part of the domain decomposition code. This flow is performed for each step in the iteration loop shown in Figure6.9.

6.3 The fast far-field approximation

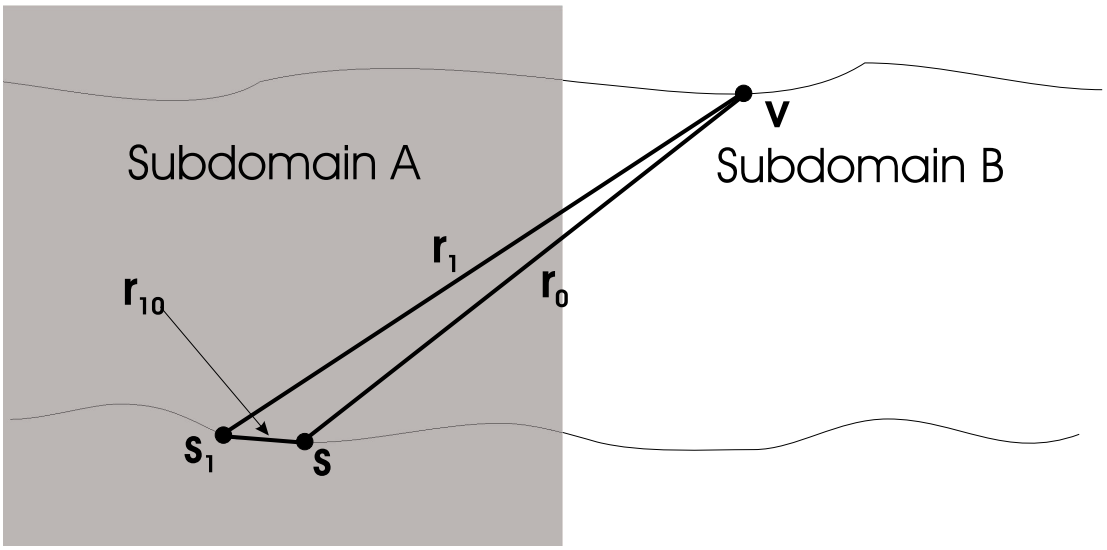

Figure 6.11: Diagram to show displacement felt at a receiver in sub-domain B from a source in sub-domain A.

The fast far-field approximation described in this section follows the same scheme as that described by Lu and Chew (1995). The improvement in performance comes in the way the wavefield is propagated from one sub-domain to another.

Consider the situation depicted in Figure6.11. The standard way to evaluate the x-component of displacement at point $\mathbf{v}$ generated by a source at point $\mathbf{s}$ is by the following expression:

$$\hat{u}_x(\mathbf{v},\mathbf{s}) = \phi_x(\mathbf{s})\hat{G}_{xx}(\mathbf{v},\mathbf{s}) + \phi_z(\mathbf{s})\hat{G}_{zx}(\mathbf{v},\mathbf{s}), \tag{6.6}$$

where $\hat{u}_x(\mathbf{v},\mathbf{s})$ is x-component of displacement at point $\mathbf{v}$ due to the source at point $\mathbf{s}$ which has x- and z-contributions of $\phi_x(\mathbf{s})$ and $\phi_z(\mathbf{s})$. $\hat{G}(\mathbf{v},\mathbf{s})$ is the displacement Green's function for a source at $\mathbf{s}$ and a receiver at $\mathbf{v}$. The computation must be carried out for every source point in sub-domain A to find the total contribution in sub-domain B. For standard ten-point Gaussian integration this means $10(N/D)$ computations for each receiver point in sub-domain B. In total, $10(N/D)^2$ computations are required for one update from

sub-domain A to B. For large sub-domains this can be a time consuming process. However, efficiency can be greatly improved by applying a far-field approximation.

Simplifications in the computation of the Green's functions can be obtained if the points $\mathbf{s}$ and $\mathbf{v}$ are considered to be far away from each other. In general, the displacement Green's function G_{xx} can be written in the form

$$\hat{G}_{xx} = c_1 H_0(k_\alpha r_0) + c_2 H_0(k_\beta r_0) + c_3 H_2(k_\alpha r_0) + c_4 H_2(k_\beta r_0), \tag{6.7}$$

where c_{1-4} are constants for a particular medium and a particular angle between source and receiver. $H_n(kr)$ are the Hankel functions of the second kind of order n for two points of separation r_0. The P-wave and S-wave wavenumbers are represented by k_α and k_β respectively.

In the far field, the zero-order Hankel functions can be expressed by the approximation:

$$H_0(kr_0) \approx \sqrt{\frac{2}{\pi k r_0}} e^{ikr_0} e^{-i\pi/4}. \tag{6.8}$$

The second-order Hankel equations can be expressed by

$$H_2(kr_0) \approx \sqrt{\frac{2}{\pi k r_0}} e^{ikr_0} e^{-i5\pi/4}. \tag{6.9}$$

Now consider another source point $\mathbf{s_1}$ placed close to the initial source point $\mathbf{s}$ (Figure 6.11). Because points $\mathbf{s}$ and $\mathbf{v}$ are considered to be far away from each other, the vectors $\mathbf{r_1}$ and $\mathbf{r_0}$ can be considered parallel. Using the notation of Figure 6.11 and assuming that $\mathbf{r_1}$ and $\mathbf{r_0}$ are parallel, the following approximation is valid:

$$r_1 \approx r_0 + (\mathbf{r_0} \cdot \mathbf{r_{10}})/r_0 \tag{6.10}$$

If a further assumption is made, that the part of the equation inside the square root remains the same for $\mathbf{s}$ and $\mathbf{s_1}$, the zero-order Hankel function for the source at $\mathbf{s_1}$ becomes:

$$H_0(kr_1) \approx \sqrt{\frac{2}{\pi k r_0}} e^{ikr_0} e^{ik(\mathbf{r_0}\cdot\mathbf{r_{10}})/r_0} e^{-i\pi/4}. \tag{6.11}$$

The second exponential term can be seen as an accurate correction factor for what could be a rapidly oscillating function. When the source is at $\mathbf{s_1}$ the Hankel

function can be written as follows:

$$H_0(kr_1) \approx H_0(kr_0)e^{ik(\mathbf{r_0}\cdot\mathbf{r_{10}})/r_0}. \tag{6.12}$$

From now on, the exponential term on the right will be referred to as e_1 (i.e. the correction factor for the source at $\mathbf{s_1}$). Using the above equations, the x-component of displacement at point $\mathbf{v}$ from the x-component of the source at $\mathbf{s_1}$ can be written as:

$$\begin{aligned}\hat{u}_{xx}(\mathbf{s},\mathbf{v}) \approx \phi_x(\mathbf{s_1})[&c_1H_0(k_\alpha r_0)e_{\alpha 1} + c_2H_0(k_\beta r_0)e_{\beta 1} + \\ &c_3H_2(k_\alpha r_0)e_{\alpha 1} + c_4H_2(k_\beta r_0)e_{\beta 1}]\end{aligned} \tag{6.13}$$

Now consider n such source points which are close to the source at $\mathbf{s}$. The x-component of displacement at point $\mathbf{v}$ from all of these points can be expressed as:

$$\begin{aligned}\hat{u}_{xx}(\mathbf{s},\mathbf{v}) \approx c_1H_0(k_\alpha r_0)\sum_{i=1}^{n}\phi_x(\mathbf{s}_i)e_{\alpha i} + c_2H_0(k_\beta r_0)\sum_{i=1}^{n}\phi_x(\mathbf{s}_i)e_{\beta i} + \\ c_3H_2(k_\alpha r_0)\sum_{i=1}^{n}\phi_x(\mathbf{s}_i)e_{\alpha i} + c_4H_2(k_\beta r_0)\sum_{i=1}^{n}\phi_x(\mathbf{s}_i)e_{\beta i}\end{aligned} \tag{6.14}$$

The process of calculating the terms inside the summation signs is known as aggregation. For a fixed source group, these terms depend only on the angle between the source reference point $\mathbf{s}$ and the receiver point $\mathbf{v}$ so Equation 6.14 can be written as:

$$\begin{aligned}\hat{u}_{xx}(\mathbf{s},\mathbf{v}) \approx c_1H_0(k_\alpha r_0)\gamma_1(\theta) + c_2H_0(k_\beta r_0)\gamma_2(\theta) + \\ c_3H_2(k_\alpha r_0)\gamma_3(\theta) + c_4H_2(k_\beta r_0)\gamma_4(\theta)\end{aligned} \tag{6.15}$$

where $\gamma(\theta)$ is the aggregation of the sources for a particular source group and θ is the angle between the source-group reference point and the receiver point. These terms need only be calculated for a few angles. The values are then interpolated for receivers which fall in between two calculated angles. After the process of aggregation, the displacement felt at any receiver point in sub-domain B due to all the whole group of sources can be computed in one step. This would

usually require a number of calculations proportional to the number of sources in the group.

6.4 Implementation of the FFA

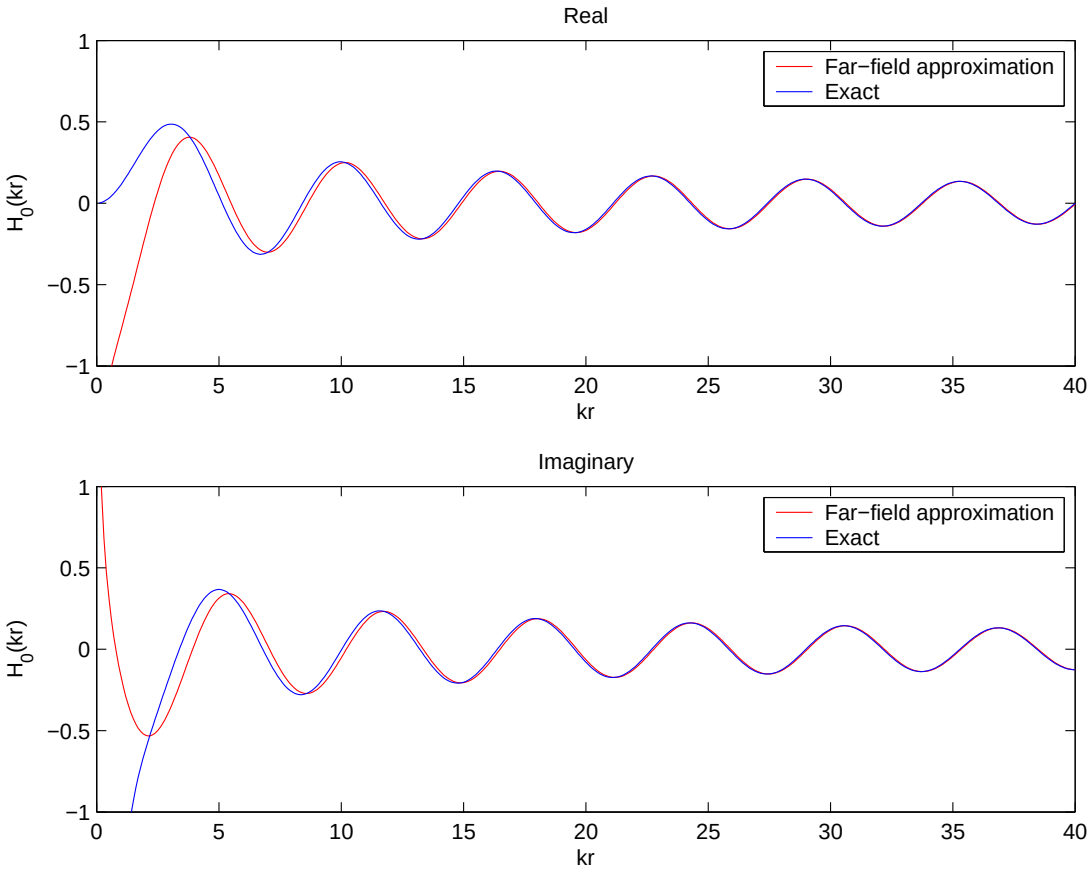

Figure 6.12: Comparison of approximate and exact Hankel functions for varying values of kr.

The gain in efficiency when using the FFA is dependent on the size of the source group used and the number of angles for which γ needs to be computed to get an accurate result.

The first approximation used is the simplification of the Hankel functions in the far field. Figure 6.12 shows a comparison of the exact and approximate calculations for the zero-order Hankel functions. The approximate result can be considered to be accurate enough after $kr = 2\pi r/\lambda \approx 25$. In other words, the approximation is accurate as long as the source-receiver offset is greater than

about 4 times the wavelength. The FFA is not valid for any source-receiver offsets which are below this threshold.

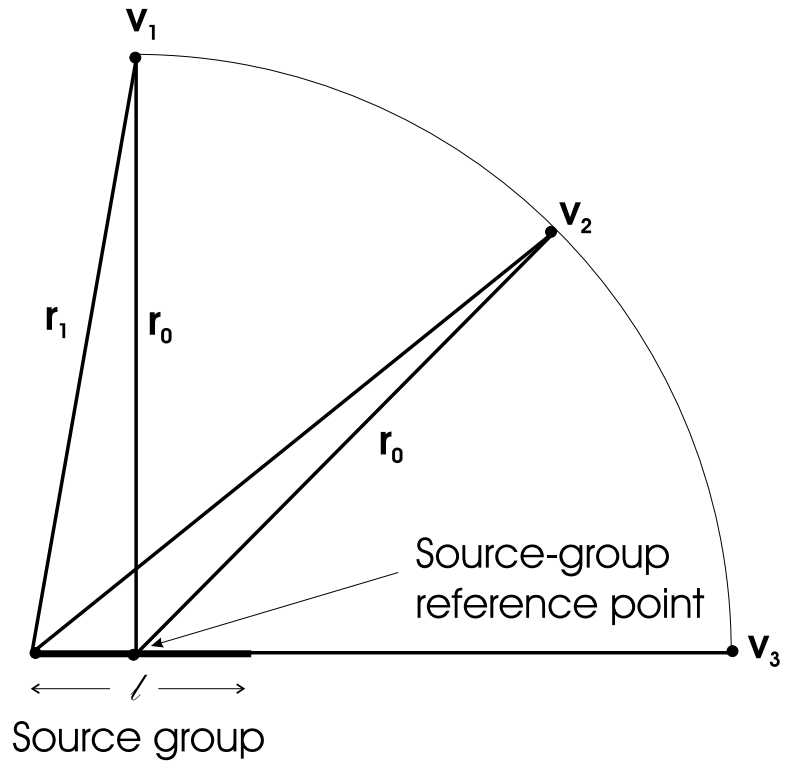

Figure 6.13: Diagram to show errors in the far-field approximation with respect to angle and distance from source group.

Consider the situation shown in Figure6.13. There is a group of forces which all lie within $l/2$ of the group reference point (where l is the diameter of the source group). The aim is to test the validity of the approximation in Equation 6.10. The worst case scenario for this approximation is for the receiver at $\mathbf{v_1}$. The error in the approximation in r_1 is:

$$\delta r_1 = \sqrt{(l/2)^2 + r_0^2} - r_0. \tag{6.16}$$

The approximation 6.12 can be considered to be accurate for cases when δr_1 is less than 100th of the shortest wavelength in the layer. Thus, the expression for maximum source-group length is obtained:

$$l_{max} = \sqrt{\frac{r_0 \lambda}{25} + \frac{4\lambda^2}{100^2}}. \tag{6.17}$$

The second term in the square root is negligible since r_0 must already be at least 4 times the longest wavelength in the model, giving

$$l_{max} \approx \sqrt{\frac{r_0 \lambda}{25}}. \tag{6.18}$$

There is a second approximation which limits the group length. This is to do with the assumption that the term in the square root in Equation 6.12 is invariant for all sources within the source group. This time the worst case scenario occurs for the situation when receiver $\mathbf{v_3}$ is under consideration. The percentage error in the Hankel function caused by a difference in the radius r of $l/2$ is:

$$\frac{\sqrt{r_0} - \sqrt{r_0 - l/2}}{\sqrt{r_0}}. \tag{6.19}$$

If this is set to be no greater than 1%, the expression for maximum group length becomes

$$l_{max} = r_0/25. \tag{6.20}$$

When computing the maximum possible source-group length, both Equations 6.18 and 6.20 must be taken into account. The minimum value of the two is taken to be the final value for l_{max}.

Next, I consider the minimum angle $\delta\theta$ over which it is possible to interpolate accurately. Figure 6.14 shows the variation of $\gamma(\theta)$ with source-receiver angle for a frequency of 25Hz, a P-wave velocity of 3000m/s and an S-wave velocity of 1500m/s. Figure 6.15 shows the same graph for a frequency of 100Hz. It is clear that the rapidity of the oscillations depends on the wavelength of the wave passing through the medium, which, in turn, depends on the frequency and the velocity of the medium.

The connection between the wavelength and the rapidity of the oscillations can be seen more clearly by looking again at Figure 6.13. For a receiver at $\mathbf{v_1}$, the contributions from both ends of the source group will be in phase since they are equidistant from the receiver point. As the receiver moves from $\mathbf{v_1}$ through $\mathbf{v_2}$ to $\mathbf{v_3}$ the contributions from the two edge points of the source group generate a displacement which is composed of two waves which pass in and out of phase. At

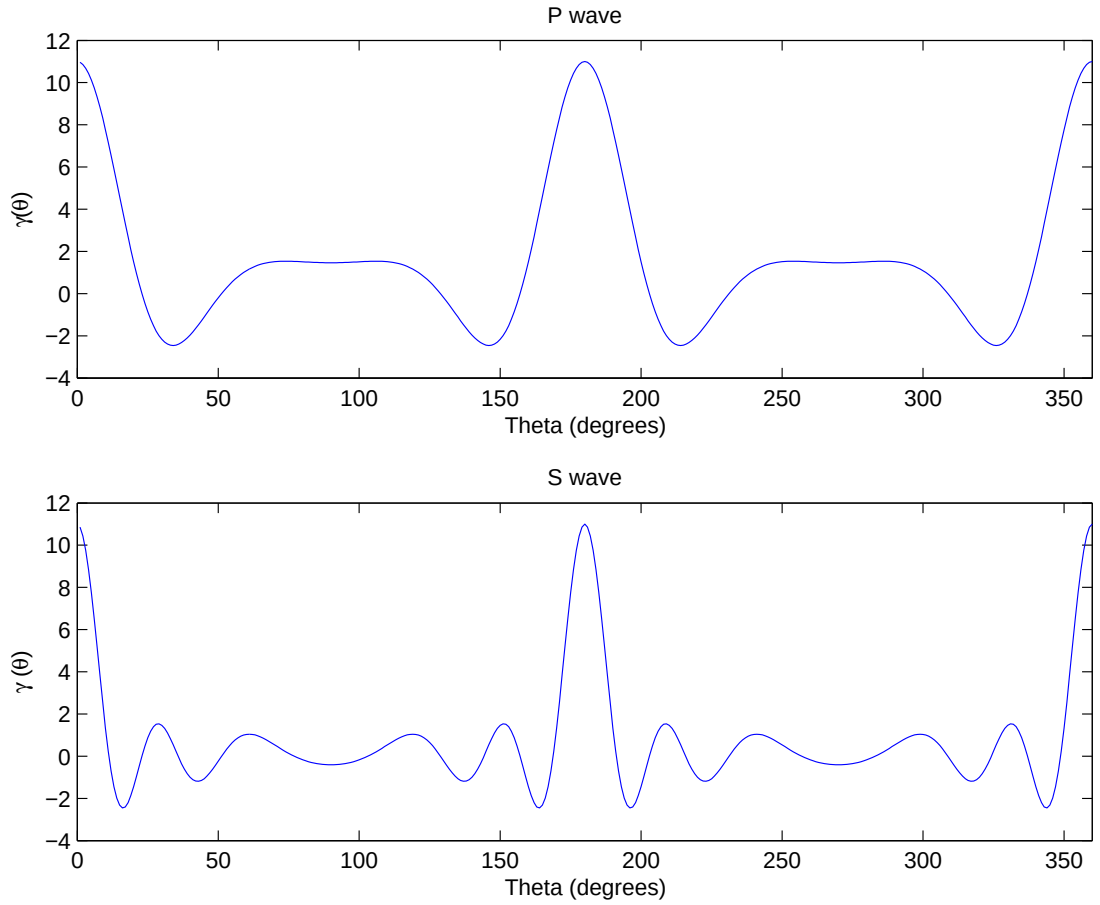

Figure 6.14: Graph to show variation of $\gamma(\theta)$ with angle; 25Hz case. Graphs show the real part of gamma for P-wave velocity of 3000m/s and S-wave velocity of 1500m/s.

$\mathbf{v_3}$, the two waves will be out of phase by an amount dependent on the 'seismic length' of the source group. The 'seismic length' is a dimensionless unit defined here as the length of the source group divided by the wavelength of the seismic wave in the medium.

If the source group happens to be four times the P-wavelength for a particular frequency, there are four oscillations between 0 and 90 degrees. The maximum value for $\delta\theta$ is chosen so that there are at least 10 points per oscillation, allowing accurate interpolation. From this analysis, the following equation arises:

$$\delta\theta_{max} = \frac{90^\circ \lambda_S}{10 \times \text{Grouplength}}, \tag{6.21}$$

where λ_S is the S-wave wavelength.

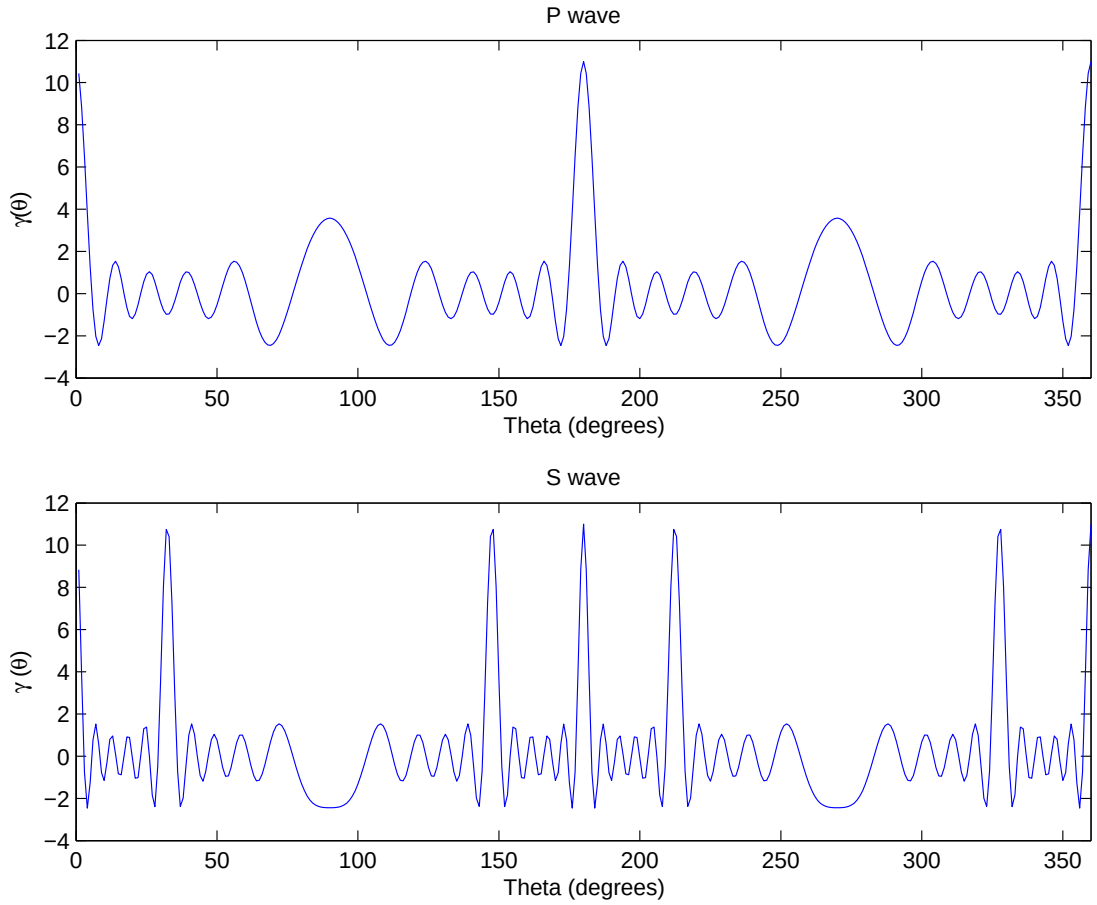

Figure 6.15: Graph to show variation of $\gamma(\theta)$ with angle; 100Hz case. Graphs show the real part of gamma for P-wave velocity of 3000m/s and S-wave velocity of 1500m/s.

Expressions have now been found to determine the parameters required for using the far-field approximation. A flow chart for how this has been implemented into the boundary element code can be seen in Figure 6.16.

6.5 Conclusions

A number of improvements in the efficiency of the boundary element method have been achieved with the use of domain decomposition and a far-field approximation.

The domain decomposition approach involves splitting the model into several sub-domains. The secondary sources for the whole model are then found by use

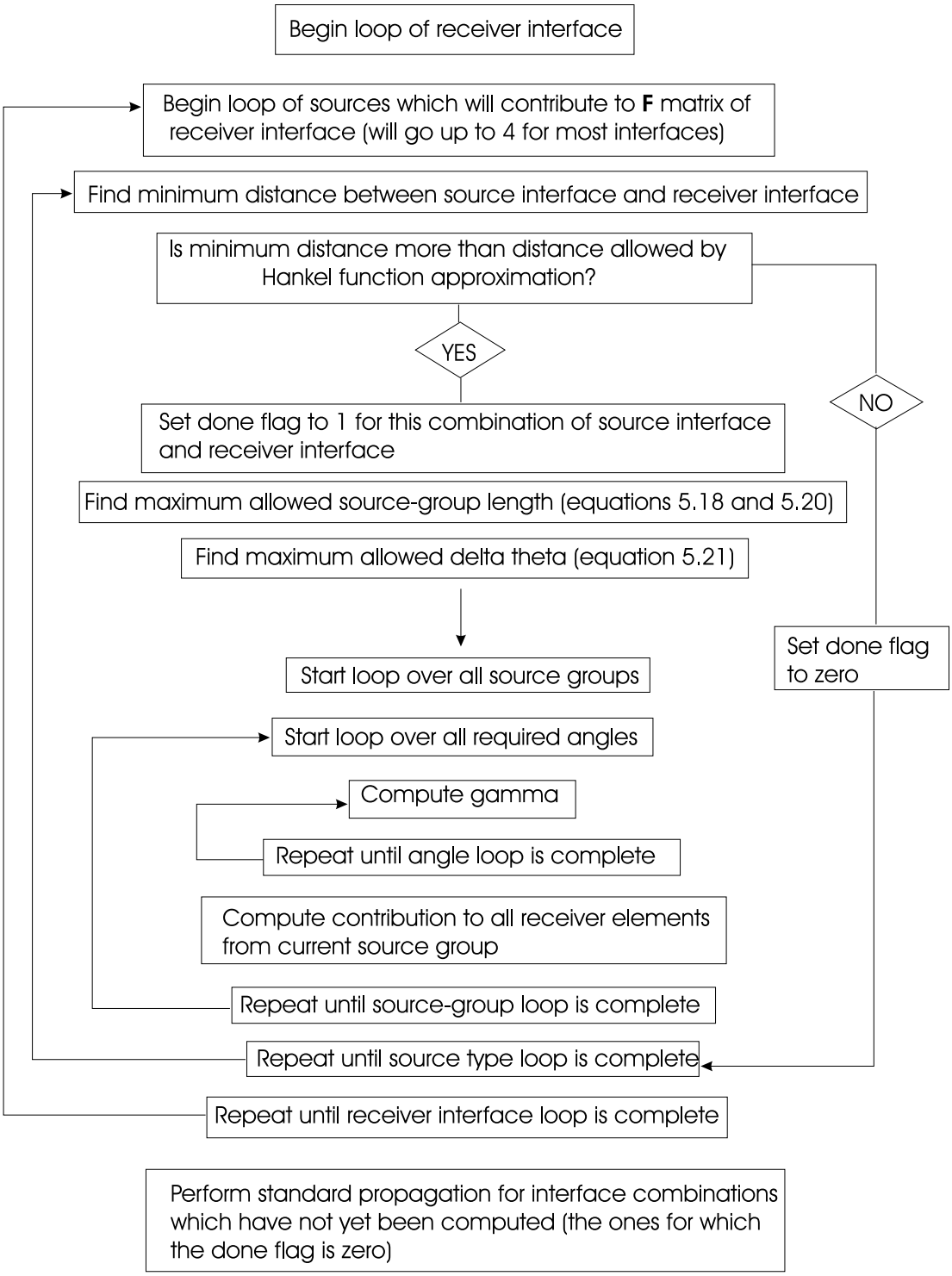

Figure 6.16: Flow diagram of the wavefield propagation part of the BEM code.

of an iterative process in which the wavefield is propagated from one sub-domain to another.

Convergence was found to be very quick for this method, particularly for large models and high frequencies. More iterations were required when more sub-domains were used. For the models considered, the accuracy of the solution was sufficient after the residual dropped below 1%.

I implemented a far-field approximation to speed up the process of propagation of the wavefield from one sub-domain to another. Two main approximations are made.

The first is a far-field approximation of the Hankel functions used to compute the Greens functions. It was found that good accuracy could be retained as long as this approximation was made only when the distance between the source and receiver was greater than 4 wavelengths.

The second is the assumption that the vector between the source-group reference point and the receiver is parallel to the vector between any other point in the source group and the receiver. Expressions were derived to find the maximum source-group length allowed whilst still retaining accuracy.

Chapter 7

Rough interface modelling of basalt

7.1 Introduction

In previous chapters, I present a numerical method based on the boundary element method (BEM) and discuss its implementation. In this chapter, the BEM is used to perform forward modelling of basalt with rough interfaces.

Most of the previous modelling of basalt with lateral heterogeneities has been carried out using the finite difference method (e.g. Lafond et al., 1999; Purnell et al., 1990; Martini and Bean, 2002). Each of these studies considered only one or two models for one frequency range. Until now, no detailed study of the effects of a laterally heterogeneous high-impedence layer has been carried out. This work attempts to fill that gap by considering roughness on many different length scales and amplitudes. Results are presented for input wavelet frequencies of 10Hz and 40Hz.

First, a flat-layered reference model is considered. A shot gather is generated for a 12km streamer using source frequencies of 10Hz and 40Hz. The main events in the seismogram are identified by comparing their traveltimes with known traveltime curves which have been computed using a simple ray-tracer (see Chapter 10). The traveltime curves for this chapter were calculated using a program written by Peter Hanssen (Hanssen, 2002).

Next, sinewave roughness is introduced into the model at the top-basalt

interface. The effect of this roughness on the propagation of the seismic wave at near- and far-offsets is discussed. Many models, with roughness of varying amplitude and wavelength, are considered for several source frequencies.

Finally, more 'realistic' models are considered with random roughness at the top and base of the basalt layer. The degree of the roughness is varied to see what effect this has on the seismic response.

7.2 Flat-layered reference model

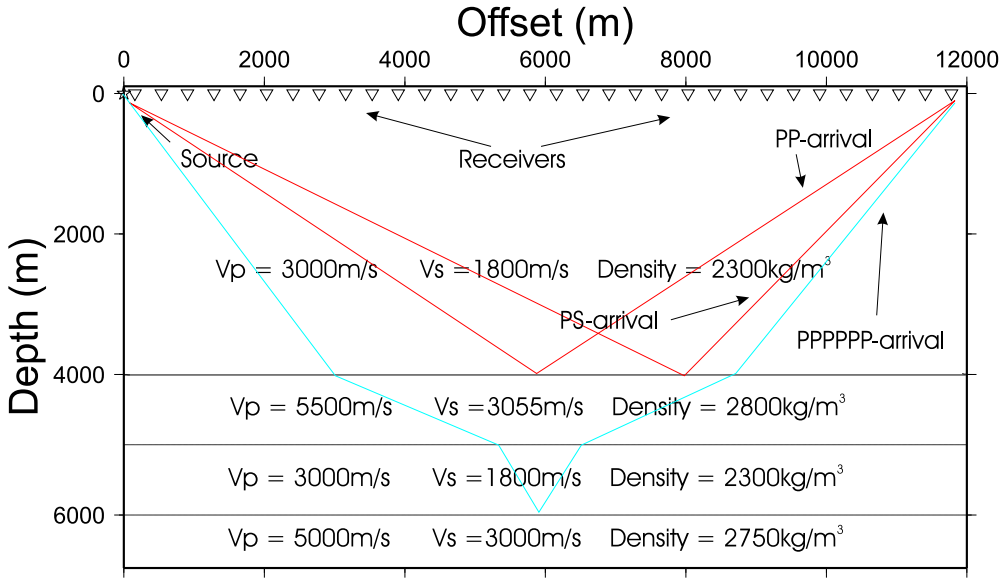

Figure 7.1: Flat-layered reference model used to generate synthetic shotgathers.

A flat-layered basalt model is shown in Figure 7.1. The acquisition geometry and basalt depth for this and all other models in this chapter are based on a seismic survey carried out in the Faeroe-Shetland Channel in 2001 (Ziolkowski et al., 2003; see Chapter 9). This model is simplified greatly from the true geology in that region. The water layer and all the other layers above the basalt are replaced by an elastic half-space, and only one interface beneath the base of the basalt is included. This is in order to ensure that all the effects seen in the synthetic shot gathers in subsequent models are due solely to the heterogeneities of the basalt.

Modelling is carried out using domain decomposition with the boundary element method (Chapter 6). There are 936 receivers at a depth of 0m with

a spacing of 12.5m. The receiver offsets extend to 12km and record displacement in the x- and z-directions.. Frequencies up to 128Hz are computed, allowing a Ricker wavelet with a modal frequency up to 40Hz. Modelling is carried out with a 2D-explosive source which is at a depth of 0m.

The thickness of the basalt is 1000m. This is certainly possible for basalts in this region since successions many kilometers thick have been found on the Faeroe Islands. These basalts thin out towards the centre of the Faeroe-Shetland Channel (Ritchie et al. 1999). With a thick basalt layer in the model, it easier to distinguish between different events on the synthetic shot gather since the base-basalt interface has been placed halfway between the top-basalt and the sub-basalt interfaces. The P-wave velocity and density of the basalt are taken from well-log and VSP data from various locations in the northeast Atlantic Margin (Planke et al., 1999). The S-wave velocity of the basalt is calculated using a P-wave to S-wave velocity ratio of 1.8 (Planke et al., 1999). The rock surrounding the basalt is given velocity and density values which reflect those for a typical sedimentary rock in the area (see Chapter 9). The properties given to the rock beneath the sub-basalt interface are taken from the model shown in Chapter 9.

A shot gather generated from the reference model can be seen in Figure 7.2 for the z-component of displacement. The input wavelet is a Ricker wavelet of 40Hz and the direct wave has been omitted from the computation. All the major events on the seismograms have been labelled according to their ray-travelpath. The traveltime curves overlaid on the shotgather can be seen in Figure 7.3. All events from the top-basalt interface are in red. The events from the base-basalt interface are shown in green and those from the sub-basalt interface are shown in blue.

Some of these raypaths are included in Figure 7.1 to explain the terminology used, e.g., PS means the raypath which travels down as a P-wave, converts to S at the top-basalt interface, and returns as an S-wave. PPSPPP represents the raypath which travels down to the base-basalt interface as a P-wave, converts to S on transmission, converts back to a P-wave on reflection at the sub-basalt interface, and returns to the receiver as a P-wave.

Traveltime curves were computed by applying Snell's law at each interface

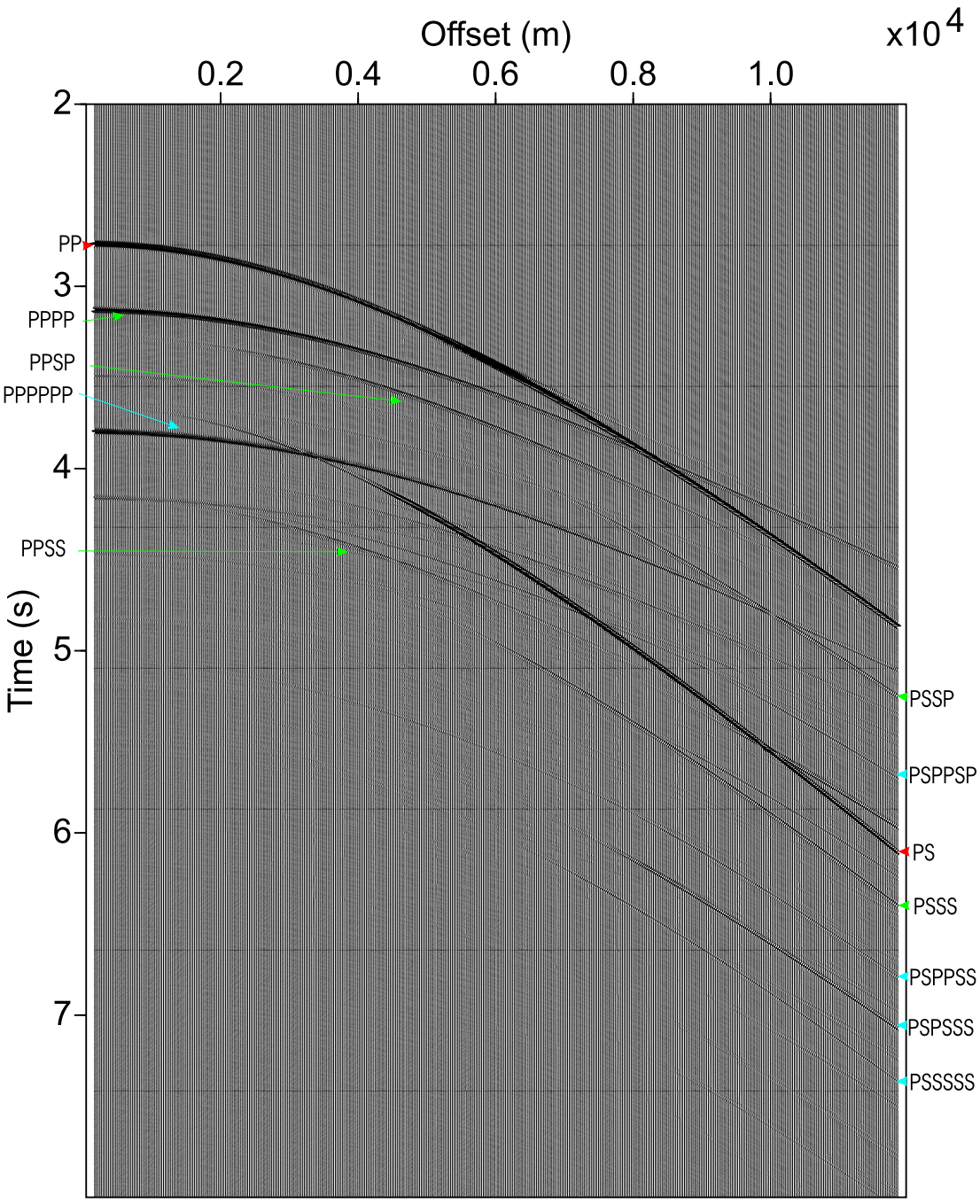

Figure 7.2: Shot gather generated from the flat-layered reference model for a 40Hz source, z-component. The banded striping apparent on this and all subsequent seismograms is due to the limited printer resolution.

in the model and computing the raypath over a number of angles. All possible ray-modes and peg-leg multiples were computed and overlaid on the synthetic shotgather to see which ones correspond to a high amplitude event. Because the

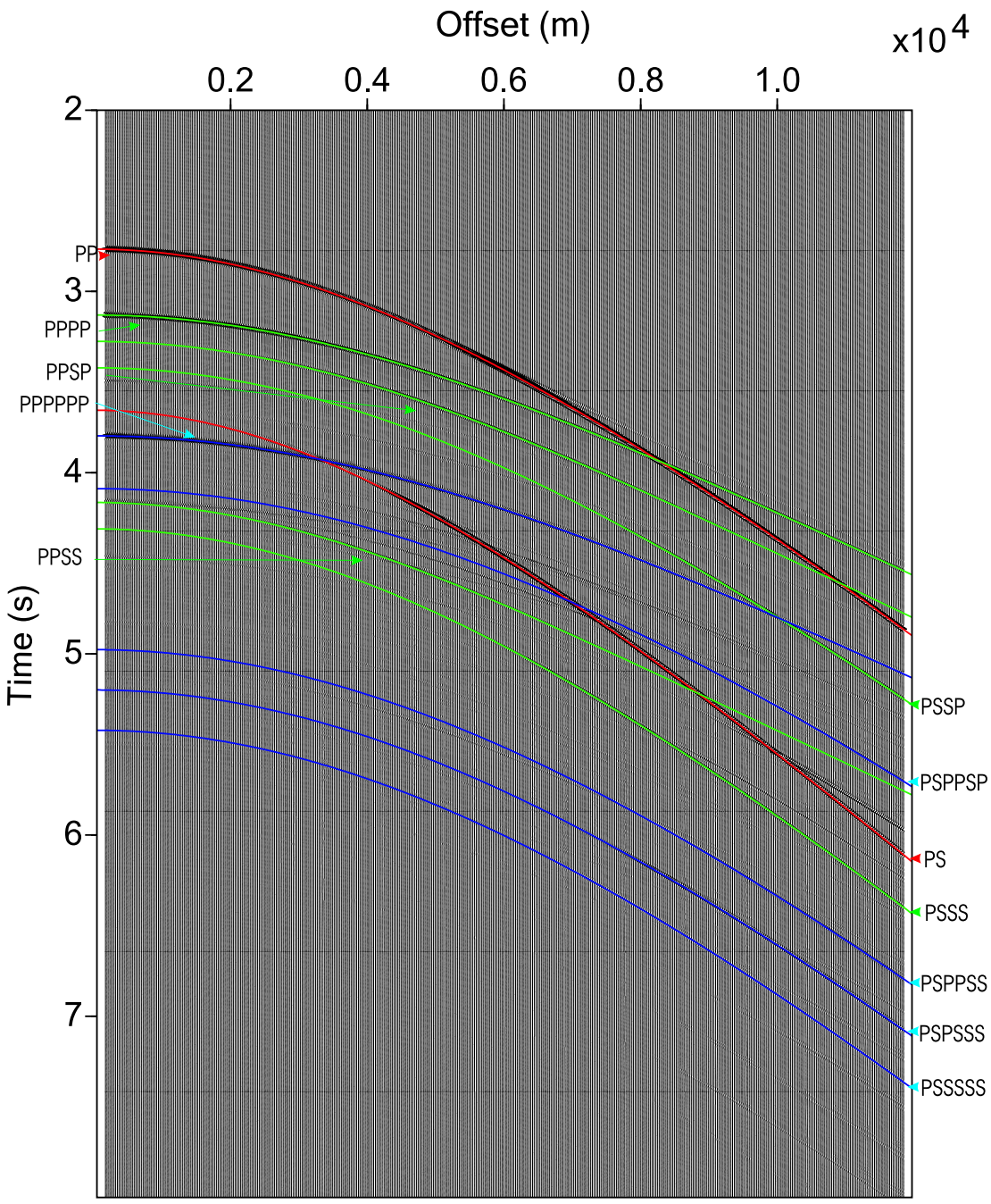

Figure 7.3: Same as Figure 7.2 with traveltime curves overlaid.

z-component of displacement is shown here, the strongest amplitude events are P-wave reflections.

Despite the high impedence contrast between the basalt and the surrounding

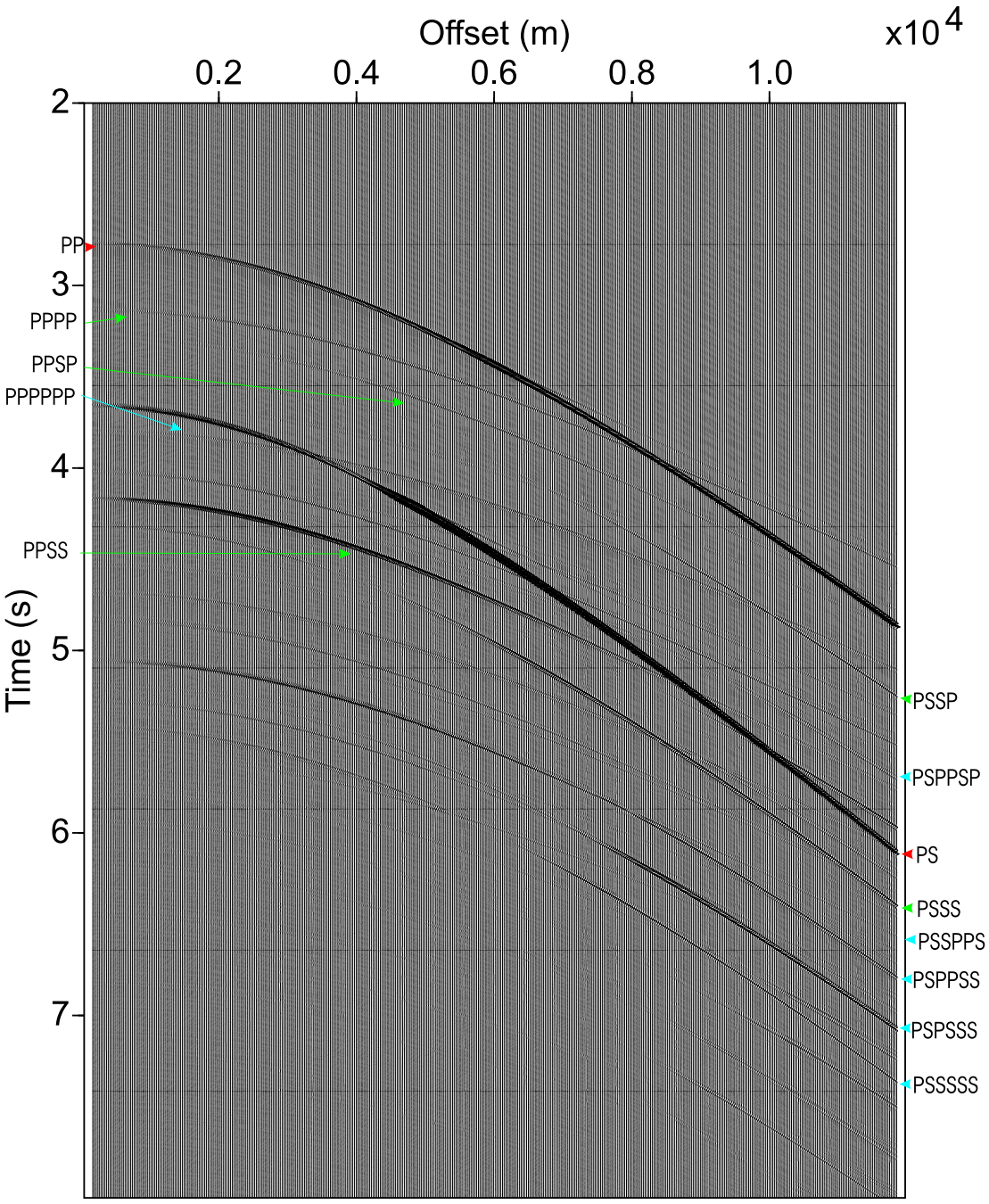

Figure 7.4: Shot gather generated from the flat-layered reference model for a 40Hz source, x-component.

layers, the P-wave base-basalt and sub-basalt events can be clearly seen. This is the case at near and far-offsets.

There are also a number of converted events, mainly at far offsets. For the base-basalt interface, the PPSP and the PPSS modes are the strongest in the

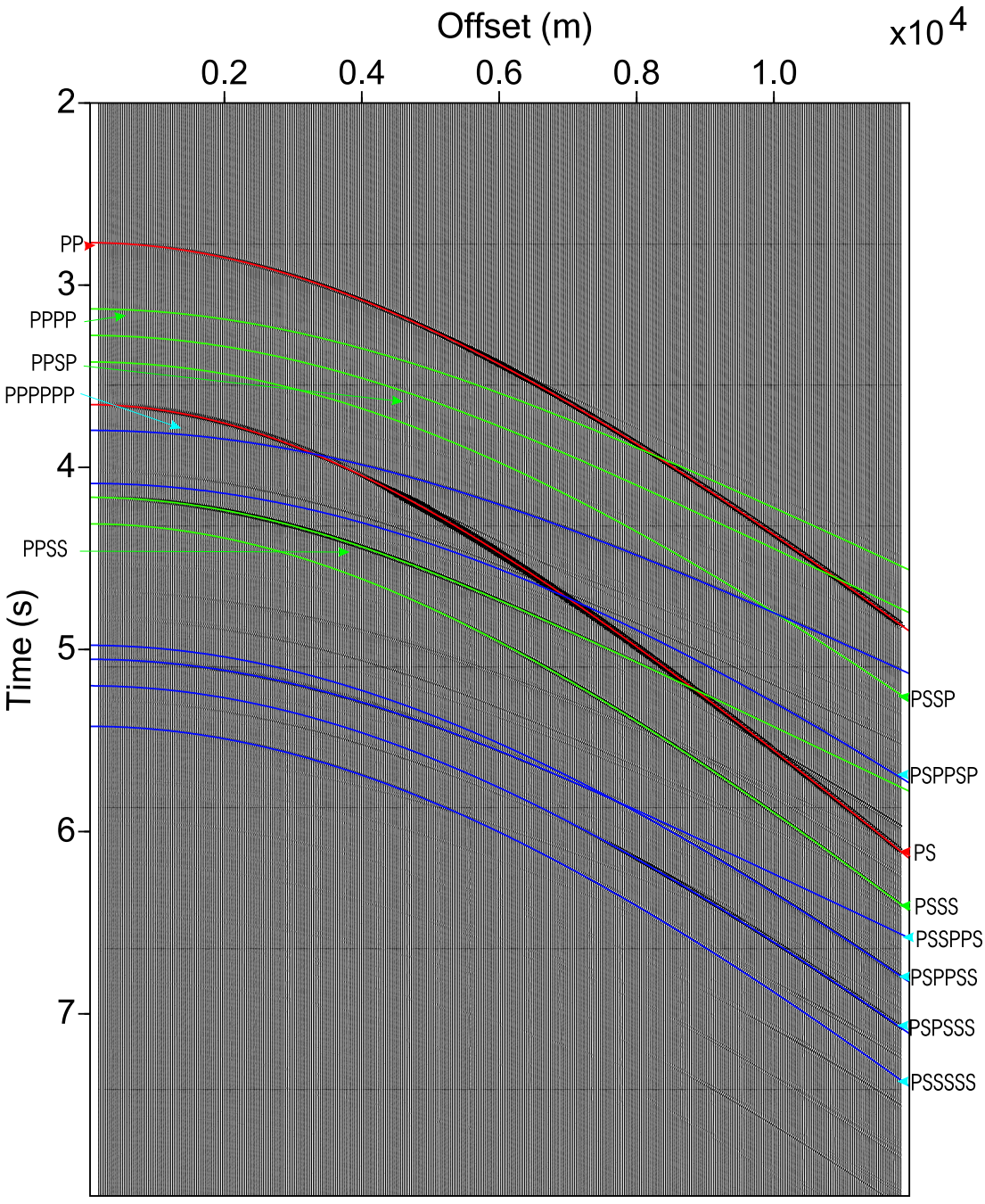

Figure 7.5: Same as Figure 7.4 with traveltime curves overlaid.

mid offsets while the PSSP and the PSSS have the greatest amplitude in the far offsets. Energy from the sub-basalt interface can also be seen in the converted wavemodes. In this case the the energy is only seen in the far offsets (in the PSPPSP, PSPPSS, PSPSSS and PSSSSS wavemodes).

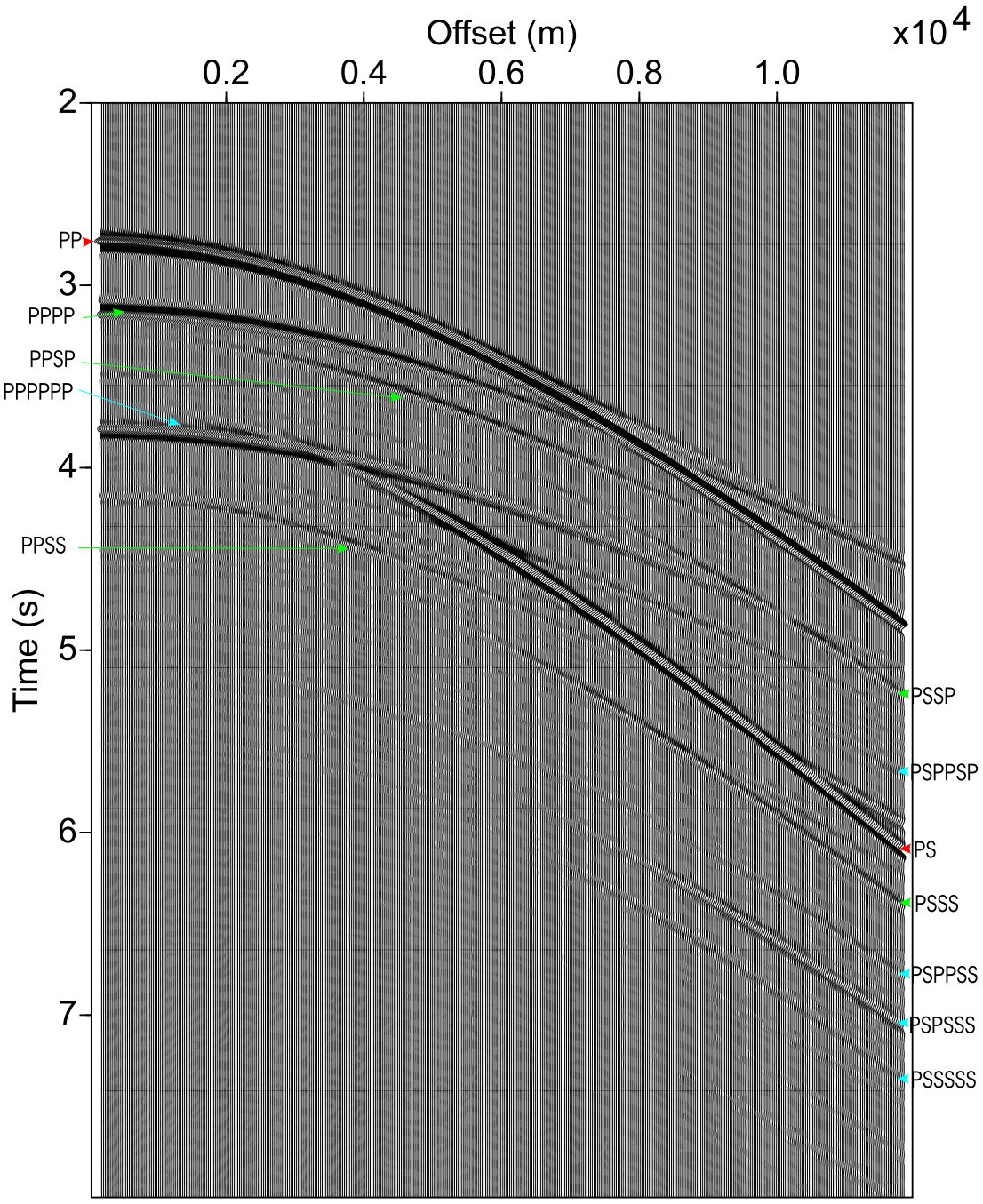

Figure 7.6: Shot gather generated from flat-layered reference model for a 10Hz source, z-component.

Figures 7.4 and 7.5 shows the same shot gather for the x-component of displacement. As one might expect, the P-wave modes now have a smaller amplitude when compared with the converted wavemodes. There is only one

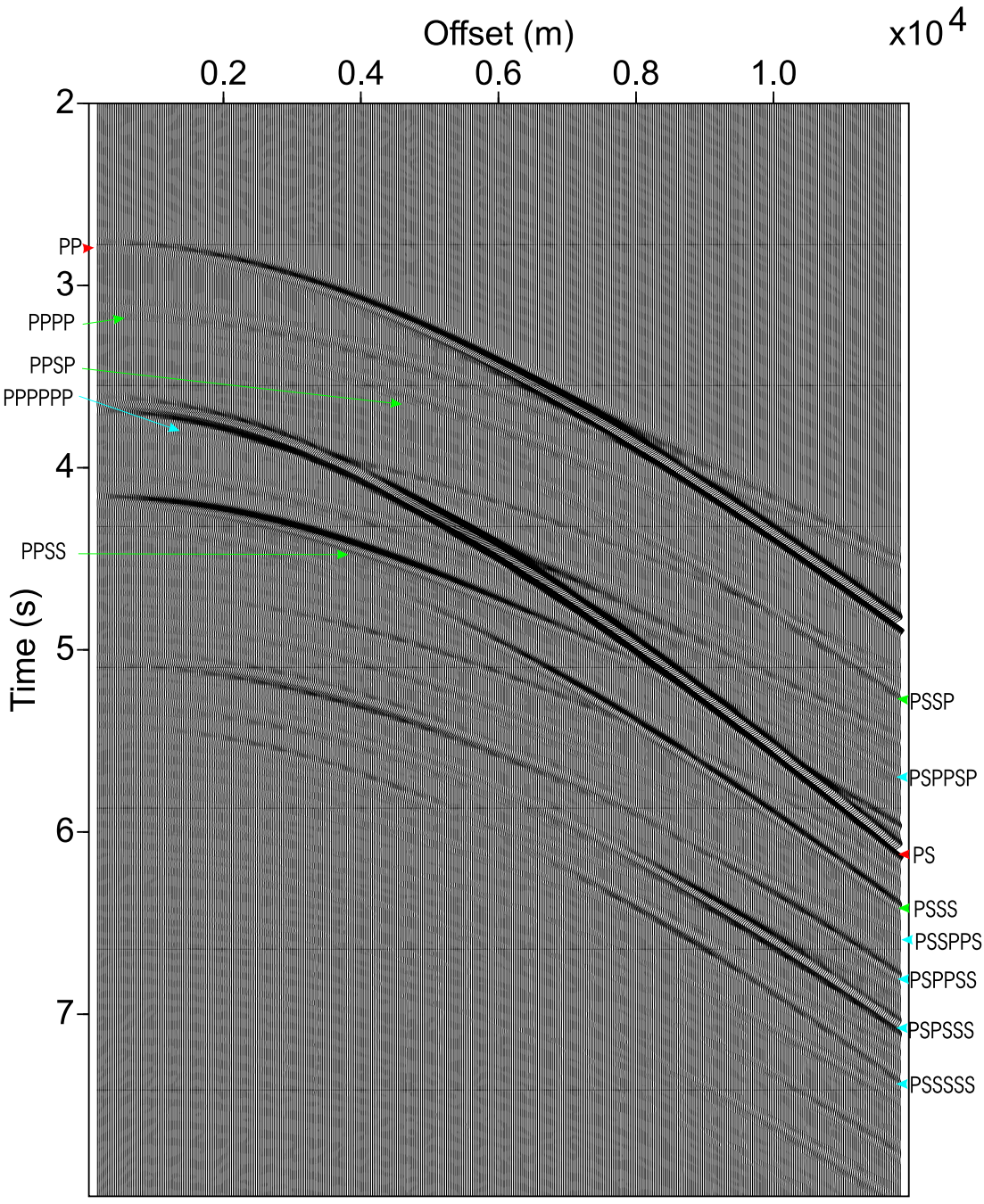

Figure 7.7: Shot gather generated from flat-layered reference model for a 10Hz source, x-component.

additional event of any note. This is the PSSPPS event from beneath the basalt and is of greatest amplitude in the mid-offset range.

Figures 7.6 and 7.7 show the same shot gathers for a central source frequency of 10Hz. All the same wavemodes are visible, although the resolution of each

event is clearly reduced because of the lower frequency content of the source. These figures are shown mainly for comparision with the rough-interface models shown in the next sections.

7.3 Sinewave-interface models

Model	Wavelength of sinewave	Peak-to-peak amplitude of sinewave
B1	120m	40m
B2	120m	20m
B3	240m	40m
B4	1000m	40m
B5	60-180m	16-64m

Table 7.1: Description of sinewave-interface models

	P-wave		S-wave	
Layer	10Hz	40Hz	10Hz	40Hz
Sandstone	300m	75m	180m	45m
Basalt	550m	137.5m	305.5m	76.375m

Table 7.2: Seismic wavelengths propagating through model at 10Hz and 40Hz

Table 7.1 lists all the sinewave-interface models considered in this section. Each model has been given a reference code to aid description in the text.

Table 7.2 shows the velocities used in each of the following models and the wavelengths which propagate through each of the layers for central source frequencies of 10Hz and 40Hz.

From the many experiments done on the nature of diffracted waves from corrugated interfaces (e.g. Paul and Campillo, 1988), one would expect the greatest disturbance to occur when the wavelength of the irregularity in the model approaches that of the seismic wave. Therefore, a wavelength of 120m is selected as the first test. A peak-to-peak amplitude of 40m is used in this model (Figure 7.8). This may be considered to be rather an extreme case, especially for flood-basalts flows, which tend to be quite flat. However, it is better to take a more heterogeneous example to start with to see if the sub-basalt interface reflections are still visible. Figure 7.9 shows the z-component of displacement for a source frequency of 40Hz. There is clearly a lot of diffracted energy throughout the whole shot gather. However, the P-wave reflections can still be clearly seen. The problem is due mainly to the diffracted energy coming from the top interface. The disruption to the base-basalt and sub-basalt events themselves is relatively

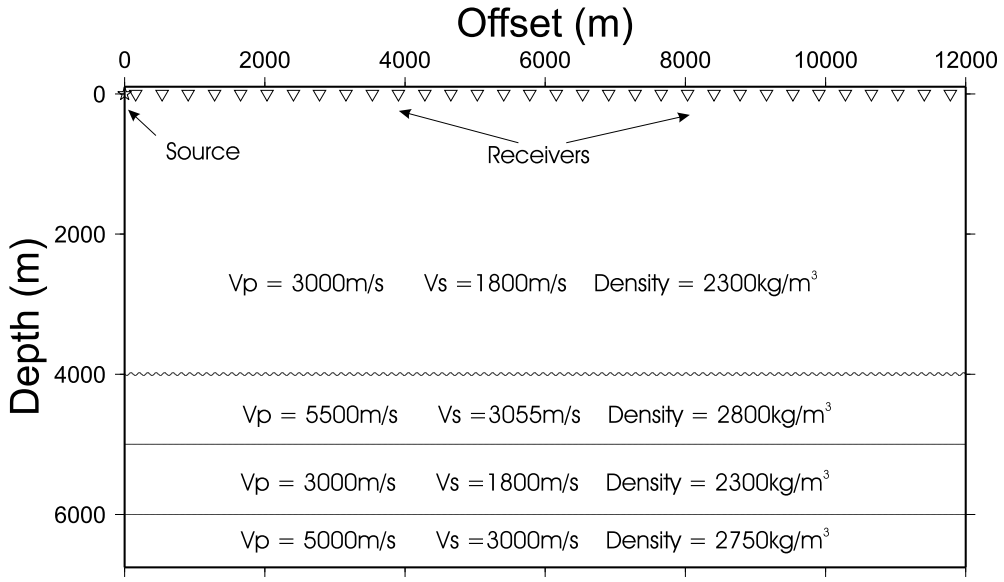

Figure 7.8: Sinewave-interface model B1

small. The diffracted energy is very regular because of the regular nature of the input model. Far offsets seem to be less affected than near offsets in this case.

The converted waves are affected even more strongly than the pure P-wave modes. The scattering of the PS conversion is a clear feature which stretches from 5 to 8 seconds in the far offsets. The converted wavemodes from beneath the basalt are severely attenuated and what is left of them is masked by the wavetrain of the PS conversion. Figure 7.10 shows the x-component of the same shot gather. Here there is some converted energy coming from beneath the basalt, especially at the far offsets. In particular, the PSSPPS and PSPSSS wavemodes are still clearly seen. These converted wavemodes do not approach the amplitudes seen in the pure P-wavemodes. Therefore, imaging using P-waves still seems to have the greatest chance of success for this model.

Figures 7.11 and 7.12 show the z and x-components of the same sinewave model for a source frequency of 10Hz. The resolution of the events is clearly decreased as in the flat-layered reference model. However, the effect of the scattering has been decreased greatly in comparsion to the 40Hz shot gather. This is probably due to the fact that the wavelength of the heterogeneity is now shorter than the average wavelength of the seismic wave propagating through the model. In fact, the P-wave events are just as clear as for the flat-layered model. The converted waves from beneath the basalt are also just as strong as for the flat-

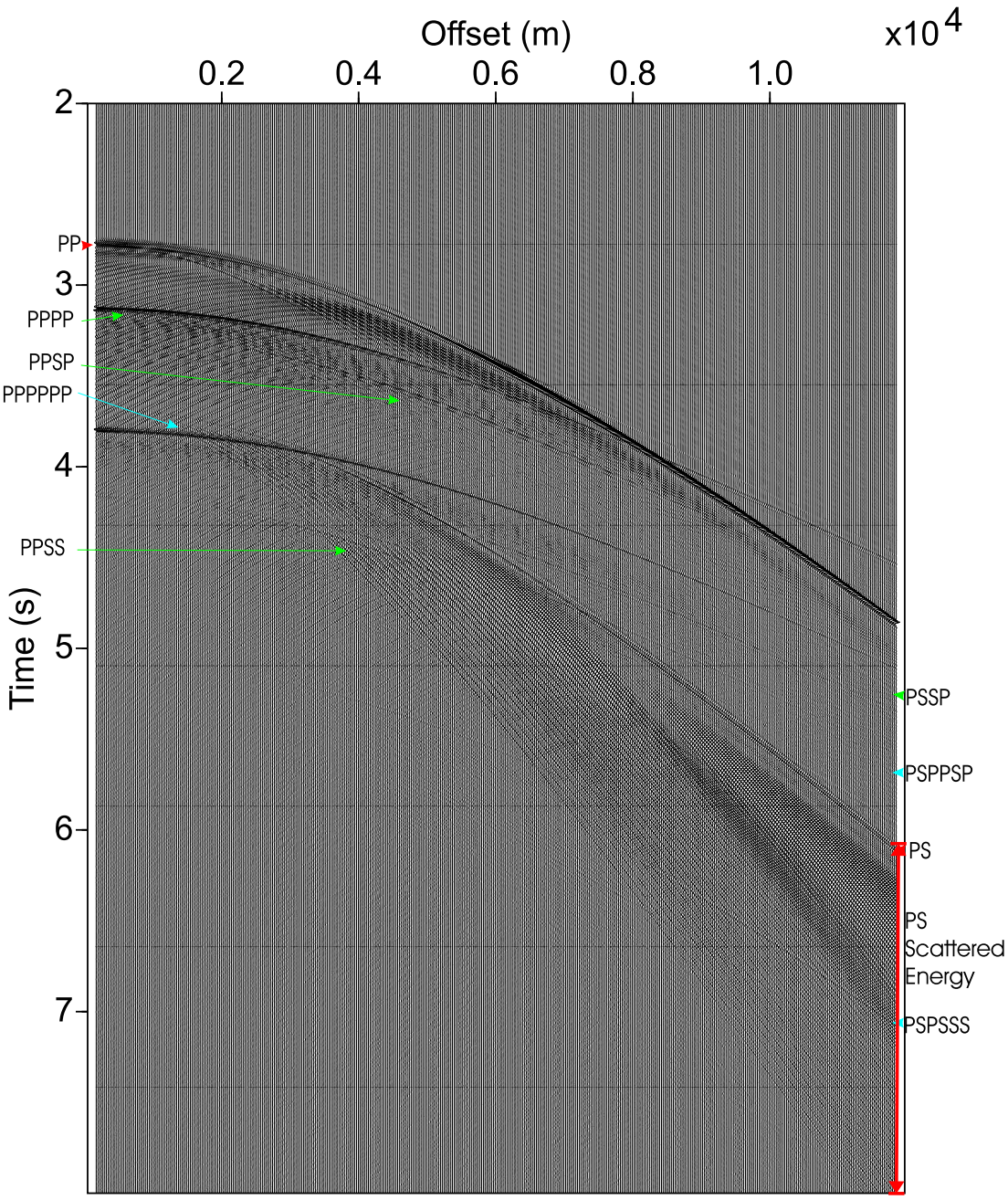

Figure 7.9: Shot gather generated from model B1 for a 40Hz source, z-component.

layered case, the only difference being that some diffracted energy is masking the coherent energy beneath.

The same model was run with a sinewave-interface of 20m peak-to-peak amplitude in order to see how the amplitude of the sinewave affected the scattering.

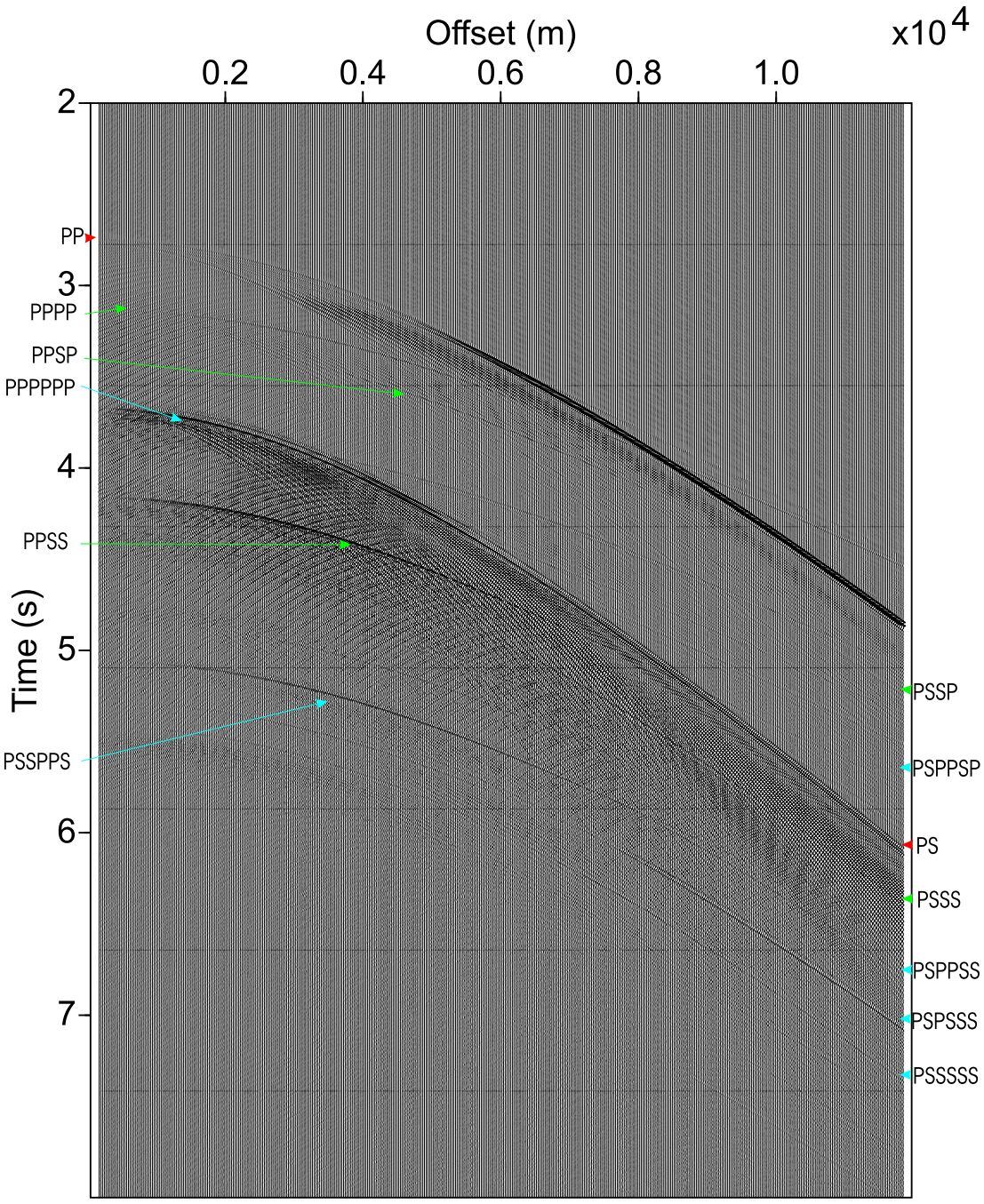

Figure 7.10: Shot gather generated from model B1 for a 40Hz source, x-component.

Figures 7.13 and 7.14 show the shot gathers for a 40Hz and 10Hz source respectively. From now on, only the z-component of each shot will be discussed. The shot gathers for this model display smaller amplitude scattering compared with the previous model. This is the case at both frequencies, although, as before, the

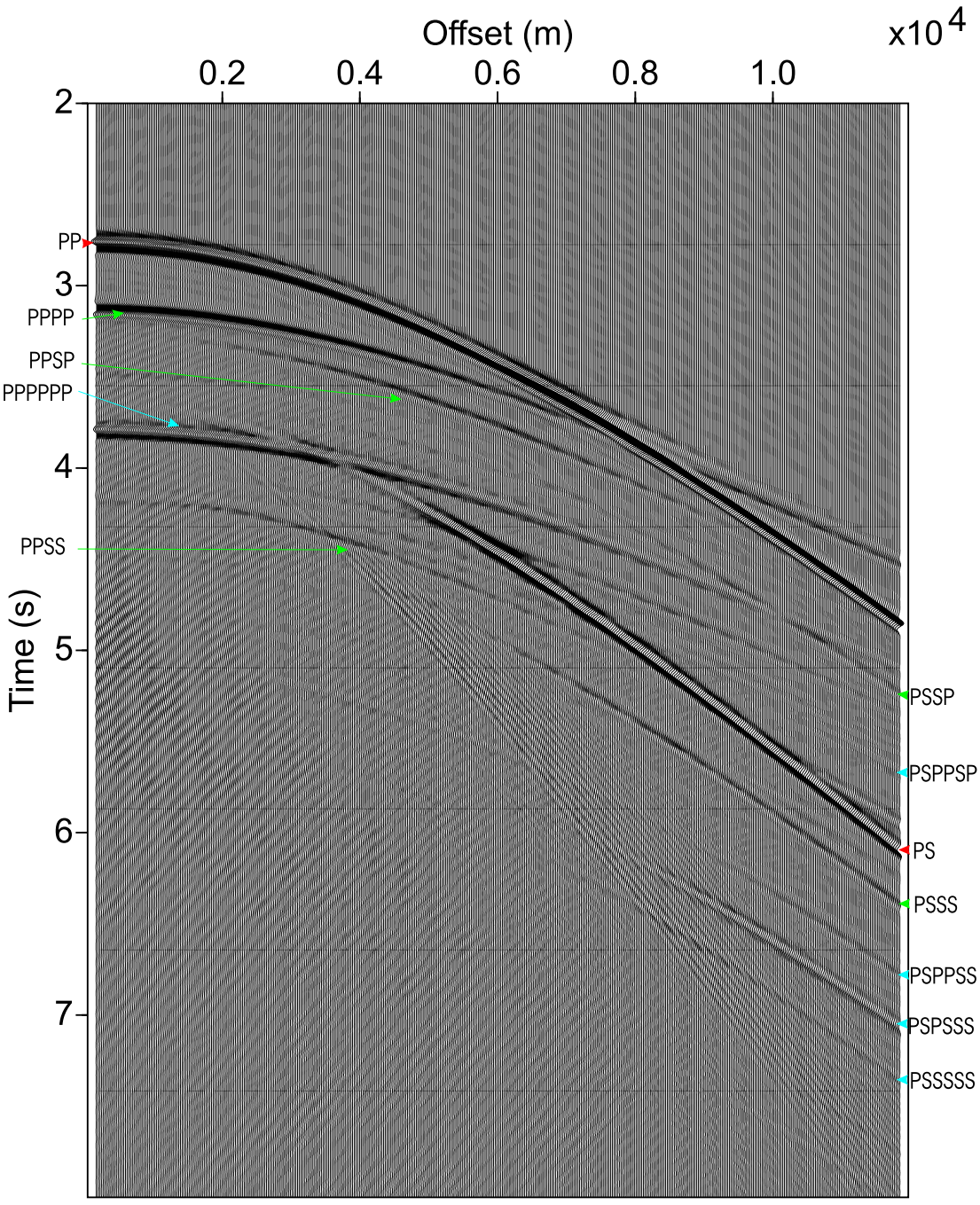

Figure 7.11: Shot gather generated from model B1 for a 10Hz source, z-component.

10Hz shot gather displays less scattering than the 40Hz. This is confirmation of what may have been expected before the modelling was carried out. The greater the amplitude of the heterogeneity, the more scattering is seen in the shot gather and the more severely the converted events are affected.

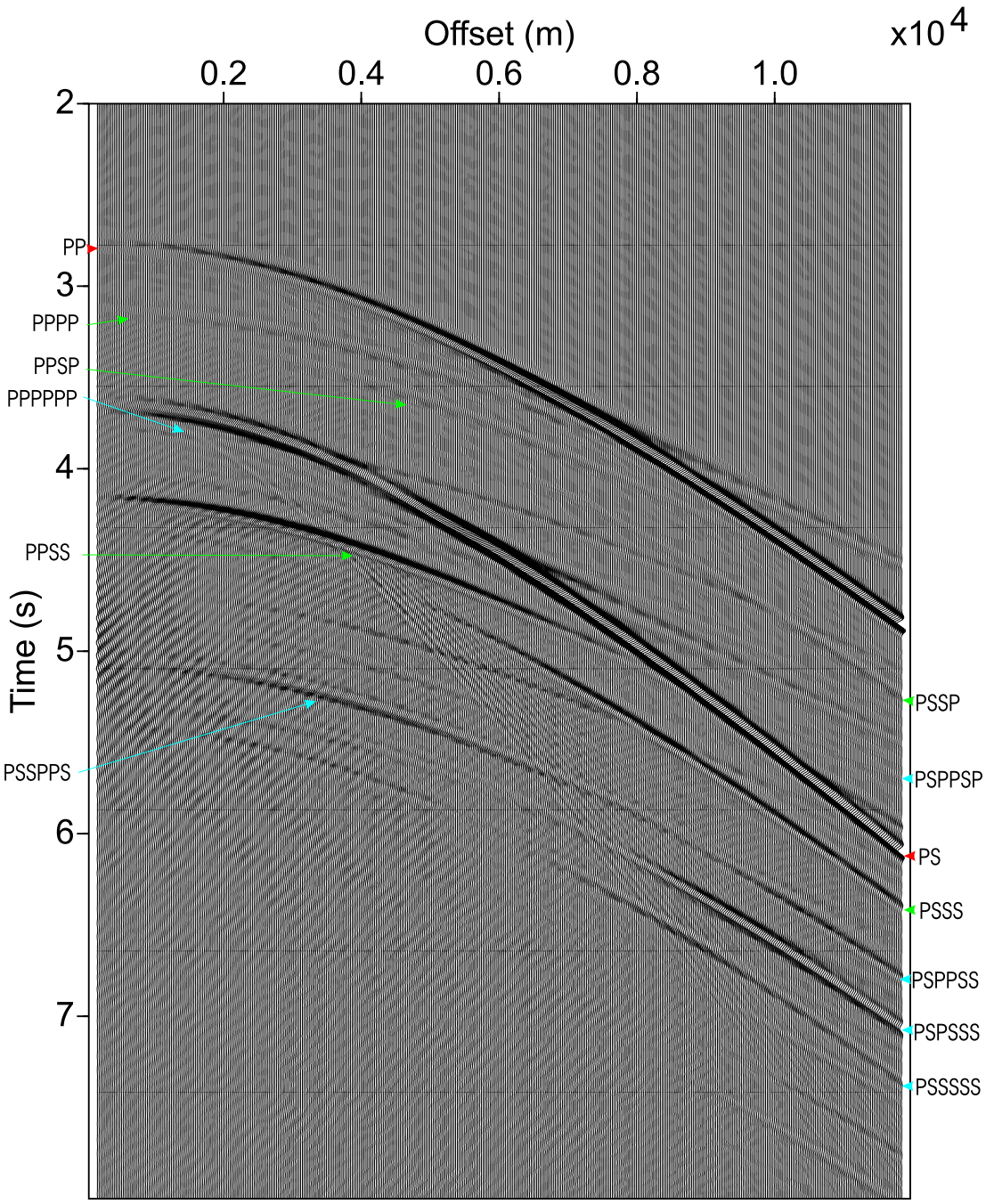

Figure 7.12: Shot gather generated from model B1 for a 10Hz source, x-component.

The next model (B3) contains a sinewave-interface with a wavelength of 240m and a peak-to-peak amplitude of 40m. Figure 7.15 shows the z-component of

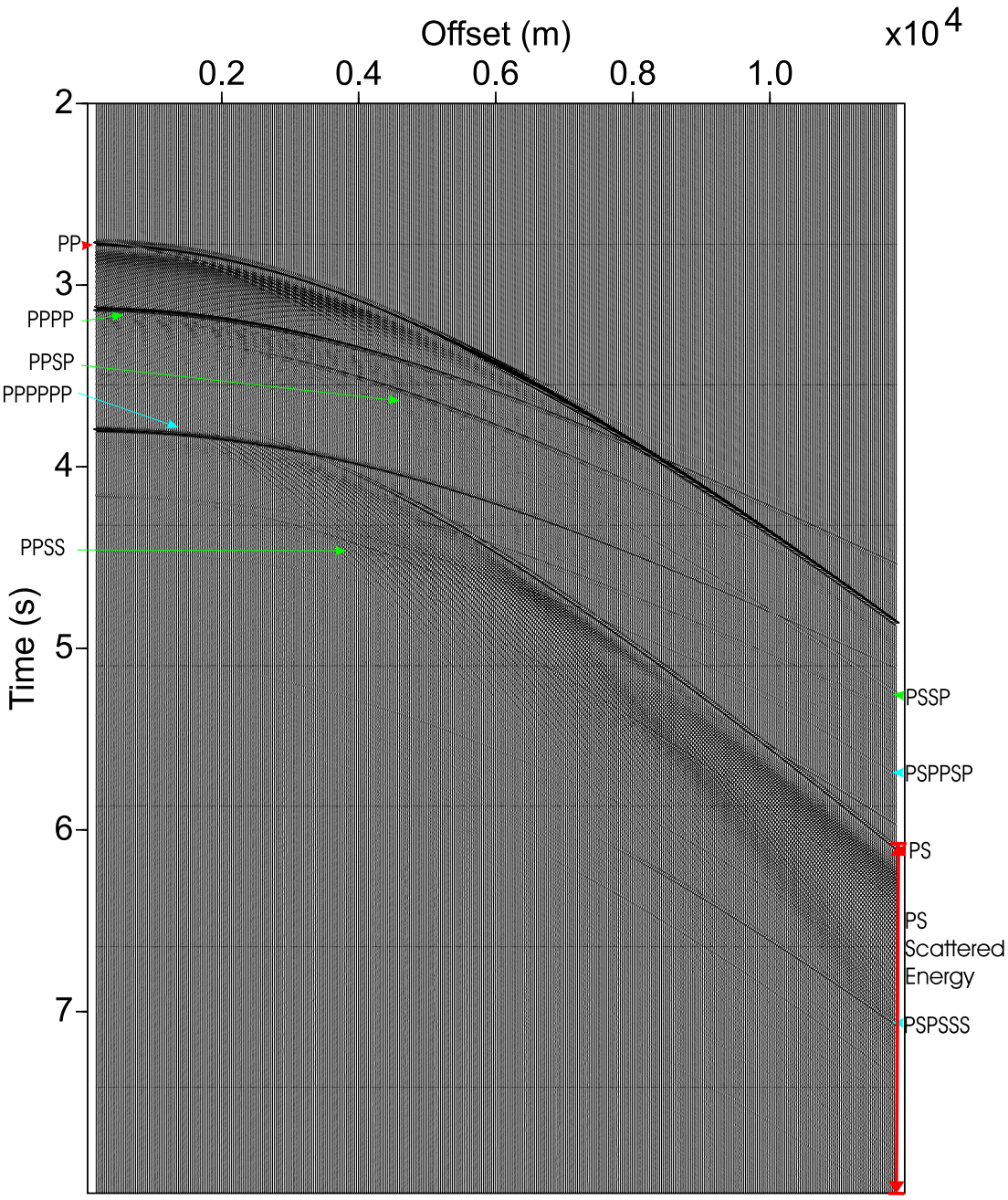

Figure 7.13: Shot gather generated from model B2 for a 40Hz source, z-component.

displacement for a 40Hz source. The difference between models B1 and B3 is in the spatial frequency of the scattered events on the shot gather. They have become more spread out now that the heterogeneity is of a longer wavelength. This is intuitive if one considers the peak of each sinewave to be a point diffractor. There are simply fewer diffraction points in model B3 than in model B1. The

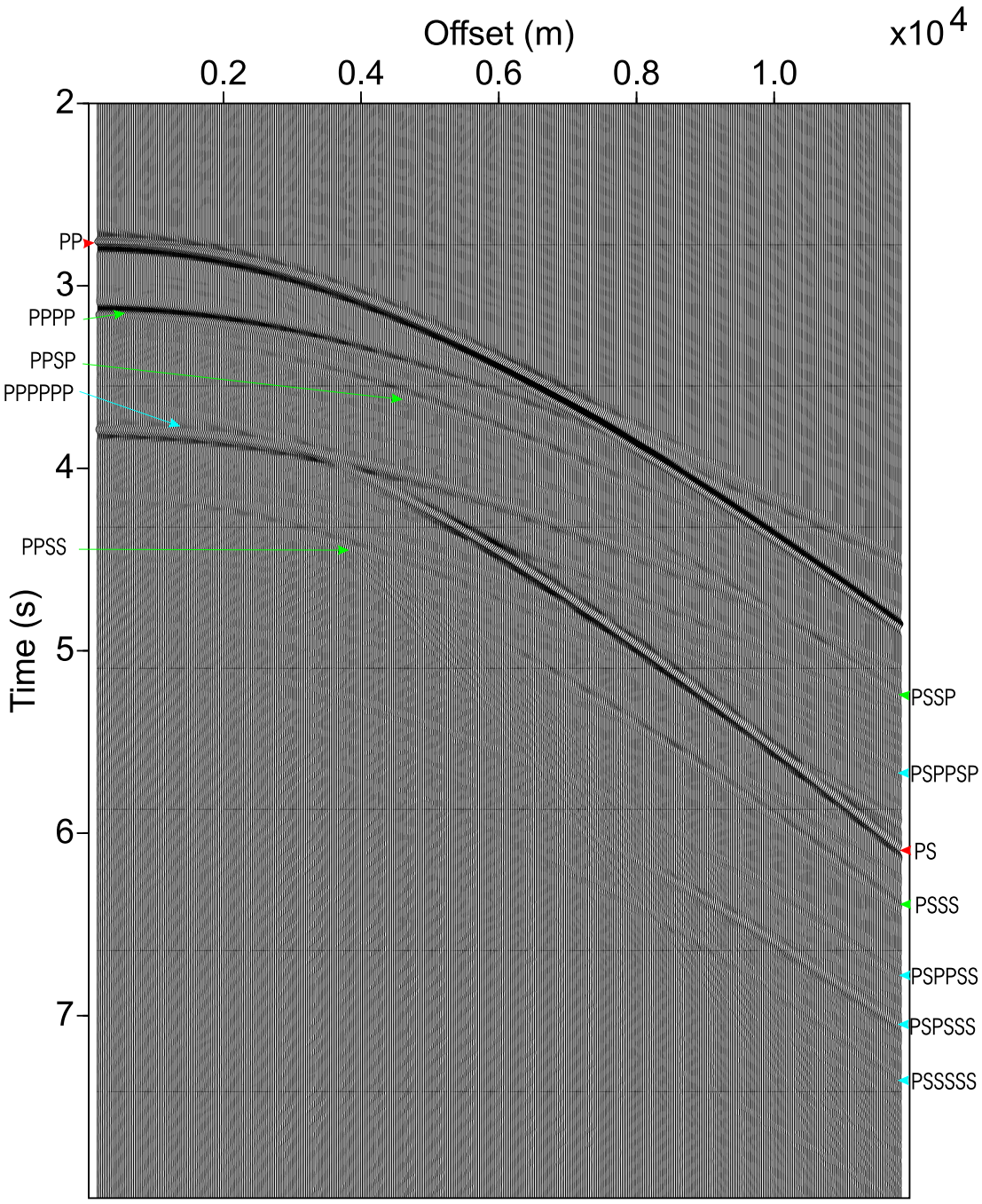

Figure 7.14: Shot gather generated from model B2 for a 10Hz source, z-component.

other important difference is that the converted waves from beneath the basalt are now much clearer and of a higher amplitude than before. The problem on the imaging side is, as before, the scattered energy from the PS conversion covering

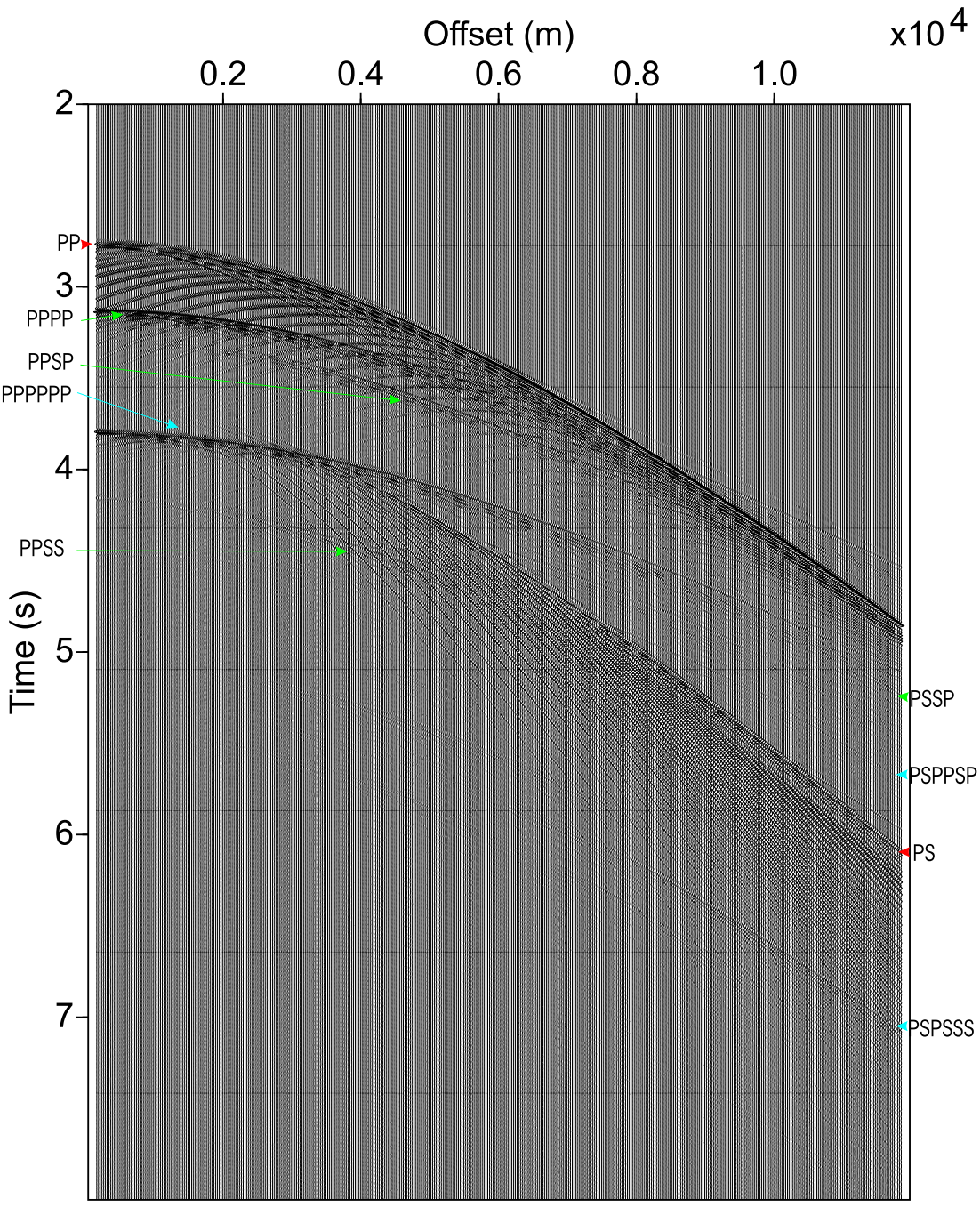

Figure 7.15: Shot gather generated from model B3 for a 40Hz source, z-component.

the events of interest. The P-wave events still represent the best chance of imaging the sub-basalt interface.

Figure 7.16 shows the shot gather for the same model for a source frequency of 10Hz. There is more scattered energy than for model B1. This is because the

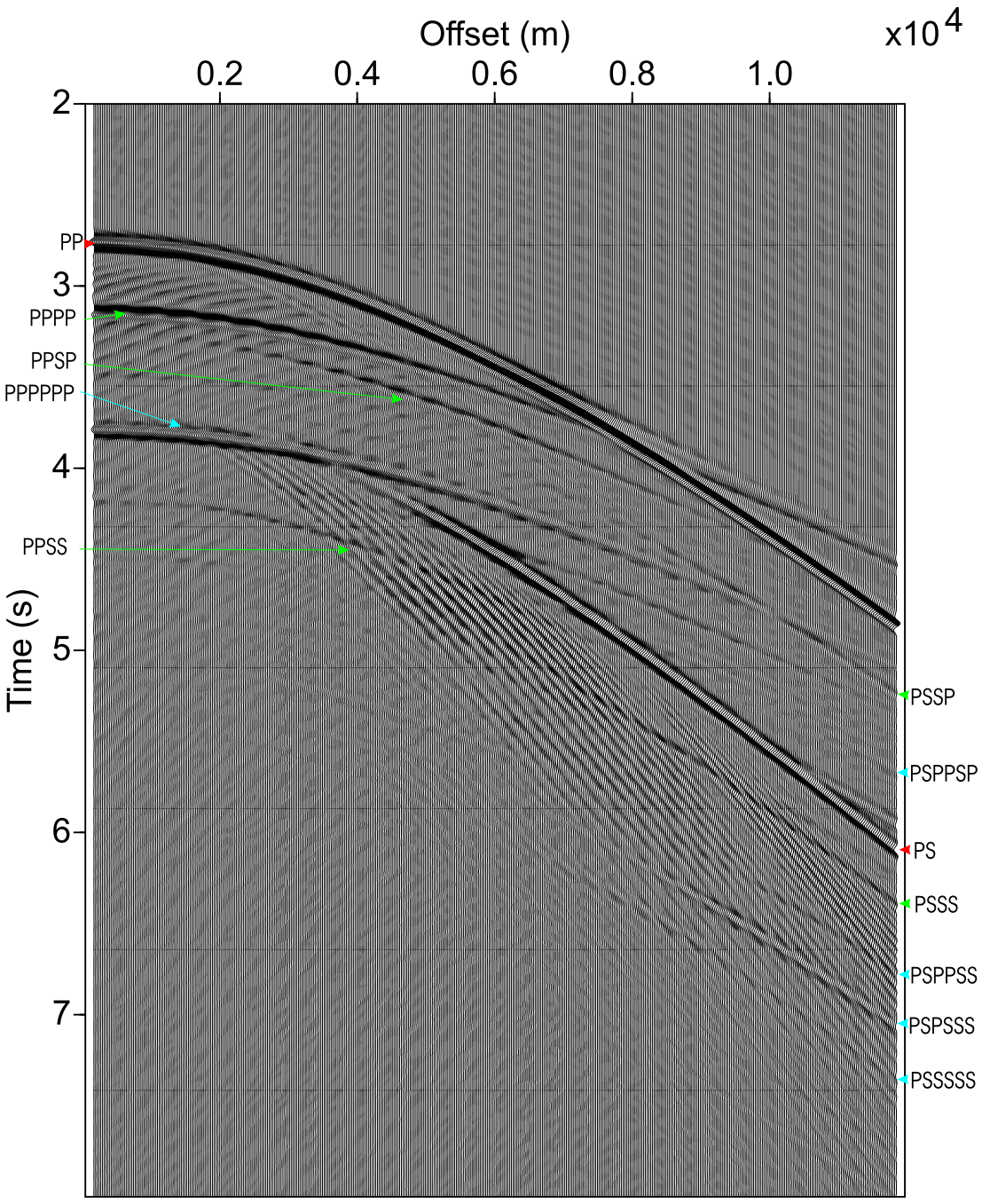

Figure 7.16: Shot gather generated from model B3 for a 10Hz source, z-component.

wavelength of the sinewave now approaches that of the seismic P-wave. For this model, it is difficult to say which frequency range would be optimal for imaging beneath the basalt. The two shot gathers display roughly the same amount of scattered energy and the important P-wave events can be seen only slightly more

clearly on the 10Hz seismograms. Therefore, in this case, it would probably be better to use the higher frequency source for the purpose of improving resolution.

The results from the previous model showed that the length scale of the

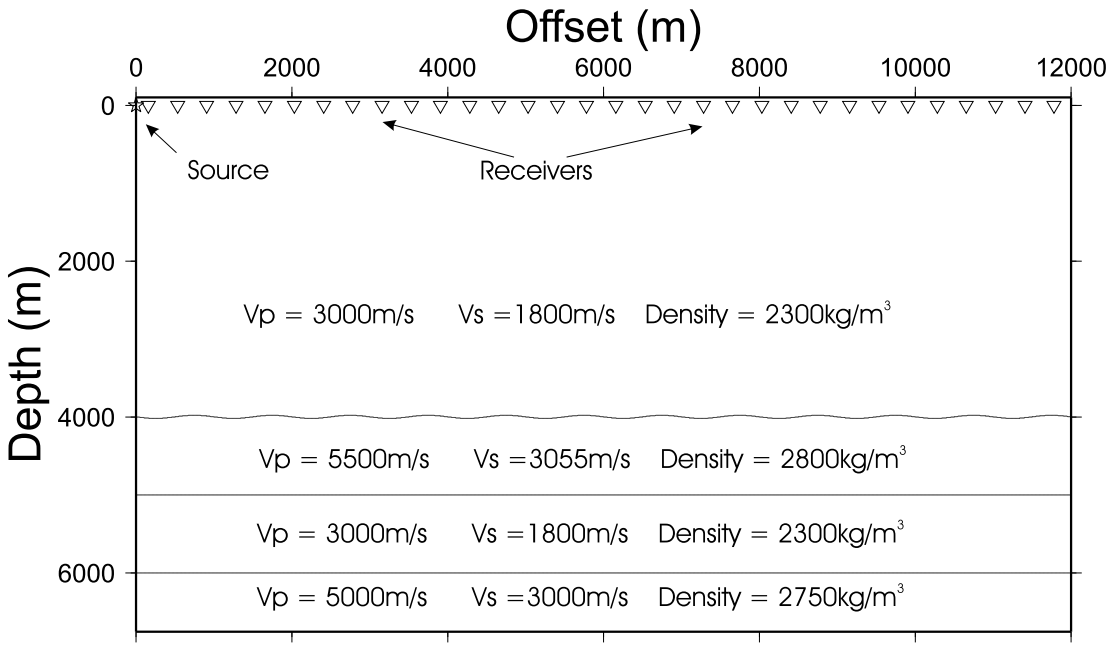

Figure 7.17: Sinewave-interface model B4

heterogeneity determines the amount of scattering for a particular seismic frequency. Model B4 gives the possibility to see what happens when the wavelength of the sinewave is much greater than that of the seismic wave. The roughness of the interface is not at all severe (Figure 7.17). Lateral heterogeneity of this level could be expected in many situations.

Figure 7.18 shows the 40Hz shotgather for this model. There is less scattered energy than for the previous models. The pure P-wave events are again the clearest and the sub-basalt interface is visible. The amplitude of the sub-basalt event now changes markedly with offset. These amplitude variation versus offset (AVO) effects may be used to gain information about the roughness of the top-basalt interface. In any case, it is clear that any AVO studies carried out on sub-basalt events should also include the effects of the overlying rough interface. The converted waves also display these AVO effects, though all wavemodes are still visible.

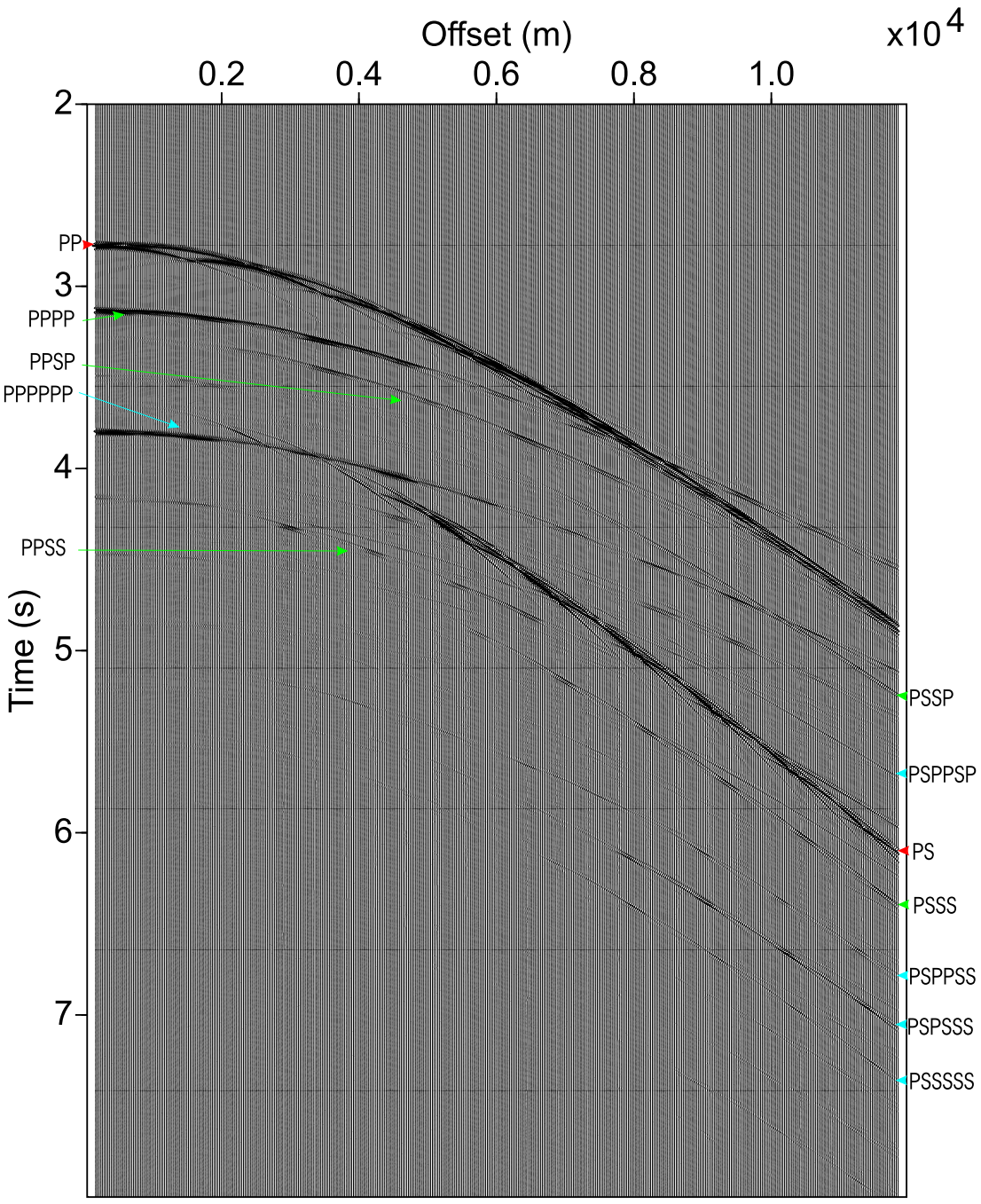

Figure 7.18: Shot gather generated from model B4 for a 40Hz source, z-component.

Figure 7.19 shows model B4 for a 10Hz source. The AVO effects are less apparent at this frequency. In particular, the continuity of the P-wave events is better than for the 40Hz shotgather. In this case, processing of the 10Hz seismic data would produce better results because of the less apparent amplitude effects.

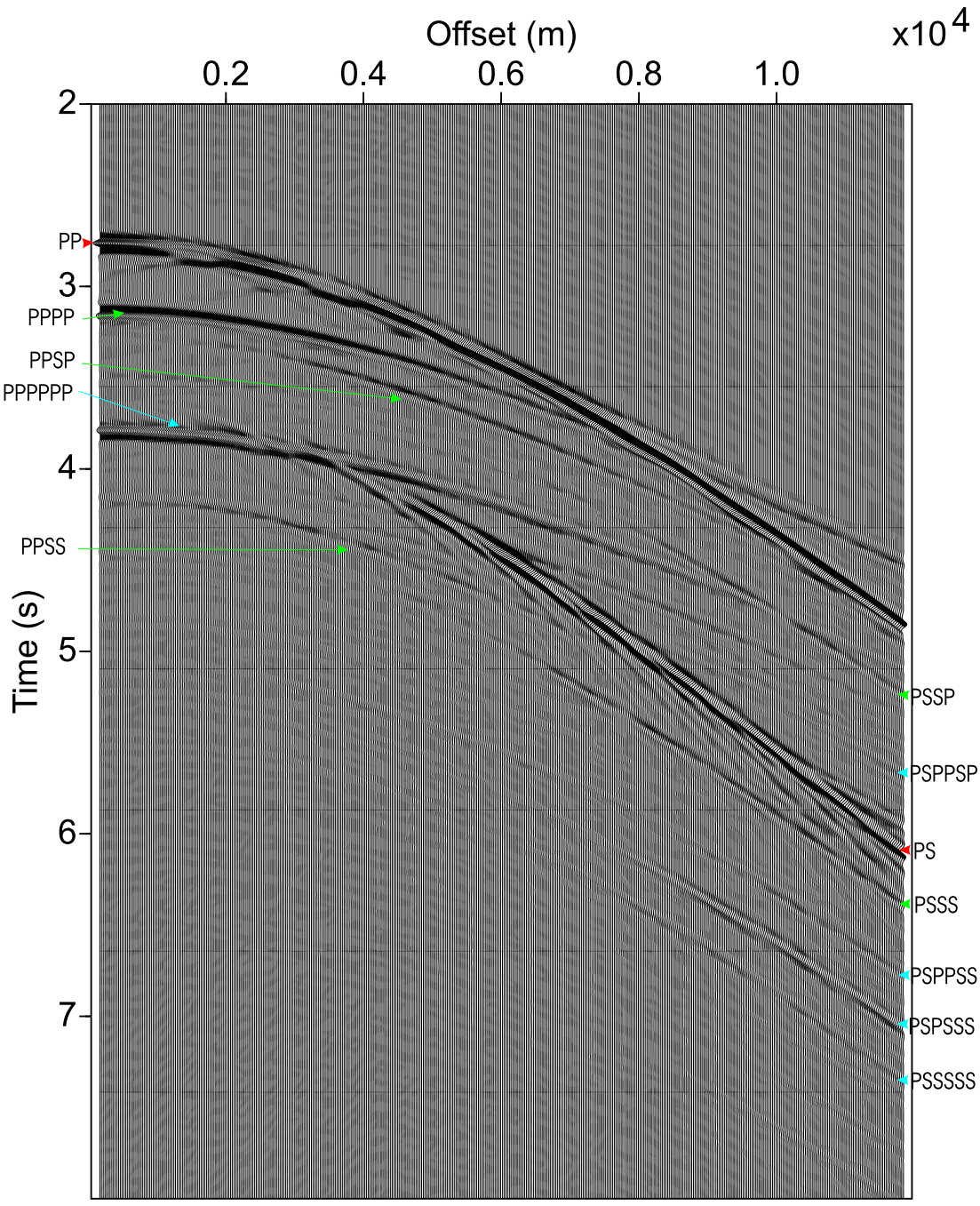

Figure 7.19: Shot gather generated from model B4 for a 10Hz source, z-component.

For long-wavelength heterogeneities, there is less scattering though more effect on the AVO of the events. The scattering is minimal, especially for the case where the scale of the heterogeneity is much larger than that of the predominant seismic wavelength (i.e. for a 40Hz source).

In model B5 a random factor is introduced into the rough interface. The

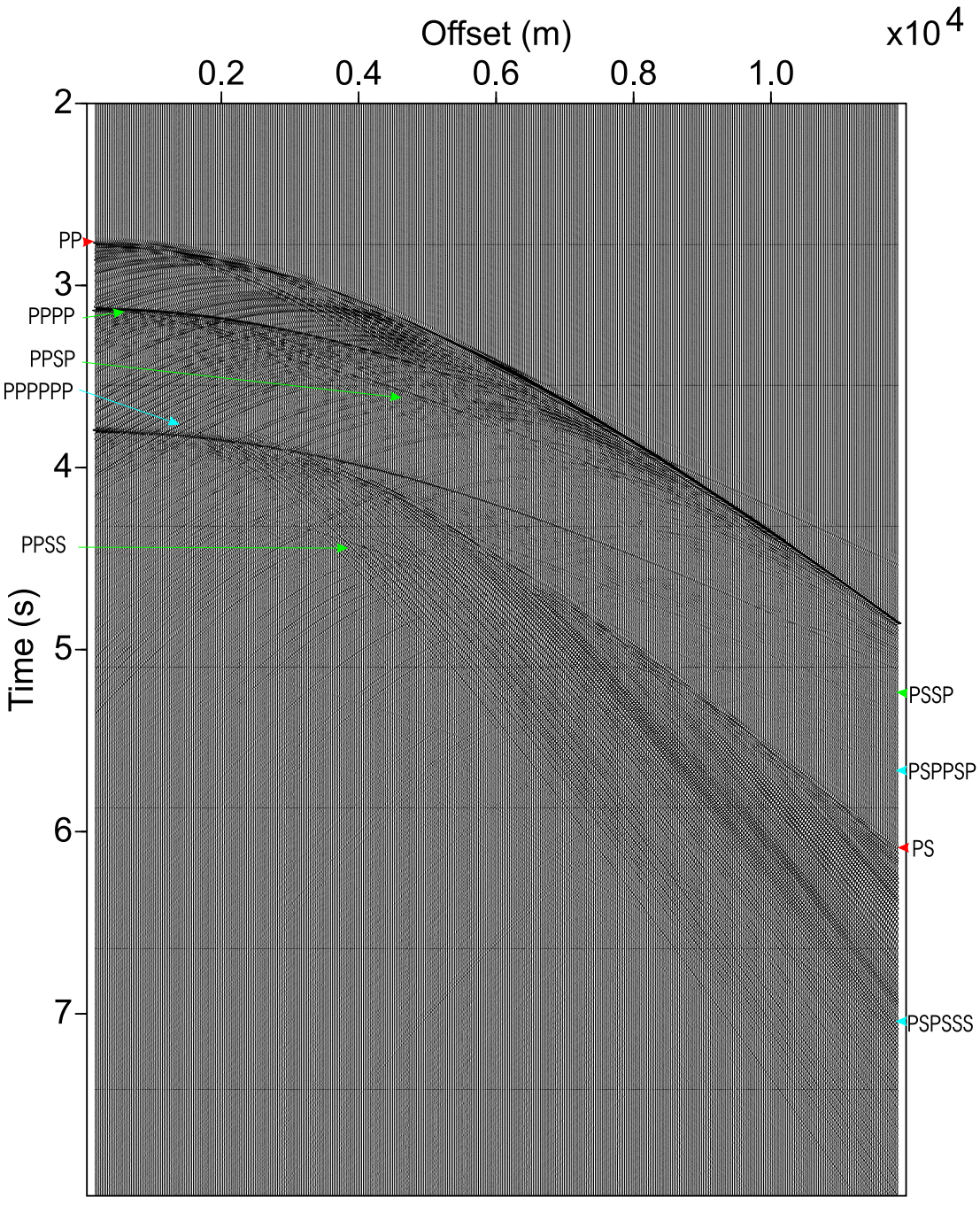

Figure 7.20: Shot gather generated from model B5 for a 40Hz source, z-component.

roughness is defined by a combination of many sinewaves which have wavelengths between 60 and 180m and peak-to-peak amplitudes between 16 and 64m. The

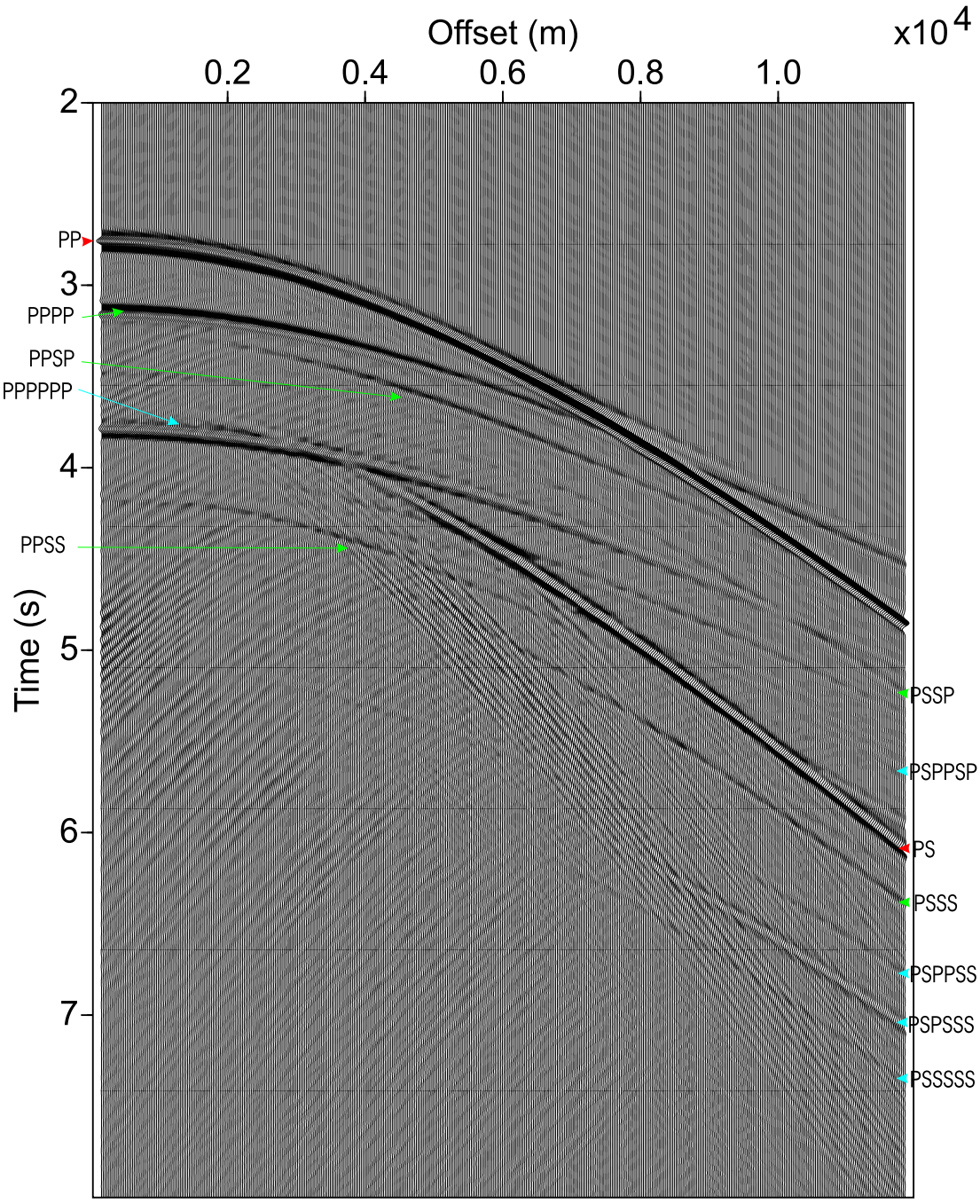

Figure 7.21: Shot gather generated from model B5 for a 10Hz source, z-component.

results for a 40Hz source (Figure 7.20) look similar to the shotgather from model B1. The main difference is that the the diffractions are now less regular. All the major P-wave and converted-wave events have been affected to the same extent as for model B1.

Figure 7.21 shows the same shotgather for a 10Hz source. There is now very little difference between this shotgather and the one for model B1. Even the regularity of the diffracted events has not changed very much. This is probably because the longer wavelengths cannot 'see' the small differences in the wavelength and amplitude of the sinewave. What is required is a wider range of lengthscales as is seen in the real geology.

7.4 Random-interface models

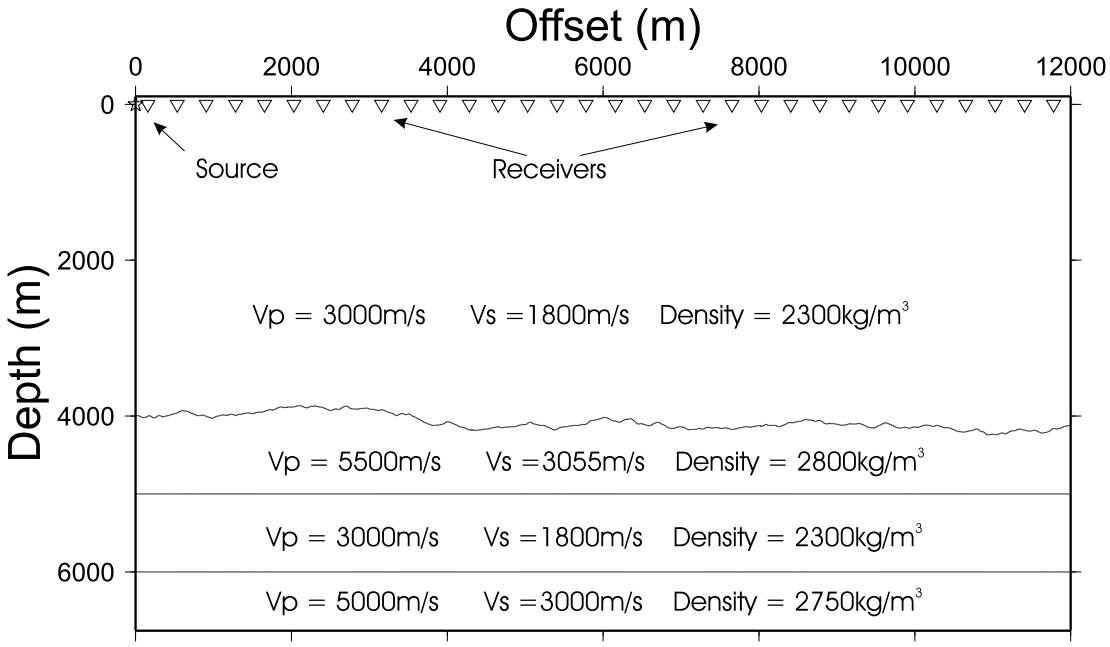

Figure 7.22: Random-interface model C1

The models in this section are designed to be more 'realistic' by making the interfaces random, not just by varying the amplitude and wavelength of a sinewave, but by building up an interface which is rough at all lengthscales. The interfaces are defined by using a random-walk style algorithm which starts at the lefthand-edge of the model and works to the right building up a fractal-type interface.

First, the interface is split into a number points which is large enough to make a realistic interface. Next, a series of random numbers is chosen which can vary between $\pm c$, where c determines the amount of heterogeneity for the interface. One number is selected for each point in the interface. The depth of each point in the interface is determined by the depth of the previous point plus the random factor for that point. In this way, a random interface is built up from left to right. The interface is then convolved with a boxcar function to ensure that sudden changes in depth do not occur between just a couple of points.

Model C1 is shown in Figure 7.22. The top-basalt interface was built up in the manner described above using a c value of 10m and a point spacing of 5m,

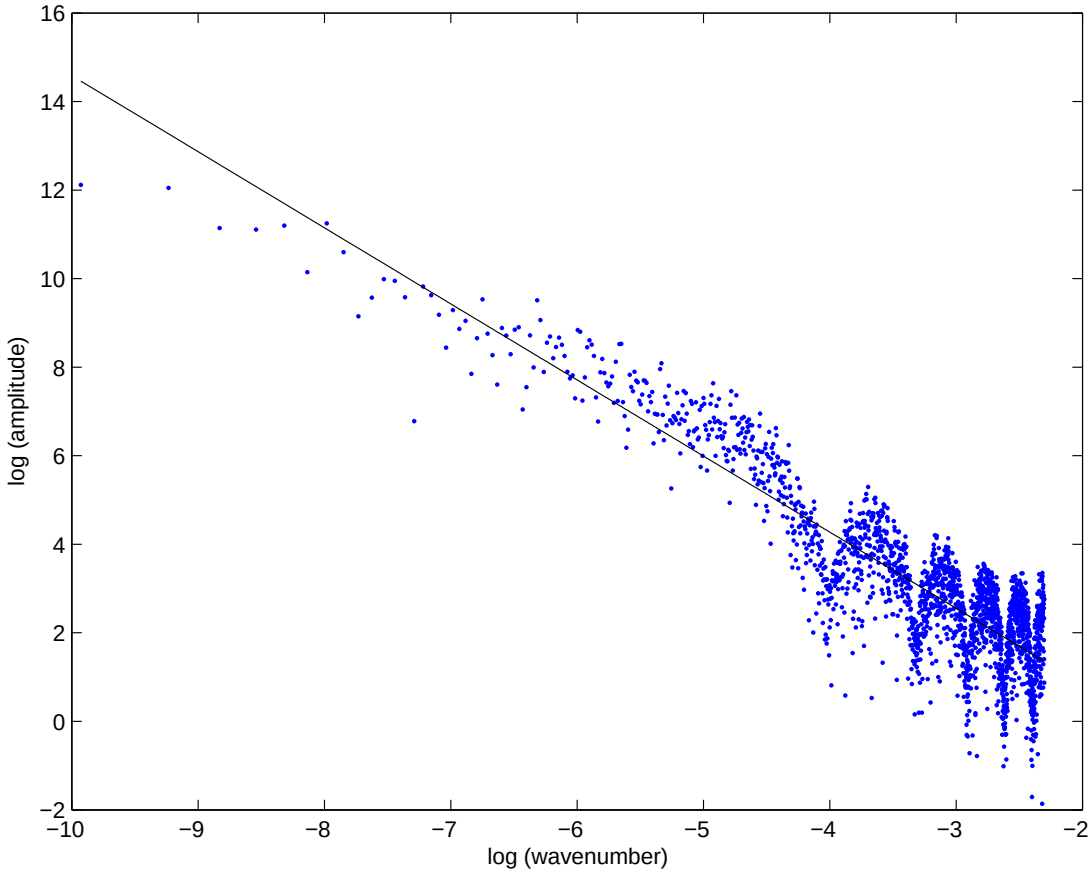

Figure 7.23: Log-log graph of amplitude against wavenumber for top-basalt interface in model C1.

and then convolved with a boxcar function to perform smoothing. Figure 7.23 shows the amplitude spectrum of this interface with varying wavenumber. This straight line nature of this log-log graph shows that the interface is fractal, i.e. it contains heterogeneity which looks the same on all length scales. It has been shown (Walia and Bull, 1997) that the interfaces of basalt exhibit fractal-type characteristics. Therefore, this interface represents a more realistic situation than the sinewave models previously discussed.

Figure 7.24 shows the 40Hz shotgather for this model. There is clear scattering at all offsets which is much less regular than the scattered energy seen in the sinwave-interface shotgathers. The pure P-wave events can still be seen, but are broken up by scattering. Imaging may still be successful for the sub-basalt interface, though there are large amplitude variations with offset. At far offsets the sub-basalt event almost disappears entirely.

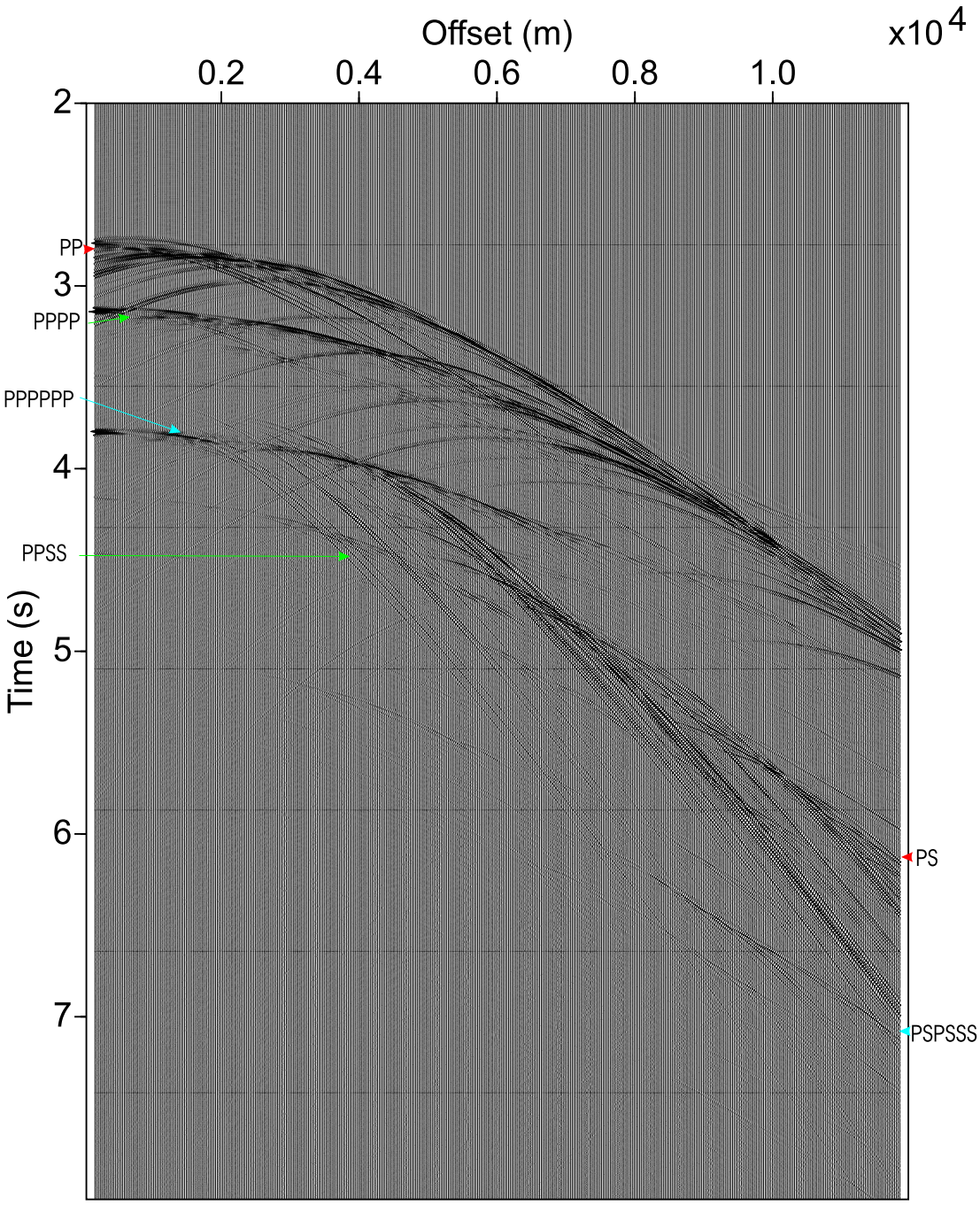

Figure 7.24: Shot gather generated from model C1 for a 40Hz source, z-component.

The converted-wavemodes from the base-basalt and sub-basalt interfaces have also survived, though to a lesser extent than the pure P-wavemodes. One of the main problems is again the wavetrain from the PS conversion masking the arrivals underneath. AVO effects are apparent in the mid and far-offsets. These changes

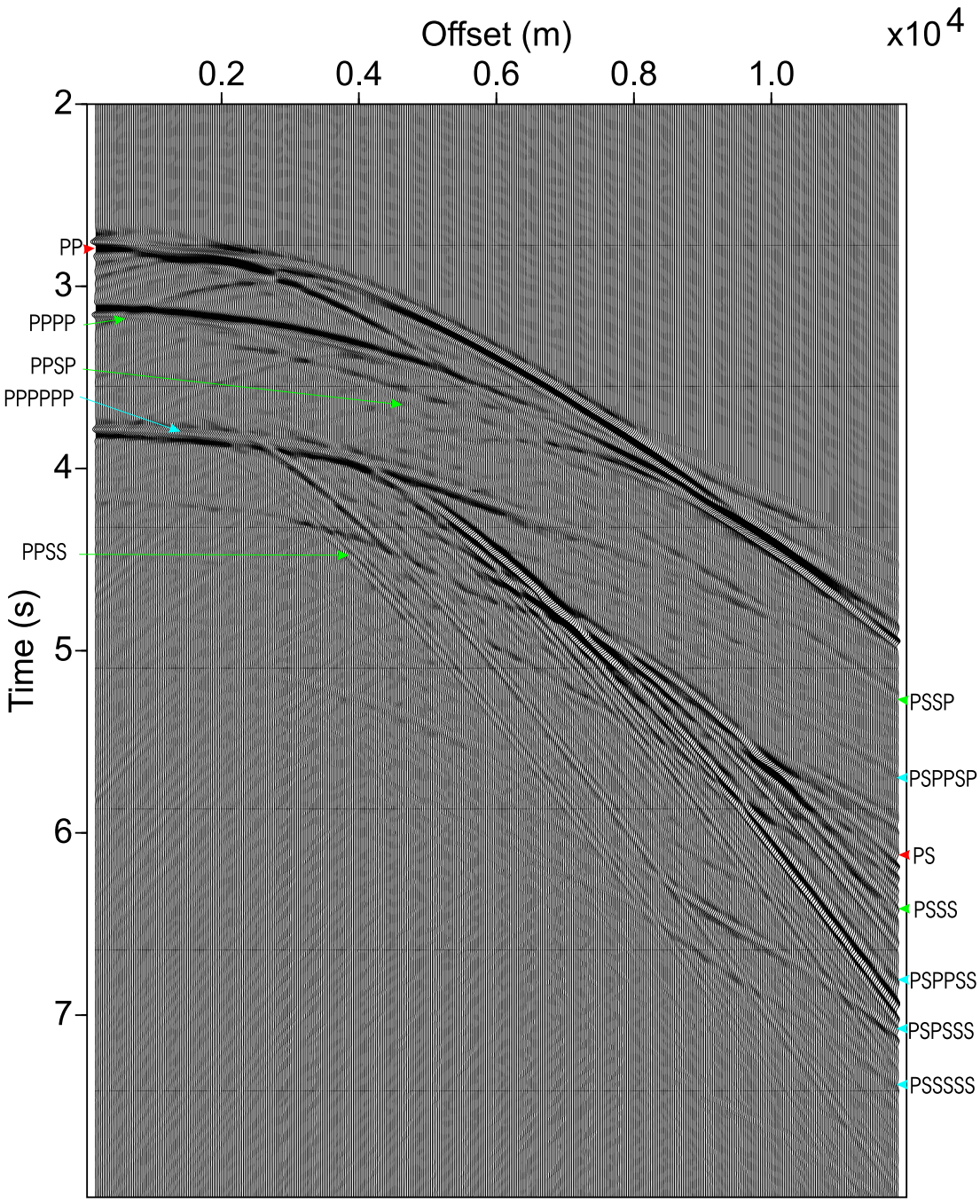

Figure 7.25: Shot gather generated from model C1 for a 10Hz source, z-component.

in amplitude are now much less systematic than for the sinewave models. Changes from high to low amplitude can be rapid from one offset range to the next, since the shot gather samples a spread of reflection points and responds to the lateral heterogeneity.

Figure 7.25 shows the 10Hz shot gather for model C1. Because there is now no clear length scale for the heterogeneity in the top-basalt interface, the low-frequency shotgather displays the same basic characteristics as the 40Hz shot-gather. The difference is that the events are more continuous. The small scale heterogeneities cannot be seen by the low-frequencies, which simply pass through unaffected. The P-wave reflection event from beneath the basalt is more continuous than for the 40Hz case. The near-offsets are, as for the high-frequency case, of a much higher amplitude than the far-offsets.

Model C2 contains a top-basalt interface which was defined with a c value of 5m. The 40Hz and 10Hz shotgathers generated from this model are shown in Figures 7.26 and 7.27. The Seismograms display the same characteristics as for model C1 though with less AVO and scattering effects. Higher amplitude heterogeneity should generate more scattering so this is expected.

Model C3 (Figure 7.28) is a combination of models C1 and C2. The top-basalt interface is defined with a c value of 5m and the base-basalt interface is defined with a c value of 10m. Model C3 is the most realistic model so far, since the basalts in this region are likely to have more rugosity at the base. This is due to in-filling of weathered rocks beneath. The top-basalt interface is more smooth since this represents the top of a horizontally travelling flow.

Figure 7.29 shows the 40Hz shotgather for this model. Even with the combination of two rough interfaces, the base-basalt and the sub-basalt interfaces are still visible for the pure P-wavemodes in the near to mid-offsets. There is little or no apparent energy in the far-offsets.

There is very little left of the converted wavemodes for either the base-basalt or the sub-basalt interfaces. This time, there is less scattering than for model C1 because the top-basalt interface does not have as much rugosity.

Figure 7.30 shows the 10Hz shotgather. As with model C1, there is less scattered energy. The P-wavemodes show more continuity and smaller amplitude variations than for the high-frequency case, though the sub-basalt event is still only visible in the near to mid-offsets.

The converted wavemodes, in contrast to the 40Hz shotgather, can be seen

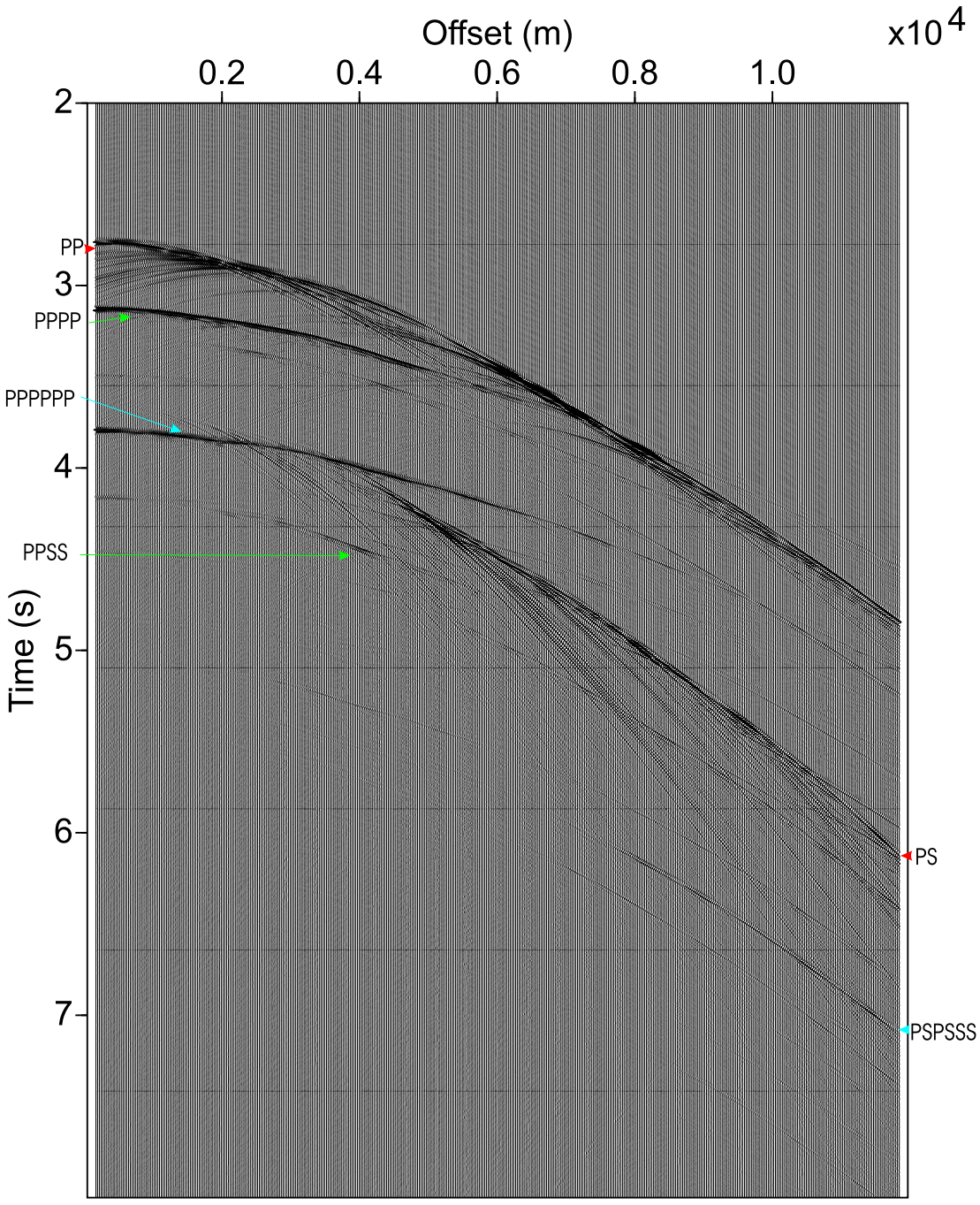

Figure 7.26: Shot gather generated from model C2 for a 40Hz source, z-component.

quite clearly. However, the pure P-wavemodes still represent the best chance of imaging beneath the basalt.

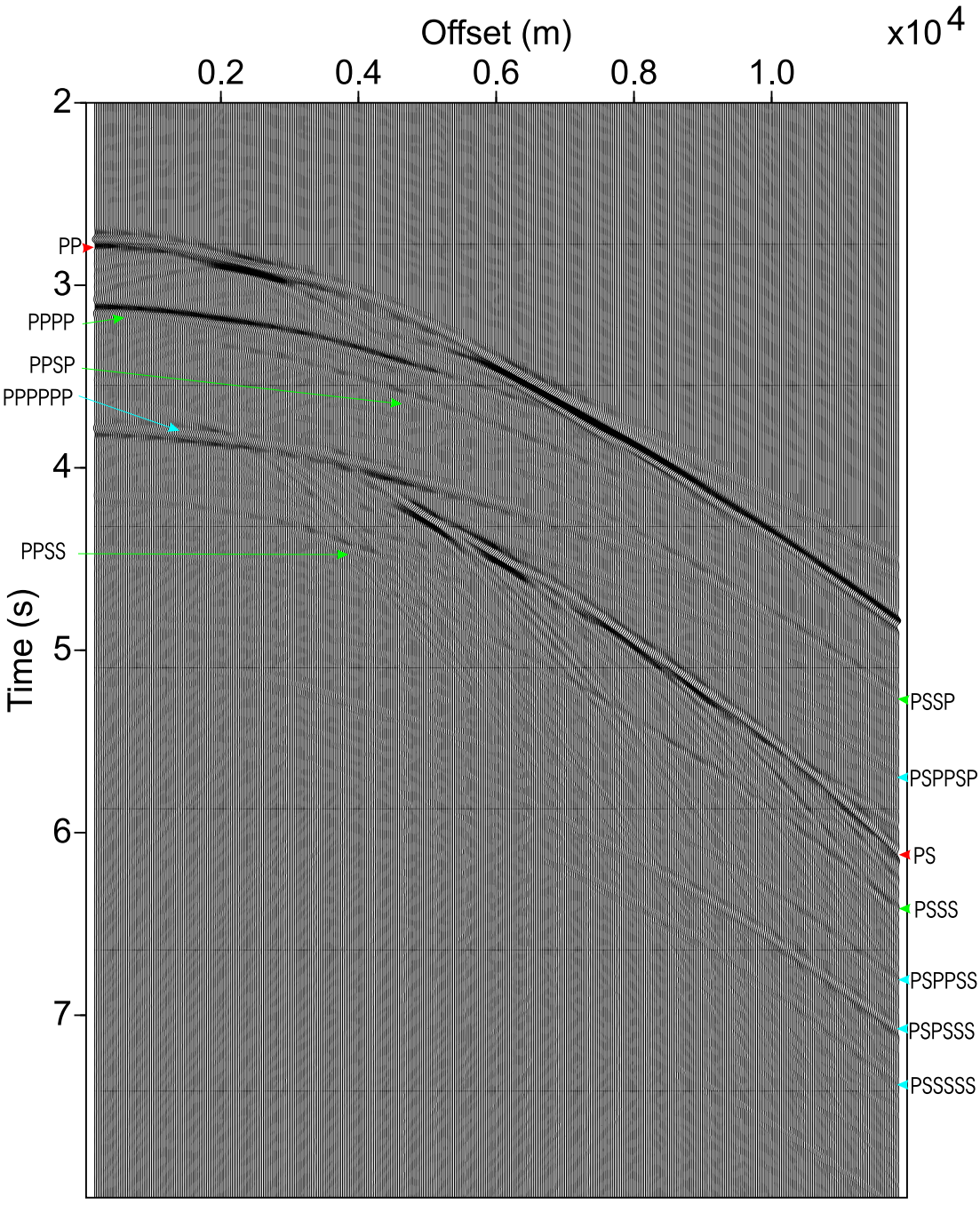

Figure 7.27: Shot gather generated from model C2 for a 10Hz source, z-component.

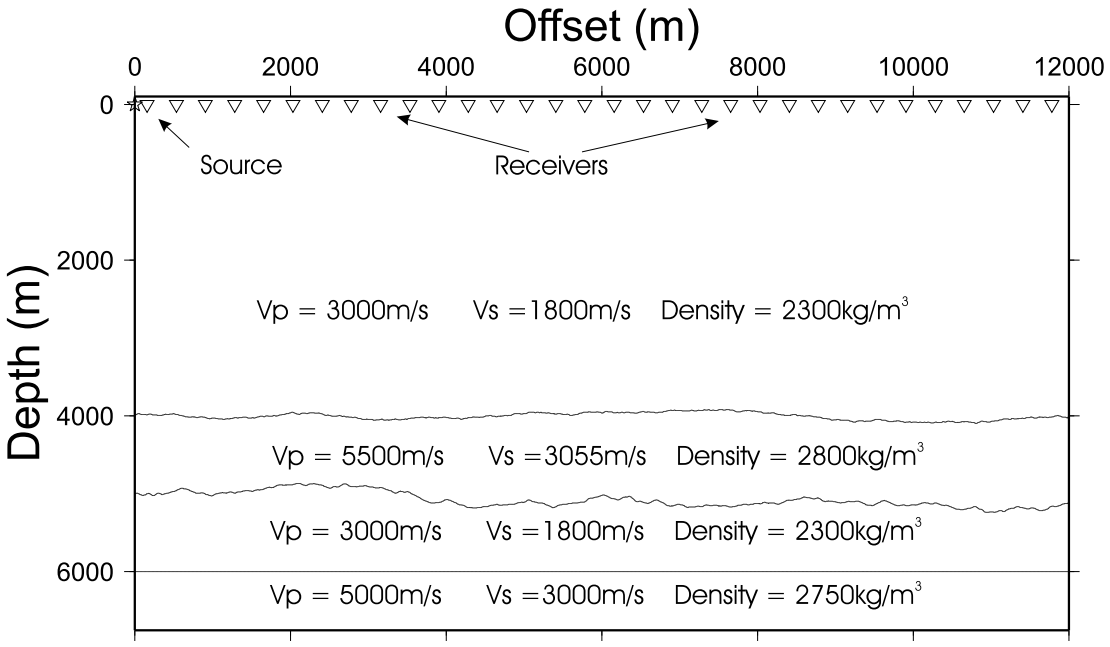

Figure 7.28: Random-interface model C3

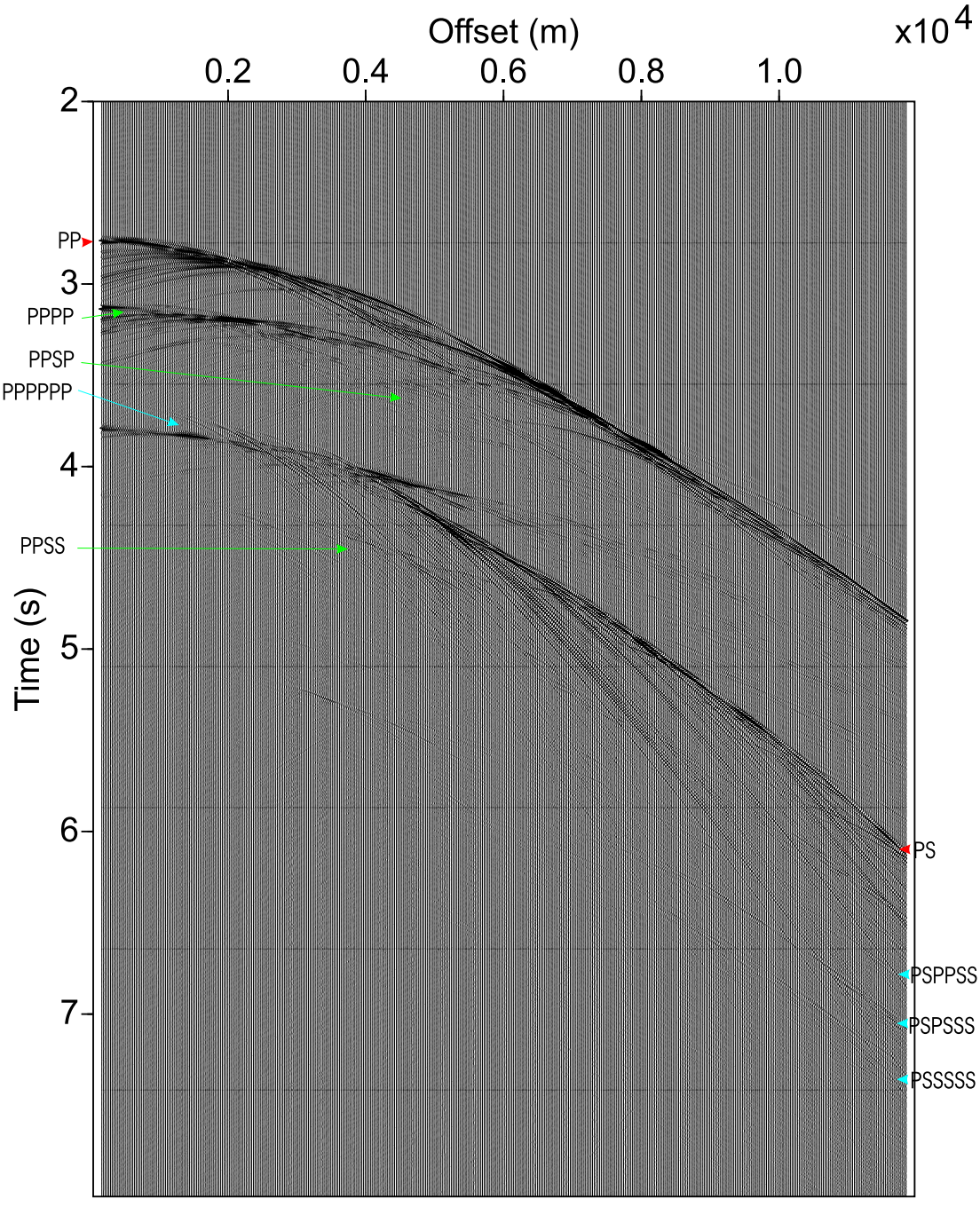

Figure 7.29: Shot gather generated from model C3 for a 40Hz source, z-component.

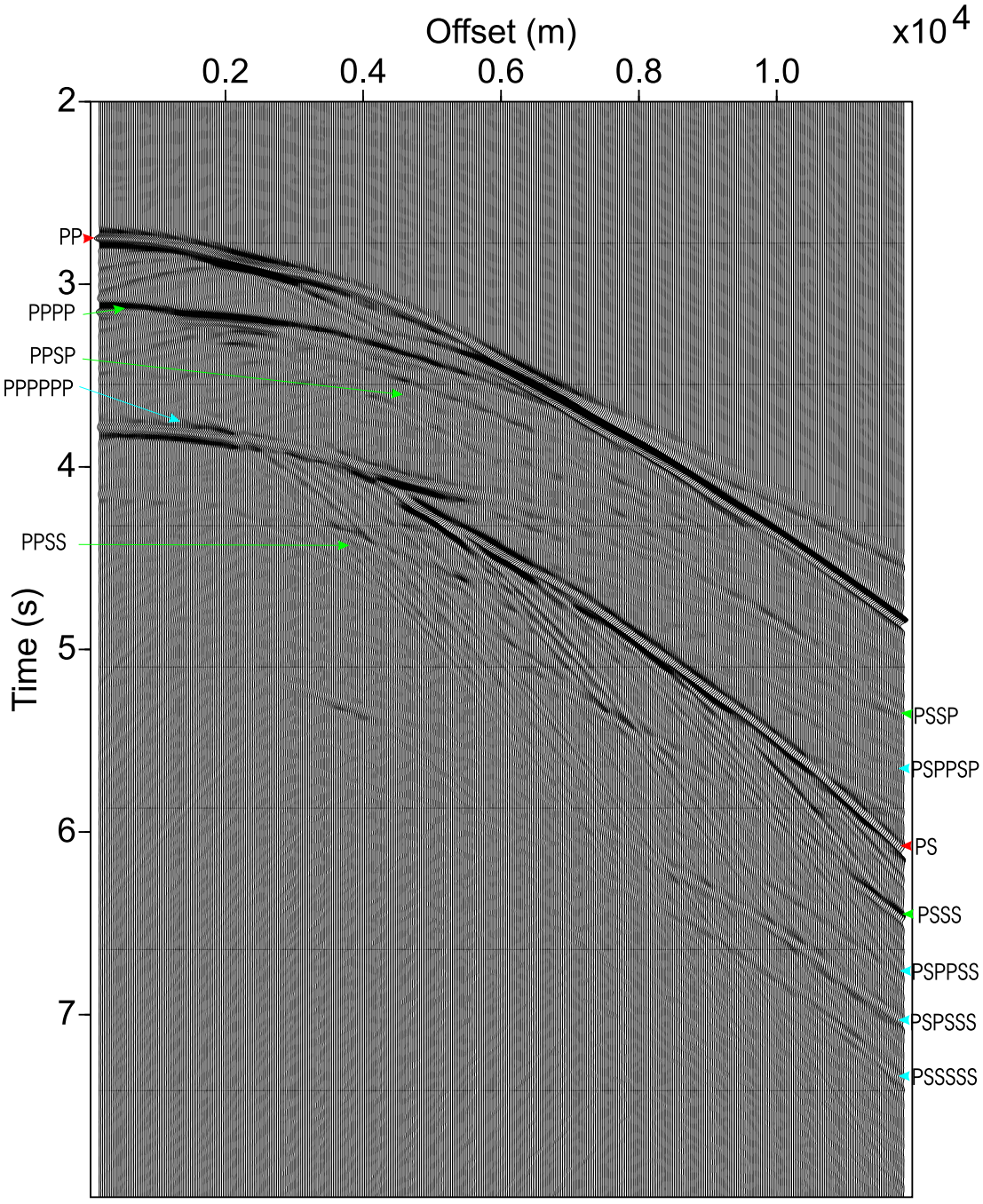

Figure 7.30: Shot gather generated from model C3 for a 10Hz source, z-component.

7.5 Discussion and conclusions

Synthetic shotgathers have been generated of models with sinewave and random interfaces using sources of 10Hz and 40Hz.

From modelling with a sinewave-interface of one wavelength, it was found that the most scattering occurs when the wavelength of the heterogeneity approaches that of the seismic wave. As expected, and in agreement with Paul and Campillo (1988), scattering is reduced when a smaller amplitude sinewave is used in the model. The scattered energy from such an interface displays a very regular pattern which mirrors the length scale of the sinewave interface.

When the seismic wavelength is much shorter than the wavelength of the sinewave (more than 3-4 times less), the scattering is reduced greatly and the effect shifts more to a change in amplitude with offset (AVO effect).

In agreement with previous work (Martini and Bean, 2002; Paul and Campillo, 1988), the wavemodes affected the most by a sinewave interface are the waves converted from P to S at the rough interface. This may be for geometrical reasons since the PS raypath is asymmetric and, therefore, perhaps more sensitive to heterogeneity. Generally, the waves passing through the rough interface are less affected than either the reflected P-waves or the PS-waves.

Modelling of an interface of several wavelengths and amplitudes has produced shotgathers with a less regular appearance. This is expected if the peak of each sinewave is treated as a point diffractor. The more random distribution of scattering points generates a more random distribution of scattering in the shot gather.

Modelling of random interfaces has revealed that P-wave events from beneath the basalt are visible at near to mid offsets, even when the interface has considerable roughness. Little or no energy is seen at far offsets. It should be remembered that these results may be model dependent. There are cases where the far offsets may be useful in imaging, especially at offsets where the critical angle is being approached.

Converted waves are more affected than the pure P-wave modes as for the simple sinewave case. For a 40Hz source, the converted waves from beneath the basalt would be difficult to use for imaging. These waves are extremely attenuated and display less continuity than the pure P-wavemodes.

Modelling with a low-frequency (10Hz) source has revealed that, in general, events from the beneath the basalt show more continuity and fewer diffractions than for the 40Hz case. AVO effects are also reduced. There is, however, still little energy seen in the far offsets for the pure P-wavemodes. The converted waves from beneath the basalt are much more visible at low frequencies.

In conclusion, the use of low frequencies and pure P-waves represents the best chance of imaging the base-basalt and sub-basalt interfaces. For extreme heterogeneity, there does not appear to be much energy seen in the far-offsets, though this may be model dependent.

Converted waves are more attenuated and more scattered than pure P-wave modes for all models considered. One of the major problems for imaging using converted-wavemodes for sub-basalt imaging is that the converted wavetrain from the top-basalt interface masks the events of interest underneath.

Methods have been developed (e.g. Martini and Bean 2002) to remove the effects of scattering due to rough interfaces and improve the image of interfaces beneath. The key to these methods is a good model of the rough interfaces. Without this it would be extremely difficult to remove the effects of scattering. It may be possible to use AVO effects, particularly in the PS-wavemode, to improve model building of the interfaces at the top and base of the basalt. Closer analysis of the AVO effects may lead to improved imaging, though this is not within the scope of this thesis.

Chapter 8

Modelling of thin-layered basalt

8.1 Introduction

In Chapter 7, I describe studies in which I model basalt with rough interfaces. In this chapter I return to flat interfaces, but consider vertical rather than lateral heterogeneity.

Though studies have previously been carried out which model the basalt as a succession of thin layers (Mack, 1997; Hanssen et al., 2003; Smallwood et al., 1998), only general conclusions about the low-pass filter nature of thin-layered basalt were offered. I take a more rigorous approach to the problem and attempt to find the precise nature of the link between the properties of the basalt layers and the response of a seismic wave passing through them.

Assuming heterogeneous basalt with a succession of thin-layered basalt flows, I carry out a detailed numerical modelling study to understand the seismic response. This could aid the optimisation of acquisition parameters and also allow the possibility of discovering something about the flow thickness from the seismic wavelet. By considering the sub-basalt reflection at near- and far-offsets I examine how the amplitude and shape of the wavelet changes and discuss possible implications for imaging.

Modelling in this chapter is performed using two methods. The plane-wave normal-incidence method developed by Treitel and Robinson (1966) has been adapted so that layers of any thickness may be included in the model (Appendix E). The output is the response in the frequency domain for a normally incident

wave. This method assumes a plane wave and is fast and accurate, but is suitable only for seismograms of normal incidence. The second method used is the reflectivity method (Appendix B), which is a full-waveform (P- and S-wave) method for near and far offsets. The method allows the use of a 3-D point source though only planar layers may be included in the model. The the modelling package used to perform the reflectivity modelling is OSIRIS (Vilmann et al., 1998).

Modelling starts with a plane-wave source which is normally incident on a simple three-layer model. This is to ascertain the connection between layer thickness and seismic response in the frequency domain. Next, more layers are added to the model. Finally, reflectivity modelling with a point source is used to generate seismograms of a more complicated succession of layers whose thickness and velocity correspond to those of the upper series volcanics on the Faeroe Islands.

8.2 Three-layer model: normally incident plane-wave source

Several studies have been carried out on the effect of highly discontinuous media on seismic wave propagation. The most famous of these is probably the paper by O'Doherty and Anstey (1971) who pointed out the importance of peg-leg multiples in the transmission of energy through a stack of layers. Burridge and Chang (1989) continued this work with a description of the progressive attenuation of a plane wave as it passes through thousands of layers. They used layer averages to develop an approximate, though in many cases very accurate, theory for the effect on a wavelet as the number of layers goes to infinity. I begin with a much more modest three-layer model, though hope to gain extra insight into the effect of highly discontinuous media on seismic wave propagation.

Consider the model depicted in Figure 8.1. The model represents two basalt flows, one above the other, and consists of two rock types: a low-velocity rock corresponding to the margins of a basalt flow, and a high-velocity rock corresponding to the massive interior of a basalt flow. To keep the model as simple as possible, the two basalt flows are sandwiched between two half spaces of

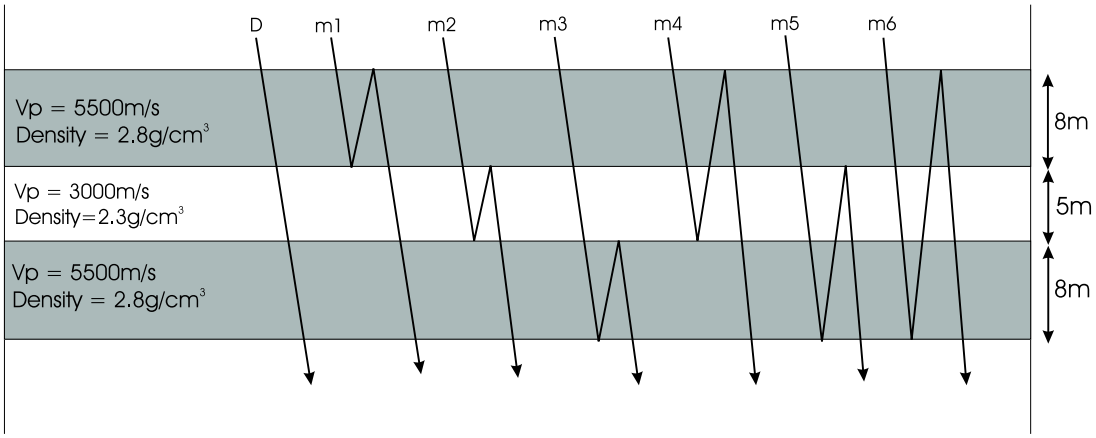

Figure 8.1: Simple three-layer basalt model depicting primary raypath and all possible two-bounce multiples at normal incidence. Raypaths are plotted at an angle to show reflection points more clearly.

homogeneous rock with the same seismic parameters as the low-velocity margins.

It is of interest to find the frequency response for an impulsive plane wave which passes downwards through this succession, reflects at some sub-basalt interface beneath the succession and then passes upwards though the same succession towards a receiver. This is the response which would be observed at a receiver in the top layer if the source were also placed in the top layer and the interface beneath the basalt were a perfect reflector.

Figure 8.2 (blue line) shows the frequency response for this model, which has been computed using the Treitel and Robinson method (Appendix E). Several maxima and minima are present which are a result of constructive and destructive interference of seismic waves within the layers. The positions of these maxima and minima are determined by the traveltime through each of the layers and are, therefore, connected to the velocity and thickness of the layers. The final response can be seen as a combination of the response from the direct wave and all the possible multiples within the succession. There is an infinite number of multiples generated by this type of model, though some contribute more than others to the final response.

To find out which of the multiples are the most important, I begin by looking

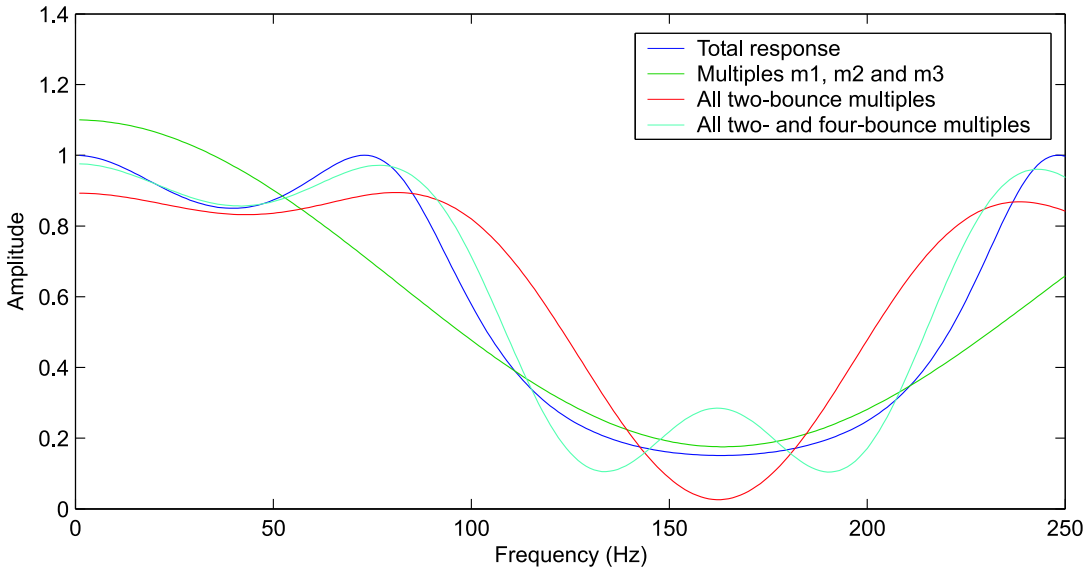

Figure 8.2: Frequency response through three-layer basalt model at normal incidence. Curves are plotted for the total response (including all multiples) and for selected multiple raypaths within the layers. The direct wave is always included in the computation.

at some of the least complicated peg-leg multiples to determine how much of a contribution they make to the final response. The normal-incidence reflection coefficient for pressure is found by the equation

$$r_{12} = \frac{\alpha_2\rho_2 - \alpha_1\rho_1}{\alpha_2\rho_2 + \alpha_1\rho_1}, \tag{8.1}$$

where α_1 and α_2 are the P-wave velocities in layer 1 and layer 2 respectively, and ρ_1 and ρ_2 are the densities. If the velocity and density values for the two-layer model are put into Equation 8.1, it is revealed that all the interfaces have a reflection coefficient of around 0.38 (the sign of the reflection coefficient depends on the interface).

The shortest two-bounce multiple raypaths, those with no more transmissions than the direct wave, (e.g. multiple m1, see Figure 8.1) have an amplitude over six times weaker than the direct wave. Therefore, the direct wave still generates a significant proportion of the energy seen in the final response. The longer period two-bounce multiples (e.g. multiple m5) have an amplitude equal to about 0.8 of

the amplitude of m1, m2 and m3. Each of the four-bounce multiples is approximately six times weaker than the two-bounce multiples, though there are more of them.

It is possible to separate contributions from each multiple path by using Z-transform notation. The method works by writing down the multiple raypaths under consideration in Z-transform notation and then summing with the direct ray to find the response (Appendix D). Using this method, different multiples can be included in the summation and the response compared to the total response (which is the sum of all multiple paths and the direct wave) to see which ones contribute the most.

Figure 8.2 (dark-green line) shows a comparison of the frequency response considering only multiples m1, m2, m3 and the direct ray. There is some agreement between the full response and the approximation. The minimum at around 160Hz and the maximum at 0Hz are already in agreement. When the remaining two-bounce multiples are added (Figure 8.2, red line), the general shape of the curves is the same at all frequencies. This shows that, for this simple model, most of the important energy is supplied by the direct ray and the two-bounce multiples.

When all possible four-bounce multiples are included in the computation of the response (Figure 8.2, light-green line), the fit improves further though the general shape of the response remains the same. If even higher order multiples were to be included, the fit would become gradually better and better though these higher orders are of less importance for this particular model.

It is important to consider why the maxima and minima appear where they do in the frequency spectrum. For this model, the direct wave is by far the most energetic ray. The frequency response is made up of interference between the direct wave and the multiples, and is dependent on the time delay between the direct wave and a particular multiple raypath. In general, destructive interference is expected when the time delay of a multiple relative to the direct ray is equal to half the period of the seismic wave or when,

$$f = \frac{1}{2\Delta t}, \tag{8.2}$$

where f is the frequency in Hz and Δt is the time delay in seconds. This is the frequency for which a minimum is expected in the response. For multiples m1 and m3, the time delay corresponds to a minimum when $f \approx 170$Hz. For m2, a minimum would be expected at around 150Hz. The actual minimum falls between these two values, at around 160Hz (Figure 8.2).

Constructive interference is expected when the time delay is 0 or equal to the period of the seismic wave:

$$f = \frac{1}{\Delta t}. \tag{8.3}$$

The maximum around 80Hz (Figure 8.2, red line) is partly a result of constructive interference between multiple m6 and the direct wave.

For multiples m4 and m5 a phase change must be taken into account. Therefore, a maximum is expected when

$$f = \frac{1}{2\Delta t}, \tag{8.4}$$

and a minimum when

$$f = \frac{1}{\Delta t}, \tag{8.5}$$

which is the opposite of the case for multiples m1, m2, m3 and m6. The delay of multiples m4 and m5 with respect to the direct wave corresponds to a minimum when $f \approx 160$Hz and a maximum when $f \approx 80$Hz.

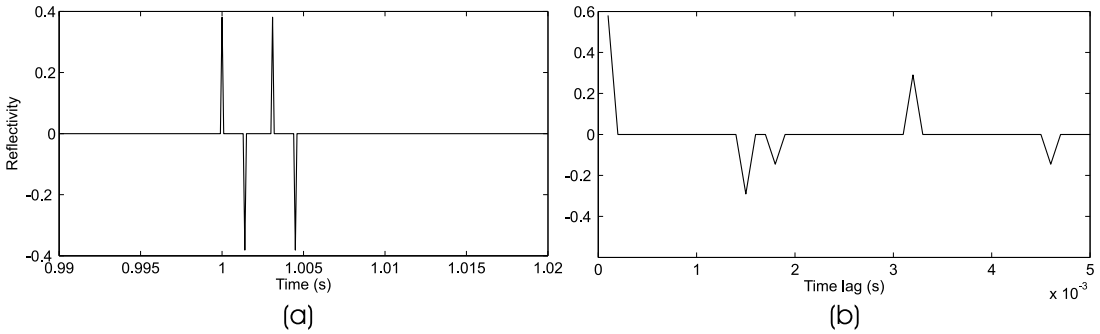

Figure 8.3: Plots showing (a) reflectivity log and (b) autocorrelation of three-layer basalt model.

A good way to look at characteristic delay times for a specific sequence is to calculate the autocorrelation of the reflectivity log of the basalt succession. Figure 8.3(a) shows the reflectivity log of the three-layer model. The two peaks and two

troughs correspond to the four interfaces in the model. The reflectivity has been calculated using Equation 8.1.

Figure 8.3(b) shows the autocorrelation of the normal-incidence reflectivity log. The biggest peak occurs when the time lag is zero, which is the case for all reflectivity logs. There are three other major events: a grouping of troughs at around 1.5ms, a peak at 3.1ms and a trough at 4.7ms. If these times are doubled, the two-way traveltimes for the corresponding interface combinations are yielded.

Peaks in the autocorrelation function occur when the sign of the reflectivity is the same for two interfaces. Therefore, the peaks correspond to multiples m4 and m5.

Troughs in the autocorrelation function occur when the sign of the reflectivity is different for two interfaces. Therefore, the troughs correspond to multiples m1, m2, m3 and m6.

	Peak in autocorrelation	Trough in autocorrelation
f_{min}	$1/\Delta t$	$1/2\Delta t$
f_{max}	$1/2\Delta t$	$1/\Delta t$

Table 8.1: Parameters used in modelling

To summarize, Equations 8.2 and 8.3 can be used for troughs in the autocorrelation function, and Equations 8.4 and 8.5 can be used for peaks (Table 8.1). Although this analysis explains the response for a simple three-layer model, the situation becomes far more complicated when many layers are considered. I discuss this in the next section.

8.3 Multi-layer Model: plane-wave modelling

In this section I consider the frequency response for a succession of 39 basalt flows, compared with three layers for the last section. As before, the interior high-velocity part of each flow is 8m, and the top and base margins make up a 5m layer. The same velocities and densities are used as for the previous model.

The frequency response for a reflection from beneath the basalt succession can be seen in Figure 8.4. The main feature is the large minimum centred around

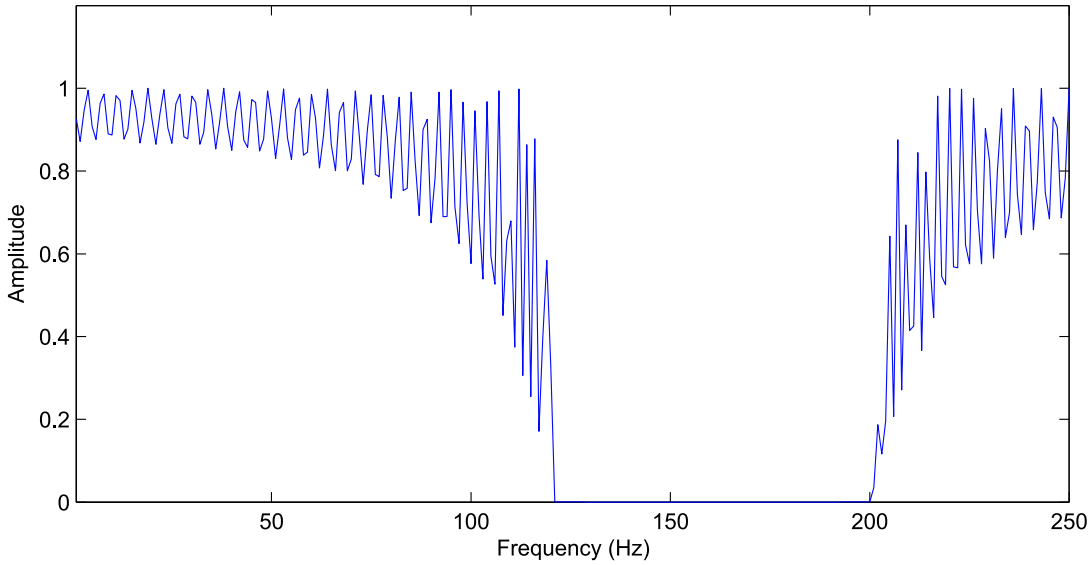

Figure 8.4: Frequency response for 39-flow model.

160Hz. The response for this model cannot be explained in terms of the time delay between the direct wave and the multiples. The direct wave is no longer important since the transmission coefficient for one basalt flow (low impedance to high impedance, then high impedance to low impedance) is roughly 0.86. Each time a pressure wave passes though one such flow its amplitude is multiplied by 0.86. There are 39 flows in the model, so a pressure wave which has an amplitude of 1 at the top of the basalt succession, has an amplitude of only 0.002 at the bottom. Therefore, it is the multiples which carry most of the seismic energy through the succession. This is generally true for any succession containing many layers (see O'Doherty and Anstey, 1971).

The response for this model is determined by the delay in time between one packet of multiple energy and another. This delay is in turn determined by the two-way traveltime through each of the layers. First I consider only the delays which are caused by two reflections within one layer. Each layer in the model has a two-way traveltime associated with it which is

$$\Delta t = \frac{2d}{v}, \tag{8.6}$$

where d is the thickness of the layer and v is the P-wave velocity. This equation can be combined with Equations 8.2 and 8.3 (because multiples of type m1, m2

and m3 are under consideration) to give

$$f_{min} = \frac{\alpha}{4d}, \tag{8.7}$$

and

$$f_{max} = \frac{\alpha}{2d}, \tag{8.8}$$

where f_{min} is the frequency at which a minimum is expected in the frequency response and f_{max} is the frequency at which a maximum is expected.

The 39-flow model consists of the same two layers alternating 39 times. For the high-impedance layer $f_{min} \approx 170$Hz. For the low impedance layer $f_{min} = 150$Hz. Similar to the two-flow case, the centre of the minimum falls in between these two values at 160Hz.

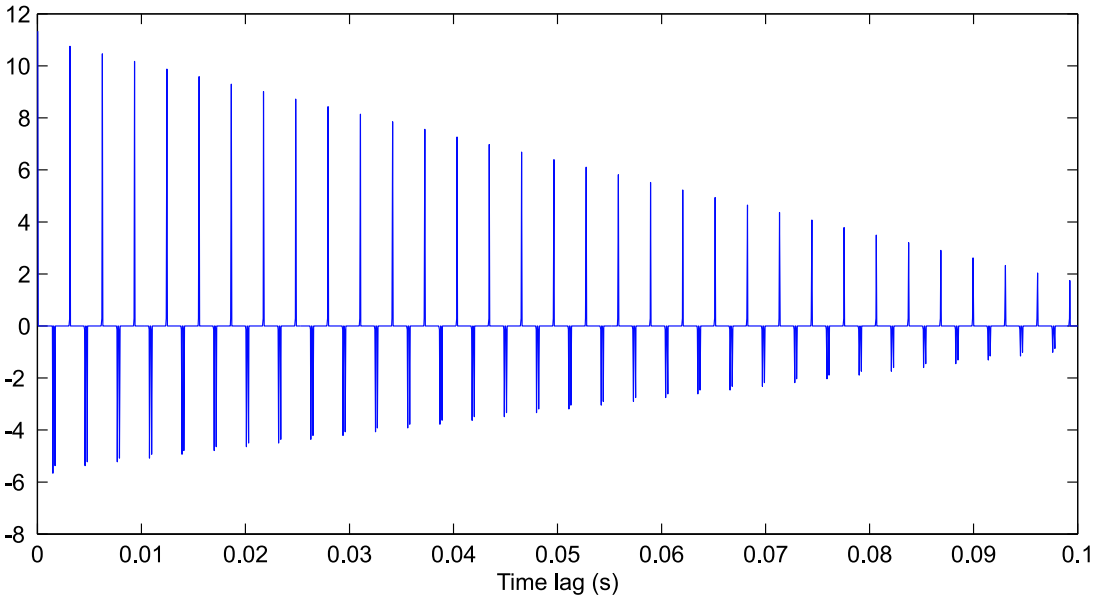

Figure 8.5: Autocorrelation for 39-flow model.

As with the two-flow case, it may be useful to calculate the autocorrelation function of the basalt succession. Figure 8.5 shows the autocorrelation function for the 39-flow model. The first trough is at 1.5ms, which corresponds to a minimum in the frequency response at 160Hz. The first peak is at 3ms which corresponds to a maximum at 80Hz and a minimum at 160Hz. The second trough corresponds to minima at about 54Hz and 160Hz. All of the other peaks and troughs also correspond to multiple delays which would generate a minimum at around 160Hz.

This explains why there is such a strong minimum in the frequency spectrum for this model around 160Hz. It is the combination of all these characteristic time delays in the sequence. Though it is possible to predict the centre of the energy minimum, it is harder to predict the point at which the energy drops to zero (at roughly 120Hz).

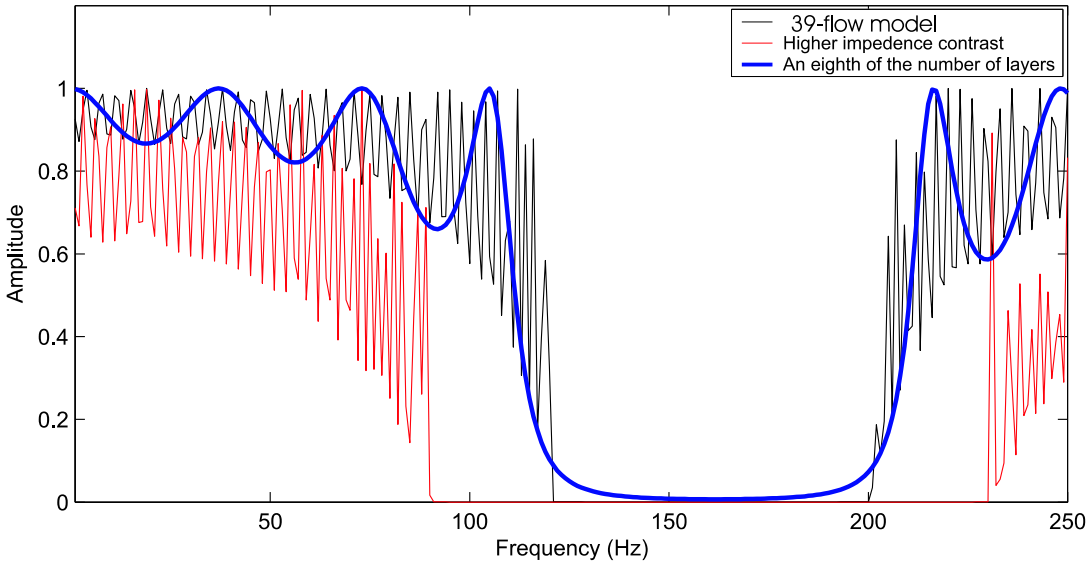

Figure 8.6: Frequency response for original 39-flow model (black), with (blue) fewer layers and (red) higher impedance contrast.

Figure 8.6 shows again the transmission response for the 39-flow model. The line plotted in red over the top is the response for the same model but with the impedance contrast set to be higher than in the original model by increasing the density, but not the velocity in the high-velocity layers. The effect is to widen the band where there is zero energy. Therefore, the impedance contrast between the layers controls the width of the minimum. Reducing the number of layers in the model but keeping the rock properties the same (Figure 8.6, blue line) does not seem to have a large effect on the overall shape of the response. The only difference is a decrease in the number of fine-scale oscillations.

In the next section, more complicated basalt models are considered which contain flows of varying thickness and velocity.

8.4 Multi-layered basalt: reflectivity modelling

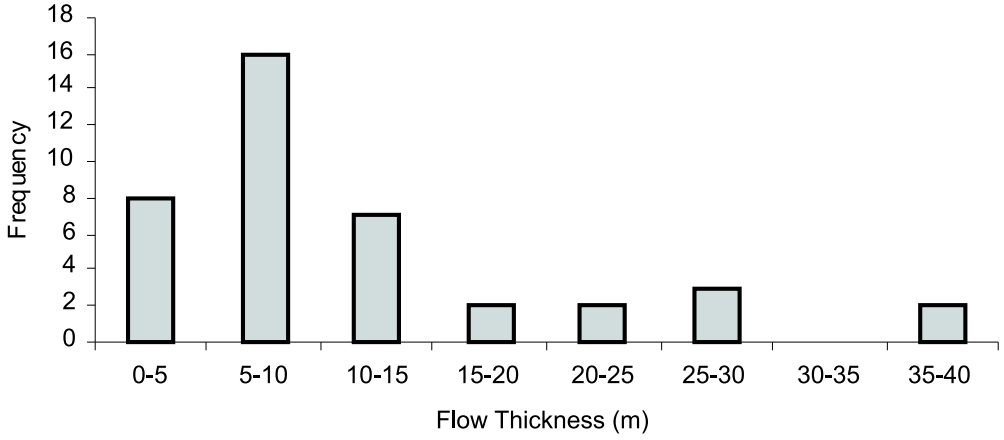

Figure 8.7: Basalt flow-thickness distribution of the upper-series volcanics on the Faeroe Islands (after White et al., 2003).

The basalt models used in this study are all based on the same basalt sequence and source-receiver geometry. The depth to the top of the basalt sequence (4500m), the depth of the sub-basalt interface (6000m) and the maximum receiver offset (12km) are taken from data shot by Veritas DGC in the summer of 2001 (Ziolkowski et al., 2003). The basalt sequence consists of a number of layers which follow the thickness distribution observed in the upper-series volcanics on the Faeroe Islands (White et al., 2003); Figure 8.7 shows this distribution. The total number of flows in each model is 39.

For each model, the precise flow sequence is randomly selected. Each flow is split into three zones (Planke, 1994): an upper chilled margin of 4m, a massive interior of varying thickness, and a lower margin of 1m. The margins are treated as low velocity zones and the interior as a high velocity zone. In cases where an interface is situated between two low velocity zones (e.g. between the lower margin of one flow and the upper margin of the flow below) the interface has been removed to reduce computation time.

P-wave velocities and densities are taken from Planke et al. (1999). S-wave velocities are calculated using a P-wave to S-wave ratio of 1.8 (Planke et al., 1999). A summary of the flow succession characteristics for each model is shown in Table

8.2. Each model was run using the OSIRIS modelling package for flat layers, once with a sub-basalt interface and once without. The purpose of this is to subtract the reflections coming directly from the basalt, leaving only the response from the interface beneath the basalt. The resulting synthetic shot gathers are analysed in the time and frequency domains.

8.5 Description of models

Model	Velocity (margins)	Velocity (interior)	Flow thickness
1	3000m/s	5500m/s	Upper-series distribution (USD)
2	3000m/s	5500m/s	Upper-series distribution
3	2500-3500m/s	5000-6000m/s	Upper-series distribution
4	2500-3500m/s	5000-6000m/s	Flow thickness doubled
5	2500-3500m/s	5000-6000m/s	Margin thickness doubled also
6	2500-3500m/s	5000-6000m/s	USD with number of flows halved

Table 8.2: Parameters used in modelling

Model 1 has flow thicknesses which follow the upper series distribution of Figure 8.4. The order of the flows varies randomly and the precise thickness is random within the flow group (e.g. a flow picked from the 5-10m group would have a random thickness somewhere between 5 and 10m). No flows are less than 1m thick, and all flows with a thickness of 5m or less are considered to consist entirely of low-velocity material. The upper margin has a thickness of 4m for each flow and the lower margin has a thickness of 1m. The velocities are average values found for the high and low velocity zones described by Planke (1994).

Model 2 has exactly the same thickness distribution as Model 1 with a different random seed, meaning the order of the flows and the precise thickness of each flow is different.

In Model 3, not only the thicknesses but also the velocities are varied, corresponding roughly to values found by Planke et al. (1999) (see Table 8.2). Model 4 is the same as Model 3 with flow thickness doubled (but not the thickness of the margins). In Model 5 the thickness of the margins is also doubled. Model 6 is the same as Model 3 with the number of flows halved.

8.6 Results

8.6.1 Models 1 and 2

The 25Hz shot gathers for Model 1 can be seen in Figure 8.8. Figure 8.8(a) shows the shot gather generated with the sub-basalt interface included, Figure 8.8(b) shows the shot gather generated without the sub-basalt interface included. Figure 8.8(c) is obtained by subtracting Figure8.8(b) from Figure 8.8(a), so that only the events from the sub-basalt interface are left on the seismogram. The strongest event from beneath the basalt is the P-wave reflection. The converted-wave arrival can also be observed, though this is less strong. Work on thin-layered basalts has already predicted this result (Hanssen et al., 2003). Therefore, I will concentrate on the P-wave reflection.

Magnified versions of the P-wave sub-basalt reflection for Model 1 at near and far (12km) offsets can be seen in Figure 8.9. Results are shown for input wavelet frequencies of 25, 50 and 70Hz. The amplitude in each case is normalised to the peak amplitude of the direct wave, i.e., the event seen at the nearest offset receiver which has come directly from the source. A coda is visible at both near and far offsets with the far-offset coda lasting almost 1 second after the start of the wavelet. The far-offset wavelet is probably longer and more complicated because of the contribution of short-period converted-wave legs in the travel-path.

Also of importance is the difference in amplitude for each frequency. The low frequencies have been attenuated far less by scattering than the high frequencies. This result agrees with previous work (e.g. Mack, 1997).

Results from Model 2 can be seen in Figure 8.10. At near offsets the length of the wavelet is similar for both plots at all frequencies. The large difference between the two models is in the phase of the wavelet.

At far offsets the difference between Models 1 and 2 is even greater. The coda for Model 2 is of a far higher amplitude than for Model 1. The coda is also longer. The differences at far offsets are due to the contribution of mode conversions which are not present in the near offsets. The amplitudes of the mode conversions go as $\sin\theta$ where θ is the incidence angle. Therefore, the effect of mode conversions become more important as the focus moves from near to far offsets. A second

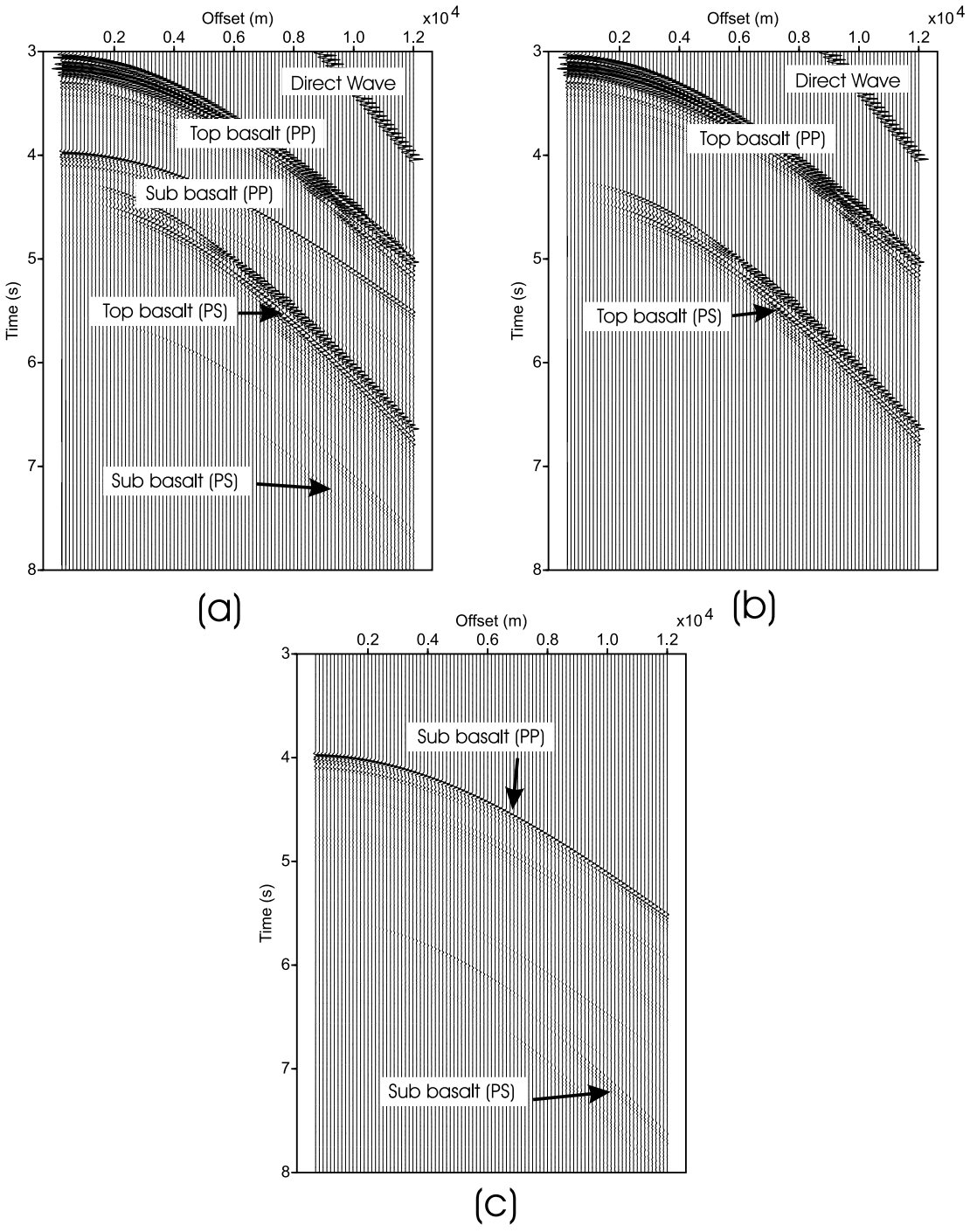

Figure 8.8: Synthetic shot gathers generated from Model 1 with a 25Hz Ricker wavelet: (a) with sub-basalt interface included in model, (b) without sub-basalt interface, (c) = (a) minus (b).

consideration is the tendency for reflection coefficients to increase with incidence angle. From Figure 8.6 it can be seen that a higher reflection coefficient leads to

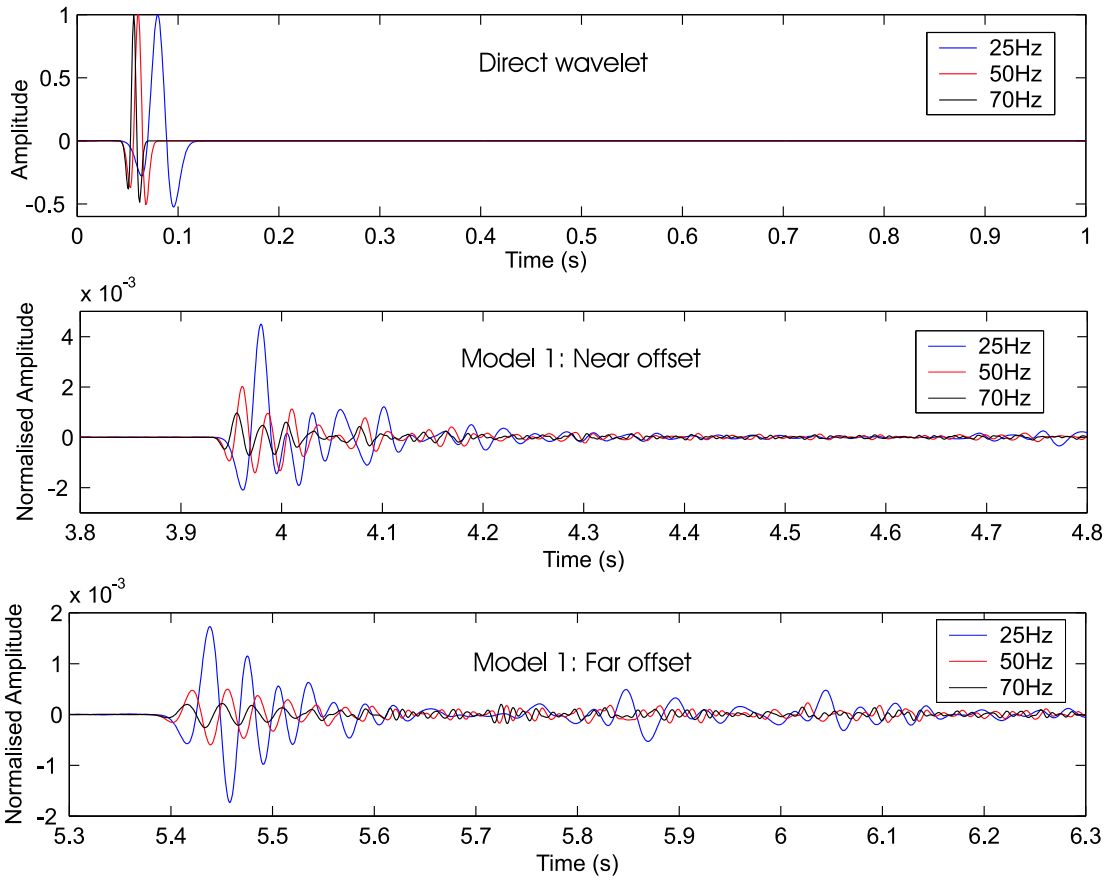

Figure 8.9: P-wave sub-basalt events for Model 1 showing: direct wave (top), near-offset sub-basalt reflection (middle), and far-offset sub-basalt reflection (bottom).

more scattering.

I now turn to the frequency domain to continue the analysis. Near- and far-offset traces were computed using an impulse wavelet of constant amplitude between almost D.C. and 250Hz. Traces were subtracted, as in the time domain modelling, to leave only the events coming from beneath the basalt. A window was placed around the P-wave sub-basalt reflection event and all values outside the window set to zero. The windowed trace was then transformed into the frequency domain using a fast Fourier transform. .

The near-offset frequency domain response for Model 1 is shown in Figure 8.11 along with the response for the same model computed for a plane-wave source (computed using the Treitel and Robinson method). Note that the frequency

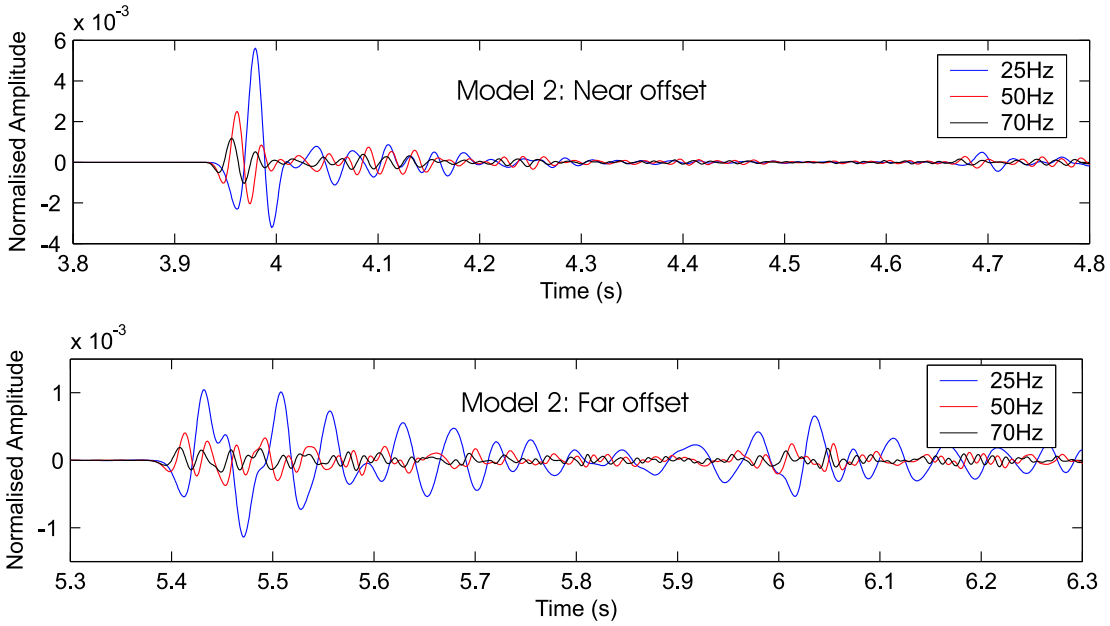

Figure 8.10: P-wave sub-basalt events for Model 2, showing (top) near-offset sub-basalt reflection and (bottom) far-offset sub-basalt reflection.

domain response computed with a point source closely agrees with the response for a plane-wave source.

Very little energy has been allowed to pass through the succession above a frequency of about 60Hz. One of the features of this near-offset response is the sudden drop-off in energy. Even for the simple 39-flow case shown in the previous section it is difficult to give a general rule for the frequency at which this happens, but it is determined by the two-way times through the layers and the impedance contrast between them.

The near-offset frequency response for Model 2 is shown in Figure 8.12. The frequency responses for Models 1 and 2 are quite similar in general appearance. Only the exact positions of the maxima and minima have changed. The most apparent difference is the peak which is present in Model 1 at around 140Hz, but not present in Model 2. It may be possible to explain this difference by looking again at the expected minimum frequencies for each layer and the autocorrelation for the basalt succession.

Figure 8.13 shows bar charts for expected minimum frequencies for every layer in the Model 1 and Model 2 successions, calculated from Equation 8.7. There is

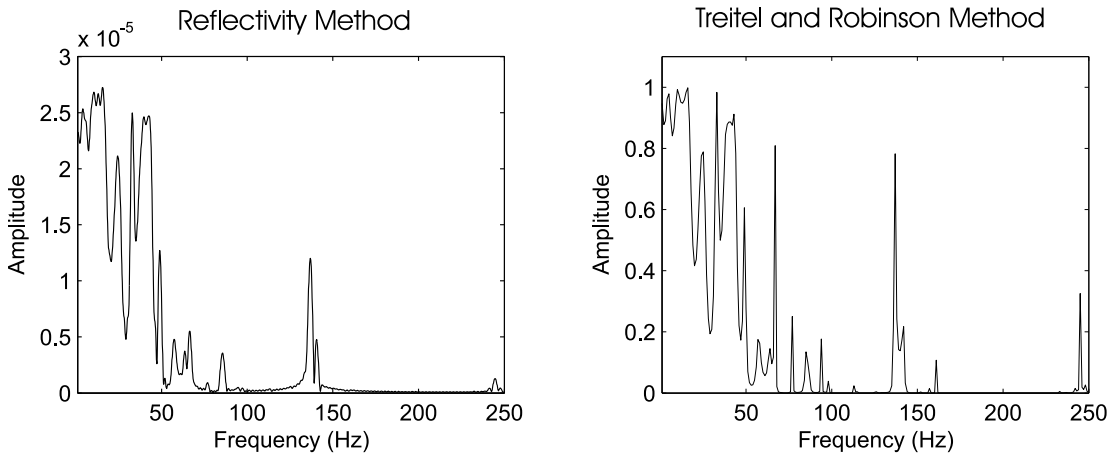

Figure 8.11: Near-offset frequency response for Model 1 using (left) reflectivity method with a point source and (right) Treitel and Robinson method with a plane-wave source.

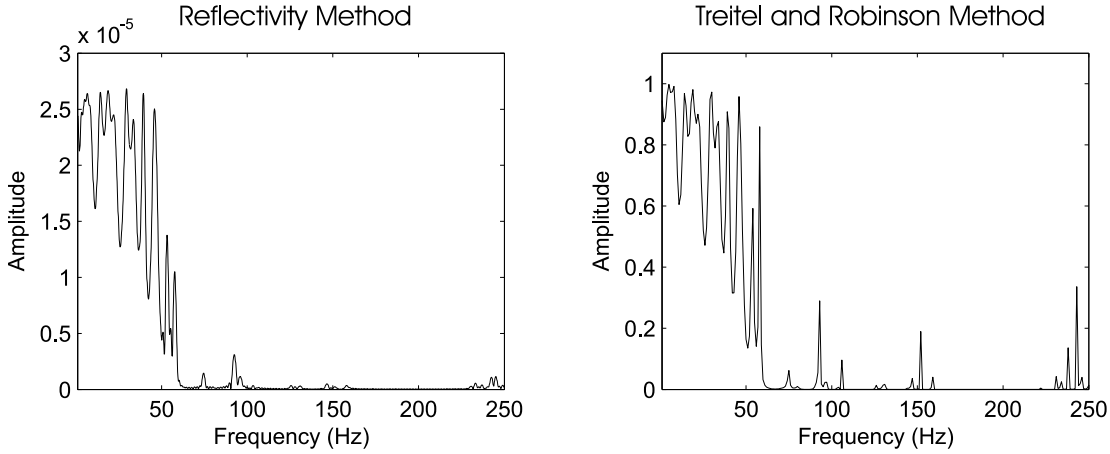

Figure 8.12: Near-offset frequency response for Model 2 using (left) reflectivity method with a point source and (right) Treitel and Robinson method with a plane-wave source.

very little difference between the two charts. The layers are of similar thicknesses, it is only the order of the layers which has changed. There are many thin layers which would generate a minimum at frequencies over 250Hz. These layers should not affect the response at lower frequencies.

The largest cluster is around 150Hz, these layers correspond to the margins of the flows which are all 5m thick, and of the same velocity and density. This implies a minimum in energy around 150Hz, which looks possible for Model 2, but is clearly not the case for Model 1. Note from Equations 8.7 and 8.8 that the expected maximum frequencies can be obtained simply by doubling the minimum frequencies. Therefore, the cluster around the 70Hz mark relates to a maximum

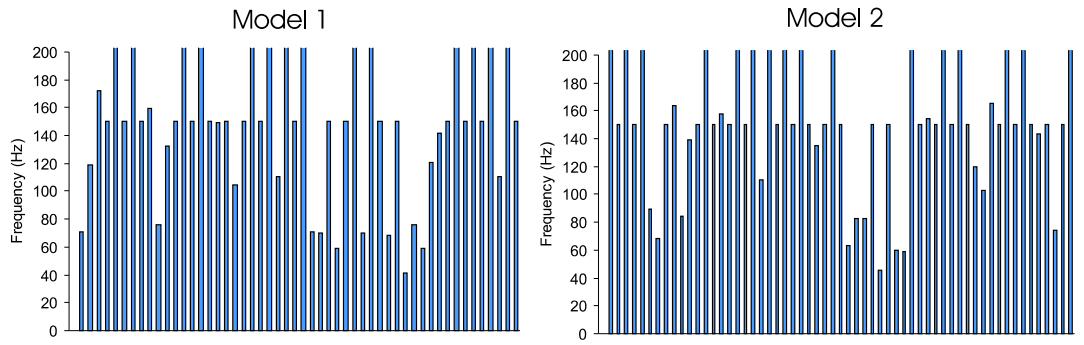

Figure 8.13: Characteristic frequency values where minimum energy may be expected for Models 1 and 2.

at 140Hz. This may provide the explanation why a maximum is present at 140Hz. Because there are a number of layers with this characteristic frequency, an energy window may be present in the succession which allows high frequencies to pass through. There is, though, still no clear explanation as to why this window may exist in the Model 1 succession but not in Model 2.

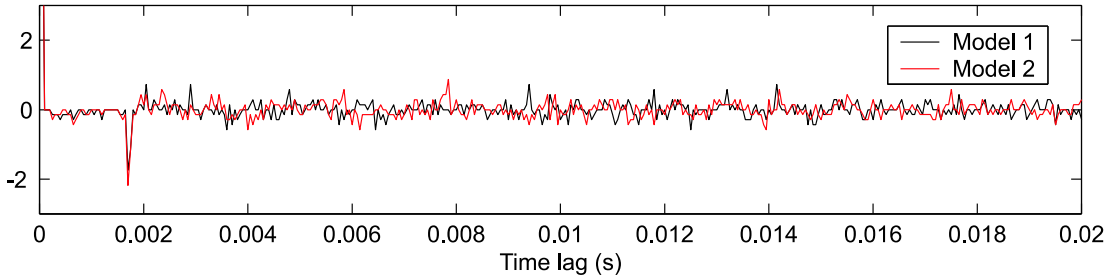

Figure 8.14: Autocorrelation function for Models 1 and 2

I look next at the autocorrelation function of the two models to see if this helps to explain the difference between the two models (Figure 8.14). There is a clear trough at 1.8ms for both models, which corresponds to a minimum at a frequency of 140Hz. The peak is due to the large numbers of layers representing the margins of the flows. There are no other large peaks in the autocorrelation function, and certainly no large differences between the two models, which could explain the presence of a peak in one frequency response but not the other. The conclusion must be that the processes involved in such a complicated structure can not so easily be interpreted.

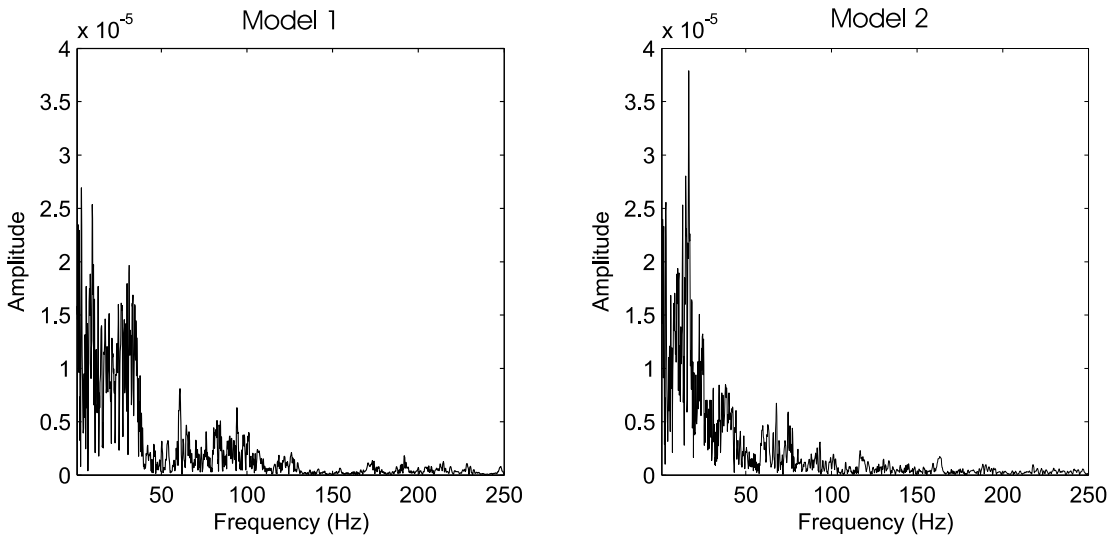

Figure 8.15: Far-offset frequency response from sub-basalt reflection for Models 1 and 2 computed with reflectivity method.

In the far-offset case, the spectrum can more confidently be described as low pass. Both models display an almost exponential decrease in amplitude with frequency. As in the near-offset case, very little energy is allowed to pass through over 60Hz. Considering the complexity of far-offset traces, it would be particularly difficult to link this spectrum to the physical properties of the stacked succession.

8.6.2 Models 3,4, 5 and 6

In these models the velocity is made random within certain realistic limits for high and low-velocity zones within each flow (Table 8.2). These are, therefore, slightly more realistic compared with the earlier models since velocities tend to vary from flow to flow in reality. Model 3 is exactly the same as Model 2 in terms of flow order and thickness; the difference is the addition of a random factor to the velocity of each layer. In the time domain at near-offset (Figure 8.16), the wavelet looks almost exactly the same as Model 2 with only slight differences in the coda.

At far offset the wavelet seems to have many differences compared with Model 2. The peak amplitude of the wavelet is almost doubled and there is less energy in the coda. The reason for this lies in the complexity of the far-offset raypaths. Converted wave modes are more important at far-offsets and are more sensitive

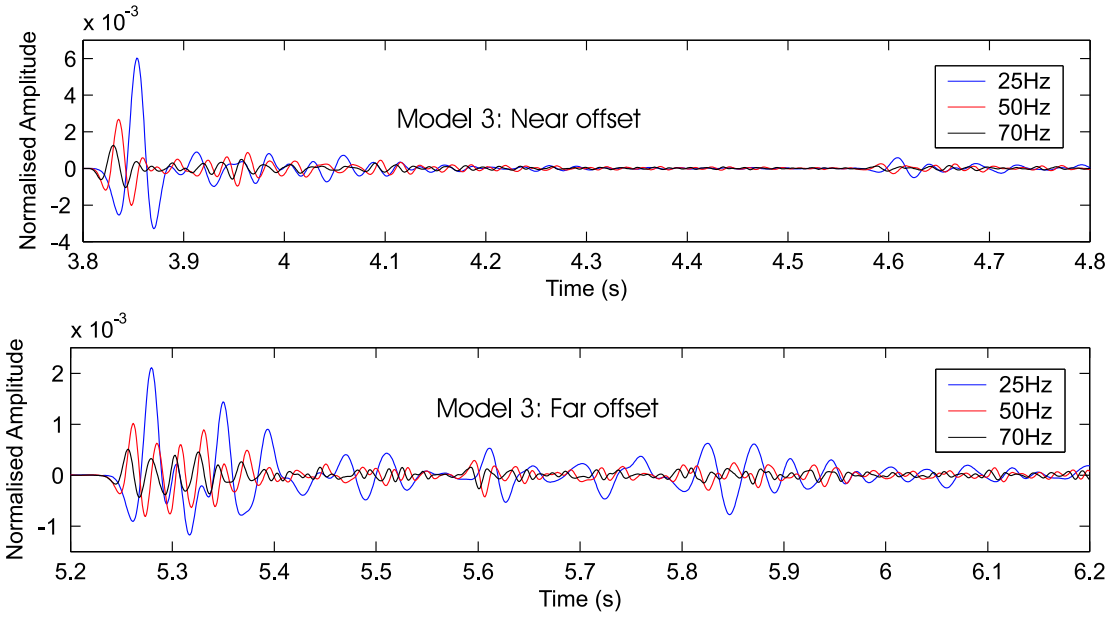

Figure 8.16: Sub-basalt reflection events for Model 3 at near and far offset.

to small changes in velocity. In the frequency domain at near offsets there is

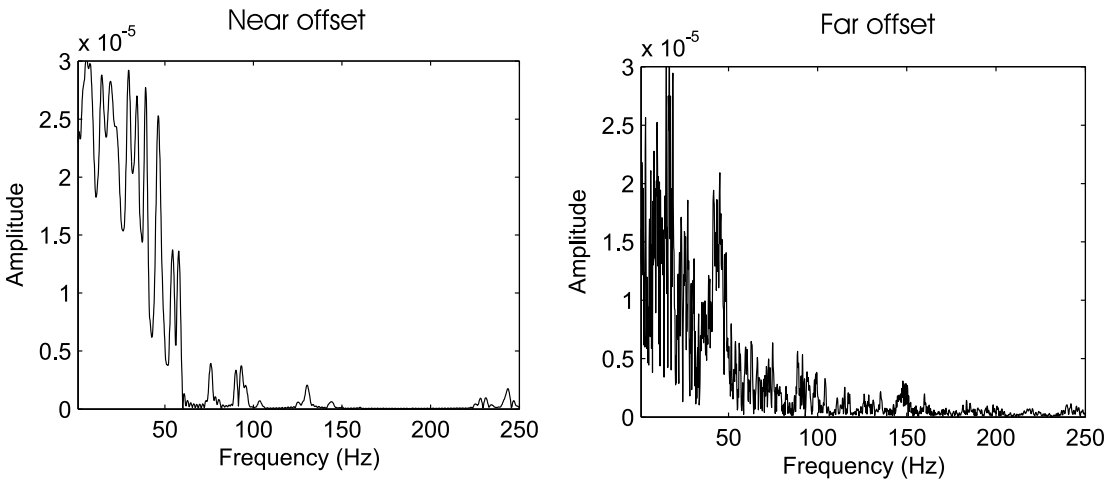

Figure 8.17: Near and far-offset frequency response from sub-basalt reflection for Model 3 using reflectivity method.

almost no difference between Model 2 and Model 3 (Figure 8.17). At far offsets the general shape of the frequency response is the same though there are some differences such as the peak just below 50Hz.

The thickness of the flows is now doubled, but not the thickness of the margins (Model 4). The wavelet from this model appears to have a much lower frequency

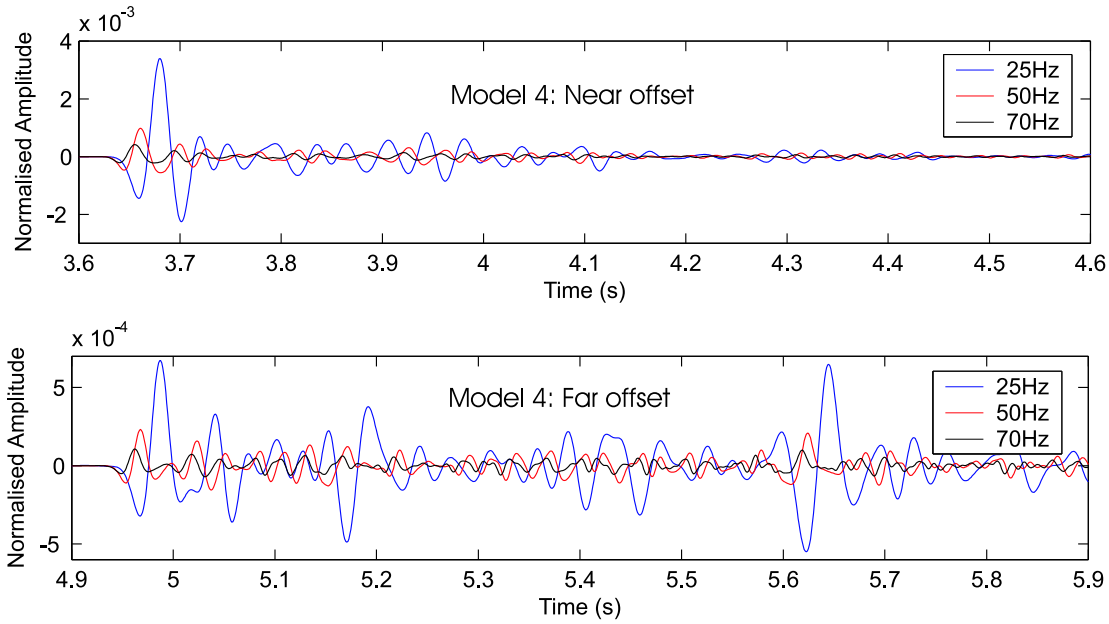

Figure 8.18: Sub-basalt reflection events for Model 4 at near and far offset.

content (Figure 8.18). Wavelets of all frequencies are attenuated more by this model than either Model 3 or Model 2, and the coda is longer. The lower frequency content is also apparent at far-offsets. The frequency response clearly shows a shift to lower frequencies at near and far offsets (Figure 8.19). There is no evidence of higher frequencies passing through the succession.

When the thickness of the flow margins is also doubled (Model 5) the attenuation of the high frequencies is even more apparent (Figure 8.20). This applies to near and far offsets. The effect of doubling the flow margins is that the cluster layers which have a similar thickness and velocity have now got a characteristic energy minimum at around 80Hz (Figure 8.22). Therefore, a maximum is expected at around 160Hz.

In the near-offset frequency response (Figure 8.21), there is indeed a large amount of energy passing through the succession between about 140Hz and 200Hz, lending weight to the idea that large numbers of layers of a similar thickness can allow a certain amount of high-frequency energy through. In most cases the earth tends to be more random than this, so high-frequency energy in the response is unlikely. Also, the addition of intrinsic attenuation in the model is likely to remove this energy. This figure also allows a check of the accuracy of the modelling. In

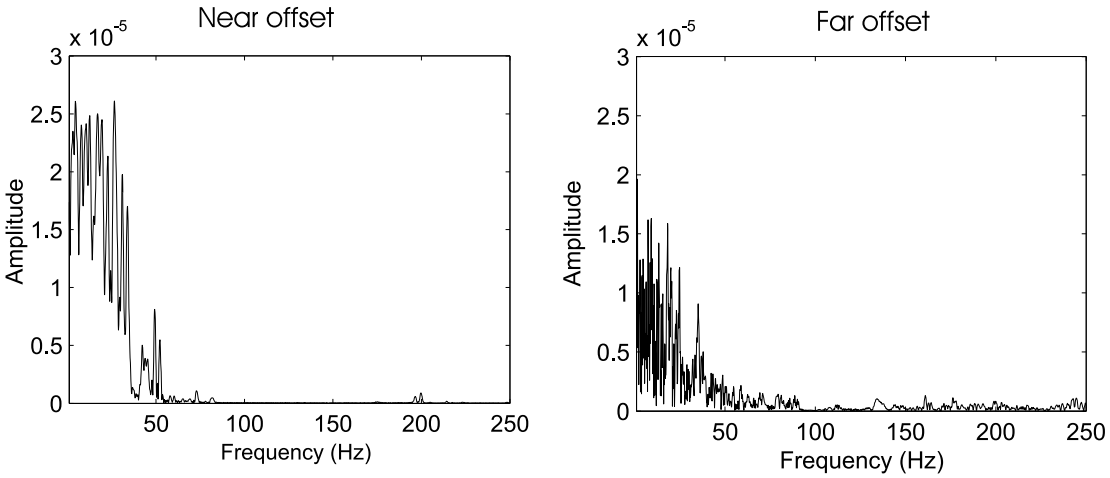

Figure 8.19: Near and far-offset frequency response from sub-basalt reflection for Model 4 using reflectivity method.

theory, the frequency response of Model 5 should be the same as that of Model 3 with all the frequencies halved. A quick inspection reveals that this is the case.

The far-offset response shows no energy peak at higher frequencies. This is again due to the complex nature of the far-offset arrivals, which are far more likely to interfere destructively at high frequencies than at low frequencies. Thus, the familiar exponential drop-off with frequency is observed.

Model 6 contains flows with roughly the same flow distribution as the other models, but comprises only 19 flows instead of 39. The result is that some high frequency is able to pass through this succession which could not pass through the previous models . Comparing Model 3 with Model 6 in the frequency domain at near offsets shows that the point where the initial drop off in energy occurs does not change drastically. The difference comes in the higher frequencies where there are several peaks due to constructive interference of certain multiples. These peaks can not really be linked directly to the thickness of layers in the basalt flows. They are a complicated combination of multiples about which it is hard to make general comments, though it is clear that the more layers there are, the more the high frequency energy gets attenuated.

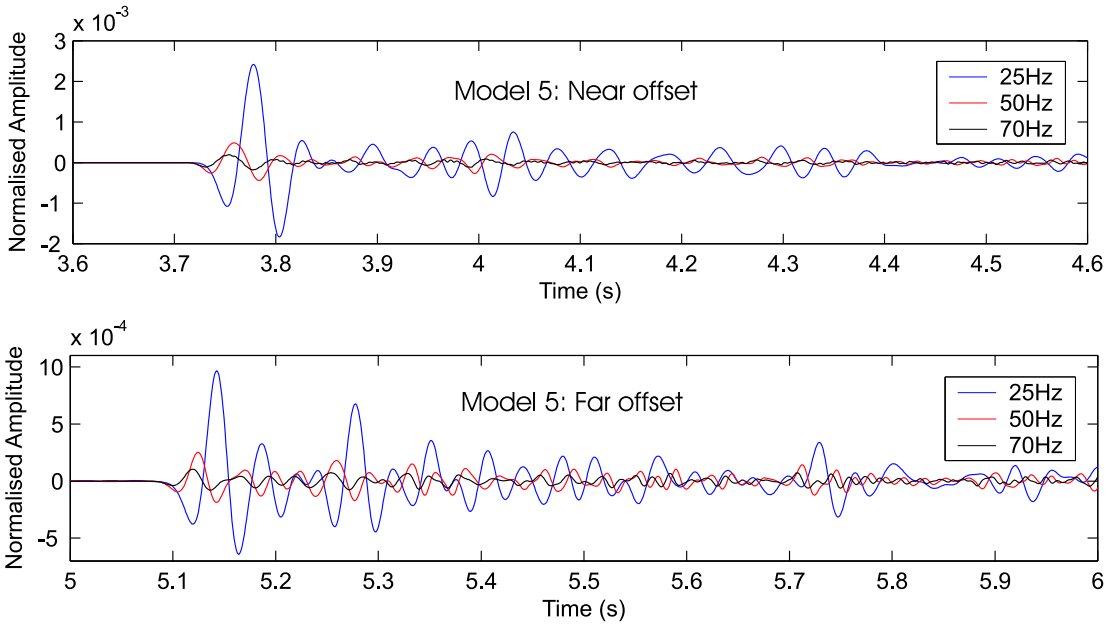

Figure 8.20: Sub-basalt reflection events for Model 5 at near and far offset.

8.7 Conclusions

The characteristics of a stacked succession of basalt layers are linked in a complex way to the seismic response of a seismic wave passing through it. Some basic conclusions can be made about the link between the seismic response and the thickness, density and velocity of the layers.

As has been already concluded by previous papers, a succession of basalt layers will let more low-frequency energy through than high-frequency energy. Although the forward problem is well understood, the interpretation of interference effects is still very difficult. Thicker layers tend to affect lower frequencies and thinner layers affect higher frequencies. This is because the first minimum in the frequency spectrum occurs when there is a delay of half a wavelength with one raypath relative to another.

The implication for this for seismic data acquisition is that low-frequency sources are needed to penetrate such a succession of basalt flows. The scattering in the layers means that this is the only way that poor transmission through the basalt can be overcome. This holds for both far offsets and for near offsets.

At near offsets, the response generally has quite a sharp cut-off at a characteristic frequency. It is hard to determine where this cut-off occurs. The exact

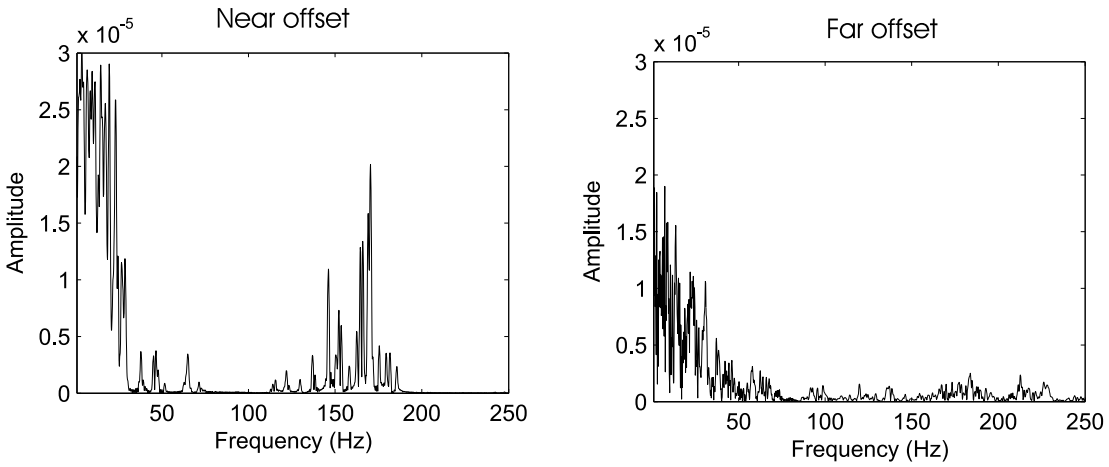

Figure 8.21: Near and far-offset frequency response from sub-basalt reflection for Model 5 using reflectivity method.

position depends on the thickness of the layers and the impedance contrast. When the number of layers is reduced, there is a greater chance of energy above the cut-off point, though the peaks do not correspond in a simple way to the thickness and velocity of the layers.

At far offsets the response generally has an exponential decrease in energy with frequency. It has not been possible to find the exact nature of this energy drop-off or find a way to link this to the characteristics of the basalt succession.

A large number of layers which have a particular thickness and velocity can allow windows where high-frequency energy passes through. In most cases in the Earth's crust, there is unlikely to be such an exact periodic succession, though many regular basalt flows may cause such a response. Where this happens, it may be possible to predict the thickness of the layers from the position of the energy peak. Where layers are more random, these windows tend not to occur. In these situations the filtering effect can be described fairly accurately as low-pass.

For seismic data processing, near-offset traces generally provide a larger amplitude wavelet with a shorter coda. Interference effects in the coda at far offsets might make imaging difficult, but may also lend themselves to deconvolution processes under certain circumstances.

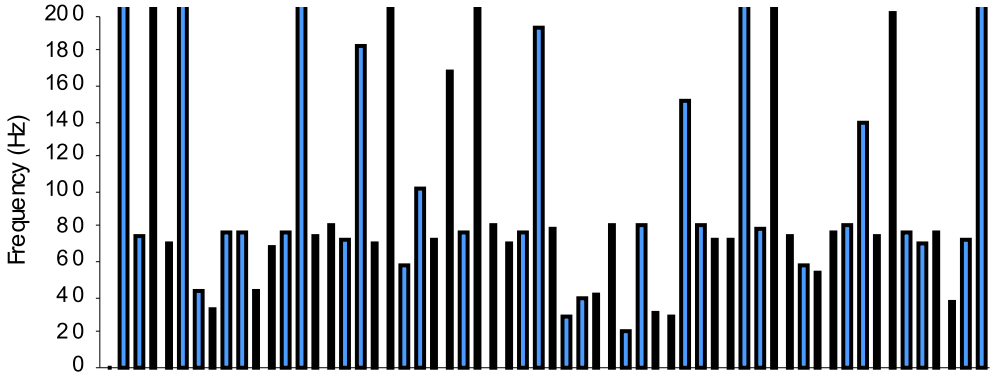

Figure 8.22: Characteristic frequency values where minimum energy may be expected for Model 5.

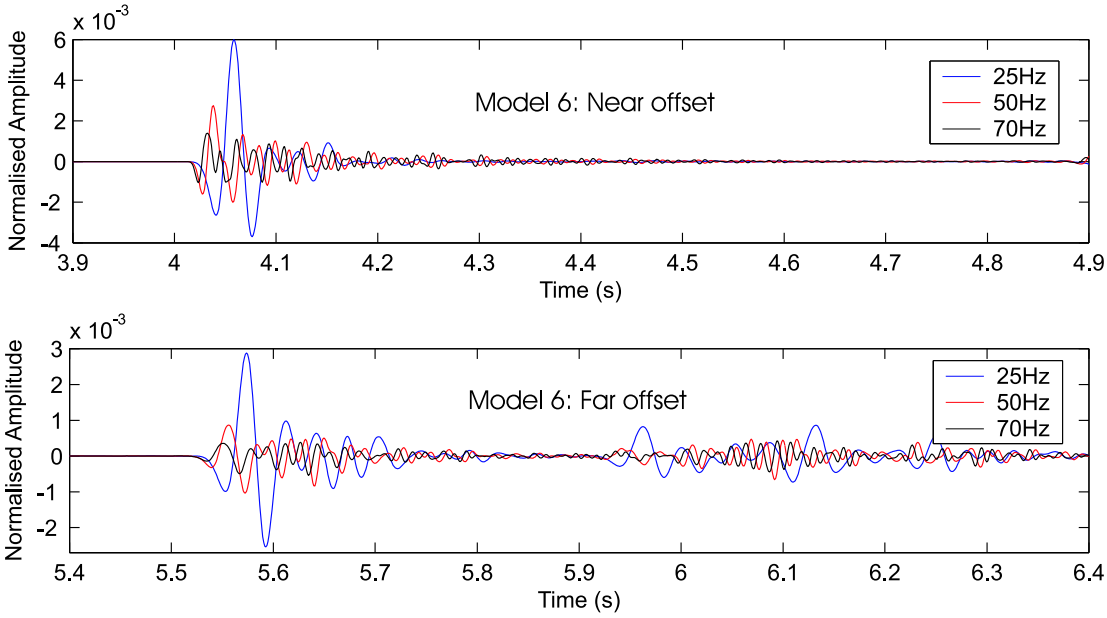

Figure 8.23: Sub-basalt reflection events for Model 6 at near and far offset.

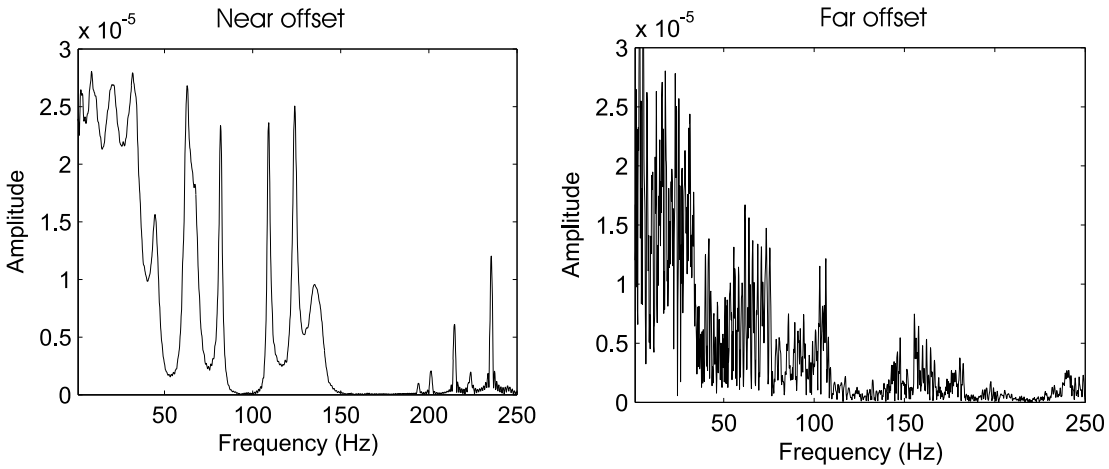

Figure 8.24: Near and far-offset frequency response from sub-basalt reflection for Model 6 using reflectivity method.

Chapter 9

Real-data analysis and modelling

9.1 Introduction

In this chapter I perform forward modelling on an earth model derived from real seismic data.

The seismic data were acquired in the Faeroe-Shetland Channel in 2001 and were processed by Veritas DGC. The final stacked section in time was interpreted within the British Geological Survey, and converted to depth using velocities from 28 wells in the area.

I use the depth model as an input for forward modelling with the boundary element method to assess the relative importance of 1) regional geology 2) high impedance contrast and 3) roughness of the top basalt interface when imaging beneath basalt. I also discuss how well the synthetic model relates to the real geology.

9.2 Data acquisition

The seismic data were acquired in 2001 by Veritas DGC over Tertiary basalts (Figure 9.1) with the purpose, in part, of looking for possible hydrocarbon-bearing sequences beneath the basalt flows (Ziolkowski et al., 2003). The acquisition parameters were designed to enhance the low frequencies following several studies showing that this approach represented the best chance for imaging beneath the basalt (Mack, 1997).

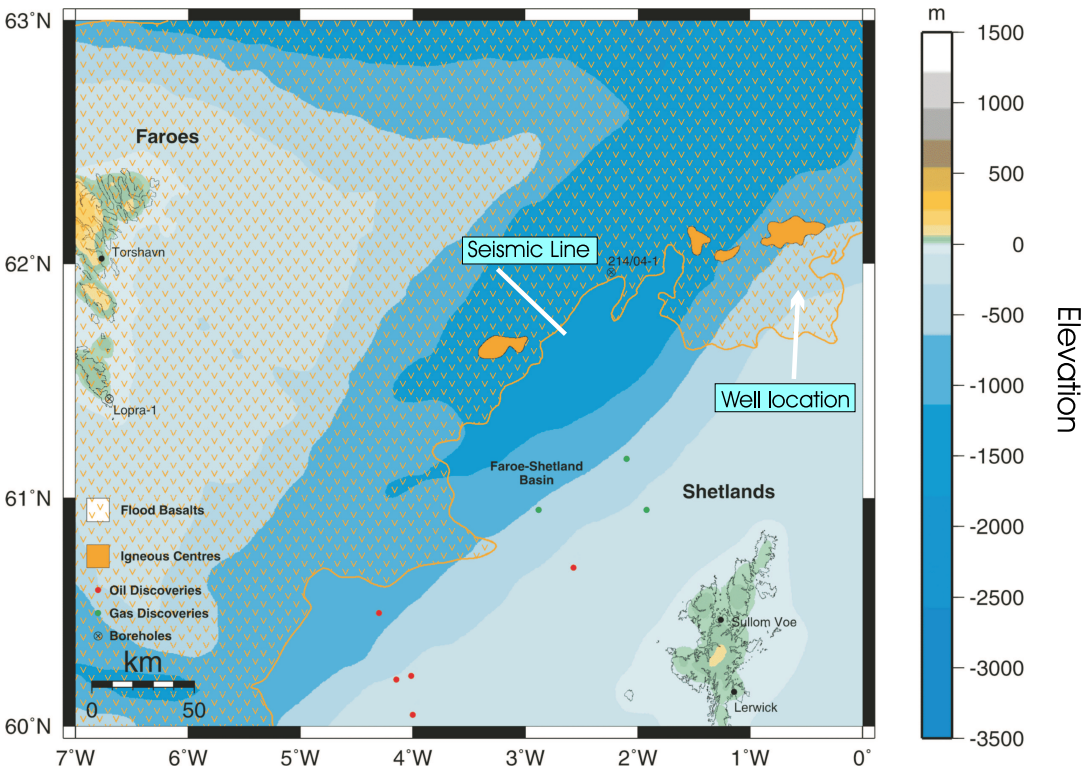

Figure 9.1: Map showing the location of the seismic profile. Also shown is the extent of the flood basalts in the area (after Hanssen, 2004).

In order to enhance the low frequencies in a marine seismic survey, two important issues were considered 1) the depth at which the airguns and hydrophones should be towed and 2) the volumes of the airguns.

9.2.1 Source and receiver depth

The system response is optimised for a given bandwidth and a single monopole source and receiver by putting the source and receiver at the same depth (Ziolkowski et al., 2003). The combined response is

$$R_c(\omega) = 4\sin^2(\omega D\cos\theta/\alpha_w), \tag{9.1}$$

where ω is the angular frequency of the source, D is the depth of the source and receiver, and α_w is the velocity of sound in water. At normal incidence, $\theta = 0$ and the response is greater than unity over the bandwidth $\pi\alpha_w/(6D) < \omega < 5\pi\alpha_w/(6D)$. For a depth of 5m (a depth commonly used in conventional seismic

reflection surveying) and a velocity of sound in water of 1500m/s, the amplitude of the response is boosted in the frequency range 30-120Hz. The deeper the source and receiver are towed, the more the boosted frequency range is shifted towards the low frequencies.

For the low-frequency survey conducted in the Faeroe-Shetland Channel , the source and the streamer were towed at a depth of 15m, corresponding to a boosted frequency range of 10-40Hz. To have towed even deeper would have improved performance further, though this would cause problems taking into account the airgun volume considerations outlined below.

9.2.2 Airgun volume

The bubble oscillation period from an airgun is given approximately by the modified Rayleigh-Willis formula

$$T = k\frac{P^{1/3}V^{1/3}}{(P_{atm} + \rho g D)^{5/6}}, \tag{9.2}$$

where P is the gun pressure, V is the gun volume, P_{atm} is atmospheric pressure, ρ is the density of water, g is gravitational acceleration, D is the depth of the gun and k is a constant. The units of these quantities must be consistant with each other, but the unit system can change to suit the user as long as the constant k is given the correct units. The equation is usually used to find ratios between two periods, so the constant k cancels out. When the airguns are towed at a greater depth, the bubble oscillation period decreases and, therefore, the frequency of the source increases. Airguns already operate close to maximum pressure so the only action which can be taken to lower the frequency of the bubble oscillation is to increase the volume of the airguns.

For the survey over the Faeroe Shetland Channel, two 33 litre (2000 cu. in.) airguns were added to the standard array. These are large guns compared with a standard array which consists of airguns usually no larger than 7.5 litres (465 cu. in.).

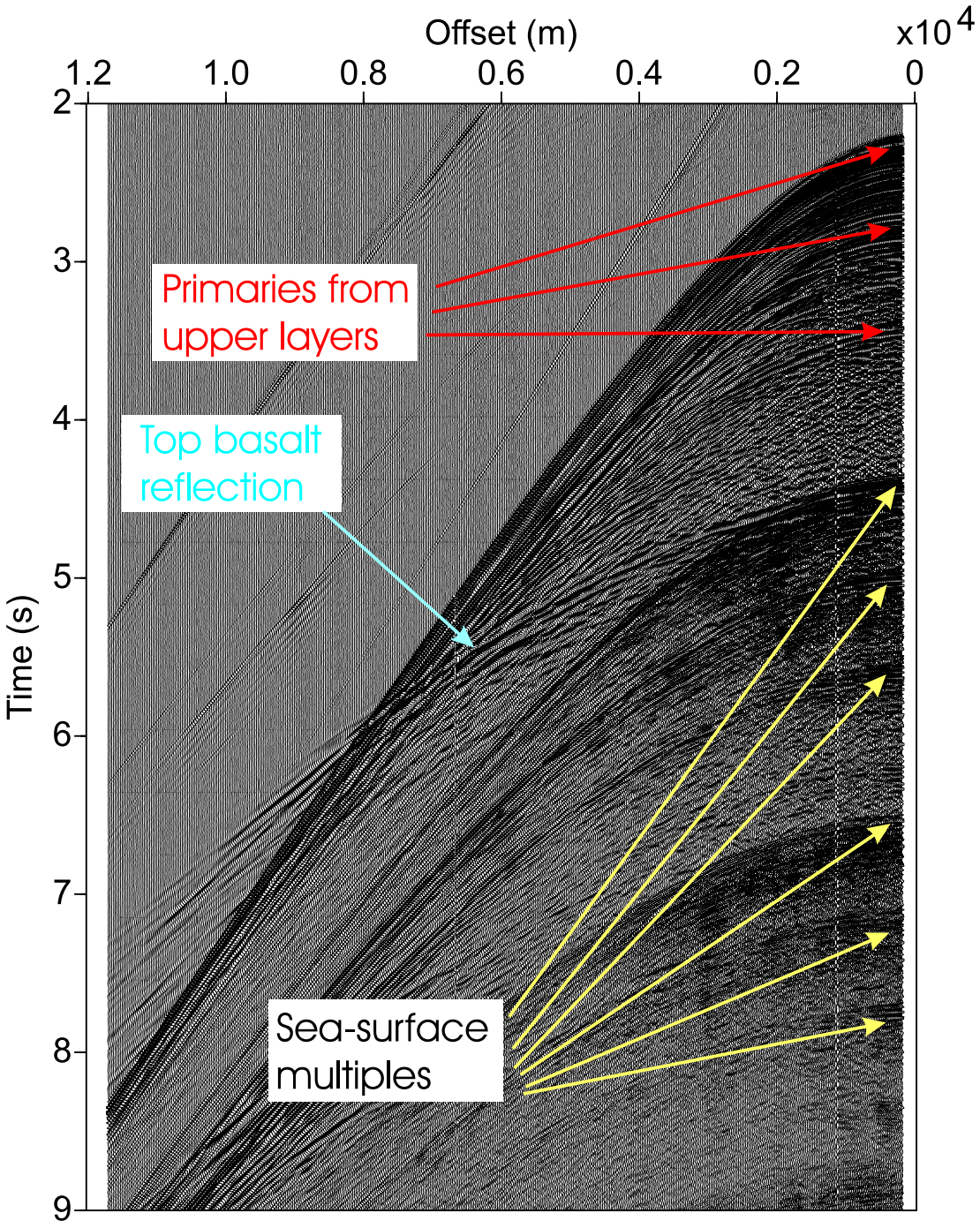

Figure 9.2: Example shot gather from seismic line. The energy seen at 6km and 2 seconds is due to a single airgun fired several seconds before the main array. This energy is used to recover the source signature of the main array.

9.2.3 Example shot gather

Figure 9.2 shows part of an example shot gather from the seismic line. This shot gather was selected because it is near the middle of the seismic line where some

sub-basalt energy was observed on the final stacked section. The hydrophone streamer consisted of 936 channels with a group length of 12.5m, and shots were fired every 37.5m. The maximum offset was approximately 12km.

Several of the more prominent features have been labelled. The top-basalt event can be seen at around 4.5s on the near-offset traces. This interface is easy to see because of the high impedance contrast between the basalt and the sediment above. The frequency of the top-basalt event is clearly much lower than that of the earlier reflections, indicating considerable attenuation from the layers above. The upper layers range from Pliocene to early Eocene in age (McInroy et al., 2004) and consist of many high amplitude reflectors. The packet of high-frequency events at 4.5 seconds and again at 6.5 seconds are sea-surface multiples. Note the coincidence of the top-basalt reflection and the start of the first packet of multiple energy. The multiples make it difficult to observe any energy coming from beneath the basalt. At far offsets, refracted arrivals are observed, though without further analysis and modelling it is difficult to say whether they represent sub-basalt energy or not.

9.3 Data processing and model building

The data were processed by Veritas DGC using standard techniques including dip-moveout and pre-stack time migration (Hanssen, 2004). The processed stacked section can be seen in Figure 9.3. The top-basalt reflector is clear and there are some hints of the base-basalt interface. The other major event is the result of a chemical transition into a rock type known as porcellanite.

The section was interpreted by Derek Ritchie of the British Geological Survey (BGS) based on regional seismic mapping (McInroy et al., 2004). He split the section into stratigraphic units, which were defined in terms of the stratigraphic horizons shown in Figure 9.4. A summary of these stratigraphic units, along with their physical properties, is shown in Table 9.1.

The physical properties for these units were derived from depth/velocity/density cross-plots which were constructed from 28 UK and Irish wells along the north-east Atlantic margin (Figures 9.5 and 9.6). The final values of velocity and density were found by David McInroy of the BGS via an iterative procedure using the

cross-plots and two-way traveltimes from the interpreted section (McInroy et al., 2004).

Alexander Henderson of the BGS used the final P-wave velocities of each unit to convert the horizon times into depths by conducting a simple vertical 'layer-cake' depth conversion down to the top-basalt interface.

The resulting model can be seen in Figure 9.7. The velocity of the basalt layers was taken from a well in the Erland igneous complex (Figure 9.1). The Lower Cretaceous, Jurassic and Permo-Triassic, and Lewisian crystalline basement units were not imaged on the seismic profile. Their presence is inferred from the results of published regional seismic-based and potential field modelling studies (e.g. Mudge and Rashid, 1987; Kimbell et al., 2004).

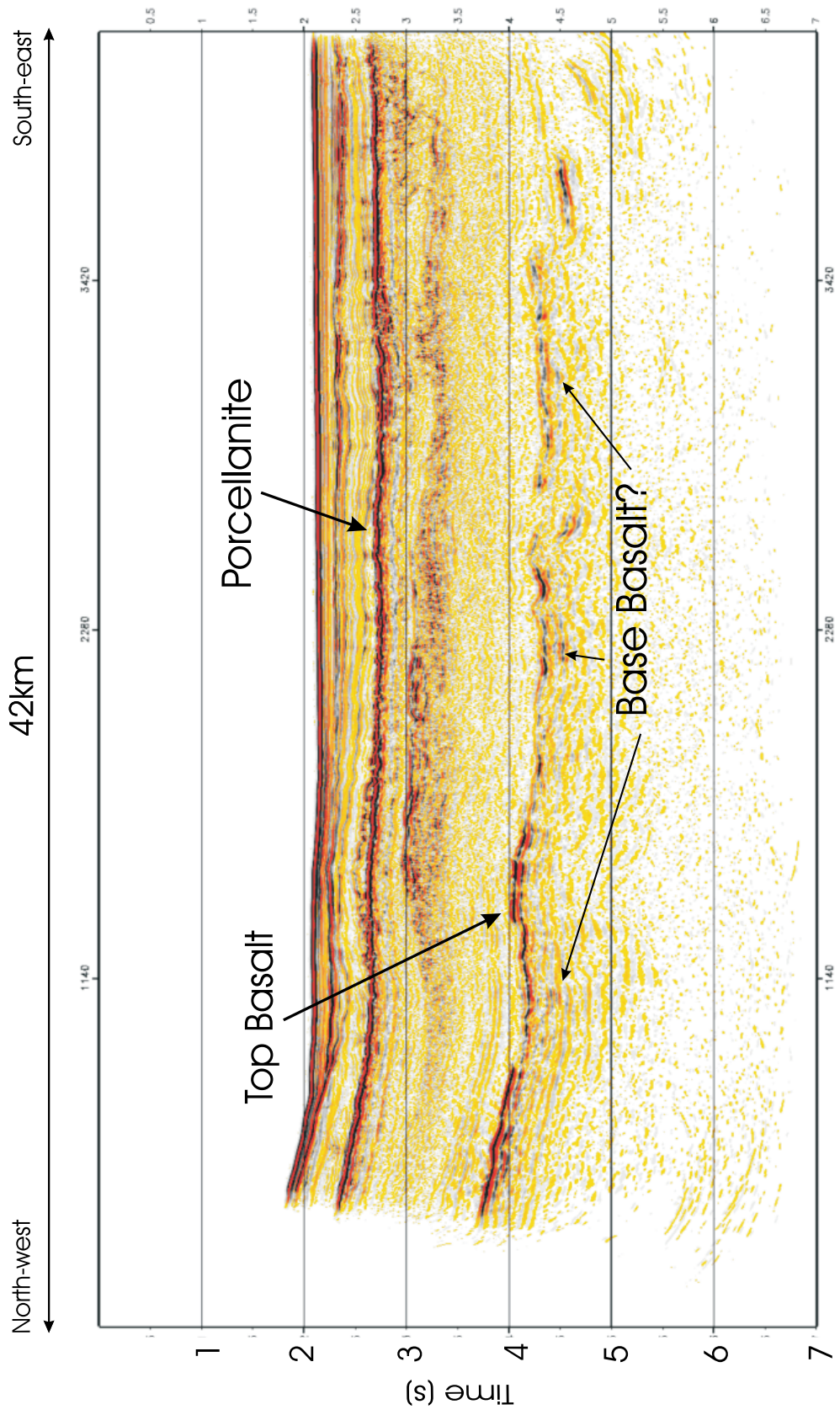

Figure 9.3: Seismic line after processing.

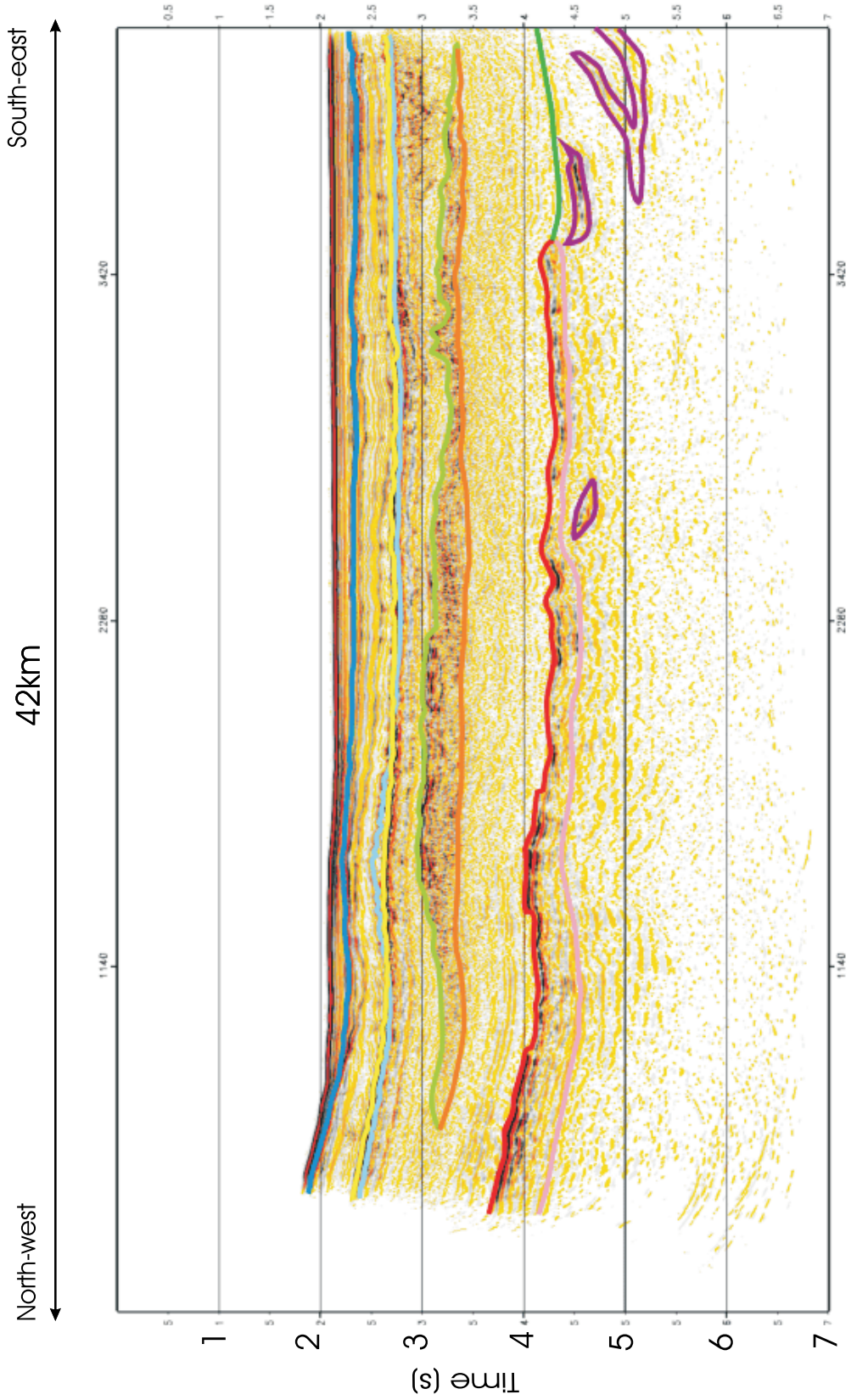

Figure 9.4: Interpreted seismic section. See Table 9.1 for colour code to horizons (after McInroy et al., 2004).

Age of stratigraphic succession	Definition	P-wave velocity(m/s)	Density (kg/m^3)
Seawater	Interval between the sea surface and sea bed	1480	1000
Pliocene	Interval between the sea bed and Intra Neogene Unconformity (dark blue).	2000	1900
Miocene	Interval between the Intra Neogene Unconformity (dark blue) and Top Palaeocene Unconformity (pale blue).	2100	2000
Late Eocene-Oligocene	Interval between the Top Palaeocene Unconformity (pale blue and Top Mid-Late Eocene (pale green) event.	2400	2150
Mid-Late Eocene	Interval between the Upper (pale green) and Lower (orange) Intra-Eocene events.	2600	2250
Early Eocene	Interval between the Lower Intra-Eocene event (orange) and the Top Palaeogene lavas (red) event.	3300	2450
Palaeogene lavas	Interval between the Top Palaeogene lavas (red) and Base Palaeogene lavas (pink) events.	3864	2450
		3864	2490
		4098	2490
		3980	2480
Upper Cretaceous	Interval between the Base Palaeogene lavas (pink)/ Top Upper Cretaceous (dark green) and an inferred Top Lower Cretaceous.	4300	2650
Lower Cretaceous	Inferred from regional seismic-based and potential field modelling publications.	5000	2750
Jurassic and Permo-Triassic	Inferred from regional seismic-based and potential field modelling publications.	5000	2750
Lewisian crystalline basement	Inferred from regional seismic-based and potential field modelling publications.	5900	2800

Table 9.1: Definition of stratigraphic intervals and associated physical properties for the seismic profile. Physical properties and densities for the Palaeogene lavas were derived from the well marked on Figure 9.1.

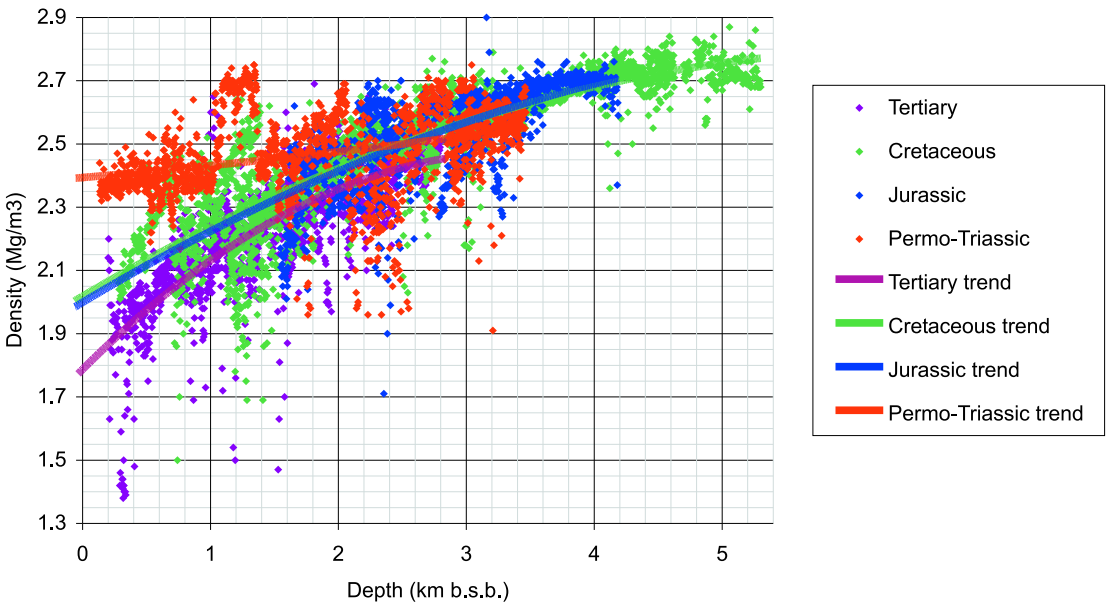

Figure 9.5: Plot of density against depth, derived from well data (from McInroy et al., 2004). Depth is in kilometres below sea bed (b.s.b.)

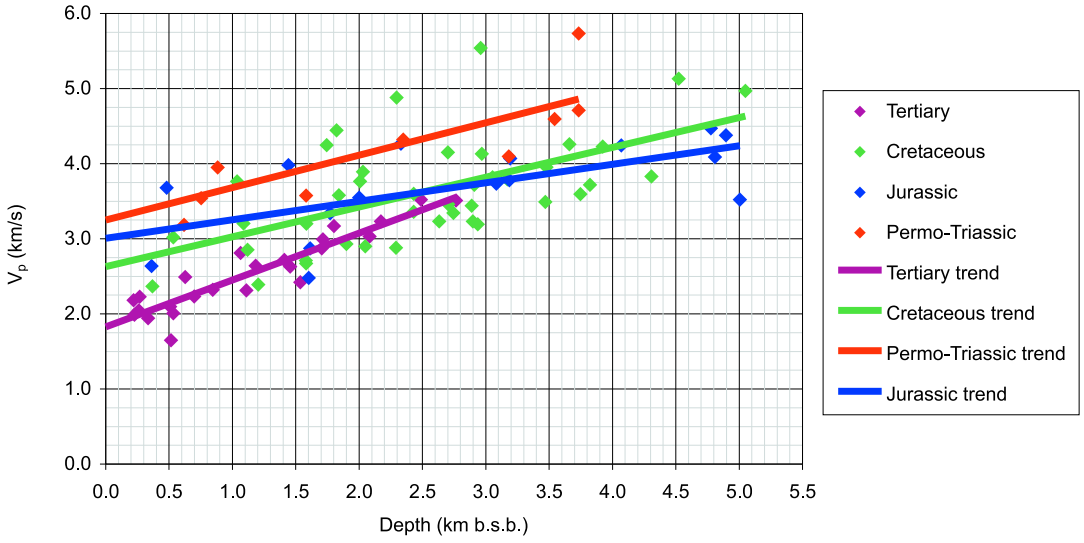

Figure 9.6: Plot of velocity against depth, derived from well data (from McInroy et al., 2004). Depth is in kilometres below sea bed (b.s.b.).

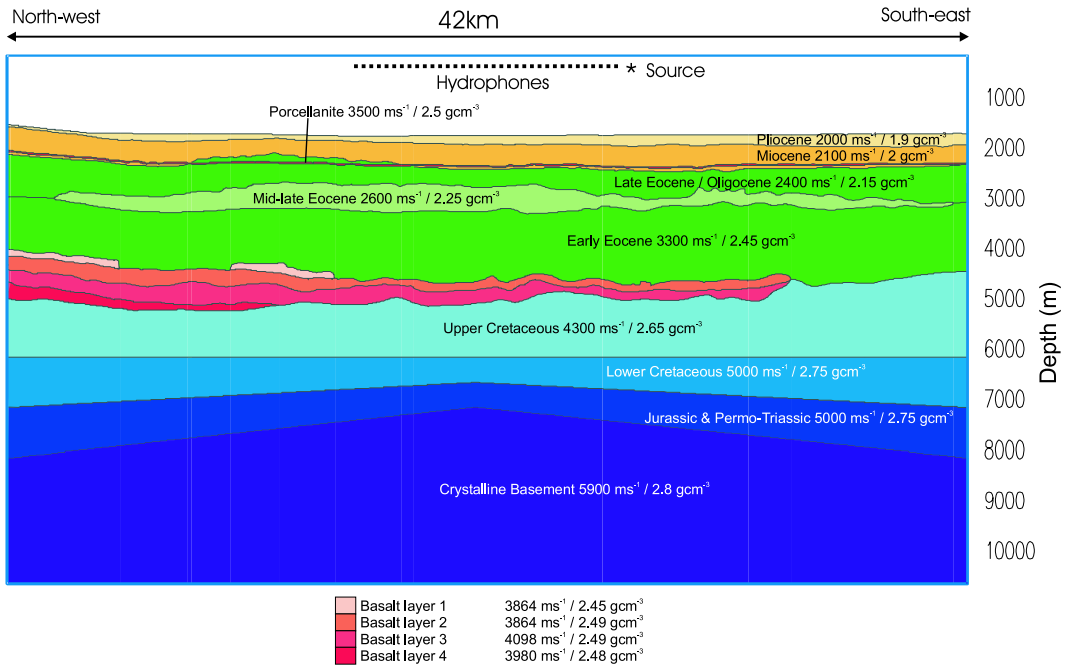

Figure 9.7: Depth section generated from interpreted processed time section. Star indicates location of shot for FFID 850, receivers to left of source.

9.4 Boundary element modelling

9.4.1 Basalt model 1

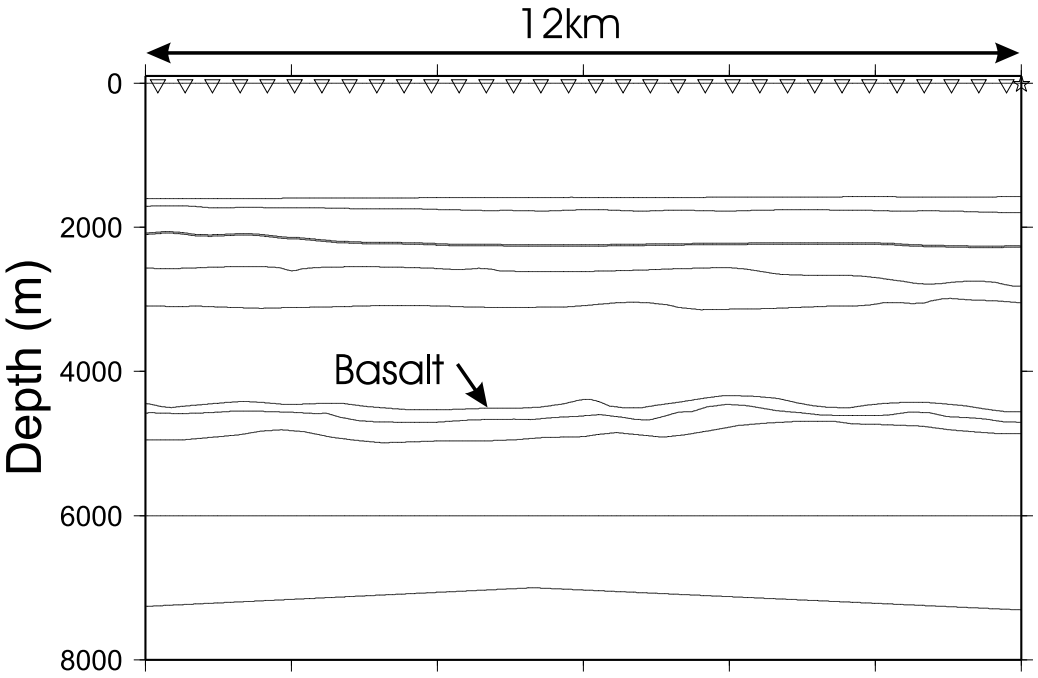

Figure 9.8: Input model for boundary element code. Source location shown as a star. Hydrophone streamer shown as triangles.

The input model for the boundary element code can be seen in Figure 9.8. This is a 12km section of the geological model which has been discretised into 1600 elements with a sample rate of one point every 7.5m in the horizontal direction. The porcellanite layer has been altered slightly so that it traces the top of the Late Eocene/Oligocene layer and no longer cross-cuts it. This slight simplification of the model ensures that the boundary element code does not have to deal with layer truncations for which it has not been tested.

The discretization of the model is fine enough that it does not affect the definition of the interfaces. An explosive source and a hydrophone 12km-long hydrophone streamer are located 15m below the sea surface. This is a simplification of the real acquisition seismic source which was an airgun array with an in-line dimension of ≈20m and a cross-line dimension of ≈60m. As in the

real-data acquisition, the hydrophone spacing is 12.5 metres and the total number of hydrophones is 936.

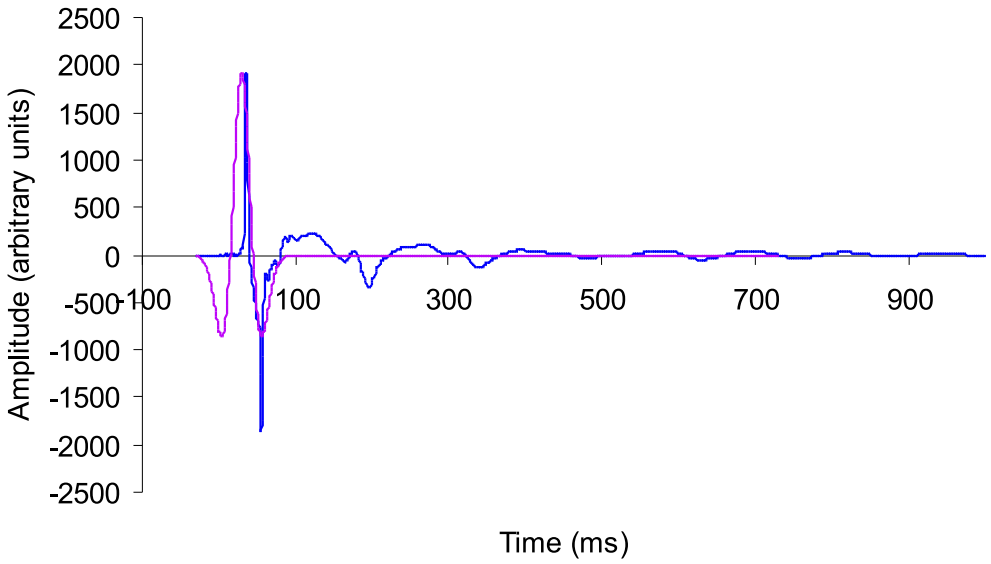

Figure 9.9: A comparison of a 15Hz Ricker wavelet and the real wavelet measured in the far field.

A Ricker wavelet of 15Hz modal frequency was chosen for the modelling. A comparison of this wavelet and a far-field measurement from the real-data acquisition can be seen in Figure 9.9. Although the Ricker wavelet clearly does not have the higher frequency content of the measured wavelet, the top-basalt event in the real data contains much lower frequencies due to the attenuation by the layers near the sea-floor (Figure 9.2). Since it is the top-basalt and sub-basalt events which are of interest, I believe a lower frequency wavelet is justified because the input model contains no attenuation in the upper layers, and I require the top-basalt event and those below in the synthetic shot gather to be similar in frequency content to the corresponding events in the real shot gather.

The results of the synthetic modelling for the model shown in Figure 9.8 can be seen in Figure 9.10. There are many features which are in agreement, but also many which differ from the real data example (Figure 9.2).

The first striking difference is that the top-basalt reflection is so weak as to be barely visible. This is in contrast to the real data where the top-basalt event is fairly strong. The low amplitude of this event in the synthetic data is due to the

small impedance contrast between the Early Eocene and the basalt layers (Figure 9.7).

The velocities for the basalt were derived from a well drilled in the Erland complex (Figure 9.1). The average velocity of flows within the Erland complex is much less than other basic Palaeogene igneous rocks within the Faeroes and Hatton-Rockall areas (McInroy et al. 2004). McInroy et al. (2004) suggest that this may be due to more extensive weathering of the Erland shield volcano. Since the seismic data were acquired over an area which is more likely to contain basalts from the Upper Series on the Faeroe Islands, the discrepancy in basalt velocities and, therefore, the discrepancy in the amplitude of the top-basalt reflection is explained.

The primary P-wave events from above the basalt agree in traveltime at near offsets with the real data. Not only this, but also the sea-surface multiples in the synthetic data appear at similar times to those in the real data. Although the frequency content of the earlier arrivals is clearly lower in the synthetic shot gather, this was expected because of the comparison shown in Figure 9.9. Unfortunately, a comparison of the top-basalt event is difficult because of the weak amplitude in the synthetic data.

More differences are seen in the far offsets. The moveout of the primary events on the synthetic data is not as large as on the real data. This can only be because the velocities for the upper layers in the input model are too high. The shallowest measurement on the plot of velocity against depth (Figure 9.6) is at around 250m below the sea bottom. Sediment near the sea bottom tends to be unconsolidated and therefore has a much lower velocity than measurements taken further down. This velocity gradient has not been taken into account in the model building process.

The unconsolidated layers also have low S-wave velocities, so the ratio of P-wave to S-wave velocity is likely to be much higher near the sea bottom as the P-wave velocity approaches that of sea water and the S-wave velocity approaches zero. Strong conversions from S to P-waves do not take place at the sea bottom in reality because of the S-wave velocity gradient. Instead, many small amplitude conversions from S-waves to P-waves occur. These converted events are spread out and therefore do not sum to make one coherent large-amplitude event. The synthetic shot gather shows several strong events which have been converted at

the sea bottom. This is because of the lack of an S-wave velocity gradient in the model, the interface at the sea floor has an S-wave velocity contrast of 1000m/s and a density contrast of $0.9gcm^3$, which is capable of producing strong S-wave to P-wave conversions.

For imaging beneath the basalt, the visibility of the sub-basalt reflections is of greatest importance. These can be seen as low-amplitude events at near offsets, disappearing in the mid offsets, and appearing again as high-amplitude events in the far offsets. The high amplitudes in the far offsets occur as the critical angle is approached at the sub-basalt interfaces. The far-offset events in the real data could also correspond to sub-basalt reflections, though the synthetic model is not accurate enough to corroborate this conjecture.

9.4.2 Basalt model 2

To improve agreement between the synthetic and real shot gathers, the velocity of the basalt was increased to $4500m/s$ and the density was increased to $2.75g/cm^3$. The resulting shot gather from model 2 can be seen in Figure 9.11. In contrast to model 1 and in agreement with the real-data example, the top-basalt reflection appears as a fairly high-amplitude event. The frequency of the event on the synthetic gather does not look greatly dissimilar from that of the real data example. In the real data example, the wavelet appears to be longer, especially at mid offsets. This is a result of the layered nature of basalts, which has not been taken into account in this particular model, but is considered in Chapter 10.

The sub-basalt reflections have changed little, despite the high impedance contrast across the top-basalt interface. This suggests that the high acoustic impedance contrast alone is not enough to explain the difficulty with imaging beneath basalt.

9.4.3 Basalt model 3

Model 3 can be seen in Figure 9.12. The only difference between this model and model 2 is that a roughness has been added to the top-basalt interface, using the same technique as that described in Chapter 7. The interface is therefore fractal in nature.

The shot gather generated for this model can be seen in Figure 9.13. There are only small differences between the results for model 2 and model 3. The top-basalt event for model 3 is slightly less continuous than for model 2, and there is scattering present. However, the sub-basalt events still seem to be affected only slightly by the added roughness.

9.5 Conclusions

An earth model was built based on data acquired in the Faeroe Shetland Channel. Velocities and densities for the model were derived from 28 wells on the Atlantic margin.

I carried out boundary element forward modelling using the earth model as an input and compared the results of the modelling with an example shot gather from the real data.

Many differences were found between the real and synthetic data including:

- Differing moveout in the far-offsets.
- Presence of converted energy in the synthetic data.
- Weak amplitude top-basalt reflection in the synthetic data.
- Presence of sub-basalt reflections in the synthetic data, but not in the real data.

The moveout in the synthetic data was not as large as the moveout in the real data. This could only mean that the velocities for the upper layers in the model were too high. The velocities for the S-waves in the synthetic model were also too high, leading to high-amplitude conversions at the sea floor which were not present in the real data. The amplitude of the top-basalt event in the synthetic data was weak as a result of the relatively low velocity and density of the basalt in the synthetic model.

The velocity and density of the basalt were increased for a subsequent model, which improved agreement between real and synthetic shot gathers. The length of wavelet in the real data compared with that of the synthetic data suggests that the basalt in the real data consists of many layers. Despite the increase in

the impedance contrast at the top-basalt interface, the sub-basalt reflections were still visible. This suggests that the high impedance contrast alone is not enough to explain the difficulty in imaging beneath basalt.

For a third model, some random roughness was added to the top-basalt interface. This caused scattering to occur from the top-basalt interface, though the scattering affected the sub-basalt reflections only slightly. Since the data for the model come from an interpreted section, the top-basalt interface is unlikely to be much more heterogeneous than it is in model 3. This suggests the roughness on the top of the basalt is not causing difficulties with imaging. However, this modelling is 2-D in which rough interfaces generate less scattering than for a 3-D model. Similar modelling would be required in 3-D to see how strong the scattering would be in that case

Other causes of problems with imaging beneath basalt are multiples and thin layering which are discussed in the next chapter in relation to the real-data example.

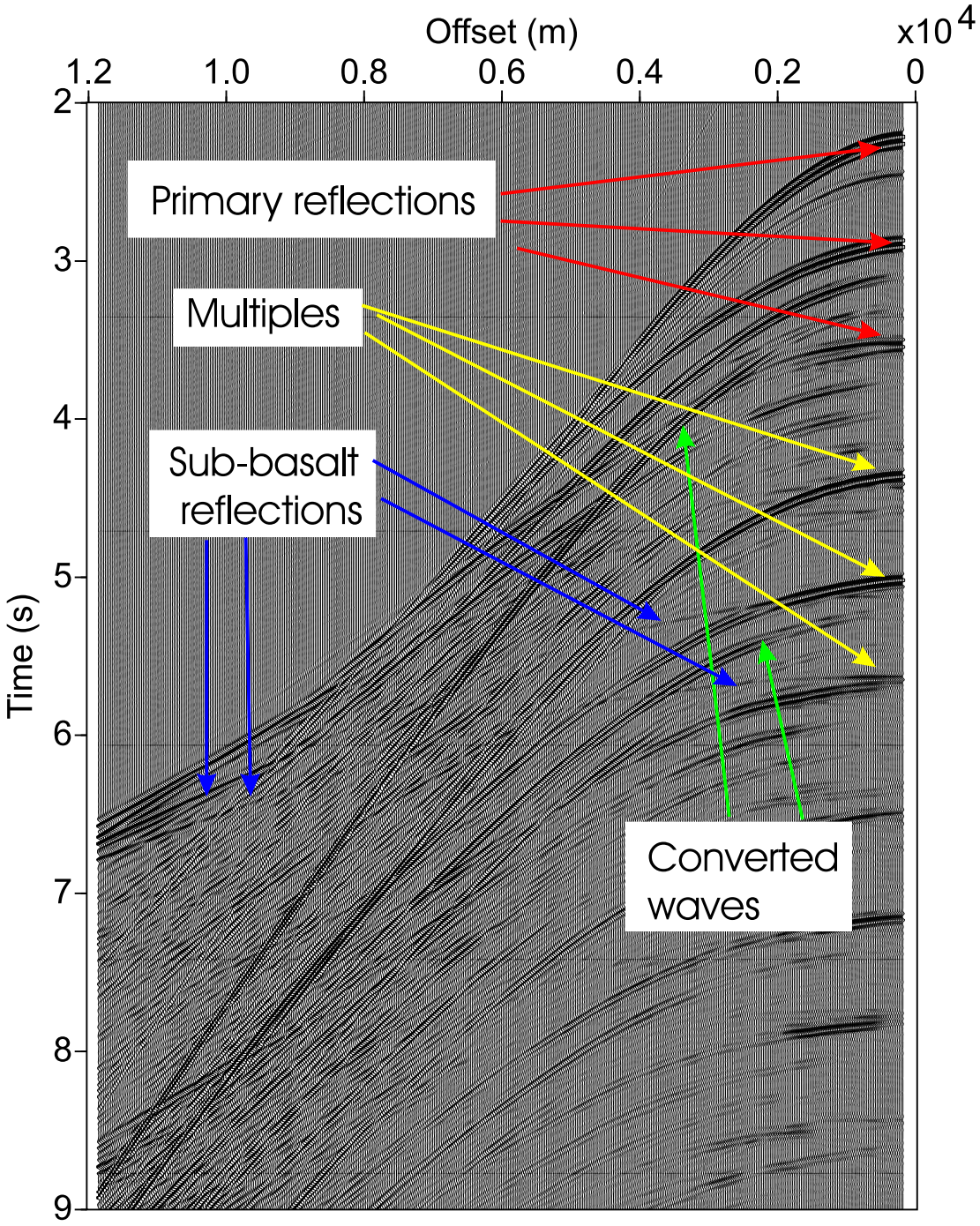

Figure 9.10: Synthetic shot gather generated from basalt model 1 (Figure 9.9).

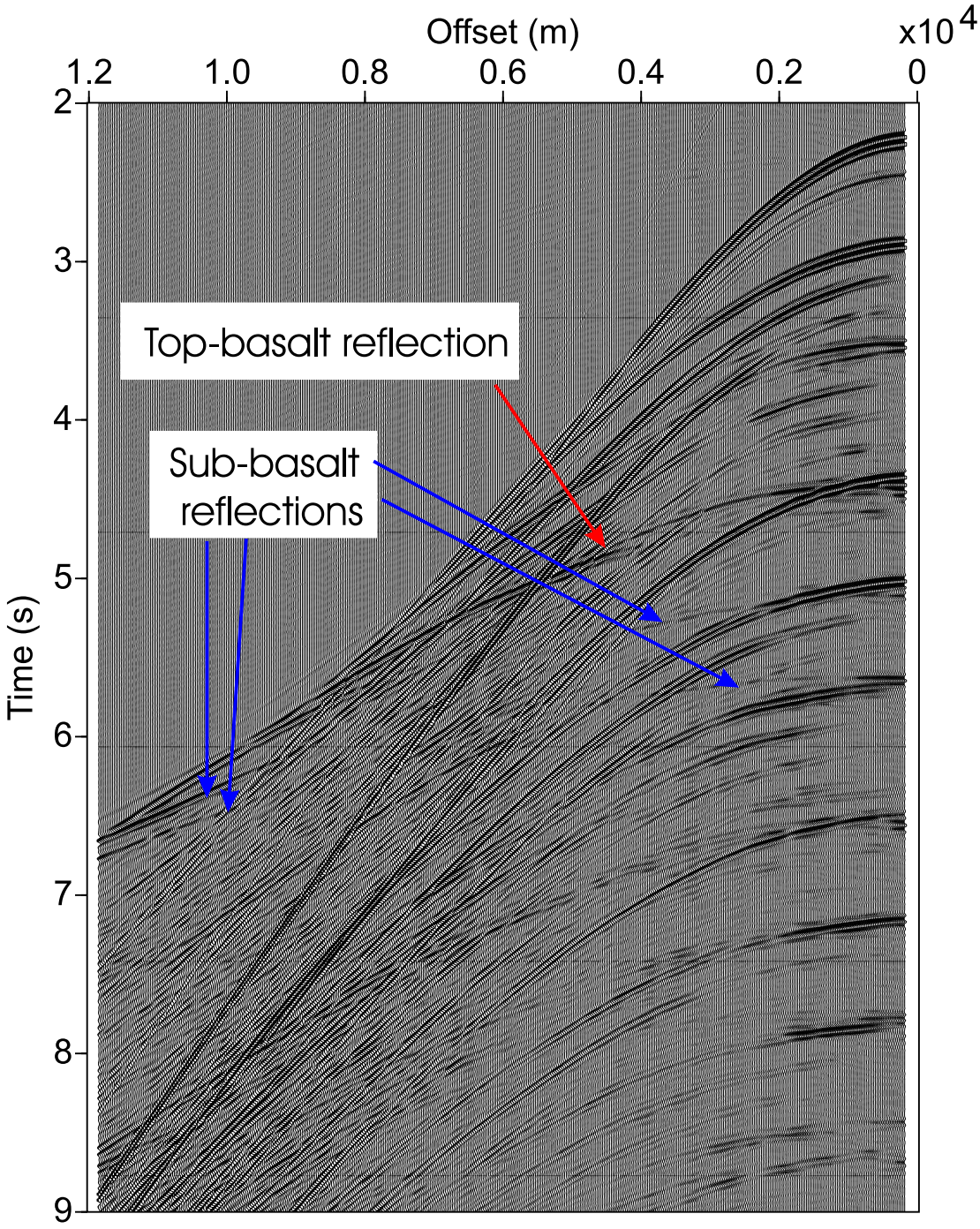

Figure 9.11: Synthetic shot gather generated from basalt model 2.

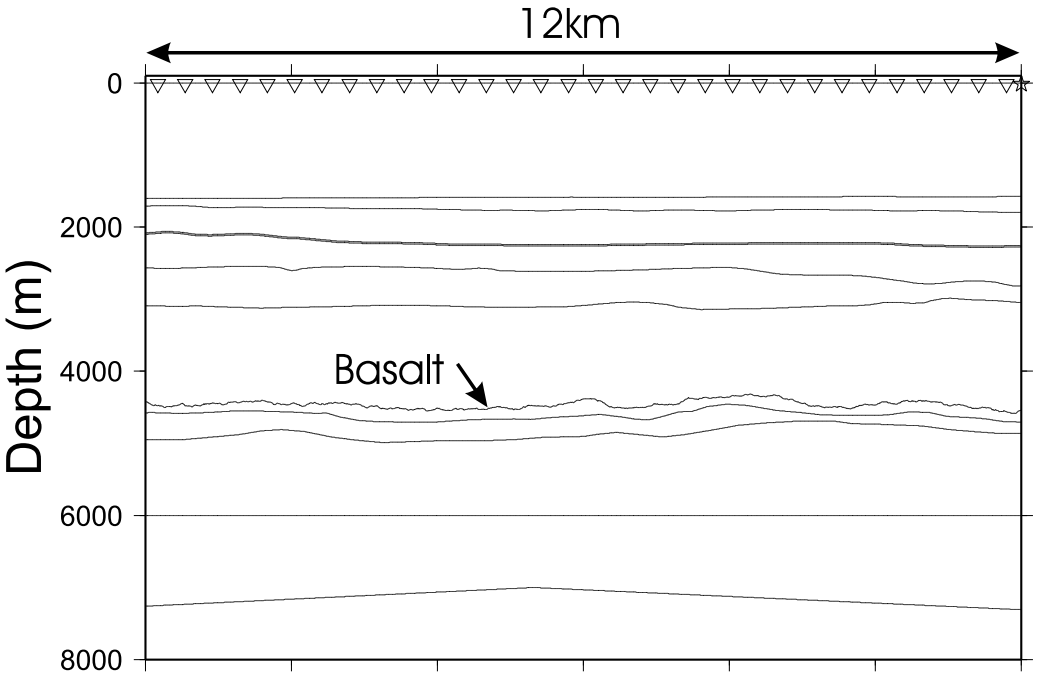

Figure 9.12: Input model 3 for boundary element code. The the top-basalt interface now has a random roughness added to it. Source location shown as a star. Hydrophone streamer shown as triangles.

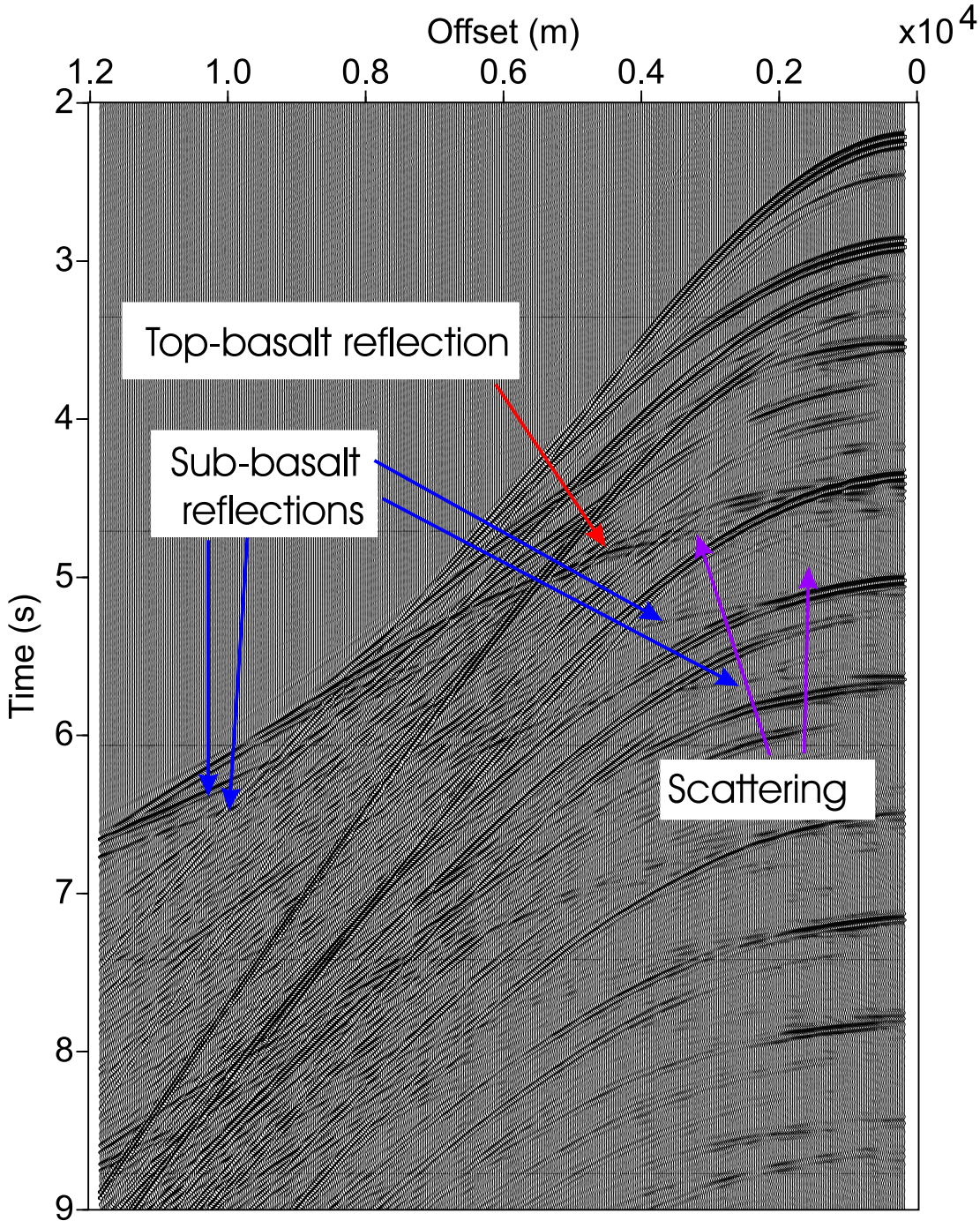

Figure 9.13: Synthetic shot gather generated from basalt model (Figure 9.12).

Chapter 10

Traveltime inversion of real data and thin-layer modelling.

10.1 Introduction

In Chapter 9 I present results from boundary-element modelling, which are generated using a model from real data acquired in the Faeroe-Shetland Channel. The model was built using an interpreted section with velocities and densities from well data.

In this chapter I use a traveltime inversion scheme to build a model directly from an example shot gather. This is an alternative method for model building to that described in Chapter 9. In that chapter the emphasis was on building a model with the correct geology. In this chapter the emphasis is on improving agreement between the synthetic and the real-data shot gathers, and mainly to improve the estimates of velocities of layers close to the sea floor in the model.

The model is simplified to a 1-D case and is input into reflectivity modelling package OSIRIS (Vilmann et al., 1998). A brief description of the reflectivity method is given in Appendix B. Four models are considered, which are as follows:

- Simple basalt consisting of two layers, sea-surface multiples included.
- Simple basalt consisting of two layers, sea-surface omitted.
- Thin-layered basalt consisting of 39 flows, sea-surface multiples included.
- Thin-layered basalt consisting of 39 flows, sea-surface omitted.

I discuss the relative importance of thin-layering and sea-surface multiples for the region in which the data were acquired.

10.2 Travel-time inversion

The travel-time inversion scheme assumes flat layers for simplicity. An important part of the scheme is ray-tracing which is described below.

10.2.1 Ray-tracing

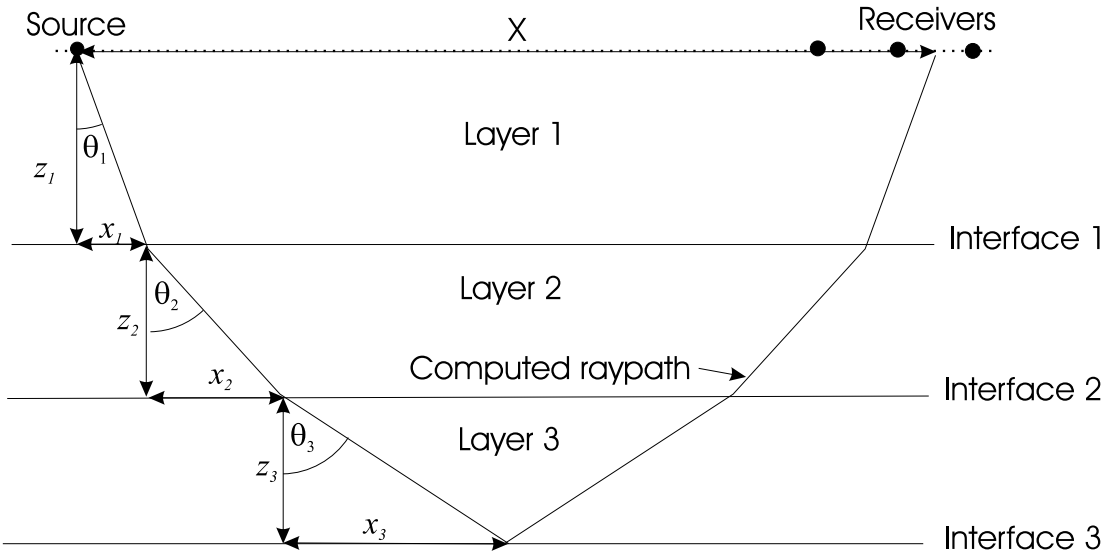

Figure 10.1: Example of single-point ray-tracing. A ray is traced from through a layered medium by applying Snell's law at each interface.

Figure 10.1 shows an example of single-point ray-tracing for flat layers where the source and receiver are at the same depth, and for P-waves only. The length x for interface n is found by trigonometry:

$$x_n = z_n \tan\theta_n, \tag{10.1}$$

where θ_n is the angle to the vertical at which the ray travels in layer n. The distance travelled by the ray in layer n is

$$l_n = \frac{z_n}{\cos\theta_n} \tag{10.2}$$

and therefore the time taken for the ray to travel from interface $n-1$ to interface n (or from the source in the case where $n = 1$) is

$$t_n = \frac{z_n}{\alpha_n \cos\theta_n}, \tag{10.3}$$

where α_n is the P-wave velocity in layer n. Angle θ_n is found via Snell's law which is

$$\frac{\sin\theta_1}{\alpha_1} = \frac{\sin\theta_2}{\alpha_2} = \frac{\sin\theta_n}{\alpha_n} \tag{10.4}$$

The offset X between the source and the point where the ray reaches the depth of the receiver is given by

$$X = 2\sum_{n=1}^{N} x_n \tag{10.5}$$

where the reflected P-wave from interface N is under consideration. The corresponding two-way traveltime is

$$T = 2\sum_{n=1}^{N} t_n. \tag{10.6}$$

Offsets and traveltimes are computed for $0 \leq \theta_1 \leq \pi/2$ with a sample spacing $\delta\theta_1$ which is made small enough so that the accuracy required for a particular application is attained. A graph of offset against traveltime can be plotted and compared with real or synthetic shot gathers (examples in Chapter 7).

If there is a requirement to know the traveltime for a receiver at a particular offset, interpolation may be carried out between the two offsets for which a traveltime has been computed. This is computationally efficient only if traveltimes for many receivers at many offsets are required.

If the traveltime to just one receiver is required, then it is faster to proceed in the following manner. First, compute the offset for $\theta = \pi/4$ then compare the computed offset with the offset of the receiver. If the receiver offset is less than the computed offset then the process continues with $\theta_1 = \pi/8$ otherwise it continues with $\theta_1 = 3\pi/8$. The process proceeds in this way until the computed offset gets within a threshold value of the receiver offset. At this point, interpolation may be carried out between the $(i-1)$th and ith iteration.

10.2.2 Travel-time inversion scheme

Before the inversion scheme could be initiated, several pieces of information were required from the real-data shot gather. First, a straight line was drawn along the first break on the direct wave (Figure 10.2). The line was extrapolated back to an offset of zero. This is the time at which the source was fired. Second, several of the higher amplitude events were ear-marked for the inversion scheme (Figure 10.2). These events include the sea-floor event, the top-basalt event and several other high amplitude events in between.

Two-way traveltimes were found for normal incidence by picking the first breaks of the events on the nearest-offset trace. This trace is actually at an offset of 156m, but the ray needs to travel around 3000m to arrive at the receiver when it is reflected at the sea floor. Therefore, to approximate the traveltime on this trace to a zero-offset traveltime is reasonable.

Traveltimes for each of the events were then picked at some far offset where the event was clearly visible (Figure 10.2). The true two-way traveltimes (i.e. the picked traveltimes with the timing of the source explosion subtracted) were used as an input to the travel-time inversion scheme.

The inversion scheme can be seen in Figure 10.3. It works layer by layer, starting with the water layer and progressing downwards. A loop then begins with the lowest reasonable P-wave velocity for the layer, working up to the highest reasonable velocity in 1m/s steps. For each velocity, a layer thickness is calculated using the zero-offset traveltime. The far-offset traveltime is computed for the same offset as the picked traveltime using the ray-tracing method described above. The difference between the picked traveltime and the computed traveltime is stored.

When travetime differences have been computed for all reasonable velocities, the best-fit velocity (i.e. the velocity for which the traveltime difference is the smallest) is taken. The scheme then continues with the second layer using the thickness and velocity from the first layer in the computations. The inversion is complete when the lowest layer in the section has been reached so that velocities and thicknesses have been found for all layers in the model.

Inversion was carried out to find P-wave velocities and layer thicknesses for the

shot gather shown in Figure 10.2. Traveltimes were computed using ray-tracing and plotted over the real shot gather (Figure 10.4). There is good agreement between the plotted curves and the picked reflection events.

Layer	Age of stratigraphic succession	Depth to base of unit (m)	P-wave velocity (m/s)
1	Seawater	1578	1468
2	Pliocene	1608	1526
3		1631	1534
4		1647	1538
5		1655	1545
6		1740	1553
7	Miocene	1803	1567
8		2043	1604
9	Late Eocene-Oligocene	2275	1857
10	Mid-Late Eocene	2415	2143
11		2722	2279
12	Early Eocene	4068	2893

Table 10.1: Values for interface depth and layer velocity found from traveltime inversion.

The events picked do not all correspond directly to interfaces from the initial model in Chapter 9 since more events were deliberately picked near the top of the section to take account of the velocity gradient. The correspondence of the old layers to the new, along with P-wave velocities is shown in Table 10.1. Events were mapped from the shot gather to the processed section in Chapter 9 using traveltimes.

10.3 Model building

Layer depths, velocities and densities for 2 new models are shown in Table 10.2. Model 1B is identical to model 1A apart from the values for density near the sea floor.

The results of the traveltime inversion provide P-wave velocities and interface depths down to the top of the basalt; they do not provide information about the basalt itself. In Chapter 9, a P-wave velocity of 4500m/s for the basalt gave a top-basalt reflection event which was similar in amplitude to that of the real data example. For the new model, the Early Eocene has a velocity much less than that

Layer	Depth to base of unit (m)	P-wave velocity (m/s)	S-wave (m/s) velocity (m/s)	Density (kg/m^3) Model 1A	Density (kg/m^3) Model 1B
1	1578	1468	0	1000	1000
2	1608	1526	143	1856	1300
3	1631	1534	150	1858	1400
4	1647	1538	153	1859	1500
5	1655	1545	159	1861	1600
6	1740	1553	166	1863	1700
7	1803	1567	178	1867	1867
8	2043	1604	210	1877	1877
9	2275	1857	428	1943	1943
10	2415	2143	675	2018	2018
11	2722	2279	792	2054	2054
12	4068	2893	1321	2294	2294

Table 10.2: Values of velocity, depth and density for new earth models.

of the model in Chapter 9. Therefore, to keep the impedance contrast between the basalt and the layer above closer to that of the Chapter 9 model, the basalt velocity and density were lowered to 4000m/s and 2636kg/m^3 respectively.

Densities for the layers above the basalt for model 1A were taken from a cross-plot of density against P-wave velocity (Figure 10.5). The cross-plot is a result of work by David McInroy of the British Geological Survey (McInroy et al., 2004; see also Chapter 9).

There are no points below a velocity of about $1900m/s$ on the plot of density against velocity. For layers of a lower P-wave velocity, one might expect the densities to decrease more rapidly than the linear relationship shown on the plot because this sediment is unconsolidated near the sea floor. Therefore, a second option for densities (model 1B) was considered in which the densities drop off more rapidly towards the sea floor.

Castagna et al. (1985) found, from sonic log, seismic and laboratory measurements, that, for water-saturated clastic silicate rocks, S-wave velocity is approximately linearly related to P-wave velocity. The empirical relationship was given as

$$\alpha = 1.16\beta + 1360, \tag{10.7}$$

where α is the P-wave velocity β is the S-wave velocity in m/s. This relationship was found to hold also for mudstones. Since all the layers above the basalt consist of either clastic silicate rocks or mudstones, Equation 1.7 should hold for all layers above the basalt. The S-wave velocity for the basalt was found assuming a P to S-wave velocity ratio of 1.8, as found by Planke et al. (1994).

10.4 Reflectivity modelling

10.4.1 Test models

The two models shown in Table 10.2 were input into the OSIRIS modelling package using an explosive 3-D source and a Ricker wavelet of 15Hz. The maximum offset is around 12km as for the models in Chapter 9. The computer on which OSIRIS runs can only compute 150 traces in one run because of memory restrictions. A full shot gather of more than 900 traces would require 6 runs of the code. Therefore, the receiver spacing for these models is set to 125m to save on computation time.

Figure 10.6 shows the real-data shot gather with every tenth trace displayed. The shot gather generated using model 1A (Table 10.2) can be seen in Figure 10.7. The main objective of the travel-time inversion has been achieved, which is to match the moveout of the synthetic and real shot gathers in the far-offset. The top-basalt event in the synthetic data also compares well with the real data. The secondary aim has also been achieved which is to reduce the amount of converted-wave energy on the synthetic seismogram. There is still some converted energy, but certainly not as much as for the models in Chapter 9.

The shot gather generated from model 1B can be seen in Figure 10.8. The difference between model 1A and model 1B can clearly be seen in the amplitude of the earlier events in the gather. In that way model 1B shows more similarity to the real data. Therefore, model 1B is selected for further modelling studies.

10.4.2 Modelling results

Four models were input into the the OSIRIS modelling package; these models are summarised in Table 10.3.

Model	Basalt features	Sea-surface multiples
2A	Single layer	Yes
2B	Single layer	No
2C	Multiple thin layers	No
2D	Multiple thin layers	Yes

Table 10.3: Models used in reflectivity modelling.

Model 2A is the same as model 1B with three interfaces added. These correspond to the base of the basalt, the base of the Upper-Cretaceous and the base of the Jurassic and Permo-Triassic on Figure 8.7. S-wave velocities for the Cretaceous, Permo-Triassic and Basement layers have been calculated assuming a P to S-wave ratio of 1.7. The P to S-wave ratio of the basalt is 1.8. The added layers are summarized in Table 10.4.

Layer	P-wave velocity m/s	S-wave velocity m/s	Density kg/m^3
Basalt	4000	2222	2636
Cretaceous	4300	2529	2650
Permo-Triassic	5000	2941	2750
Basement	5900	1705	2800

Table 10.4: Rock properties of layers beneath the top-basalt interface.

The receiver spacing is 25m with a total offset of 12km. The results from model 2A can be seen in Figure 10.9. The general appearance of the synthetic shot gather agrees well with the real shot gather (Figure 10.2). The differences are due mainly to the number of layers included near the sea floor. More layers could be added to the model, which would also reduce the converted-wave energy in the synthetic shot gather because of the smoother velocity gradient. This seems unnecessary considering that the purpose of the modelling is to determine the problem with imaging beneath basalt, not above it.

The sub-basalt interfaces are visible in the near offsets and of quite a high amplitude in the far offsets. This is in agreement with the boundary element modelling of Chapter 9. It is clear that, for the sub-basalt interfaces, there is little difference between the results of the 2-D boundary element modelling in

Chapter 9 and this flat-layered model. Thus, a change in the geological model *above* the basalt has not altered the effect of the imaging *beneath* the basalt.

For the real-data example (Figure 10.2) is is clear that if such sub-basalt events are present, then they are likely to be obscured by the sea surface multiples. It is only in the far offsets where they may be seen.

Model 2B is the same as model 2A except that the water layer has now been made into a half space. The results from model 2B can be seen in Figure 10.10. This is the shot gather that would result if perfect sea-surface multiple removal could be performed on the shot gather from model 2A, and if the source and receiver ghosts were removed. The sub-basalt events are more visible than for model 2A, and are not cross-cut by multiple energy which would affect the imaging. A comparison of Figures 10.9 and 10.10 reveals how much of the energy is due to the sea surface. It is clearly very important to remove as much of the sea-surface multiple energy as possible in the processing flow.

The seismograms from models 2A and 2B have had exactly the same amount of gain applied to them. Therefore, it may seem strange that the sub-basalt reflections are stronger for model 2A, even though they are contaminated by multiple energy (this can be seen more clearly in the near offsets). The reason for this lies in the system response of the source, receiver and sea-surface which is described in Chapter 9. In model 2B, any energy travelling upwards away from the source is lost, because there is no interface there to redirect it downwards. In model 2A, the sea-surface acts to boost the signal because the source is 15m from the surface and the central frequency of the wavelet is 15Hz (see Chapter 9). However, this means for model 2A that the multiple energy is also boosted by the same amount. Therefore, although the amplitude of the sub-basalt events looks higher for model 2A, relative to the multiple energy, it is unchanged.

In model 2C, the single-layered basalt is replaced with a thin-layered basalt which is the same as the basalt succession used for Model 3 in Chapter 8. The layer thicknesses correspond to those found in the Upper Series volcanics on the Faeroe Islands. Figure 10.11 shows the results of modelling from model 2C. The top-basalt event has now become a longer, more complicated wavelet due to peg-leg multiples within the basalt succession. The sub-basalt events are unchanged in the near offsets. This can be explained by Figure 8.17 in Chapter 8. At normal incidence, very little scattering attenuation occurs below 60Hz. Since I am using a

15Hz wavelet in the modelling (which contains frequencies up to 45Hz maximum), attenuation due to scattering should not be expected. At far offsets (Chapter 8, Figure 8.17) scattering attenuation affects all frequencies to some extent. Figure 10.11 shows that both of the sub-basalt events have been attenuated in the far offsets, as predicted by the modelling in Chapter 8.

Also worth mentioning is the behaviour of the diving wave from the top basalt interface in the far offsets. The results from Model 2C show a marked decrease in energy, which is not apparent in the shotgather for Model 2B. This energy decrease is in good agreement with the real shotgather (Figure 10.2). The diving wave can be used to estimate the thickness of the basalt by looking at the 'step-back', i.e., the offset at which the diving wave grazes the interface below the basalt and therefore does not return to the receiver (see White et al., 2003).

Model 2D combines the problems of thin layers and sea-surface multiples. The sub-basalt events shown in Figure 10.12 are obscured by multiples in the near and mid offsets and are attenuated by scattering due to thin layering in the far offsets. However the sub-basalt events in the far offsets can still clearly be seen, despite the attenuation from the thin layering. Imaging using these events in the far offset could be successful, though event identification could be difficult without the benefit of knowing the velocity model beforehand.

10.5 Conclusions

A traveltime inversion scheme for flat layers has been presented. Traveltime inversion was carried out on a real data shot gather to build a velocity model down to the top-basalt interface.

Densities were derived from well log data, and S-wave velocities were calculated assuming a linear relationship between P- and S-wave velocity.

Sub-basalt interfaces were added to the model and reflectivity modelling was carried out out. Four models were considered: single-layered basalt including sea-surface multiples, single-layered basalt without sea-surface multiples, multi-layered basalt without sea-surface multiples and multi-layered basalt including sea-surface multiples.

Results of the modelling revealed that, although the events above the top-

basalt interface were altered by the new input model, the sub-basalt events had the same characteristics as for the modelling in Chapter 9. This is despite the fact that the model has changed from a 2-D model in Chapter 9 to a flat-layered model in this chapter.

Most of the energy in the real-data shot gather is due to sea-surface multiple energy. The multiple energy obscures sub-basalt energy in the near to mid offsets.

The thin-layering of the basalt hardly affects the amplitudes of the sub-basalt events in the near offsets. This is true for the case where thickness of the basalt layers corresponds to that of the Upper-Series volcanics on the Faeroes and the frequency of the wavelet is 15Hz. In the far offsets, the amplitude of the sub-basalt events is attenuated due to the scattering in the basalt succession.

It could still be possible to image using far-offset arrivals. The main problem would be with event identification. Near-offset imaging could also be achieved with effective multiple removal algorithms.

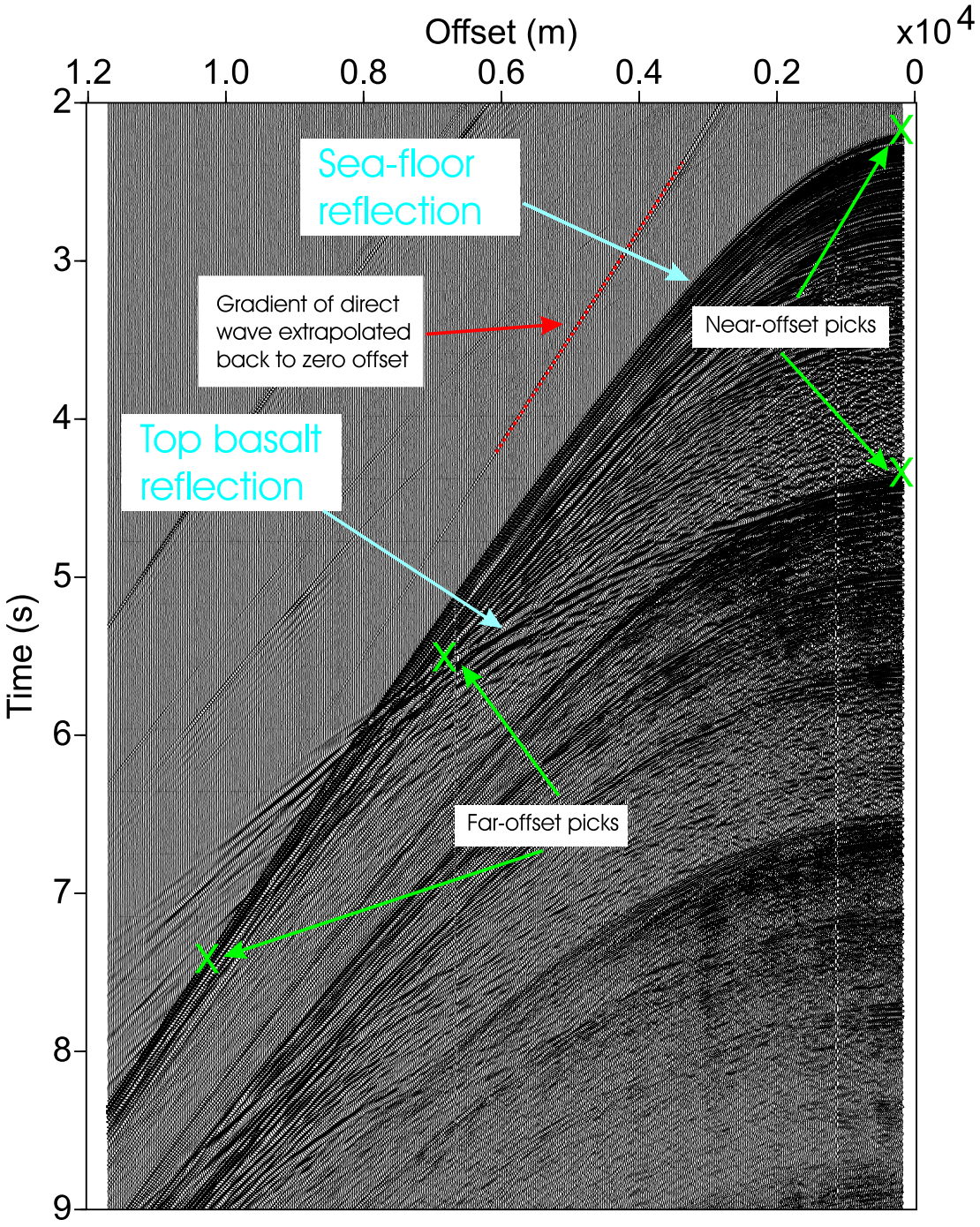

Figure 10.2: Picking for traveltime inversion. The X's show possible near and far-offset picks for the sea-floor and top-basalt reflections.

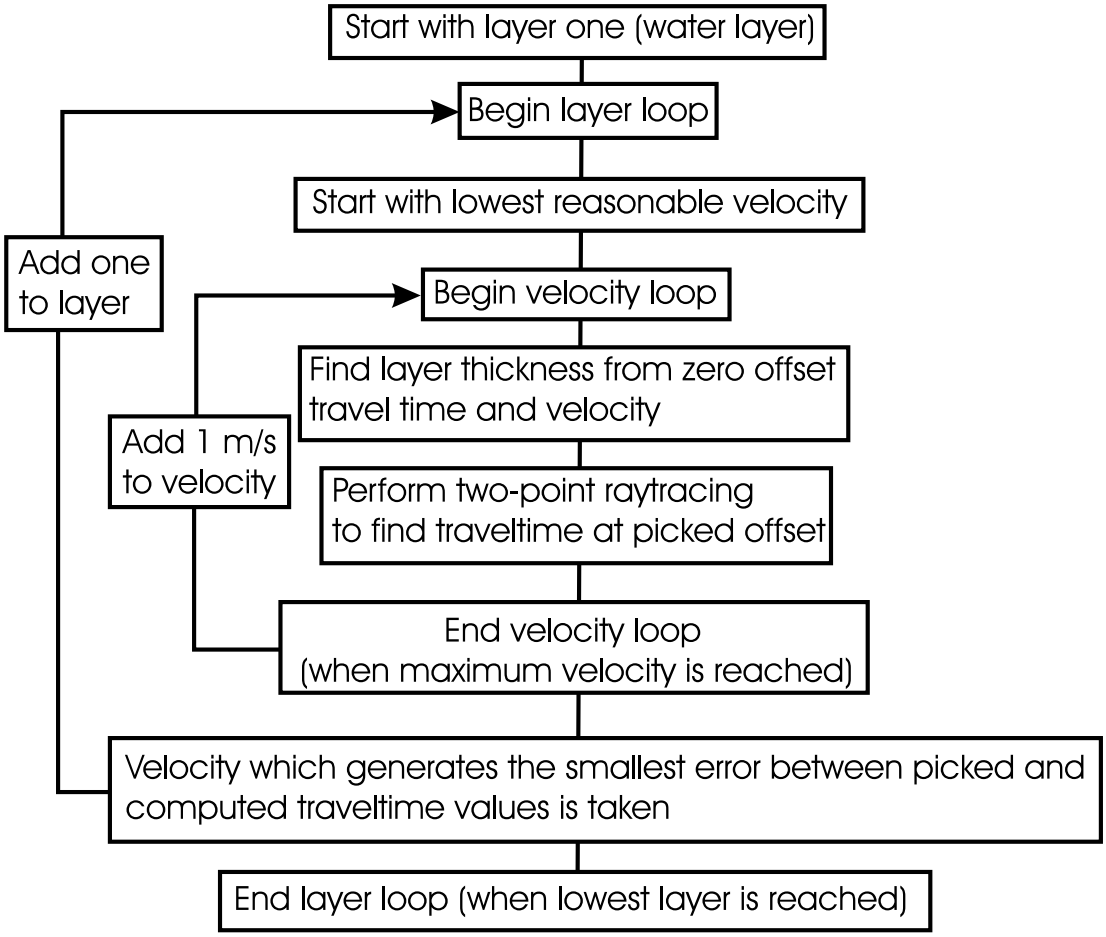

Figure 10.3: Traveltime inversion scheme.

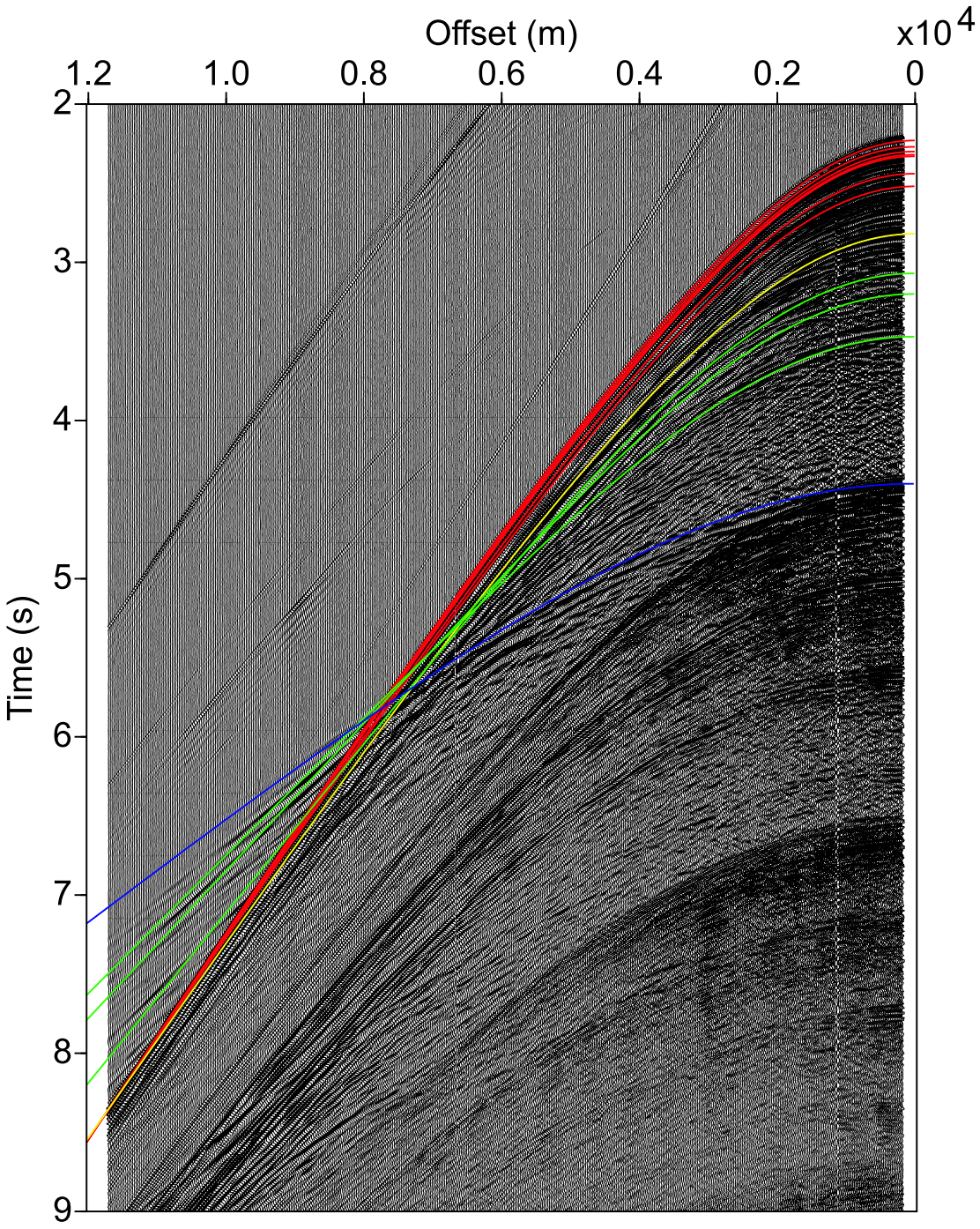

Figure 10.4: Real-data shot gather with results of traveltime inversion plotted on top.

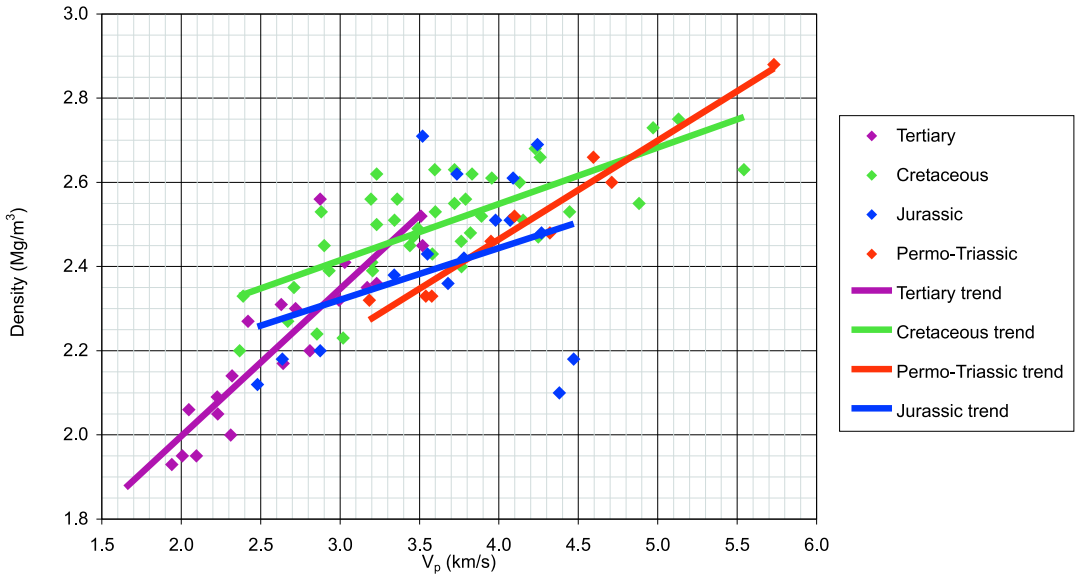

Figure 10.5: Cross-plot of density against velocity, derived from well data (after McInroy et al., 2004).

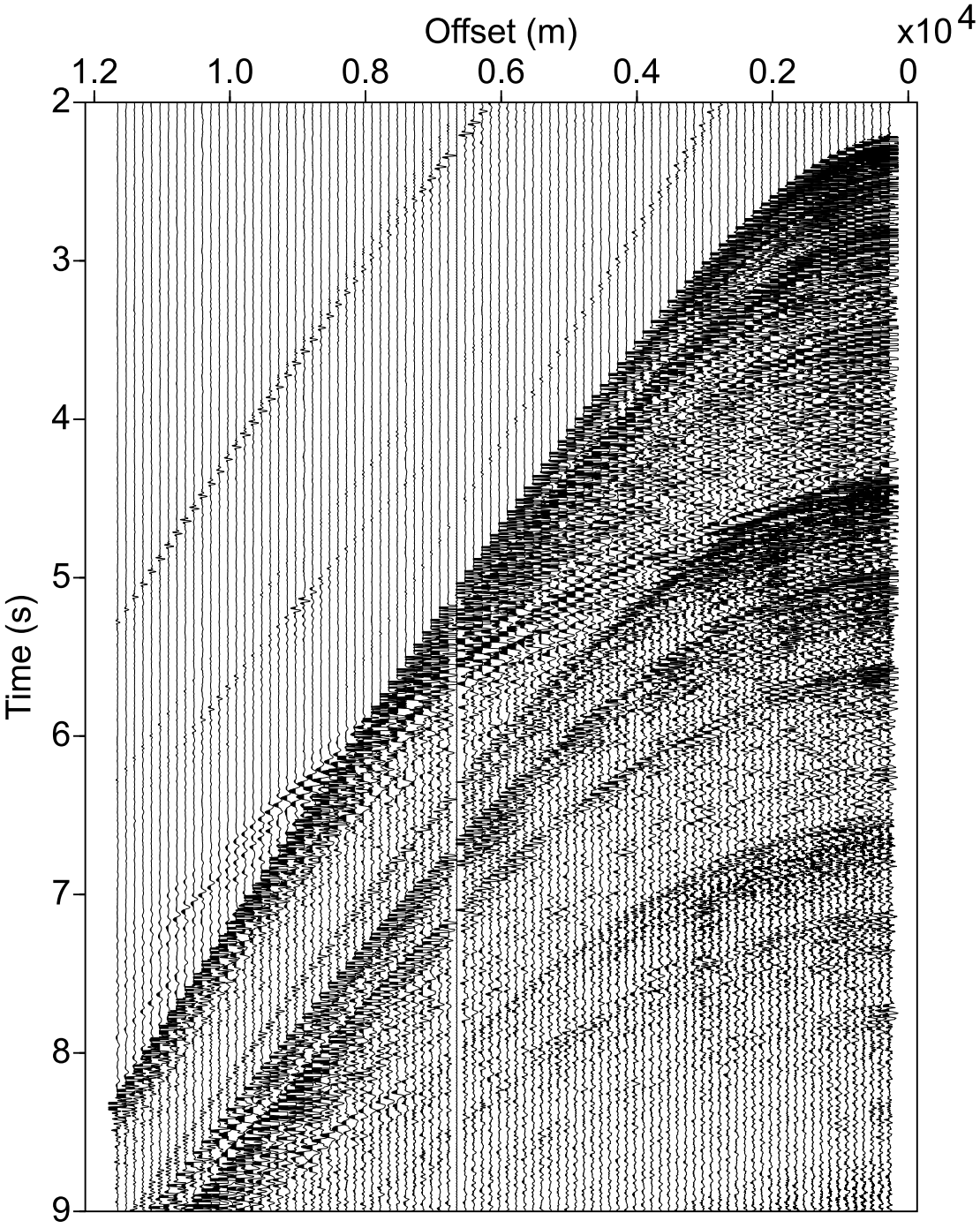

Figure 10.6: Real-data shot gather. Only one in every ten traces is plotted for easy comparison with Figures 10.7 and 10.8.

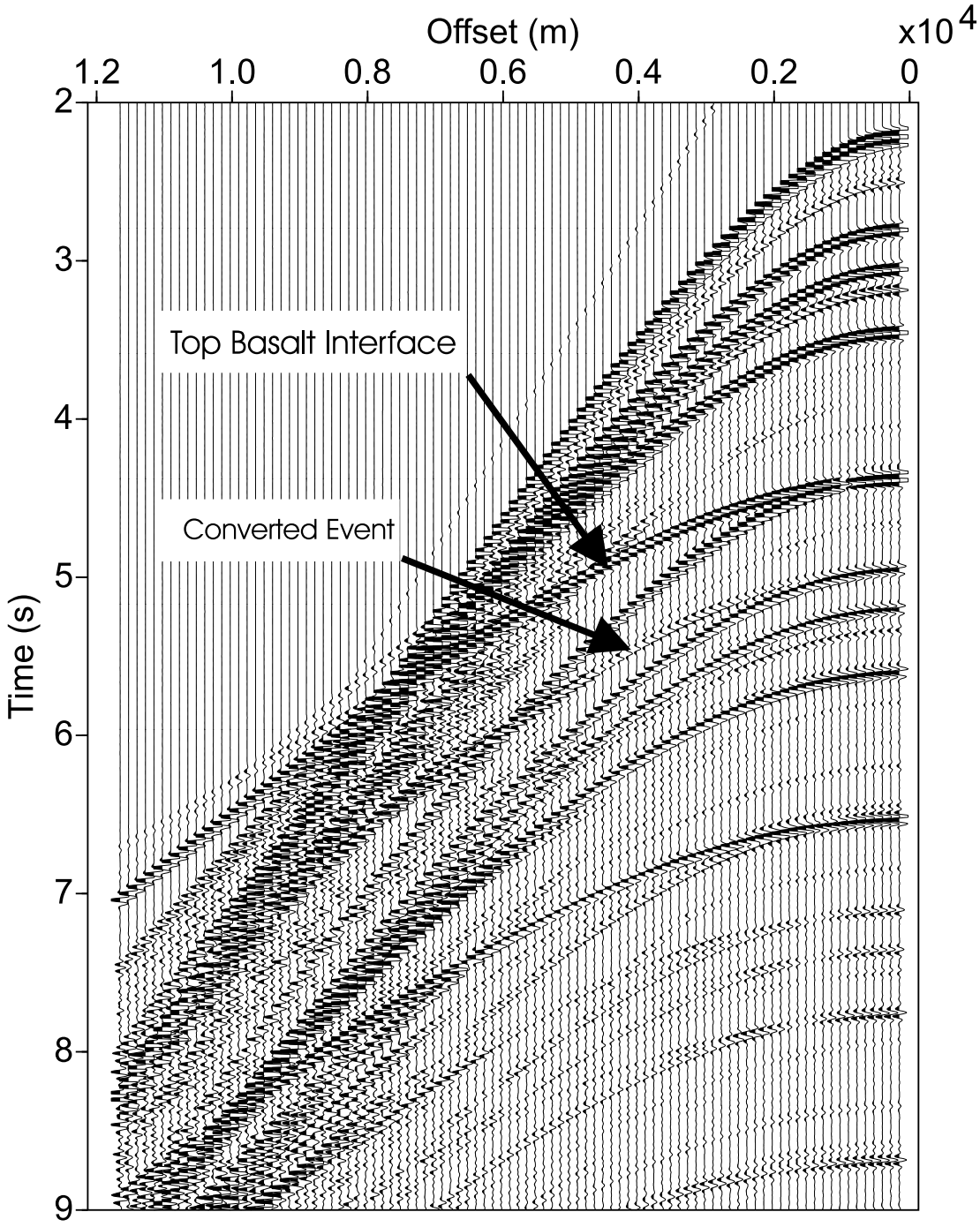

Figure 10.7: Synthetic seismogram generated from model 1A using the reflectivity method.

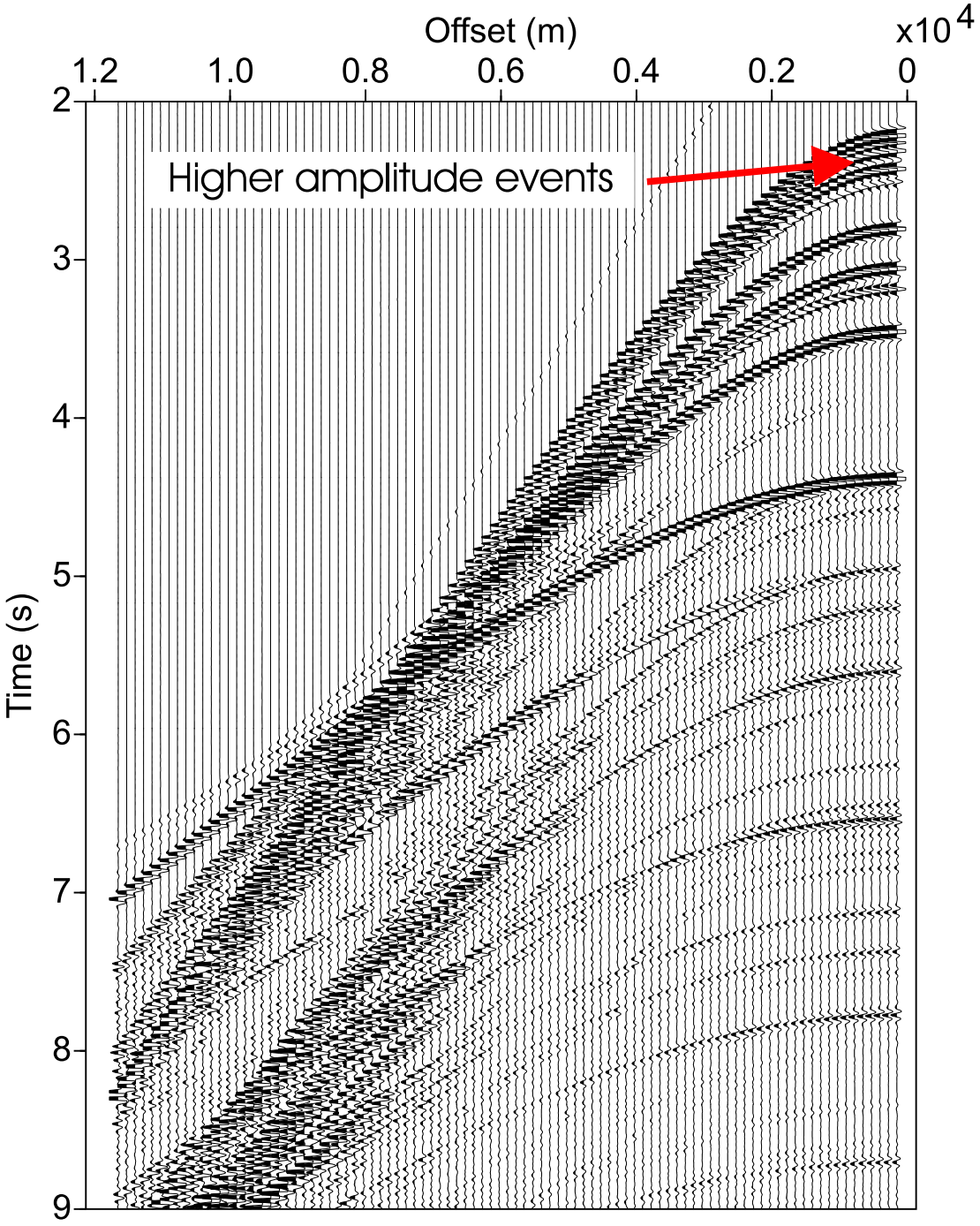

Figure 10.8: Synthetic seismogram generated from model 1B using the reflectivity method.

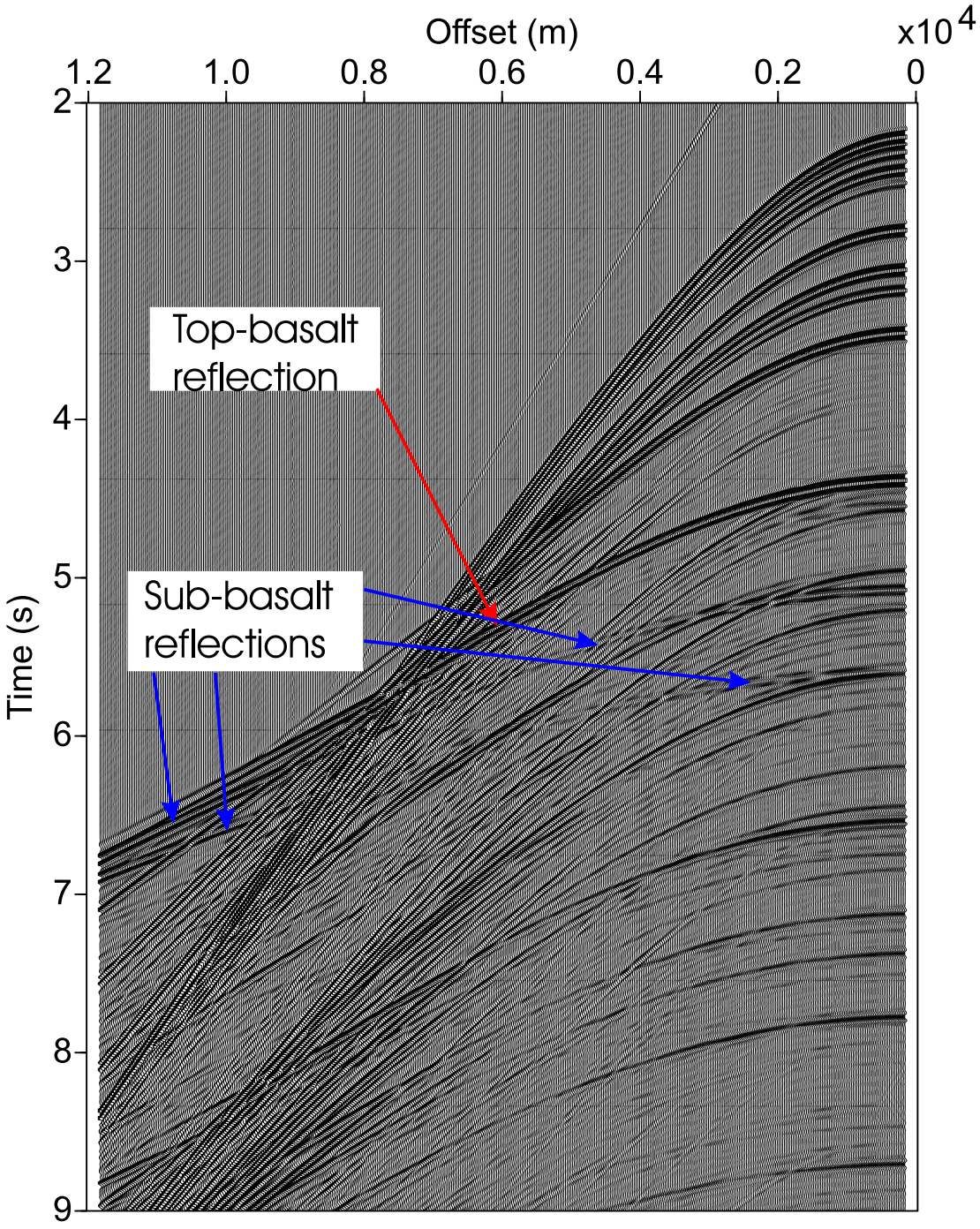

Figure 10.9: Synthetic seismogram generated from model 2A using the reflectivity method.

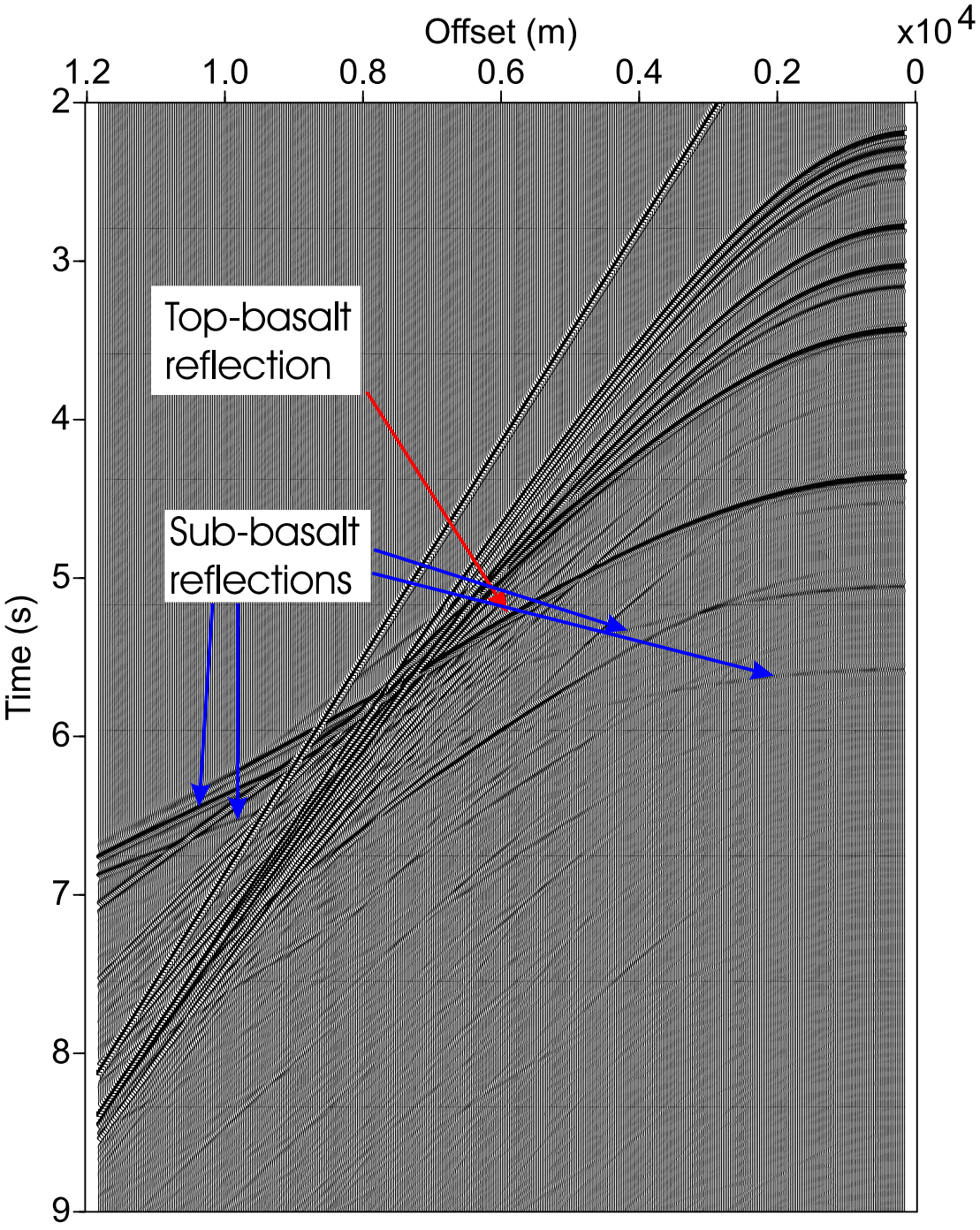

Figure 10.10: Synthetic seismogram generated from model 2B using the reflectivity method.

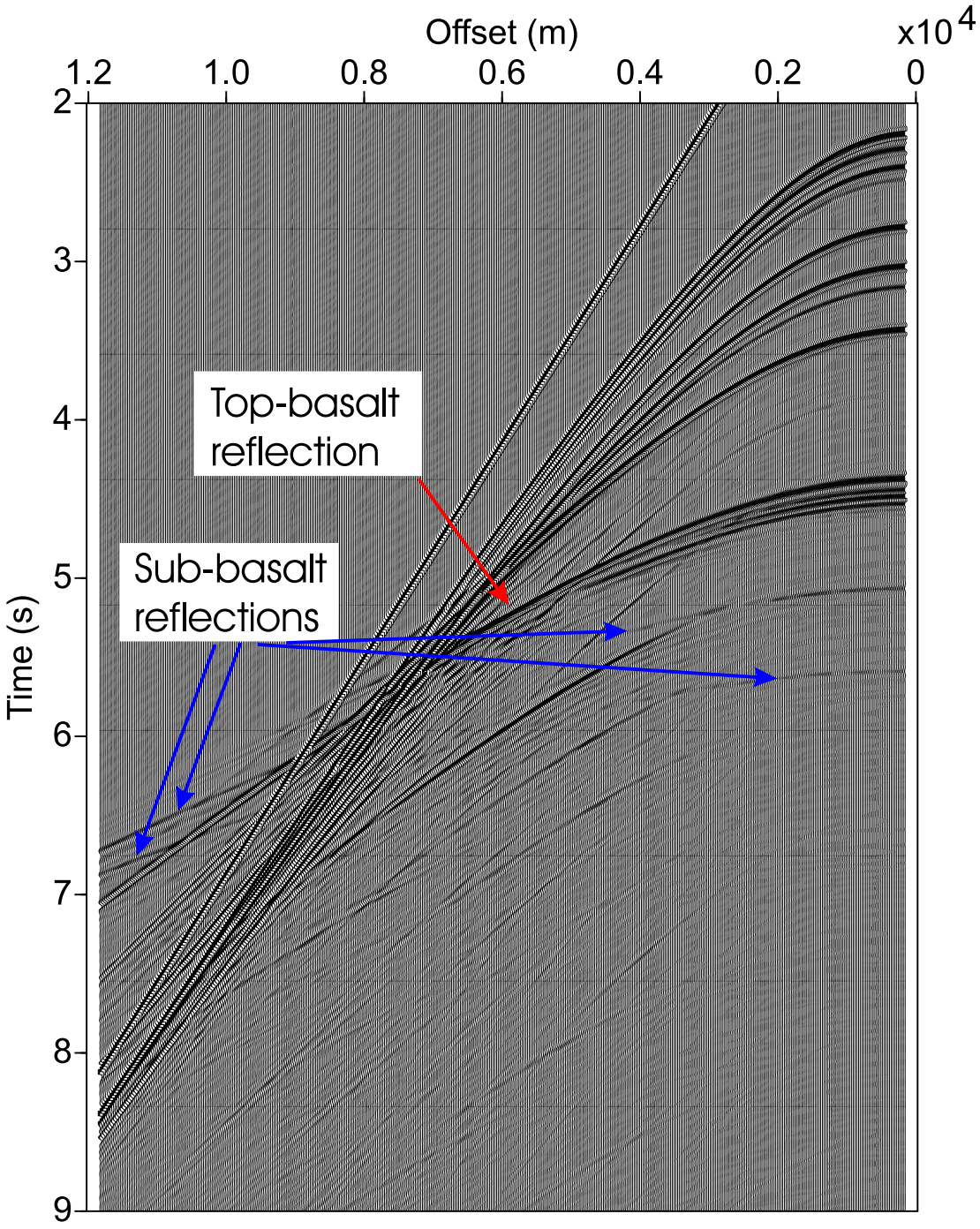

Figure 10.11: Synthetic seismogram generated from model 2C using the reflectivity method.

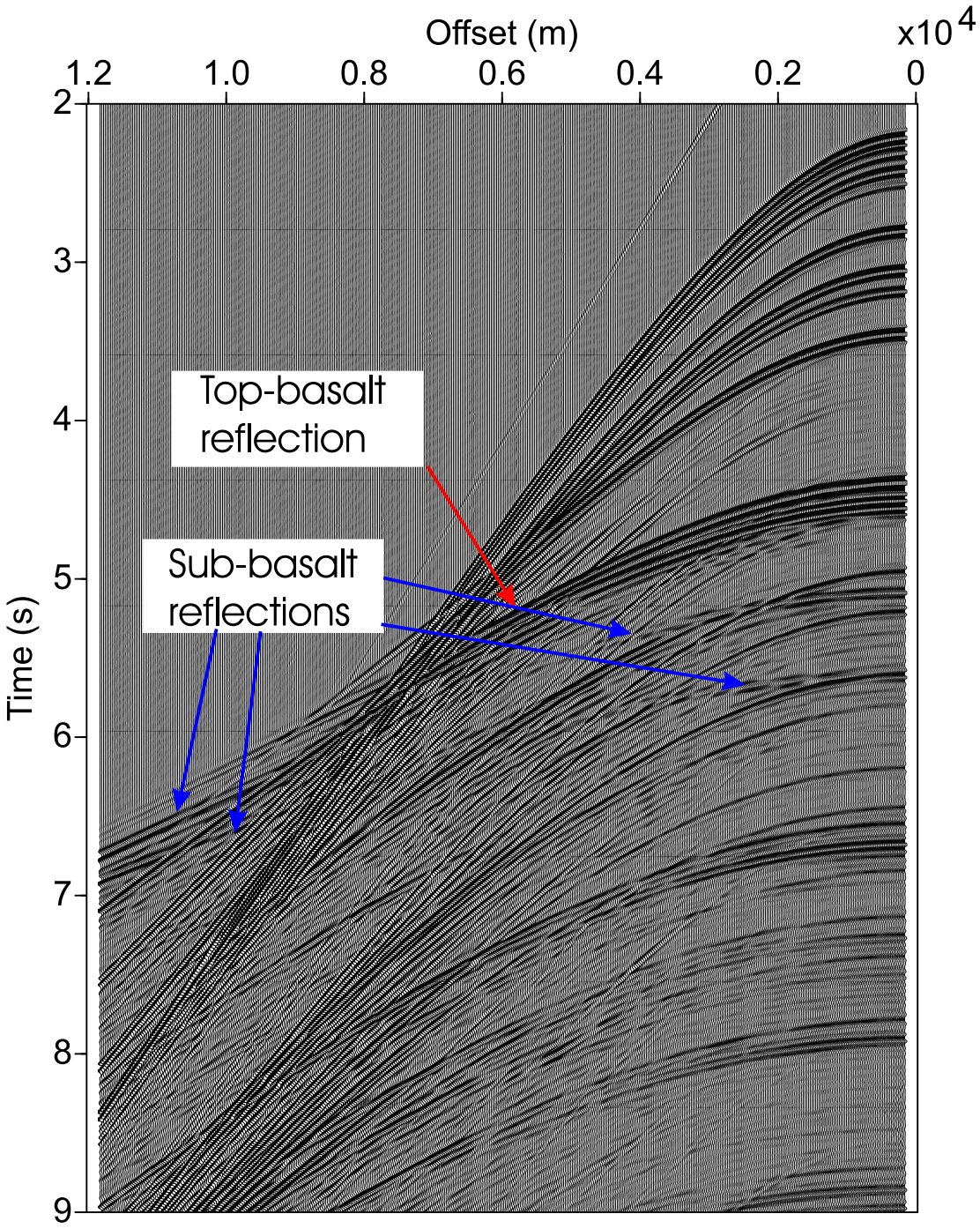

Figure 10.12: Synthetic seismogram generated from model 2D using the reflectivity method.

Chapter 11

Discussion and Conclusions

11.1 Introduction

This thesis covers two topics which are linked by forward modelling of seismic waves through basalt. In Chapters 3, 4, 5, 6, 7 and 9, I introduce, test, develop, and finally use the boundary element method for modelling seismic waves in an exploration environment. In Chapters 2, 7, 8, 9 and 10, I discuss the problems of imaging beneath basalt with seismic waves in the north-east Atlantic margin and perform forward modelling to enhance understanding of what the real issues are for sub-basalt imaging. The link between these two areas is in Chapters 7 and 9, where I used the boundary element method for modelling basalt.

The conclusions for this thesis split neatly into two sections: 1) the suitability of the boundary element method for modelling in an exploration environment and 2) what I consider to be the main problem (or problems) with imaging beneath basalt in the north-east Atlantic margin and, in particular, in the Faeroe-Shetland Channel.

11.2 Boundary element modelling in an exploration environment

The boundary element method has been used very little in exploration seismology in comparison to methods such as finite difference and reflectivity. In this thesis

I have analysed the suitability of the indirect boundary element method for modelling in an exploration seismology environment.

In Chapter 5, I show that the boundary element method is consistent with reflectivity and finite difference code as long as the 'rules of thumb' are followed. These rules are not particular to the boundary element method. In the past, rules have also been developed for the finite difference method which relate to grid spacing, time sampling and velocity smoothing.

I have established that the effects of model truncation (edge effects) can be almost completely removed by adding edge zones of forty elements on both sides of the model (including 20 absorbing elements), and that this worked for all frequencies. Of course, the reflectivity method assumes infinitely long interfaces so it does not have this problem, The finite difference method, however, suffers from severe edge effect problems which are removed to some extent by absorbing edge zones. Usually the model has to be widened to lessen these effects.

One of the reasons for the lack of interest in boundary methods may be because of the complexity of the formulation of the method. Another is certainly because of the large matrices which need to be inverted in order to generate synthetic seismograms. Because of the amount of time required to invert these matrices, the boundary element method tends to be slower than finite difference code running a similar model.

In Chapter 6, I introduce a method to speed up computation with the boundary element method whilst still retaining accuracy. The improvement in efficiency is dependent on the speed of convergence. Convergence is, in turn, dependent on the number of sub-domains making up the model and the length of the model. A comparison of computational run-time between FD and BEM with domain decomposition is given below.

Run-time comparison

The three-layer rough-interface models shown in Chapter 7 are 12km long and are computed up to a maximum frequency of 128Hz. Eight shot gathers were generated for each model (of which only one was used for the analysis in Chapter 6).

The total computation time for 16 nodes was around 12 hours. This is equivalent to a computation time of 8 days for one node.

The computation time for the same model run with the finite difference code on one node would be 10 days. There are several factors to consider here. The first point is that the input model for the finite difference code would be too big to fit in the memory of one node. Therefore, it too would need to be split into several sub-domains to run the model at all.

The boundary element method with domain decomposition and a far-field approximation performs slightly better than basic finite difference code for this particular model. If twice as many layers were present in the model then the boundary element method would take twice as long. The finite difference method would take the same amount of time as for the three-layer model.

The boundary element code was parallelised with relative ease because the computation for one frequency is independent of another. Therefore, no communication is required between nodes, and the time taken by two nodes is roughly half of that taken by one node. The finite difference code is more difficult to parallelise because, in theory, every point in the grid is dependent on every other point. Parallel versions of FD code involve continual communication between nodes, which means parallelisation is not as efficient.

The boundary element method has the ability to compute many shot gathers in one go. Eight shot gathers were generated in one run with the boundary element method with only a slight increase in computational run-time compared with the time taken for one shot gather. The time taken for the FD code to run eight shot gathers would be roughly eight times the amount of time taken for one.

A further advantage of the BEM over FD is the ability to select an input wavelet of any type and frequency after computation is complete (as long as the maximum frequency of the wavelet does not exceed the maximum frequency computed). This is true for all frequency domain methods.

In summary, the boundary element method is a useful technique in the following circumstances:

- When the model contains few layers
- When many shot gathers are required for the same model

- When parallel computing facilities are available
- When input wavelets of different frequencies and types are required for the same model.

A problem that FD and the BEM have in common is the problem of low S-wave velocity. In Chapter 10, I present a model in which S-wave velocities go down to 143m/s. It would take vast amounts of computing time to generate seismograms for such a model with FD or BEM code because of the fine spatial discretization required. A combination of reflectivity and boundary element methods may be able to solve this problem, but this is not within the scope of this thesis.

11.3 Sub-basalt imaging

In Chapters 7, 8, 9, and 10 I perform forward modelling to enhance understanding of the effect basalt has on the seismic wave. Modelling mainly concentrated on the following:

- Rough interfaces.
- Scattering attenuation due to thin layering.
- High impedance contrast.
- Sea-surface multiples.

The modelling in Chapters 9 and 10 put these problems into a real setting based on seismic data acquired in the Faeroe-Shetland Channel.

Previous studies (e.g. Martini, 2001) have found rough interfaces at the top-basalt interface to be a major source of the problems in sub-basalt imaging. The studies in Chapter 6 suggest that, although considerable scattered energy is present from the top-basalt PP- and PS-waves, the rough models considered did not affect sub-basalt energy to a significant degree. There is evidence of extreme roughness in the Rockall Trough (Martini, 2001) but not in the Faeroe-Shetland Channel data, upon which my modelling studies in Chapter 9 are based. If scattering were an important mechanism, then the top-basalt event in the real-data example would display considerable scattering as in the synthetic modelling

of Chapter 7. This leads me to believe that basalt roughness does not contribute greatly to the sub-basalt imaging problem in the Faeroe-Shetland Channel.

I show in Chapter 8 that a succession of basalt layers can have an extreme effect on seismic energy propagating through it. I also conclude that the effect on the seismic wave is dependent on the wavelength relative to the thickness of the individual layers in the succession. For a velocity and thickness distribution which is consistent with the upper-series basalts on the Faeroe Islands, transmitted seismic energy for frequencies higher than 60Hz is almost non-existent at normal incidence. For frequencies below 60Hz there is good transmission of energy through the basalt. At far offsets the transmission of energy displays an exponential decrease with increasing frequency.

From observations of frequency content of the top-basalt reflection event in the real seismic data, I conclude that the peak frequency of the event is around 15Hz. A wavelet with peak frequency of 15Hz should not be affected much by the thin layers in the basalt at near offsets. A decrease in penetration of energy was observed at far offsets in the synthetic data, which could affect imaging.

One of the main problems with the data acquired in the Faeroe-Shetland Channel is that of sea-surface multiples. It can be seen from the modelling in Chapter 10 how much of the energy on a shot gather is due to sea-surface multiples. Since there is more multiple energy in the real data, this masks possible sub-basalt energy to an even greater extent than in the synthetic data.

The remaining issue is one of impedance contrasts of sub-basalt interfaces and the top-basalt interfaces. The velocity and density of the basalts in Chapters 7 and 8 are towards the higher end of those expected for basaltic lavas in the north-east Atlantic margin. Despite this, energy is able to penetrate the basalt.

The velocity and density values used for the basalt in Chapters 9 and 10 were, at first, taken from a well which was close to the seismic line. The velocities from this well were found to be inconsistent with other measurements of basalts in the north-east Atlantic margin. The velocity and density of the basalt were subsequently raised to fit the real data in terms of the relative amplitude of the top-basalt event. It is possible that the values of density and velocity used for basalt in these models is still lower than those in reality. This would mean that the events from beneath the basalt would be slightly weakened with respect to the top-basalt event.

There is also a possibility that the velocity and density contrasts for the sub-basalt interfaces could be lower in reality than in the model. There is no strong geological evidence that there are substantial stratigraphic units between the Upper Cretaceous and the crystalline basement (see Figure 8.7; Derek Ritchie, pers. comm.). Smaller amplitude events could easily be hidden by multiple energy, which can never be perfectly removed.

To summarise, the most likely reasons for the difficulties with sub-basalt imaging in the Faeroe-Shetland Channel are:

- High attenuation of energy in layers above the top basalt interface.
- High impedance contrast between the basalt and the layers above.
- Low impedance contrast between sub-basalt layers.
- Sea-surface multiples.

However, the possibility of imaging problems related to rough interfaces and thin layering still exists. A significant problem associated with the modelling is the compilation of a realistic earth model to use as an input. Although a considerable effort was made to make the earth model as close to reality as possible, the model is still a best estimate based on the data which were available. Unfortunately there was no well on the seismic profile which means that the accuracy of the model cannot be confirmed. A clear difference between the synthetic and real data is the lack of noise in the former. The presence of noise in the real data makes the task of imaging weak events more difficult.

As far as the thin layers are concerned, scattering effects become stronger as the thickness of the individual basalt flows increases. Therefore, if the basalt flow thickness follows more closely the distribution of the lower series and not the upper series, quite strong scattering of a 15Hz wavelet could occur (see Figure 8.21).

11.4 Implications for acquisition and processing

Because of the attenuation of high frequencies in the layers above the basalt, low-frequency acquisition is very important. Even though the survey described in

Chapter 8 was designed to boost the lower frequencies, the energy reflected from the top basalt is of a much lower frequency than the source wavelet. Thus, much of the energy from the airguns was wasted even for the the top-basalt interface. The chances of imaging beneath a high-velocity, high-density layer like basalt are greatly reduced, even if the rough interface scattering and the thin layering have no effect whatsoever.

On the processing side, sea-surface multiple removal is an important step in imaging beneath basalt in this region. In other regions (e.g. the Rockall Trough) where the water depth is greater, sea-surface multiples are not so much of a problem. Nothing can be done about the high-impedance contrast between basalt and the layers above. Only by improving signal to noise ratio by removing as much of the multiple energy as possible can improvements be made.

11.5 Future work

Considering the frequency content of the top-basalt event in the real data, a profile concentrating on even lower frequency acquisition is advised. This may not be practical at this time though seems to be the only way to get energy to penetrate to the top basalt (and then through it). The higher frequency energy is clearly of no use in this setting.

Because of previous work (e.g. Ker and Rodriguez, 2002; see Chapter 2) concluding that intrinsic attenuation in basalt is negligible compared with scattering attenuation (due to thin layering), I have not performed modelling with intrinsic attenuation in the basalt. It would be of interest to carry out modelling studies of the effects of fractures and vesicles (voids in the rock caused by gas present in the basalt flows) on the seismic wave. Modelling could be carried out using the boundary element method or finite element method and would give an idea of whether these effects could contribute to problems with imaging beneath basalt.

References

K. Aki and K. L. Larner. Surface motion of a layered medium having an irregular interface due to incident plane SH waves. *Journal of Geophysical Research*, 75 (5):933–954, 1970.

K. Aki and P. G. Richards. *Quantitative Seismology: Theory and Methods*. W. H. Freeman and Company, San Francisco, 1980.

F. Avedik, V. Renard, J. P. Allenou, and B. Morvan. Single bubble air-gun array for deep exploration. *Geophysics*, 58:366–382, 1993.

P. K. Banerjee and R. Butterfield. *Boundary Element Methods in Engineering Science*. McGraw-Hill, London, 1981.

S. C. Bergman. Geological heterogeneities in Paleogene North Atlantic basaltic volcanic rocks - impact on seismic modelling. *Sub-basalt Imaging Workshop, Barbican Centre, London*, 1997.

M. Bouchon. A simple, complete numerical solution to the problem of diffraction of SH waves by an irregular surface. *J. Acoust. Soc. Am.*, 77(1), 1985.

M. Bouchon and K. Aki. Discrete wave-number representation of seismic-source wave fields. *Bull. Seism. Soc. Am.*, 67:259–277, 1977.

M. Bouchon, M. Campillo, and S. Gaffet. A boundary integral equation - discrete wavenumber representation method to study wave propagation in multilayered media having irregular interfaces. *Geophysics*, 54:1134–1140, 1989.

M. Bouchon, C. A. Schultz, and M. N. Toksöz. A fast implementation of boundary integral equation methods to calculate the propagation of seismic waves in laterally varying layered media. *Bull. Seism. Soc. Am.*, 85:1679–1687, 1995.

J. Bulat. The Rockall Continental Margin: A review of existing seismic data. *British Geological Survey Technical Report WB/91/9*, 1991.

R. Burridge and H. W. Chang. Multimode, one-dimensional wave propagation in a highly discontinuous medium. *Wave Motion*, 11:231–249, 1989.

M. Campillo and M. Bouchon. Synthetic SH seismograms in a laterally varying medium by the discrete wavenumber method. *Geophys. J. R. astr. Soc.*, 83: 307–317, 1985.

J. P. Castagna, M. L. Batzle, and R. L. Eastwood. Relationships between compressional-wave and shear-wave velocities in clastic silicate rocks. *Geophysics*, 50(04):571–581, 1985.

C. Cerjan, D. Kosloff, R. Kosloff, and M Reshef. A nonreflecting boundary condition for discrete acoustic and elastic wave equations. *Geophysics*, 50: 708–705, 1985.

J. T. Cherry and W. R. Hurdlow. Numerical simulation of seismic disturbances. *Geophysics*, 31:33–49, 1966.

P. Christie, I. Gollifer, and D. Cowper. Borehole seismic results from the Lopra deepening project. *Sub-basalt imaging conference, Cambridge: Journal of Conference Abstracts*, 7(2):138–139, 2002.

N. Dancer and N. W. Pillar. Successful sub-basalt imaging with enhanced low frequnecy 3D seismic data: Corrib Field, West of Ireland. *Frontier Exploration of Volcanic Continental Margins, Abstracts of the 2 day international conference, Geological Society of London*, 2002.

A. Dobson, X.-Y. Li, A. Ziolkowski, and E. Liu. Effects of lateral heterogeneity in basalt on seismic waves - a modelling study using the boundary element method. *EAGE 64th Conference and Technical Exhibition, Florence, Italy, 27-30 May 2002, Extended Abstracts*, 2002.

J. Falk. *Ph.D. Thesis: Efficient Seismic Modeling of Small-Scale Inhomogeneities by the Finite Difference Method*. Shaker Publishing, 1998.

J. Falk, E. Tessmer, and D. Gajewski. Tube wave modelling by the finite difference method with varying grid spacing. *Pure and Applied Geophysics*, 148(1/2), 1994.

M. M. Fliedner and R. S. White. Seismic structure of basalt flows from surface seismic data, borehole measurements and synthetic seismograms modelling. *Geophysics*, 66(6):1925–1936, 2001.

M. M. Fliedner and R. S. White. Depth imaging of basalt flows in the Faeroe-Shetland Basin. *Geophys. J. Int.*, 152:353–371, 2003.

J. Fruehn, M. Fliedner, and R. S. White. Integrated wide-angle and near-vertical subbasalt study using large-aperture seismic data from the Faeroe-Shetland region. *Geophysics*, 66(5):1340–1348, 2001.

H. Fujiwara. The fast multipole method for integral equations of seismic scattering problems. *Geophys. J. Int.*, 133:733–782, 1998.

F. Gilbert and G. Backus. Propagator matrices in elastic wave and vibration problems. *Geophysics*, 31:326–332, 1966.

N. Hald and R. Waagstein. Lithology and chemistry of a 2-km sequence of Lower Tertiary tholeiitic lavas drilled on Suduroy, Faeroe Islands (Lopra-1) *in* Noe-Nygaard, A. and Rasmussen, J. Eds., The Deep Drilling Project 1980-1981 in the Faeroe Islands. *Føroya Fródskaparfelag, Tórshavn*, pages 15–38, 1984.

P. Hanssen. *Ph.D. Thesis: The Influence of Basalt Layers on Seismic Wave Propagation*. The University of Edinburgh, 2002.

P. Hanssen. Processing for sub-basalt imaging using a low-frequency setup in the Faroe-Shetland basin. *British Geological Survey Commissioned Report*, 2004.

P. Hanssen and X. Y. Li. The effect of thin layering on sub-basaltic imaging: modelling studies using borehole data. *Edinburgh Anisotropy Project, Research Report*, 8:563–589, 2001.

P. Hanssen, A. Ziolkowski, and X. Y. Li. A quantitative study on the use of converted waves for sub-basalt imaging. *Geophysical Prospecting*, 51:183–193, 2003.

M. Joppen and R. S. White. The structure and subsidence of Rockall Trough from two-ship seismic experiments. *Journal of Geophysical Research*, 95(B12): 19821–19837, 1990.

H. Kawase. Time domain response of a semicircular canyon for incident SV, P, and Rayleigh waves calculated by the discrete wavenumber boundary element method. *Bull. Seism. Soc. Am.*, 78:1415–1437, 2002.

B. L. N. Kennett. *Seismic wave propagation in stratified media*. Cambridge University Press, 1983.

S. Ker and S. Rodriguez. Seismic properties of the Faeroe basalt formations: the LOPRA-1 VSP case study. *Sub-basalt imaging conference, Cambridge: Journal of Conference Abstracts*, 7(2):158–159, 2002.

T. Kerrane, M. van der Baan, J. M. Kendall, and N. Taylor. Imaging sub-basalt structures using converted waves. *Sub-basalt imaging conference, Cambridge: Journal of Conference Abstracts*, 7(2):162–163, 2002.

G. S. Kimbell, J. D. Ritchie, H. Johnson, and R. W. Gatliff. In press: Controls on the structure and evoluation of the NE Atlantic margin revealed by regional 3D gravity modelling. In *Doré A. G. (ed), Petroleum Geology of Northwest Europe: Proceedings of the 6th Conference*. Geological Society, London, 2004.

L. Kiørbie and S. A. Petersen. Seismic investigation of the Faeroe basalts and their substratum*in* Scrutton, R. A. and Stoker, M. S. and Shimmield, G.B. and Tudhope, A. W., The Tectonics, Sedimentation and Palaeoceanography of the North Atlantic Region. *Geological Society Special Publication No. 90*, pages 111–122, 1995.

L. Knopoff and F. Gangi. Seismic reciprocity. *Geophysics*, 24(4):681–691, 1959.

C.F. Lafond, S. Kaculini, and F. Martini. The effects of basalt heterogeneities on seismic imaging of deeper reflectors. *Society of Exploration Geophysicists International Exposition and 69th Annual Meeting, Houston*, 1999.

T. Laier, H. P. Nytoft, O. Jørgensen, and G. H. Isaksen. Hydrocarbon traces in the Tertiary basalts of the Faeroe Islands. *Marine and Petroleum Geology*, 14 (3):257–266, 1997.

X.-Y. Li and C. MacBeth. Imaging beneath basalt using converted waves in marine seismic data. *EAGE 59th Conference and Technical Exhibition, Geneva, Switzerland, 26 May-30 May 1997, Extended Abstracts*, 1997.

X.-Y. Li, C. MacBeth, and K. Hitchen. Using converted shear-waves for imaging beneath basalt in deep water plays. *British Geological Survey Technical Report*, 1997.

S. K. Longshaw, J. Sunderland, and I. Horn. Mode conversion and multiples. *68th Annual International Meeting, Soc. Expl. Geophys., Expanded Abstracts*, 2:1369–1372, 1998.

C.-C. Lu and W. C. Chew. Far field approximation for calculating the RCS of large objects. *Micro. Opt. Tech. Lett*, 8(5):238–240, 1995.

Z. Lunnon, P. Christie, and R. White. An evaluation of peak and bubble tuning in sub-basalt imaging: modelling and results. *65th Mtg. Eur. Assn. Geosci. Eng., Exp. Abs.*, 2003.

H. Mack. Seismic response of Tertiary basalt flows in the northeast Atlantic - a modelling study. *EAGE 59th Conference and Technical Exhibition, Geneva, Switzerland, 26 May-30 May 1997*, 1997.

R. Madariaga. Dynamics of an expanding circular fault. *Bull. Seism. Soc. Am.*, 66:639–666, 1976.

S. Mallick and N. Frazer. Practical aspects of reflectivity modeling. *Geophysics*, 52(10):1355–1364, 1987.

F. Martini. *Ph.D. Thesis: Seismic Imaging Below Basalt.* University College Dublin, 2001.

F. Martini and C. J. Bean. Application of pre-stack wave equation datuming to remove interface scattering in sub-basalt imaging. *First Break*, 20(6):395–403, 2002.

D. B. McInroy, J. D. Ritchie, and R. W. Gatliff. A geological interpretation of the TX01-2A seismic profile: commercial in confidence. *British Geological Survey Commissioned Report*, 2004.

D. C. Mudge and B. Rashid. The geology of the Faeroe Basin area. In *Brooks, J. and Glennie, K. W. (eds) Petroleum Geology of Northwest Europe: Proceedings of the 3rd Conference.*, pages 751–763. Graham and Trotman, London, 1987.

R. F. O'Doherty and N. A. Anstey. Reflections on amplitudes. *Geophys. Prosp.*, 19(03):430–458, 1971.

C. Ortiz-Alemán, F. J. Sánchez-Sesma, J. L. Rodríguez-Zúñiga, and Luzón Francisco. Computing topographical 3D site effects using a fast IBEM/conjugate gradient approach. *Bull. Seis. Soc. Am.*, 88(2):393–399, 1998.

G. Pálmason. Seismic refraction measurements of the basalt lavas of the Faeroe Islands. *Tectonophysics*, 2(6):475–482, 1965.

A. Paul and M. Campillo. Diffraction and conversion of elastic waves at a corrugated interface. *Geophysics*, 53:1415–1424, 1988.

H. A. Pedersen, V. Maupin, and M. Campillo. Wave diffraction in multilayered media with the Indirect Boundary Element Method: application to 3-D diffraction of the long-period surface waves by 2-D lithospheric structures. *Geophysical Journal International*, 125:545–558, 1996.

S. Planke. Geophysical response of flood basalts from analysis of wire line logs: Ocean drilling program site 642, vøring volcanic margin. *J. Geophys. Res.*, 99 (B5):9279–9296, 1994.

S. Planke, E. Alvestad, and O. Eldholm. Seismic characteristics of basaltic extrusive and intrusive rocks. *The Leading Edge*, 18(3):342–348, 1999.

S. Planke and O. G. Flovenz. Seismic properties of flood basalt. *Geophysics for lithology predictions, Norwegian Petr. Soc.*, 1996.

T. Pointer, E. Liu, and J. A. Hudson. Numerical modelling of seismic waves scattered by hydrofractures: application of the indirect boundary element method. *Geophysical Journal International*, 135:289–303, 1998.

W. H. Press, S. A. Teukolsky, W. T. Vetterling, and B. P. Flannery. *Numerical Recipes in FORTRAN: Second Edition*. Cambridge Univeristy Press, 1992.

J. Pujol and S. B. Smithson. Seismic wave attenuation in volcanic rocks from VSP experiments. *Geophysics*, 56(9):1441–1455, 1991.

G. W. Purnell. Imaging beneath a high-velocity layer using converted waves. *Geophysics*, 57(11):1444–1452, 1992.

G. W. Purnell, Y. Shin, G. Hampson, and J. A. McDonald. Effects of interface roughness on wave propagation. *60th Annual International Meeting, Soc. Expl. Geophys., Expanded Abstracts*, pages 1561–1564, 1990.

J. D. Ritchie, R. W. Gatliff, and P. C. Richards. Early Tertiary magmatism in the offshore NW UK margin and surrounds. In *Fleet, A. J. and Boldy, S. A. R., Eds., Petroleum Geology of Northwest Europe: Proceedings of the 5th Conference: Geological Society, London*, pages 573–548, 1999.

E. A. Robinson and S. Treitel. Principles of digital filtering. *Geophysics*, 29(03): 395–404, 1964.

J. T. Rutledge and H. Winkler. Attenuation measurements from vertical seismic profile data: leg 104, site 642. *Proc. Ocean Drill. Program Sci. Results*, 104: 965–972, 1989.

F. J. Sánchez-Sesma and M. Campillo. Diffractions of P, SV, and Rayleigh waves by topographic features: a boundary integral formulation. *Bulletin of the Seismological Society of America*, 81(6):2234–2253, 1991.

F. J. Sánchez-Sesma, M. Campillo, and K. Irikura. A note on the Rayleigh hypothesis and the Aki-Larner method. *Bull. Seis. Soc. America*, 79(6):1995–1999, 1989.

F. J. Sánchez-Sesma and Luzón. Seismic response of three-dimensional alluvial valleys for incident, P, S and Rayleigh waves. *Bull. Seism. Soc. Am.*, 85, 1995.

R. A. Scrutton. Results of a seismic refraction experiment on Rockall Bank. *Nature*, 227:826–827, 1972.

J. R. Smallwood, R. S. White, and R. K. Staples. Deep crustal reflectors under Reydarfjördur, eastern Iceland: crustal accretion above the Iceland mantle plume. *Geophys. J. Int.*, 134:277–290, 1998.

B. Smith, P. Bjørstad, and W. Gropp. *Domain Decomposition: Parallel Multilevel Methods for Elliptic Partial Differential Equations*. Cambridge, 1996.

A. M. Spencer, Ø. Birkland, G. Ø. Knag, and R. Fredsted. Petroleum systems of the Atlantic margin of north-west Europe. In *Fleet, A. J. and Boldy, S. A. R., Eds., Petroleum Geology of Northwest Europe: Proceedings of the 5th Conference: Geological Society, London*, pages 231–246, 1999.

R. Spitzer, R. S. White, and P. A. F. Christie. Sub-basalt imaging along the iSIMM profile - integration of surface and ocean bottom data. *66th Mtg. Eur. Asson. Geosci. Eng., Exp. Abs.*, 2004.

M. S. Stoker, K. Hitchen, and C. C. Graham. *United Kingdom offshore regional report: The geology of the Hebrides and West Shetland shelves, and adjacent deep-water areas*. London: HMSO for the British Geological Survey, 1993.

D. B. Taylor. Double contour integration for transmissions from point sources through anisotropic layers as used in ROCPAC software. *Geophys. J. R. Astr. Soc.*, 91:373–381, 1994.

S. Treitel and E. A. Robinson. Seismic wave propagation in layered media in terms of communication theory. *Geophysics*, 31(1):17–32, 1966.

O. Vilmann, P. Gerstoft, and S. Krenk. High-speed forward modelling applied in seismic data processing. *Ødegaard and Danneskoild-Samsøe ApS, Report 89.238/9*, 1998.

J. Virieux. P-SV wave propagation in heterogeneous media: a velocity stress finite-difference method. *Geophysics*, 51:889–901, 1986.

R. K. Walia and J. M. Bull. Modelling rough interfaces on seismic relfection profiles - the application of fractal concepts. *Geophysical Research Letters*, 24 (16):2067–2070, 1997.

R. S. White. A hot-spot model for early Tertiary volcanism in the N Atlantic *in* Morton, A. C., and Parson, L.M., Eds.,Early Tertiary Volcanism and the Opening of the NE Atlantic. *Geological Society Special Publication No. 39*, pages 3–13, 1988.

R. S. White, P. A. F. Christie, N. J. Kusznir, A. Roberts, A. Davies, N. Hurst, Z. Lunnon, C. J. Parkin, A. W. Roberts, L. K. Smith, R. Spitzer, A. Surendra, and V. Tymms. iSIMM pushes frontiers of marine seismic acquisition. *First Break*, 20, 2002.

R. S. White, J. R. Smallwood, M. M. Fliedner, B. Boslaugh, J. Maresh, and J. Fruehn. Imaging and regional distribution of basalt flows in the Faeroe-Shetland Basin. *Geophysical Prospecting*, 51(1):215–231, 2003.

O. Yilmaz. *Seismic Data Analysis*. Soc. of Expl. Geophys., 2001.

T. Yokoi. On accuracy improvement by the higher order Born approximation for solutions of indirect boundary element method with the sparse matrix approximation: in press. *J. Phys. EartPhys. Earth Planet Int.*, 2003.

T. Yokoi and H. Takenaka. Treatment of an infinitely extended free surface for indirect formulation of the boundary element method. *J. Phys. Earth*, 43: 79–103, 1995.

A. Ziolkowski, Taylor D. B., and R. G. K. Johnston. Marine seismic wavefield measurement to remove sea-surface multiples. *Geophysical Prospecting*, 47(6): 841–870, 1999.

A. Ziolkowski and J. T. Fokkema. Tutorial: The progressive attenuation of high-frequency energy in seismic reflection data. *Geophysical Prospecting*, 34:981–1001, 1986.

A. Ziolkowski, P. Hanssen, R. Gatliff, H. Jakubowicz, A. Dobson, G. Hampson, X.-Y. Li, and E. Liu. Use of low frequencies for sub-basalt imaging. *Geophysical Prospecting*, 51:169–182, 2003.

Appendix A

Green's functions for 2-D isotropic media

A.1 Elastic medium

The displacement in direction i at location $\mathbf{x}$ from a unit body force in direction j at location $\boldsymbol{\xi}$ for P-SV wave motion is given by (Sánchez-Sesma and Campillo, 1991):

$$\hat{G}_{ij}(\mathbf{x},\boldsymbol{\xi}) = \frac{1}{i8\rho}\big[\delta_{ij}A - (2\gamma_i\gamma_j - \delta_{ij})B\big] \qquad i,j = 1,3, \tag{A.1}$$

and

$$\begin{aligned} A &= \frac{H_0^2(k_\alpha r)}{\alpha^2} + \frac{H_0^2(k_\beta r)}{\beta^2}, \\ B &= \frac{H_0^2(k_\alpha r)}{\alpha^2} - \frac{H_0^2(k_\beta r)}{\beta^2}, \end{aligned} \tag{A.2}$$

where ρ is density, α is P-wave velocity, β is S-wave velocity, $k_\alpha = \omega/\alpha$, $k_\beta = \omega/\beta$, $r = \sqrt{(x_1-\xi_1)^2 + (x_3-\xi_3)^2}$, $\gamma_i = (x_i - \xi_i)/r$ and H_n^2 is the Hankel function of the second kind and order n. The equivalent expression for traction is

$$\begin{aligned} \hat{P}_{ij}(\mathbf{x},\boldsymbol{\xi}) = \frac{i\mu}{2\rho r}\Big\{ &\Big[B + \frac{\lambda D(k_\alpha r)}{2\mu\alpha^2}\Big]\gamma_j n_i + \Big[B + \frac{D(k_\beta r)}{2\beta^2}\Big] \\ &\times[\gamma_i n_j + \gamma_k n_k \delta_{ij}] + (C - 4B)\gamma_i\gamma_j\gamma_k n_k\Big\} \end{aligned} \tag{A.3}$$

and

$$C = \frac{D(k_\alpha r)}{\alpha^2} - \frac{D(k_\beta r)}{\beta^2},$$
$$D(p) = pH_1^2(p), \tag{A.4}$$

where $\mathbf{n}$ is the unit normal vector; λ and μ are the Lamé constants where $\lambda = \alpha^2\rho - 2\mu$ and $\mu = \beta^2\rho$.

A.2 Fluid medium

The potential Green's function in a fluid is given by (Pointer et al., 1998):

$$\hat{\Phi}(\mathbf{x}, \boldsymbol{\xi}) = \frac{1}{4i} H_0^2(k_f r), \tag{A.5}$$

where $k_f = \omega/c$ and c is the wave speed in the fluid. At a boundary, the normal displacement Green's function in the fluid is given by:

$$\hat{G}(\mathbf{x}, \boldsymbol{\xi}) = n_i \frac{\partial \hat{\Phi}(\mathbf{x}, \boldsymbol{\xi})}{\partial x_i} = \frac{ik_f}{4} H_1^2(k_f r) n_k \gamma_k. \tag{A.6}$$

The normal traction Green's function in the fluid is:

$$\hat{T}(\mathbf{x}, \boldsymbol{\xi}) = -\rho\omega^2 \hat{\Phi}(\mathbf{x}, \boldsymbol{\xi}) = \frac{i\rho\omega^2}{4} H_0^2(k_f r). \tag{A.7}$$

Appendix B

The reflectivity method

The following description of the reflectivity method comes from Kennett (1983), and Mallick and Frazer (1987).

The reflectivity method is specific to a stratified earth model of plane horizontal layers. It works by solving the the equation of motion (see Chapter 3):

$$\rho \ddot{u}_i = f_i + \tau_{ij,j}, \tag{B.1}$$

and Hooke's law

$$\tau_{ij} = c_{ijkl} e_{kl} = c_{ijkl} u_{k,l}, \tag{B.2}$$

where ρ is density, f_i is body force density, τ_{ij} is the stress tensor, e_{kl} is the strain tensor, u_k is displacement and c_{ijkl} is the elastic tensor.

A cylindrical coordinate system is adopted (r, ϕ, z) where r is the radial component, ϕ is the azimuthal component and z is the depth.

For the modelling in this thesis, only isotropic models are considered. For isotropy, Hooke's law is simplified to

$$\tau_{ij} = \lambda \delta_{ij} e_{kk} + 2\mu e_{ij}, \tag{B.3}$$

where λ and μ are the Lamé parameters. With these constraints, P-SV wave motion (motion in the radial and vertical directions) is decoupled from SH wave motion (motion in the azimuthal direction). Two separate systems of equations are set up (see Kennett, 1983 for details), one for P-SV wave motion which comprises 4 equations, and one for SH wave motion which comprises 2 equations. These equations still involve partial derivatives with respect to the horizontal

coordinates and time. It is possible to reduce these equations to a set of equations involving derivatives only in depth.

In order to achieve this, the problem is transformed using a Fourier-Hankel transform:

$$\begin{aligned} F\text{–}H_m[\Psi] &= \hat{\Psi}(k,m,\omega) \\ &= \frac{1}{2\pi}\int_{-\infty}^{\infty} dt\ e^{i\omega t}\int_{0}^{\infty} dr\ rJ_m(kr)\int_{-\pi}^{\pi} d\phi\ e^{-im\phi}\Psi(r,\phi,t), \end{aligned} \tag{B.4}$$

where k is horizontal wavenumber, ω is angular frequency, and J_m is the Bessel function of the first kind and of order m.

In the Fourier-Hankel domain, the displacements in a medium are replaced by an integral of cylindrical waves over wavenumber and azimuth. The system of displacement-traction equations becomes

$$\partial_z \mathbf{b}(k,m,z,\omega) = \omega \mathbf{A}(p,z)\mathbf{b}(k,m,z,\omega) + \mathbf{F}(k,m,z,\omega). \tag{B.5}$$

where $\mathbf{b}$ is a vector containing the unknown values of traction and displacement, $\mathbf{A}$ is a matrix involving P- and S-wave velocities and $\mathbf{F}$ is a source vector.

The cylindrical-wave decomposition allows the use of the propagator matrix formulations of Gilbert and Backus (1966). In this method the displacements and tractions in each layer are seen as a combination of up-going and down-going waves. The boundary conditions for the formulation are that there is zero traction at the uppermost interface and that there are no up-going waves in the half-space below the lowest interface in the model. This formulation is used to solve the above equation for any number of horizontal planar layers, by assuming continuity of traction and displacement at each interface. The method proceeds recursively from the lowest interface to the highest, for a given frequency ω and horizontal wavenumber k.

Once the $\mathbf{b}$ matrices have been computed for all required wavenumbers, frequencies, and the required number of azimuthal orders (depending on the type of source), the following transform is performed to yield the response in the time domain:

$$u_z(r,\phi,z,t) = \frac{1}{2\pi}\int_{-\infty}^{\infty} d\omega e^{-i\omega t}\int_{0}^{\infty} dk\ k\sum_m U(m,z)J_m(kr)e^{im\omega}, \tag{B.6}$$

where U is the vertical displacement component of the matrix $\mathbf{b}$.

In the reflectivity method, it is the reflectivity of a stack of layers which is found. Consider the simple case of a succession of planar layers sandwiched between two half spaces. There is a reflectivity matrix:

$$M = \begin{bmatrix} PP & SP \\ PS & SS \end{bmatrix}. \tag{B.7}$$

for the top and base of each layer in the succession and for each wavenumber. The reflectivity matrices at the top and base of a layer are connected by a phase matrix which represents simply the traveltime through that layer. The reflectivity matrices of one layer and the next are connected by a propagator matrix equation. This matrix equation requires the reflection and transmission coefficients for the interface between the two layers to be known. Assuming no up-coming waves in the lower half-space, the propagator matrices can be used recursively to find the reflectivity matrix at the base of the upper half space. It is then simple to integrate over wave number as before and compute the displacement in the upper half space.

The transmission matrices through the succession can be found in a similar manner.

Appendix C

The finite difference method

Finite difference methods were being used as early as 1966 (Cherry and Hurdlow). The following description of the finite difference method is taken from Virieux (1986) and Falk (1998).

The finite difference method works by approximating the equation of motion (see Chapter 3), and Hooke's law. These equations for a 2-D isotropic medium with a horizontal axis x and a vertical axis z pointing downwards are as follows:

$$\begin{aligned} \rho\frac{\partial^2 u_x}{\partial t^2} &= \frac{\partial \tau_{xx}}{\partial x} + \frac{\partial \tau_{xz}}{\partial z}, \\ \rho\frac{\partial^2 u_z}{\partial t^2} &= \frac{\partial \tau_{xz}}{\partial x} + \frac{\partial \tau_{zz}}{\partial z}, \end{aligned} \tag{C.1}$$

and

$$\begin{aligned} \tau_{xx} &= (\lambda + 2\mu)\frac{\partial u_x}{\partial x} + \lambda\frac{\partial u_z}{\partial z}, \\ \tau_{zz} &= (\lambda + 2\mu)\frac{\partial u_z}{\partial z} + \lambda\frac{\partial u_x}{\partial x}, \\ \tau_{xz} &= \mu\Big(\frac{\partial u_x}{\partial z} + \frac{\partial u_z}{\partial x}\Big), \end{aligned} \tag{C.2}$$

where the body force term has been omitted; (u_x, u_z) is the displacement vector, τ_{xx} is the stress tensor ρ is the density, and λ and μ are the Lamé parameters.

These equations are solved by approximating the spatial and temporal derivatives. The approach by Virieux (1986) is to transform the system of equations

into equations involving first order derivatives in time:

$$\begin{aligned} \frac{\partial v_x}{\partial t} &= b\Big(\frac{\partial \tau_{xx}}{\partial x} + \frac{\partial \tau_{xz}}{\partial z}\Big), \\ \frac{\partial v_z}{\partial t} &= b\Big(\frac{\partial \tau_{xz}}{\partial x} + \frac{\partial \tau_{zz}}{\partial z}\Big), \end{aligned} \tag{C.3}$$

and

$$\begin{aligned} \frac{\partial \tau_{xx}}{\partial t} &= (\lambda + 2\mu)\frac{\partial v_x}{\partial x} + \lambda \frac{\partial v_z}{\partial z}, \\ \frac{\partial \tau_{zz}}{\partial t} &= (\lambda + 2\mu)\frac{\partial v_z}{\partial z} + \lambda \frac{\partial v_x}{\partial x}, \\ \frac{\partial \tau_{xz}}{\partial t} &= \mu\Big(\frac{\partial v_x}{\partial z} + \frac{\partial v_z}{\partial x}\Big), \end{aligned} \tag{C.4}$$

where (v_x, v_z) is the velocity vector and b, the lightness or buoyancy, is the inverse of density.

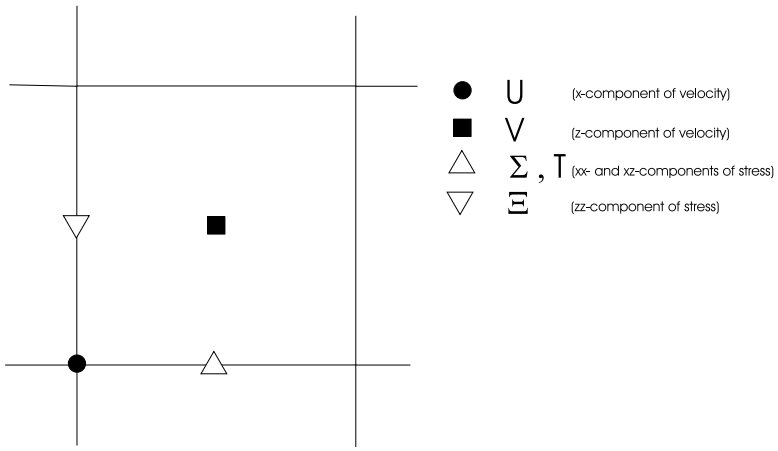

Figure C.1: Discretization of the medium on a staggered grid after Virieux (1986). Black symbols are for velocities at time $k\Delta t$. White symbols are for stresses at time $(k+1/2)\Delta t$.

The model is discretized into a grid. The grid scheme used by Virieux (1986) and originally by Madariaga (1976) is known as a staggered grid because the displacement and stress are not evaluated at the same points in the grid (Figure C.1). The system is also staggered in time since displacements and stresses are also evaluated at different times. With this discretization of the model the above

equations become:

$$\begin{aligned} U_{i,j}^{k+1/2} &= U_{i,j}^{k-1/2} + B\frac{\Delta t}{\Delta x}(\Sigma_{i+1/2,j}^{k} - \Sigma_{i-1/2,j}^{k}) \\ &\quad + B\frac{\Delta t}{\Delta z}(\Xi_{i,j+1/2}^{k} - \Xi_{i,j-1/2}^{k}), \\ V_{i+1/2,j+1/2}^{k+1/2} &= V_{i+1/2,j+1/2}^{k-1/2} + B\frac{\Delta t}{\Delta x}(\Xi_{i+1,j+1/2}^{k} - \Xi_{i,j+1/2}^{k}) \\ &\quad + B\frac{\Delta t}{\Delta z}(T_{i+1/2,j+1}^{k} - T_{i+1/2,j}^{k}), \end{aligned} \tag{C.5}$$

and

$$\begin{aligned} \Sigma_{i+1/2,j}^{k+1} &= \Sigma_{i+1/2,j}^{k} + (L+2M)\frac{\Delta t}{\Delta x}(U_{i+1,j}^{k+1/2} - U_{i,j}^{k+1/2}) \\ &\quad + L\frac{\Delta t}{\Delta z}(V_{i,j+1}^{k+1/2} - V_{i,j}^{k+1/2}), \\ T_{i+1/2,j}^{k+1} &= T_{i+1/2,j}^{k} + (L+2M)\frac{\Delta t}{\Delta z}(V_{i,j+1}^{k+1/2} - V_{i,j}^{k+1/2}) \\ &\quad + L\frac{\Delta t}{\Delta x}(U_{i+1,j}^{k+1/2} - U_{i,j}^{k+1/2}), \\ \Xi_{i,j+1/2}^{k+1} &= \Xi_{i,j+1/2}^{k} + M\frac{\Delta t}{\Delta z}(U_{i,j+1}^{k+1/2} - U_{i,j}^{k+1/2}) \\ &\quad + M\frac{\Delta t}{\Delta x}(V_{i+1,j}^{k+1/2} - V_{i,j}^{k+1/2}). \end{aligned} \tag{C.6}$$

where k is the index for time discretization, i for x-axis discretization and j for z-axis discretization, Δt is the grid step in time, Δx and Δz are the grid steps for the x-axis and for the z-axis respectively. Velocity $(U, V) = (v_x, v_z)$ at time $(k + 1/2)\Delta t$, and stress $(\Sigma, \Xi, T) = (\tau_{xx}, \tau_{zz}, \tau_{xz})$ at time $(k + 1)\Delta t$ are computed explicitly from velocity at time $(k - 1/2)\Delta t$ and stress at time $k\Delta t$. B is the buoyancy inside the medium and L, M are the Lamé paramters λ and μ.

The initial conditions for this scheme are zero stress and zero velocity everywhere in the medium for $t = 0$. An explosive source is included in the model by adding incremental amplitudes to the stresses Σ and Ξ at the source location.

Important factors in FD modelling are the selection of the grid spacing and time discretization. These must be sufficiently small to avoid grid dispersion which causes inaccurate results. However, when the grid-spacing is smaller, more

grid-points are required to cover the model area. This increases computation time.

The FD scheme used in ELA2D (Falk et al., 1994) is similar to the one outlined above though it is based on direct approximations of Equations C.1 and C.2. For a fourth-order time integration (used in Chapter 4) the following time sample spacing is suggested (Falk, 1998)

$$\Delta t = \frac{2.422}{v_{max}} \sqrt{\frac{2.48^2}{\Delta x^2} + \frac{2.48^2}{\Delta z^2}}^{-1} \tag{C.7}$$

where v_{max} is the highest phase velocity in the model. The following spatial sampling is suggested

$$\Delta x < \frac{v_{min}}{5 f_{max}} \tag{C.8}$$

where v_{min} is the lowest phase velocity in the model and f_{max} is the cut-off frequency of the source wavelet.

Appendix D

The Z-transform

D.1 The Z-transform

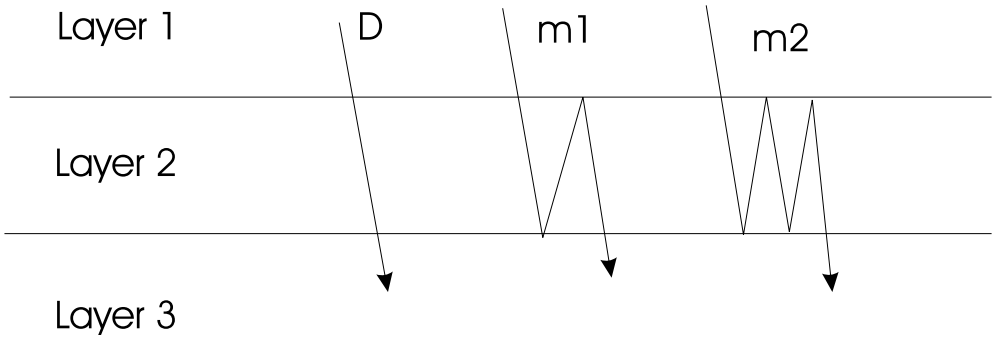

Figure D.1: Thin-layer model with normal incidence direct raypath (D) and two multiple raypaths (m1 and m2). Raypaths drawn at an angle for clarity.

Following a similar formulation to that of Ziolkowski and Fokkema (1986), consider the thin layer depicted in Figure D.1. The aim is to find the frequency response for a number of raypaths. An impulsive plane pressure wave of unit amplitude is normally incident on the top interface at time t=0. I begin by writing down an expression for the time domain series which describes the pressure at the top of layer 3 when only the direct ray D and the first two peg-leg multiples are considered:

$$x_t = T_{12}T_{23}(Z_0 + R_{21}R_{23}Z_1 + (R_{21}R_{23})^2 Z_2), \tag{D.1}$$

where Z_0 represents a time delay equal to the time taken for ray D to reach the top of layer 1. Z_1 and Z_2 represent a time delay equal to the time taken for

rays $m1$ and $m2$ to reach the top of layer 3 respectively. T_{ab} is the transmission coefficient for a ray passing from layer a to layer b and is given by

$$T_{ab} = \frac{\rho_b \alpha_b}{\rho_b \alpha_b + \rho_a \alpha_a}, \tag{D.2}$$

where α_a is the P-wave velocity and ρ_a is the density in layer a. R_{ab} is the reflection coefficient and is given by

$$R_{ab} = \frac{\rho_b \alpha_b - \rho_a \alpha_a}{\rho_b \alpha_b + \rho_a \alpha_a}. \tag{D.3}$$

The frequency response can easily be obtained from Equation D.1 by setting Z to be:

$$Z_n = e^{i\omega \Delta t_n} \tag{D.4}$$

where $i = \sqrt{-1}$, ω is angular frequency and Δt_n is a time delay associated with Z_n (Robinson and Treitel, 1964). The frequency domain response can be written as:

$$T(\omega) = T_{12} T_{23} (1 + R_{21} R_{23} e^{i\omega \Delta t_1} + (R_{21} R_{23})^2 e^{i\omega \Delta t_2}). \tag{D.5}$$

The modulus of this expression is taken to find the amplitude response.

To find the transmission response when more multiple paths are considered, the expression for these must simply be added to Equation D.1 with the correct amplitude and delay applied.

To find the total response for a single thin layer including all multiples, an infinite series is formed which converges to

$$T(\omega) = \frac{(1 - R_{12}^2) e^{i\omega \Delta t}}{1 - R_{12}^2 e^{2i\omega \Delta t}}, \tag{D.6}$$

where Δt is the traveltime through the thin layer (Ziolkowski and Fokkema, 1986).

Appendix E

The Treitel and Robinson method

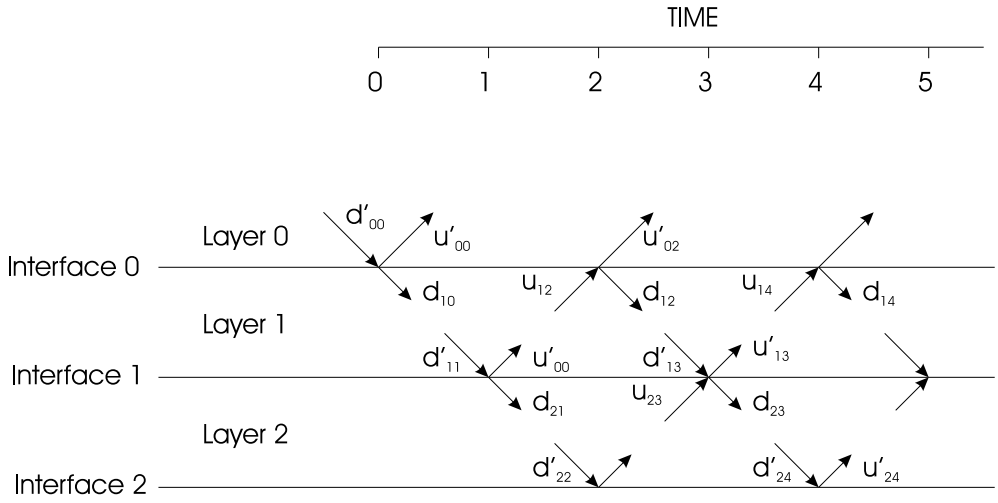

Figure E.1: Downgoing and upgoing raypaths in layered media at normal incidence, after Treitel and Robinson (1966). Horizontal axis is time.

This description follows the formulation given in Treitel and Robinson (1966). The method enables fast computation of the transmission or reflection response for a number of layers at normal incidence. Code based on this method is used in Chapter 8 for some simple basalt models.

Figure E.1 shows a number of horizontal layers which all have the same vertical travetime. The figure shows all possible up- and down-going wavepaths in the layers after a source has been set off at the base of layer 0 at a time $t = 0$.

The downgoing waves at the top of a particular layer n may be summarised

in the following way:

$$D_n(Z) = d_{n,n-1}Z^{n-1} + d_{n,n+1}Z^{n+1} + d_{n,n+3}Z^{n+3} + ... \tag{E.1}$$

where Z represents a time delay equal to the traveltime through one layer. The remaining down- and up-going waves can be described in a similar way.

For interface n at time instant j the following two equations are valid

$$u'_{n,j} = R_n d'_{n,j} + T'_n u_{n+1,j}. \tag{E.2}$$

$$d_{n+1,j} = T_n d'_{n,j} + R_n u_{n+1,j}, \tag{E.3}$$

where T and R are the transmission and reflection coefficients for interface n. After some manipulation of Equations E.2 and E.3 (see Treitel and Robinson, 1966) the following equations are derived:

$$T_n D_n(Z) = Z^{-1} D_{n+1}(Z) + R_n Z^{-1} U_{n+1}(Z) \tag{E.4}$$

$$T_n U_n(Z) = R_n Z D_{n+1}(Z) + Z U_{n+1}(Z) \tag{E.5}$$

These equations can be written in matrix form as:

$$\begin{bmatrix} D_n(Z) \\ U_n(Z) \end{bmatrix} = M_n \begin{bmatrix} D_{n+1}(Z) \\ U_{n+1}(Z) \end{bmatrix}, \tag{E.6}$$

where

$$M_n = \begin{bmatrix} Z^{-1}/T_n & R_n Z^{-1}/T_n \\ R_n Z/T_n & Z/T_n \end{bmatrix}. \tag{E.7}$$

For interface zero we have

$$\begin{bmatrix} D'_0(Z) \\ U'_0(Z) \end{bmatrix} = N_0 \begin{bmatrix} D_1(Z) \\ U_1(Z) \end{bmatrix}, \tag{E.8}$$

where

$$N_0 = \begin{bmatrix} 1/T_0 & R_0/T_0 \\ R_0/T_0 & 1/T_0 \end{bmatrix}. \tag{E.9}$$

A combination of these matrices can be used to find relationships between

layers which are far apart:

$$\begin{bmatrix} D_0'(Z) \\ U_0'(Z) \end{bmatrix} = N_0 M_1 M_2 M_3 M_4 \begin{bmatrix} D_5(Z) \\ U_5(Z) \end{bmatrix}, \tag{E.10}$$

If we write the product of all the matrices between layer 0 and layer N as Q_n and assume an impulse source at the base of layer 0 at time $t = 0$ then we have:

$$\begin{bmatrix} 1 \\ U_0'(Z) \end{bmatrix} = Q_n \begin{bmatrix} D_{N+1}(Z) \\ 0 \end{bmatrix}. \tag{E.11}$$

There can be no up-coming waves in layer $N + 1$ since we define that as a half-space and there is no reflecting interface in it. To solve for D_{N+1} is now trivial. The frequency domain transmission response is found simply by setting $Z = e^{i\omega\delta t}$, where δt is a unit of time small enough that all sequences of layering can be defined with reasonable accuracy.